

Controlling the Formation of Vesicle Structures and Their Fixation by Polymerization

vorgelegt von

Master of Science - Chemistry

Hacer Yalcinkaya

geboren in Of, Türkei

von der Fakultät II - Mathematik und Naturwissenschaften

der Technischen Universität Berlin

zur Erlangung des akademischen Grades

Doktor der Naturwissenschaften

-Dr. rer. nat.-

genehmigte Dissertation

Promotionsausschuss

Vorsitzender: Prof. Dr. Reinhard Schomäcker (Technische Universität Berlin)

Gutachter: Prof. Dr. Michael Gradzielski (Technische Universität Berlin)

Gutachter: Prof. Dr. Helmut Schlaad (Universität Potsdam)

Tag der wissenschaftlichen Aussprache: 04.03.2019

Berlin 2019

*To Yusuf Yalçınkaya
(31.10.2018)*

Acknowledgements

First of all, I would like to acknowledge my supervisor Prof. Dr. Michael Gradzielski for his endless support, valuable guidance, and advices during my PhD work. I am very grateful for being a member of his research team in Berlin and greatly appreciate his scientific discussions as well as his friendly contributions on my professional and personal times during my PhD.

I would like to thank Prof. Dr. Helmut Schlaad for kindly being a reviewer of the present thesis. I am also thankful to Prof. Dr. Reinhard Schomäcker for being the chairman of the examination of this work. I am very grateful to Dr. Olga Koshkina for her friendly help on reading and correcting the thesis and her fruitful inputs and discussions.

I am thankful to Prof. Thomas Zemb (Marcoule, France) and Dr. Christoph Herfurth (Fraunhofer IAP, Potsdam) for their valuable scientific discussions and advices on the present work. I am especially grateful to Prof. Yeshayahu Talmon (Technion, Haifa, Israel) and his student Maor Ram-on for cryo-TEM measurements together with his very helpful discussions and advices. I am additionally very thankful to Dr. Ingo Hoffmann for NSE measurements, later his friendly help on analysing and interpreting of the data.

I am deeply thankful to Dr. Katharina Bressel, for all her scientific guidance, discussing many times in patience, and encouraging me almost my entire PhD time.

I have appreciated a lot to work with many people during the neutron beamtimes. As local contacts during SANS beamtimes I would like to thank Dr. Artem Feoktystov, Dr. Gaetano Mangiapia and Dr. Marie-Sousai Appavou from MLZ, Garching; Dr. Peter Lindner and Dr. Sylvain Prevost from ILL, Grenoble. I have had the pleasure to know them and work with them and am grateful for all their support and scientific inputs.

I would like to thank Dr. Daniela Fliegner who has encouraged me a lot, willing to listen and help me with her very friendly advices.

I am very much grateful to our secretaries Maria Bühlh and Petra Erdmann, CTA's Jana Lutzki, Michaela Dzionara and Dr. Rene Straßnik for all their help to have a PhD time free of any administrative, technical and experimental problems.

I am also thankful to Sven Thiel for rheology measurements and Michaela Dzionara for NMR measurements.

Moreover, I would like to thank all the members of Stranski Laboratorium for their kindness and friendship during my time in Berlin; especially my officemate Sven Riemar and Dr. Leonardo Chiappisi for their friendly support, generosity and scientific inputs.

I would like to acknowledge the financial support by the Deutsche Forschungsgemeinschaft (DFG) via the grant GR1030/17-1 that gave me the opportunity to work on this PhD project.

Special thanks to my 4F: Funda and Fulya Boztas, Fatma Ilgen and Fatma Durmus. Without their support despite the distance, it would not be possible to have such success. I am very grateful to my dear friend whom I know since my childhood, Dr. Nazmiye Dönmez for her endless support. Additionally, I want to thank a lot to my refik-i hub Mojdeh Heidari and zuzu Christoph Bartsch for our very nice friendship, their support and endless encouragement. My dear friend Tuna from Bremen and Elif Gönül who was there all my PhD time listening and advising me with all her kindness during our long Berlin walks, thank you so much.

Last but not least, I am deeply grateful to my entire family from 3 countries, my mum and dad, Rahime and Hikmet Yalcinkaya, who trusted and supported me during my whole life in patience; my aunt Ayten and her daughter Meltem for their endless support and being as a real family to me in Germany, Aysegül and Mesut for being that nice siblings of me. I am very thankful to Cenk Olgun for his continuous encouragement, valuable help in any case, and also proofreading of the present thesis. I am very much grateful to all the above-mentioned people for their love, trust and support.

Publications

Some parts of this thesis have been or will be published as:

- H. Yalcinkaya, A. Feoktystov, M. Gradzielski, *Formation of Well-Defined Vesicles by Styrene Addition to a Nonionic Surfactant and their Polymerization Leading to Viscous Hybrid System*, Langmuir (2018), 34 (31), 9184-9194. **DOI:** 10.1021/acs.langmuir.8b01377.
- H. Yalcinkaya, K. Bressel, P. Lindner, M. Gradzielski, *Controlled Formation of Vesicles with Added Styrene and their Fixation by Polymerization*, Journal of Colloids and Interface Science, (2018), 531, 672-680. **DOI:** 10.1016/j.jcis.2018.07.097.
- H. Yalcinkaya, G. Mangiapia, M.-S. Appavou, I. Hoffmann, M. Ram-on, Y. Talmon, M. Gradzielski, *Formation of Vesicle Templated Polymer Nanopcapsules and Calcein Encapsulation*, (in prep.)

Other publications:

- L. Chiappisi, H. Yalcinkaya, V. K. Gopalakrishnan, M. Gradzielski, T. Zemb, *Catanionic surfactant systems-thermodynamic and structural conditions revisited*, Colloid Polymer Science, (2015), 293, 3131-3143. **DOI:** 10.1007/s00396-015-3739-9.

Table of Contents

1	Introduction	1
1.1	Theory	1
1.1.1	Colloidal Forces	2
1.1.2	Micelles	5
1.1.3	Vesicles	7
2	Motivation	17
3	Materials and Methods	21
3.1	Methods	21
3.1.1	Density	21
3.1.2	Refractivity Measurements	21
3.1.3	Refractive Index Increment Measurements	21
3.1.4	Viscosity	22
3.1.5	Light Scattering	22
3.1.6	Small Angle Neutron Scattering	25
3.1.7	Neutron Spin-Echo Spectroscopy (NSE)	33
3.1.8	Cryogenic Transmission Electron Microscopy (cryo-TEM)	34
3.1.9	Rheology	35
3.1.10	Nuclear Magnetic Resonance Spectroscopy (NMR)	36
3.1.11	UV-vis Spectrometry	37
3.1.12	Fluorescence Spectroscopy	37
3.2	Materials and Experimental	39
3.2.1	Chemicals	39
3.2.2	Sample Preparation	44
4	TDMAO/L35/Styrene System	47
	Introduction	47
4.1	TDMAO/L35 /Styrene	48
4.1.1	Phase Behaviour	48
4.1.2	Light Scattering	50
4.1.3	Small Angle Neutron Scattering (SANS)	56
4.2	Polymerization of the TDMAO/L35/Styrene System	62
4.2.1	Nuclear Magnetic Resonance (NMR)	63
4.2.2	Phase Behaviour	63
4.2.3	Small Angle Neutron Scattering (SANS)	64
4.2.4	Rheology	65
4.3	Summary	68
5	TDMAO/LiPFOS/L35/Styrene System	71

Introduction	71
5.1 TDMAO/LiPFOS/L35/Styrene	72
5.1.1 Phase Behaviour	72
5.1.2 Light Scattering	74
5.1.3 Small Angle Neutron Scattering (SANS).....	77
5.2 Polymerization of the TDMAO/LiPFOS/L35/Styrene System	79
5.2.1 Phase Behaviour	79
5.2.2 Light Scattering	80
5.2.3 Small Angle Neutron Scattering (SANS).....	82
5.2.4 Nuclear Magnetic Resonance (NMR)	83
5.3 Summary	85
6 The Effect of Acrylate Monomers.....	87
Introduction	87
6.1 TDMAO/L35/Acrylate System	88
6.1.1 Phase Behaviour	88
6.1.2 Light Scattering	90
6.1.3 Small Angle Neutron Scattering (SANS).....	93
6.2 TDMAO/LiPFOS/L35/Acrylate Monomers.....	99
6.2.1 Phase Behaviour	99
6.2.2 Light Scattering	101
6.2.3 Small Angle Neutron Scattering (SANS).....	103
6.3 Polymerization of the TDMAO/LiPFOS/L35/Hexyl Acrylate System.....	111
6.3.1 Phase Behaviour	111
6.3.2 Nuclear Magnetic Resonance (NMR)	112
6.3.3 Light Scattering	114
6.3.4 Small Angle Neutron Scattering (SANS).....	117
6.3.5 Cryogenic Electron Microscopy (Cryo-TEM)	120
6.3.6 Neutron Spin Echo (NSE)	123
6.3.7 Encapsulation Efficiency.....	126
6.4 Summary	132
7 Summary and Outlook.....	135
8 References	138
9 Appendix	151
9.1 Appendix of Chapter 4	151
9.1.1 Refractive Index Increment	151
9.1.2 Determination of Aggregation Numbers	152
9.1.3 Density of the aggregates	152
9.1.4 Kratky-Porod Plots	153

9.1.5	Small Angle Neutron Scattering (SANS) of Polymerized Samples	155
9.2	Appendix of Chapter 5	156
9.2.1	Refractive Index Increment	156
9.2.2	Kratky-Porod Plots	156
9.2.3	Small Angle Neutron Scattering (SANS) of Samples after 1.5 Years.....	159
9.2.4	Small Angle Neutron Scattering (SANS) of samples before and after polymerization 160	
9.2.5	Calculation of the Polymer Shell Thickness.....	162
9.3	Appendix of Chapter 6	163
9.3.1	Appendix to Studies with Dodecyl Acrylate Monomer	163
9.3.2	Appendix to Studies with Isooctyl Acrylate Monomer	164
9.3.3	Appendix to Studies with Hexyl Acrylate Monomer	165

Abstract

In recent years, nanostructures have drawn much interest due to their potential applications in biomedicine, energy conversion, detergency or electronics. Controlling their formation and stability is one of the key issues to obtain such versatile structures with enhanced morphological properties. Especially vesicles are interesting nanostructures with their hollow spherical geometry, allowing encapsulation or transportation of hydrophobic or hydrophilic agents. These structures can be enriched with the aid of polymers, either supporting the structures from the outside or strengthening the inner side of their hydrophobic membrane through the insertion of polymerizable monomers.

In that context, a spontaneously formed model vesicle system from nonionic tetradecyldimethylamine oxide (TDMAO), anionic perfluoro surfactant (LiPFOS), and Pluronic L35 copolymer was comprehensively studied in order to be stabilized by polymerization and further used as nanocarriers. Earlier studies had shown that this system generates small, monodisperse and well-defined vesicles. We have used this model system as a template and by inserting various hydrophobic monomers into their bilayer, the effect of monomer and its polymerization on the initial nanostructures were investigated systematically. For that purpose, hydrophobic monomers (styrene, butyl-, hexyl-, dodecyl-, and isoocetyl acrylate) were dissolved into the micellar TDMAO/L35 mixture prior to the vesicle formation. Then monomer laden vesicles were prepared by mixing them with LiPFOS. Subsequently, structures became permanently fixed by UV initiated polymerization process under mild conditions, in water and at 18 °C. Then the systems were characterized elaborately using different methods such as turbidity, UV-vis, Light Scattering (LS), Small Angle Neutron Scattering (SANS), rheology, Nuclear Magnetic Resonance (NMR), Cryogenic Transmission Electron Microscopy (cryo-TEM), Neutron Spin-Echo (NSE) and fluorescence spectroscopy.

In particular, scattering experiments revealed an interesting effect of styrene monomer in micellar TDMAO/L35 mixtures which induces a structural evolution from rod-like micelles to vesicles and then to the microemulsion droplets along with increasing the monomer concentration. When polymerization was applied to the vesicle regime, it generated viscous systems, which contain worm-like aggregates. On the other hand, it was shown by SANS experiments that microemulsions with high styrene amounts lead to nanolattices with retaining their size after polymerization. Secondly, it was shown that in the presence of LiPFOS, styrene

loaded vesicles were successfully stabilized via polymerization, yielding nanocapsules with larger sizes and higher polydispersity values than the initial system.

As a third approach acrylate monomers in general showed an explicit transition from monomer dissolved micelles to the vesicles, keeping the low polydispersity of the model vesicle system. Among with the other acrylates, hexyl acrylate did not show any disruptive effect on the formation of well-defined vesicles during its loading into the hydrophobic membrane. Accordingly, small, and monodisperse monomer loaded vesicles were formed already with low monomer content (10-30 mM). Therefore, hexyl acrylate was chosen for fixating the structures via polymerization and structural fixation was confirmed by light scattering, SANS and cryo-TEM measurements. In the last step, the encapsulation properties of the formed polymeric nanocapsules were examined. Prepared nanocarriers were loaded with calcein, a water-soluble fluorescence dye, which can be entrapped into the vesicle core and outside aqueous media. Quenching of the untrapped calcein in the presence of Cobalt (II) chloride, allowed us to obtain the encapsulation efficiency of these polymeric nanocapsules. As a result, it was shown that polymer stabilized vesicles have higher efficiency for being used as nanocarrier system.

Zusammenfassung

In den letzten Jahren haben nanostrukturierte Systeme aufgrund ihrer potenziellen Anwendungen in Biomedizin, Energieumwandlung, Waschprozessen oder Elektronik viel Interesse geweckt. Die Kontrolle ihrer Bildung und Stabilität ist eines der Hauptprobleme, um solche vielseitigen Strukturen mit verbesserten morphologischen Eigenschaften zu erhalten. Insbesondere Vesikel sind interessante Nanostrukturen mit ihrer hohlkugelförmigen Geometrie, die die Einkapselung oder den Transport von hydrophoben oder hydrophilen Agentien ermöglicht. Diese Strukturen können mit Hilfe von Polymeren modifiziert werden, die entweder die Strukturen von außen unterstützen oder die Innenseite ihrer hydrophoben Membran durch die Einführung von polymerisierbaren Monomeren verstärken.

In diesem Zusammenhang wurde ein sich spontan bildendes Modellvesikelsystem aus nichtionischem Tetradecyldimethylaminoxid (TDMAO), anionischem Perfluortensid (LiPFOS) und Pluronic L35 Copolymer umfassend untersucht, um es durch Polymerisation zu stabilisieren und als Nanoträger weiter zu verwenden. Frühere Studien hatten gezeigt, dass dieses System kleine, monodisperse und wohldefinierte Vesikel erzeugt. In dieser Arbeit wurde dieses Modellsystem als Templat verwendet und der Zusatz verschiedener hydrophober Monomere in die Doppelschicht bezüglich des Einflusses von Monomer und des folgenden Polymerisationsprozesses auf die anfänglich vorliegenden Nanostrukturen systematisch untersucht. Zu diesem Zweck wurden unterschiedliche hydrophobe Monomere (Styrol, Butyl-, Hexyl-, Dodecyl- und Isooctylacrylat) vor der Vesikelbildung in der mizellaren TDMAO / L35-Mischung gelöst. Monomer beladene Vesikel wurden dann hergestellt, indem sie mit LiPFOS gemischt wurden. Anschließend wurden diese Strukturen unter milden Bedingungen in Wasser durch UV-Licht bei 18 °C polymerisiert. Die Systeme wurden umfassend mit verschiedenen Methoden wie Trübung, UV-Vis, Lichtstreuung (LS), Kleinwinkel-Neutronenstreuung (SANS), Rheologie, Kernspinresonanz (NMR), Kryo-Transmissionselektronenmikroskopie (Kryo-TEM), Neutronenspin-Echo (NSE) und Fluoreszenzspektroskopie charakterisiert.

Insbesondere Streuexperimente zeigten eine interessante Wirkung von Styrol Monomer auf mizellare TDMAO / L35-Gemische, nämlich mit wachsender Monomerkonzentration erfolgt eine strukturelle Entwicklung von stäbchenförmigen Mizellen zu Vesikeln und dann zu den

Mikroemulsionströpfchen. Polymerisation im Vesikelregime führte zu viskosen Systemen, die wurmartige Aggregate enthalten. Dagegen zeigten SANS-Experimente, dass die Polymerisation von Mikroemulsionen mit hohem Styrolanteil zu Nanolatices führt, wobei die Größe erhalten bleibt. Zweitens wurde gezeigt, dass in Gegenwart von LiPFOS styrolbeladene Vesikel erfolgreich durch Polymerisation stabilisiert wurden, was zu größeren Nanokapseln mit höheren Polydispersitätswerten als das ursprüngliche System führte.

Als dritten Ansatz zeigten Acrylatmonomere im Allgemeinen einen expliziten Übergang von gelösten Monomermizellen zu Vesikeln, wobei die geringe Polydispersität des Modellsystems erhalten blieb. Von den Acrylaten war Hexylacrylat am geeignetsten und die Beladung der hydrophoben Membran zeigte keine störende Wirkung auf die Bildung gut definierter Vesikel. Dementsprechend wurden kleine und monodisperse monomerbeladene Vesikel bereits mit geringem Monomergehalt (10-30 mM) gebildet. Daher wurde Hexylacrylat zum Fixieren der Strukturen durch Polymerisation ausgewählt und die strukturelle Fixierung wurde durch Lichtstreuung, SANS- und Kryo-TEM-Messungen bestätigt. Im letzten Schritt wurden die Verkapselungseigenschaften der gebildeten polymeren Nanokapseln untersucht. Zubereitete Nanoträger wurden mit Calcein beladen, einem wasserlöslichen Fluoreszenzfarbstoff, der im Vesikelkern und außerhalb vorliegen kann. Das Quenchen des nicht eingeschlossenen Calceins in Gegenwart von Cobalt (II) chlorid ermöglichte es, die Verkapselungseffizienz dieser polymeren Nanokapseln zu bestimmen. Als Ergebnis wurde gezeigt, dass polymerstabilisierte Vesikel eine höhere Effizienz aufweisen, um als Nanotransportsysteme verwendet zu werden.

Symbol Index

N_A :	Avogadro constant: $N_A = 6.022 \times 10^{23} \text{ mol}^{-1}$
κ :	bending modulus
k_B :	Boltzmann constant: $k_B = 1.381 \cdot 10^{-23} \text{ J/K}$
K :	capillary constant
μ_g^0 :	chemical potential
C :	coefficient in the interatomic pair potential
Γ :	decay rate
τ or t :	delay time
ρ :	density at 25°C
ε :	dielectric constant
D :	diffusion coefficient
η :	dynamic viscosity
D_{eff} :	effective diffusion coefficient
J_1 :	first order Bessel function of the first kind
Σ :	sum formula
$I(0)$:	forward scattering
$\bar{\kappa}$:	Gaussian modulus
α :	head group area
R_h :	hydrodynamic radius
ν :	kinematic viscosity
l_c :	length of the amphiphile
\log :	logarithm to the base 10
G' :	loss modulus
μ :	mean location parameter
v_m :	molecular volume
\ln :	natural logarithm
ρ_1 and ρ_2 :	number of atoms per unit volume of two interacting particles
ω :	oscillating frequency
$U(r)$:	pair interaction potential
r or R :	particle radius
V_p :	particle volume
ε_0 :	permittivity of medium
Φ :	phase or volume fraction of particles

n :	refractive index
dn/dc_g :	refractive index increment
$\Delta\rho$ or ΔSLD_s :	scattering length density difference between shell and matrix
θ :	scattering angle
q :	modulus of the scattering vector
G_0 :	shear modulus
$\dot{\gamma}$:	shear rate
β :	space average radius of gyration
G' :	storage modulus
σ :	surface charge density
$t, t_0, D, \Delta R$:	thickness
τ :	turbidity coefficient or relaxation time
σ :	variance
S_0 :	vesicle outer surface area
V :	volume
v :	volume of the chain, and
f_p :	volume fraction of particles
λ :	wavelength
c_g :	weight concentration of sample
wt%:	weight fraction
η_0 :	zero shear viscosity

Abbreviations

Agg:	aggregate
Nagg:	Aggregation number
M_{wapp} :	apparent molecular weight
AIBN:	azobisisobutyronitrile
Bkg:	background
BPO:	benzoyl peroxide
BA:	Butyl acrylate
C_0 :	bilayer's spontaneous curvature
CTAB:	cetyltrimethylammonium bromide
CTAT:	cetyltrimethylammonium toluenesulfonate
CMC:	critical micelle concentration
c:	concentration
CEVS:	controlled environment vitrification system
cryo-TEM:	cryogenic transmission electron microscopy
D_2O :	deuterium oxide
DLVO:	Derjaguin, Landau, Verwey, and Overbeek (theory)
AOT:	Dioctyl sulfosuccinate sodium salt
DVB:	divinyl benzene
DTAB:	dodecyltrimethylammonium bromide
DLS:	dynamic light scattering
M_{weff} :	effective molecular weight
EE:	encapsulation efficiency
$P(q)$:	form factor
FWHM:	full width at half maximum
A:	Hamaker constant or vesicle surface area or amplitude
HS:	hard sphere or monomodal lognormal distributed spherical model
MLZ:	Heinz Maier-Leibnitz Zentrum
HA:	hexyl acrylate
ILL:	Institut Laue-Langevin
I:	intensity
$S(q,t)$:	intermediate scattering function
IUPAC:	International Union of Pure and Applied Chemistry
Q:	invariant

K:	inverse Debye length
IOA:	isooctyl acrylate
JCNS:	Jülicher Zentrum für Forschung mit Neutronen
LiPFOS:	lithium perfluorooctylsulfonate
L ₁ :	micellar phase
M _w :	molecular weight
NSE:	neutron spin echo
NMR:	nuclear magnetic resonance
¹ N:	number density
N:	number of segments in the tail
O/W:	oil in water
p:	packing parameter
L35:	Pluronic L35
PDI:	polydispersity index
PEO and EO:	polyethylene oxide and ethylene oxide
PI-PCEMA:	poly(isoprene)-block-poly(2-cinnamoyl methacrylate)
PMOXA-PDMS-PMOXA:	poly(2-methyl-oxazoline)-block-poly(dimethylsiloxane)-block-poly(2-methyl-oxazoline)
PTFE:	Polytetrafluoroethylene
c ₁ and c ₂ :	principal curvatures for bilayer
PO:	propylene oxide
R _g :	radius of gyration
<i>R_{toluene}</i> :	Rayleigh ratio for toluene
SD:	sample to detector distance
SLD:	scattering length density
L:	segment length of surfactant tail
SANS:	small angle neutron scattering
SDBS:	sodium dodecylbenzenesulfonate
SDS:	Sodium dodecyl sulfate
L ₃ :	sponge phase
SLS:	static light scattering
S(q):	structure factor
T:	temperature or transmittance
TDMAO:	tetradecyldimethylamine oxide
TEOS:	tetraethyl orthosilicate
TMOS:	tetramethyl orthosilicate

t:	time
UV:	Ultraviolet
UV-vis:	Ultraviolet–visible
R_{ves} :	vesicle outer radius
L_{ves} :	vesicle phase
DMPA:	2,2-Dimethoxy-2- phenylacetophenone
HDODA:	1,6-hexandiol diacrylate

1 Introduction

1.1 Theory

Amphiphilic molecules play an important role in colloidal science due to their dual function of having hydrophobic and hydrophilic groups together within the same compound. In aqueous media they arrange in such a way that the hydrophilic head group prefers to stay in water and the hydrophobic tail reduces its contact with water to minimum. This more favourable organisation of amphiphiles in water engenders at the air-water interface, a simple monolayer, which lowers the surface tension and therefore surfactants are termed as surface active agents. Surfactant molecules are rather dynamic species showing the tendency for self-assembly in water. Along with the external environmental changes they rearrange and transfer themselves rapidly to various aggregate types. As a result, different morphologies such as spherical, rod-like micelles or vesicles can be formed depending on the molecular geometry which is described by the packing parameter. Earlier Tanford developed the relation between the geometry of the aggregates and amphiphile properties depending on the hydrophobic effect which in principle leads to the aggregation ¹. The term packing parameter was later proposed by Israelachvili in 1976, suggesting the relation between the molecular properties as head group area, volume of hydrophobic tail, chain length and external variables such as temperature, ionic strength, pH or salinity ^{2,3}. The packing parameter is described by [equation 1.1](#) and predicts the shape of the spontaneously formed aggregates.

$$p = \frac{v}{a \cdot l_c} \quad (1.1)$$

Here v , a and l_c are the volume of the chain, head group area and length of the amphiphile chain, respectively. Assembly into different geometries can be simply expected based upon the shift of packing parameter for instance into spherical aggregates when $p < 1/3$, worm-like micelles for $1/3 < p < 1/2$, vesicles for $1/2 < p < 1$ and planar bilayers for $p \sim 1$ ([Figure 1.1](#)). The packing parameter is determined by the amphiphile structure or admixing cosurfactants which are amphiphilic additives, not forming micelle themselves, but which can take a part in micelle formation thereby typically lowering the interfacial curvature ^{4,5}. These aggregates have

a wide application area from detergency to biomedicine and therefore their dynamic and static behaviour has been studied thoroughly in the past years.

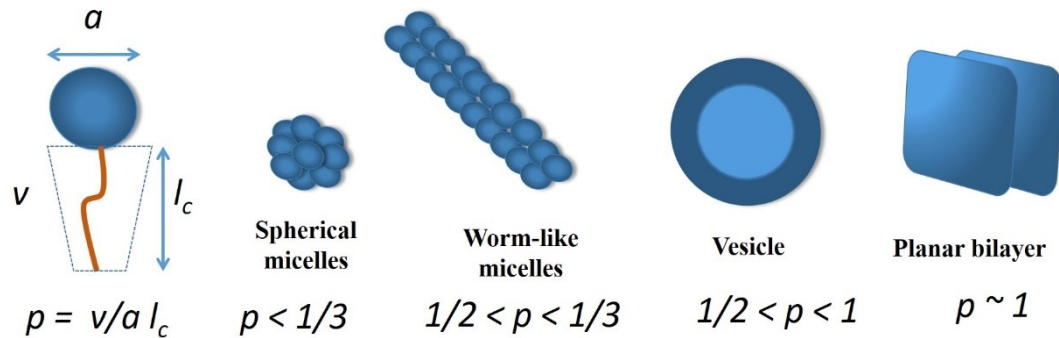


Figure 1.1. Different geometries predicted by the packing parameter.

1.1.1 Colloidal Forces

During the self-assembly process, colloidal particles interact by virtue of various forces related with all the components in the colloidal system. These forces influence the stability of the whole dispersion and self-assembling efficiency, thus a detailed understanding is needed.

Brownian motion, suggested by Robert Brown in 1827, is the driving force for diffusion and collision of colloidal particles. This random and continuous motion is driven by the thermal energy, $\frac{3}{2}kT = \frac{1}{2}mv^2$ where the translational velocity can be deduced. In this context, some relations were developed for describing the particle motion. Einstein suggested the term diffusion coefficient, relating the particle diffusion in a suspension with its size, Avogadro's number, absolute temperature and the solvent viscosity (Stokes-Einstein equation: $D = \frac{kBT}{6\pi\eta R}$)⁶. Afterwards, this equation was derived further with considering the time dependence of the particle motion by another relation between the root mean-square displacement $\langle x^2 \rangle^{1/2}$ and time t (Einstein-Smoluchowski equation: $\langle x^2 \rangle^{1/2} = (2Dt)^{1/2}$)⁷. Another derivation of the time related diffusion coefficient was presented in the Langevin equation $m \frac{dv}{dt} + 6\pi\eta R = f_B(t)$ where m is the mass of the particle⁸. This equation accounts for the Brownian time constant as the particles are much bigger than the molecules existing in the media, their response time is bigger than the applied force, $= \frac{m}{6\pi\eta R}$.

Van der Waals interaction is the attractive force between molecules as well as particles as a result of the dipole-dipole, dipole-induced dipole and induced dipole-induced dipole (London dispersion) interactions. These interactions all promote the net van der Waals force and depend on $1/R^6$ separation distance of small spherical particles⁹. For a distance D of particles longer than 10 nm, the London dispersion decays faster to $1/R^7$ which is called retardation effect because of the long time needed for the transfer of the electric field of the dipole from one atom to another one and its response¹⁰. Hamaker established a connection between additivity derived from London dispersion by integrating the interatomic Van der Waals pair potentials which assumes the non-retarded interactions. $A = \pi^2 C \rho_1 \rho_2$, A is the Hamaker constant, C is coefficient in the interatomic pair potential: $W(D) = -CD^{-6}$, ρ_1 and ρ_2 are the number of atoms per unit volume of two interacting particles and D is the particle edge to edge separation distance. Relating the geometry with the interactions, one can reach the Van der Waals force between the spherical vesicles as $W(D) = AR/12D^2$, R being the reduced radius $R = \frac{R_1 R_2}{R_1 + R_2}$. Similarly, the force between a sphere and a planar surface is obtained as $=AR/6D^2$.

Additionally, Lifshitz continuum theory brings a different approach by considering the medium and the particles separately avoiding the additivity problem, and the phases here are interacting by electrical field fluctuations. The force can be calculated from the dielectric constants, refractive indices, molecular rotational frequencies and electronic absorption frequencies.

Electrostatic interactions are another important force in colloid science. Surfaces in water are basically charged with bound or adsorbed ions and these charges make an electrical field which is attracting the counterions. The layer formed by the charges and the counterions, is defined as *electrical double layer* and has been studied intensively. Helmholtz explained this interaction with a model of a metal surface with adsorbed ions and showed the change of interaction potential between the surface and the solution. The diffuse double layer idea was suggested by Gouy-Chapman which is based on the thermal diffusion of ions from the surface to the solution. The exponential decay of the potential with increasing distance from the surface can be obtained from Poisson-Boltzmann equation. Moreover, Stern presented another model to explain the charged surface and the diffuse layer of the interface. Due to his model the potential depends on both, the distance from the surface, which causes a linear decay, and the exponential decay in the diffuse layer.

On the other hand, two charged surfaces in a media is also another interesting point to be examined. In this case both the electric double layer and Van der Waals interactions are taken into consideration. The (Derjaguin, Landau, Verwey, and Overbeek,) *DLVO* theory basically

explains this interaction considering the attractive Van der Waals and repulsive electric double layer forces both are additively stabilizing the dispersion. The energy per unit area can be summarized as $W_{total} = W_{vdW} + W_{edl}$ therefore, the DLVO force can be approximated with $F = \frac{2\pi R\sigma^2 e^{-\kappa D}}{\kappa\epsilon\epsilon_0} - \frac{AR}{12\pi D^2}$, where κ is the inverse Debye length, A is the Hamaker constant, ϵ and ϵ_0 are the dielectric constant of the medium and permittivity constant of vacuum, respectively, D is the distance between the spherical particles, σ is the surface charge density and R the radius¹⁰. The DLVO force dependence on distance and ion concentration shows characteristic behavior, depicted in [Figure 1.2](#). For small distances between the particles, the Van der Waals attraction becomes larger than the electrical double layer repulsion because it increases exponentially

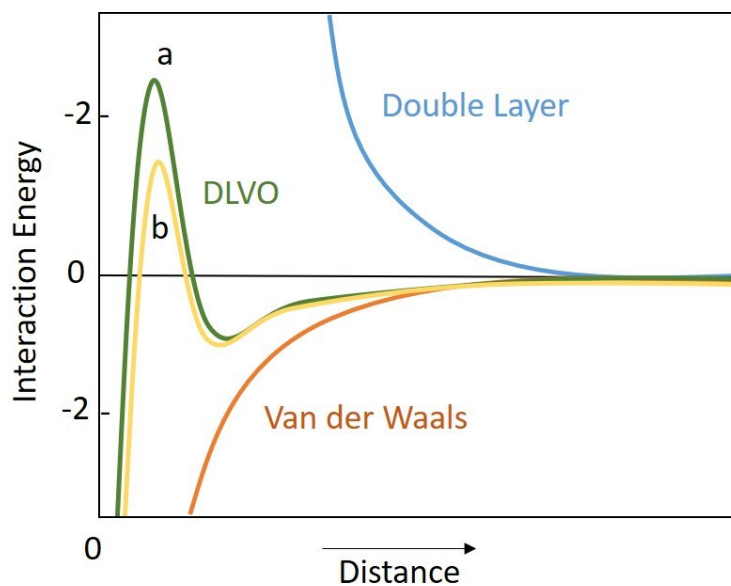


Figure 1.2. DLVO interaction energy vs. distance profile.

faster. Additionally, Van der Waals is effective at high salt levels or small surface charge densities (lower electrostatics) while for the opposite case, repulsion is more dominated. In [Figure 1.2](#), DLVO change from *a* to *b* can be seen when the surface potential decreases with increasing electrolyte concentration.

The Repulsive Hydration Force is an additional force beyond the DLVO model, which describes interactions between the particles at short distance even closer than a few nanometers. The repulsive forces here arise from the water layer which is bound to the hydrophilic surface tightly and by this way can be stabilized even at high ionic strength ^{11,12}. Aggregation occurs from the Van der Waals interaction, because the stabilizing surface charges are shielded by the electrolyte. Equation $W = W_0 e^{-D/\lambda_0}$ describes the hydration repulsion between two hydrophilic surfaces with D distance where $\lambda_0 \sim 1$ nm and W_0 depends on the hydration of the surfaces and usually is in the range of 3-30 mJ/m² at T = 25°C ^{9,13}.

Concentration and the size of the ions have significant effects on hydration forces wherefore they directly affect the H-bonding network in water which is the main reason of this type of forces ^{10,14,15}.

The Attractive Hydrophobic Force is prevailing when the water molecules interact with the hydrophobic molecules. To reduce the total free energy and shift to an energetically favorable state, water attracts to other water molecules while causing an attraction between the hydrophobic ones. This attraction has an important role to understand the particle fusion especially the vesicle-vesicle interactions. It is stronger than the Van der Waals, since the hydrocarbon surfaces attracts stronger ⁹. The hydrophobic interaction energy between two hydrophobic surfaces in water is expressed as $W = -2\gamma_i e^{-D/\lambda_0}$ where γ_i is between 10-50 mJ/m² and λ_0 being 1-2 nm ¹⁰.

1.1.2 Micelles

Amphiphilic molecules in water form aggregates termed as micelles, with the arrangement of their non-polar tail and polar head group. Micelle formation concept was suggested at earlier 1900 and evolved from starch solutions to soap and detergency with the work of McBain who described the micelle formation from monomeric molecules ^{16,17}. While surfactants at low concentration in water are existing as monomers at high concentrations they form micellar aggregates. Basically this critical concentration for micelle formation is called CMC (*critical micelle concentration*) and was introduced by Davies and Bury in 1930¹⁸. The CMC is an important characteristic of surfactants; above the CMC micellar aggregates are forming in equilibrium. Below CMC, typically already at much lower concentration, the surfactants are adsorbed at the water-air interface and form a densely packed film there. Different parameters as temperature, pH, pressure, and electrolytes have effects on the CMC, for instance pressure cause an increase of volume and temperature mainly changes the ΔH_{mic} ¹⁹⁻²¹.

Another important phenomenon is the *Krafft temperature* or *point*, where the solubility increases drastically and above it, surfactants form micelles. Thus, the CMC meets the solubility curve^{22,23} and below the Krafft point, surfactants are present as monomers.

Many studies were established to develop different models for predicting micellization. In addition to Israelachvili's packing parameter model described above, Tanford suggested the free energy model where the energy is related with transferring the surfactant molecule from the water to the aggregate state²⁴.

$$(\Delta\mu_g^0) = (\Delta\mu_g^0)_{Transfer} + (\Delta\mu_g^0)_{Interface} + (\Delta\mu_g^0)_{Head\ group} \quad (1.2)$$

First term describes the negative free energy from the transfer of the unfavorable contact of the hydrophobic tail from water; second term is a positive value of free energy that arises from the unavoidable interaction of the surface of the tail and water interface and the last term comes from the positive contribution from the repulsive interaction of headgroups of the amphiphile. The interfacial free energy was defined as a combination of interfacial tension, σ , and surface area, a . Repulsion of the headgroups increases with decreasing distance and is inverse to a . Accordingly, the change of the chemical potential evaluates to $(\Delta\mu_g^0) = (\Delta\mu_g^0)_{Transfer} + \sigma a + \alpha/a$ where α is the headgroup repulsion parameter. In thermodynamic equilibrium, $\frac{\partial}{\partial a}(\Delta\mu_g^0) = 0$ here $\sigma - \frac{\alpha}{a^2} = 0$ and $a = \left(\frac{\alpha}{\sigma}\right)^{1/2}$. The aggregation number N_{agg} , is then related with area per molecule a ; $N_{agg} \propto 1/a$. To summarize, this model provides information about the basics of micellization, the tail transfer which is responsible for aggregation, affects the CMC not the size and shape of the structures, the residual contact is the reason for growing of the aggregates and the headgroup repulsion controls the size growth²⁴.

Later, this approach was developed further by Nagarajan and Ruckenstein²⁵. According Tanford's theory, the surfactant headgroup controls the aggregation. However, the role of the tail is mainly neglected. Nagarajan and Ruckenstein extended this theory considering the packing entropy of tail. Thus, the headgroup area is related with the tail length and the final shape. One end of the tail is fixed at the water-surfactant interface while the other end locates flexibly in the core. It deforms non-uniformly to fit in the core and behaves in compliance with packing and uniform density constrains. The free energy observed from this conformational constrain is termed as tail deformation energy. For spherical micelles, it is expressed by:

$\frac{(\Delta\mu_g^0)_{def}}{kT} = \left(\frac{9p\pi^2}{80}\right) \left(\frac{R_s^2}{NL^2}\right)$ where R_s is the core radius, p is packing factor, L segment length of tail, N is the number of segments in the tail ($N=l_s/L$, l_s is the extended length of tail). Adding

this into Tanford's equation, shape transitions are related with tail length as well as the head group area.

$$(\Delta\mu_g^0) = (\Delta\mu_g^0)_{Transfer} + (\Delta\mu_g^0)_{Interface} + (\Delta\mu_g^0)_{Head\ group} + (\Delta\mu_g^0)_{Packing} \quad (1.3)$$

Different shape geometries such as spheres, cylinders or ellipsoids have different advantages based upon the application fields, for instance rod-like micelles have interesting rheological properties and viscoelastic behavior^{26,27}. These structures can be induced either by the amphiphile's molecular structure or some other additives such as additional amphiphiles, oils or cosurfactants. The latter is a surface-active compound which does not form micelle alone, however, when cooperating with the surfactants, its small headgroup gives rise to the packing parameter and therefore new geometries can be formed.

In micellar systems solubilization has a significant importance. Due to the IUPAC definition *micellar solubilization* means, the incorporation of solubilize into or on the formed micelles²⁸. The interior of micelle is a good host for hydrophobic compounds and small molecules can be solubilized more easily than the larger ones²⁹. However, the distribution of solubilize is affected by the head group of amphiphile and can be located either in interfacial or in the interior site of the micelle. When a non-polar molecule is added with an increasing amount to a constant concentration of surfactant, micelles swell with increasing its curvature until a certain point. At that point micelles become large enough that the solubilize captured inside seems similar to its pure bulk. The new transparent, stable system is called as *microemulsion*, consisting of spherical droplets with size in a range of 3 – 30 nm^{30,31}.

1.1.3 Vesicles

Among the structures described up to now, especially vesicles have attracted much attention because of their interesting hollow spherical geometry. These closed bilayers are analogs as biological membranes either for transport of hydrophobic compounds in the lipid shell or hydrophilic ones in their aqueous core. Many investigations on vesicles have been done in terms of understanding the behaviour of the system. Furthermore, these aggregates have a wide application area from cosmetics and detergency formulations to nanoreactors, or for energy conversion and pharmaceutical applications^{32–35}.

In general, vesicles can be formed from different type and classes of compounds. When aqueous dispersions of phospholipids form vesicles, the formed kinetically stable structures are called *liposomes*^{36,37}. *Glycolipids* known as the main component of the cell membranes are another

class that can form vesicles^{38,39} and successfully being used as drug carriers⁴⁰ in biotechnology⁴¹. *Catanionic vesicles* are vesicles formed from oppositely charged surfactant mixtures such systems consisted of sodium dodecyl sulfate and cationic dodecyltrimethylammonium bromide⁴²; cetyltrimethylammonium tosylate and anionic sodium dodecylbenzene sulfonate⁴³; or cetyltrimethylammonium bromide and anionic sodium octyl sulfate⁴⁴. Interestingly, at equimolar compositions of both surfactants precipitation takes place, while for an excess of either cationic or anionic surfactant thermodynamically stable vesicles are formed^{45–48}. Additionally, different studies have shown that zwitterionic surfactants, polyelectrolytes, short chain alcohols and copolymers can play a role in the formation of vesicles^{49–51}.

Vesicles can be divided in two classes depending on having either one single bilayer or more. The first class is called *unilamellar vesicles* and consists of only one bilayer. This class also can be subdivided in categories based upon their size. For instance, small unilamellar vesicles have radii of 5 – 50 nm and large unilamellar vesicles have the radii of 50 nm – 10 μm (Figure 1.3). The second type of vesicles are *multilamellar vesicles* which have various shells of vesicles like onion shape^{52,53}. While unilamellar vesicles are found in dilute systems; multilamellar vesicles often are observed in concentrated systems.

Mainly, the surfactant's molecular structure influences the final shape in addition to the environmental factors such as temperature, pH or ionic strength. As described above, changing

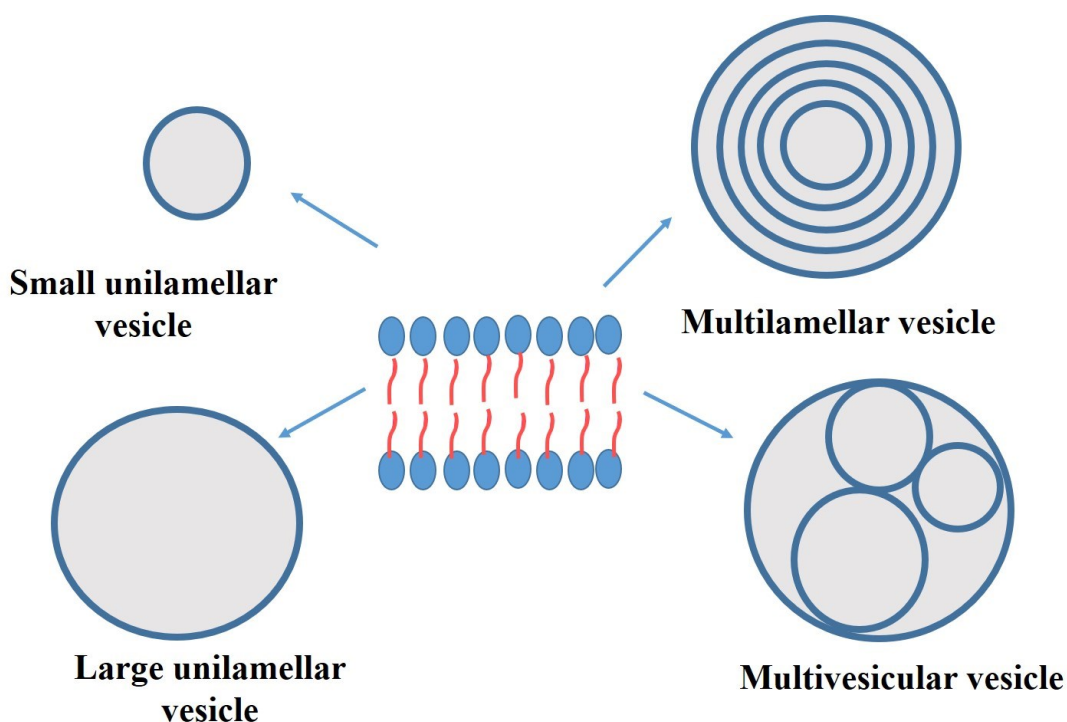


Figure 1.3. Different vesicle types.

the packing parameter, one observes the transition in the geometry and for vesicles packing parameter lies between $\frac{1}{2}$ and 1. Tanford presented the critical chain length of hydrocarbon which is the effective chain length in the liquid state $l_c = (0.154 + 0.1265n)$ nm for chains with n hydrocarbon atoms¹. Additionally, the volume of hydrocarbon chain is defined as $v_c = (27.4 + 26.9n) \times 10^{-3} \text{ nm}^3$ ¹. For vesicles with N number molecules, outer vesicle radius R_0 , and thickness t_0 ; the outer volume V_0 can be calculated by: $V_0 = N v_c = \frac{4}{3}\pi[R_0^3 - (R_0 - t_0)^3]$, and the outer surface area is given as: $S_0 = 4\pi R_0^2$. From these equations the area per head group then can be written as $a = \frac{4\pi R_0^2}{N_0}$. This equation can be changed for the ratio between the actual and optimal area: $\frac{a}{a_0} = 3 \left(\frac{v_c}{a_0 l_c} \right) l_c \frac{R_0^2}{[R_0^3 - (R_0 - t_0)^3]}$ and for vesicle formation the head group area is needed to approach an optimal value⁵⁴. As seen from the equation, the packing parameter given in [equation 1.1](#) $p = \frac{v_c}{a_0 l_c}$ relates the head group area to the chain length, outer vesicle radius and outer layer thickness. When the p and l_c are fixed, the ratio can change depending on the radius and thickness. The minimum radius thereof can be reached once thickness becomes equal to the chain length and $R_{min} = \frac{3 + [3(4p-1)]^{1/2}}{6(1-p)} l_c$ where p refers to the packing parameter⁵⁴. It is noticeable that the minimum size of the vesicle is depending on two factors: the packing parameter and the chain length.

It has to be noted that the vesicles prefer a value for packing parameter closer to $\frac{1}{2}$ and planar bilayers are formed at $p = 1$. Surfactants with small headgroup and bulky tail are required for changing the packing conditions to such range. Thus, double-chain surfactants, or perfluoro surfactants, or addition of cosurfactants such as medium-chain alcohols can be used for this purpose^{51,55}.

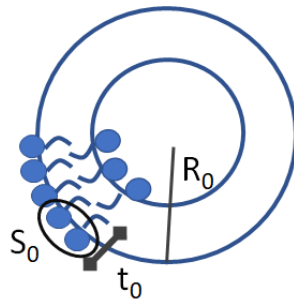


Figure 1.4. Geometrical parameters of vesicle: S_0 : outer surface area, t_0 : thickness of the outer layer, R_0 : outer vesicle radius.

Another important term for vesicle formation is the bending elasticity of the bilayer which is fundamentally described by two parameters: the mean bending modulus κ , and the Gaussian modulus $\bar{\kappa}$. Hence, the free bending energy of the bilayer is expressed by the formula $F_b = \int dA[(\kappa/2)(c_1 + c_2 - 2c_0)^2 + \bar{\kappa}c_1c_2]$, where c_1 and c_2 are the principal curvatures while c_0 is the bilayer's spontaneous curvature and A is the surface area^{56,57}. When the Gaussian modulus $\bar{\kappa} \ll 0$; geometry shifts from planar bilayers to vesicles⁵⁸. With the help of this approximation, the energy needed for the formation of different geometries from the surfactant layer can be calculated.

In the case of mixed surfactant bilayers, Safran et al presented that energetically stable vesicles can form through the interactions between two species⁵⁹. This induces an asymmetry of composition which is coupled between the local curvature. In mixed surfactant bilayers, an exchange of the amphiphiles occurs from lower to upper monolayer. When the coupling is rather strong, geometry evolves to spontaneous bending⁵⁹. Later on, Ligoure and Porte theoretically defined the bending characteristics of mixed vesicles consisting of two surfactants not at fixed composition but at fixed chemical potential⁶⁰. They showed the size of this so-called enthalpically stabilized vesicles depends on the relative concentration of both surfactant types. In another work, the effect of chain length on bending rigidity and spontaneous curvature was calculated theoretically revealing that the addition of short chain amphiphiles to the vesicles consisted of long chain lipids lowers the bending rigidity⁶¹.

1.1.3.1 Preparation of vesicles

Different preparation methods had been developed to provide sufficient conditions for vesicle preparation. However, the most important point taken into consideration here, is the properties expected from the final product. Size, polydispersity, permeability, surface charge potential, long time stability are some important factors that depends on the preparation methods. Below we briefly summarize the more general methods for vesicle preparation.

One of the most classical way is the *sonication* of lipid dispersions for homogenizing the amphiphilic compound, in such case Vortex mixing can provide enough mechanical power and has been used extensively⁶²⁻⁶⁴. However the final product does not have uniform size distribution and reproducibility is a big problem for this method⁶⁵.

Thin-film hydration is another method where a solution of surfactant is prepared in a volatile solvent. A thin film of amphiphile is prepared by evaporating the solvent and vesicles are formed by dissolving the remained film in water⁶⁴.

Additionally, by the way of *high-pressure extrusion* through the membrane filters with a certain pore size, leads to the formation of highly monodisperse vesicles⁶⁶. The microfluidization method is when the high-pressure extrusion is applied to lamellar phases, the lamellar structures are demolished by the shear forces and consequently forms vesicles⁶⁷.

In some studies vesicles were also formed from the way of *reverse evaporation*⁶⁸. This means an aqueous phase is dispersed in an organic solvent. Therefore, a water-in-oil emulsion is formed by sonification. Later on, the solvent is removed under the pressure. The remaining part is centrifuged then filtered to obtain the vesicles with sizes depending on the filtration pore sizes. Also, nowadays supercritical carbon dioxide is reported being used as an alternative to organic solvents⁶⁹.

It was shown that polyelectrolytes can be used to form hollow nanospheres which are very similar to vesicles. Step-by-step deposition of oppositely charged polyelectrolytes on a spherical surface can basically shape as a hollow sphere. Subsequently the substrate is removed and the final structure forms vesicles⁷⁰.

1.1.3.2 Formation of vesicles

One of the key issues in the preparation of vesicles that effects the formation process is the need of input of external energy. Studies have shown that in general the formation can be done in two ways: the shear induced or the spontaneous formation of vesicles.

Shear-induced formation indicates that as an external energy, shear force can be applied to the planar bilayers and induces a transition to vesicle structures. There have been many studies in the literature on this type of vesicles formation. For instance, SDS/dodecane/pentanol/water system as well as AOT/brine showed this transition where at high shear rates, planar lamellar structures shifted to multilamellar vesicles^{56,71}. It was shown that the size of the vesicles is related with the inverse square root of the shear rate $\dot{\gamma}$. Additionally, along with the vesicle formation, viscosity increases. The reason for this is that planar lamellar structures do not show a high flow resistance due to their orientation in the flow field, and accordingly their viscosity is low. In contrast, vesicles are often densely packed resulting in a remarkable effect on the viscosity⁷².

Another study revealed the shear-induced transition from sponge phase (L_3) to vesicles which is reversible⁷³. In a similar manner, Candau and Manohar showed in their work that vesicles can also transform to cylindrical micelles with applied shear⁷⁴.

Spontaneous formation of vesicles is the other challenging subject in this context. As described above, an external energy input is necessary for most of the vesicle preparation methods. For a spontaneous formation, this driving force is not required, however a type of shear is applied to homogenize the system. One of the first examples of vesicles formed spontaneously, can be given as vesicles consisted of the didodecyldimethylammonium surfactant with the presence of hydroxide ions^{75,76}. Another study reported that anionic carboxylate surfactants can form spontaneously vesicle together with an acidic cosurfactant as a function of pH^{77,78}.

Mixtures of cationic and anionic surfactants are interesting systems leading to the formation of vesicles⁴⁵. These catanionic systems require an excess of one of the components for preventing the precipitation at equimolar ratio. Sodium dodecylsulfate/dodecyltrimethyl-ammonium bromide, cetyltrimethylammonium bromide/ sodium octyl sulfate or cetyltrimethylammonium tosylate/sodium dodecylbenzenesulfonate catanionic surfactant mixtures can be presented in this category⁴²⁻⁴⁴. Alcohols or amine compounds have been used as cosurfactants changing the packing parameter and taking a part in the formation of vesicles. For instance, the work on hexanol in tetradecyldimethylamine oxide (TDMAO) and decane system examines deeply the structural formation and transition of vesicles⁵¹. Using surfactants with polymeric hydrophilic headgroups such as PEO group, is another way to induce the vesicle formation as well as enhancing the stability⁷⁹. Spontaneous formation can be also applied to non-aqueous systems. Vesicles have been observed in the system of hexaethyleneglycol hexadecyl ether or sucrose monoalkanoate in decane⁸⁰.

The *theoretical basis* of spontaneous vesicle formation is still been worked on. Nevertheless, it is known that the curvature elasticity has a key role in the energetic stabilization. As an example, in the case of catanionic vesicles, the inner and outer layer composition difference leads to an effective curvature of equal and opposite signs, whereupon energetically stabilized vesicles are formed^{56,59}. For the first time Helfrich introduced the relation between the theoretically calculated size distribution of vesicles and bending moduli via the equation⁸¹: $f(R) = \frac{8R^3}{\langle R^2 \rangle^2} \exp(-2R^2 \langle R^2 \rangle^2)$, where $\langle R^2 \rangle^2$ is the mean square radius.

Moreover, when the bending modulus is significantly larger than kT , it is also possible that the unilamellar vesicles are stabilized by the spontaneous curvature C_0 ⁸². Such an example can be given for the system consisted from CTAB and sodium perfluoro-octanoate where the vesicles were stabilized with low polydispersity⁸²

1.1.3.3 Polymer stabilized vesicles

Much research in recent years has focused on developing methods for avoiding the vesicle fusion and enhancing their stability. Basically, this can be achieved by supporting the vesicles either from *outside* or *inside* the membrane (Figure 1.5). For instance silica precursor, TEOS (tetraethyl orthosilicate) or TMOS (tetramethyl orthosilicate) have been used for this aim forming a silica shell and supporting the membrane from the outside. This method is nowadays commonly used for the formation of silica hollow nanosphere⁸³. Steric stabilization can be also achieved by using block copolymers⁸⁴ or inserting hydrophobic moieties into the vesicle membrane which reduces to mobility, and hence, enhances the stability. As an example, Semple presented the work where cholesterol was incorporated into the vesicle membrane⁸⁵ and investigated its functionality in the lipid membrane.

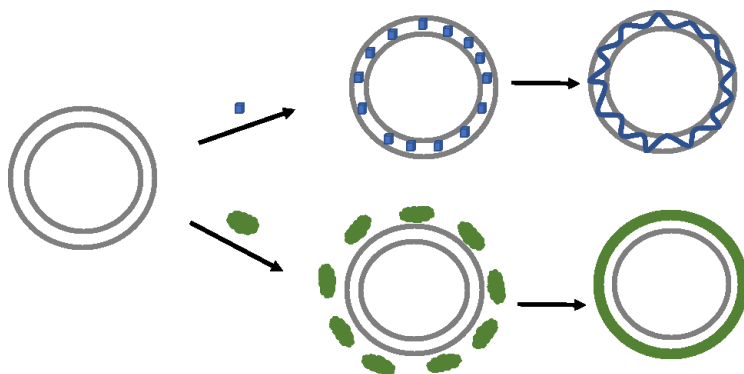


Figure 1.5. Representation of vesicle stabilization methods.

A common way for keeping the stability of these submicron structures and the quality of the permeability, is to strengthen the bilayer with the help of polymers⁸⁶. The formed polymer stabilized hollow spherical nanostructures are termed as *polymer nanocapsules* (Figure 1.6). Due to the hollow spherical geometry, their cavity allows to restrain the hydrophilic agents, and the polymeric membrane can provide a controlled release^{87,88}. Furthermore, the hydrophobic moieties can also be isolated in the hydrophobic membrane and can be transported by this way. Different methods to design the polymer nanocapsules are presented so far (Table 1.1), involving the formation from preformed polymers or the polymerization reactions starting from the organic monomers. Nanocapsules formed by dispersing preformed polymers can be prepared using solvent evaporation, nanoprecipitation, dialysis or supercritical fluid technology. For this purpose, emulsions are prepared by dissolving the polymers in different solvents⁸⁹. In the solvent evaporation method, volatile solvents are used and after the evaporation of the solvent, emulsion is converted into the nanoparticle suspension. In

nanoprecipitation technic, also called solvent displacement method, preformed polymers precipitate from an organic solvent, which is later displaced with the aqueous phase ⁸⁹. Dialysis provides the formation of small and narrow distributed nanoparticles by dissolving the polymer in an organic solvent placed in the dialysis tube while the outside media is a non-solvent ⁹⁰. In this method, nanoparticles are formed via solvent displacement, which leads to the polymer aggregation. Supercritical fluid technology was developed for providing environmentally safe preparation method. Instead of organic solvents, here polymer solution is prepared in a supercritical fluid and thereby, nanoparticles were formed by rapid expansion of the solution ⁹¹.

Table 1.1. Different preparation methods of polymer nanocapsules.

Polymer Nanocapsule	
From preformed polymer	From monomer
Solvent evaporation	Controlled radical polymerization
Nanoprecipitation	Emulsion
Dialysis	Miniemulsion
Supercritical fluid technology	Microemulsion

Producing polymer nanocapsules from monomers offers a straight approach to obtain the designed nanoparticles with objected properties. In addition to industrially used controlled-radical polymerization, micro-, mini-, and emulsion polymerization methods are commonly used techniques that allows the formation of nanoparticles with different sizes. In conventional emulsion polymerization, main components are water, low water soluble monomer, water-soluble initiator and surfactant ⁹². Monomer is dispersed in the solution and diffuses through the micelles, and accordingly reaction occurs when dissolved monomer collides with the initiator. Unlike the conventional emulsion, mini-emulsion method contains co-stabilizer and the use of high-shear ⁹³. In micro-emulsion polymerization, reaction starts from the thermodynamically stable micro-emulsions along with the addition of water-soluble initiator ⁹⁴. [Table 1.2](#) summarizes the differences between these polymerization methods and the product properties.

Table 1.2. Different properties among the emulsion polymerization types ⁸⁹.

Properties	Emulsion	Mini-emulsion	Micro-emulsion
Particle size	50-300 nm	10-30 nm	30-100 nm
Droplet size	1-10 μ m	20-200 nm	~10 nm
Thermodynamic stability	Non-stable	Non-stable	Stable
Polydispersity	Low	Very low	Very low

The important points to take into consideration are the stability, rigidity, controllability, permeability and versatility of the final product. Therefore, preparation methods are of great importance. In addition to above mentioned methods, using polymerizable surfactants or amphiphilic block copolymers which can support the bilayer membrane from the inner side provides advantages to control the desired properties of the final product ⁹⁵⁻⁹⁷. It was shown that vesicles formed and stabilized from amphiphilic block copolymers are stable structures and their polymer shell properties are controllable by simply changing the block length and polymer moiety ⁹⁸. In the work of Liu and Ding, poly(isoprene)-block-poly(2-cinnamoyl methacrylate) PI-PCEMA diblock copolymer in hexane-tetrahydrofuran mixtures formed stable and water-soluble polymer nanocapsule with the size of 50-60 nm radius ⁹⁹. Another work was done by Meier where vesicles with controllable size of 50 to 500 nm were formed from poly(2-methyl-oxazoline)-block-poly(dimethylsiloxane)-block-poly(2-methyl-oxazoline) PMOXA-PDMS-PMOXA triblock copolymers in water.

Later, the polymerization reaction of functional amphiphiles carrying styryl groups in vesicle membranes was presented, strengthening the network with copolymerization and establishing a two-dimensional interpenetrating network in the vesicle bilayer ¹⁰⁰. Moreover, synthesis of cationic, anionic, and zwitterionic surfactants with polymerizable chains have attracted attention, as the permeability of the vesicles can be enhanced by this way ¹⁰¹.

An effective way for polymerization of vesicles can be done by *inserting hydrophobic organic monomers* within the bilayers followed by *fixating them by polymerization*. For the first time Murtagh and Thomas introduced the polymerization in the vesicle bilayer concept in the 1980s ¹⁰² with the cross-linking polymerization of styrene and divinyl benzene where they successfully stabilized the vesicle size. Following works of non-cross-linked polymerization of styrene showed that phase separation occurred in the bilayer after the polymerization which caused the formation of so-called parachute like structures ¹⁰³. Pulsed-laser polymerization experiments were used to analyze the mechanism of the parachute morphology ¹⁰⁴. This

problem became one of the key issues which needs in general to be considered while stabilization by polymerization.

In other work, polymeric nanocapsules consisting of cross-linked polystyrene or cross-linked polymethacrylates were synthesised by incorporation of the monomers into the vesicle bilayer^{86,105,106}. Kaler reported cross-linked polymerized vesicles in mixtures of styrene and divinylbenzene monomers with the cationic surfactants cetyltrimethylammonium toluenesulfonate (CTAT) or dodecyltrimethylammonium bromide (DTAB) with the branched chain anionic surfactant sodium dodecylbenzenesulfonate (SDBS)¹⁰⁶. In another work, polymerization kinetics of styrene containing surfactants were investigated by Fendler¹⁰⁷. Jung and co-workers presented the phase separation during the polymerization of styrene in dioctadecyldimethylammonium bromide (DODAB) vesicles. The formed structures had so called parachute-like shape and this phenomena was investigated via small angle neutron scattering (SANS)¹⁰⁸. More recently, Pinkhassik and co-workers reported the formation of polymer nanocapsules produced by the polymerization of hydrophobic monomers in the hydrophobic interior of the bilayers of different types surfactant vesicles. Accordingly, they investigated the encapsulation capacities with entrapping catalysts into the nanocapsules^{109–111}.

This method drew much interest because of its ease instead of complex synthesis, it allows for the use of common surfactants and afterwards to the removal of the surfactant templates. Furthermore, mostly polymerization reactions need rough reaction conditions, which later can have disruptive effects on self-assembled structures. However, this method can allow mild reaction conditions for instance using UV initiated polymerization at low temperatures. Finally, the properties of the nanocapsules produced this way (such as permeability, stability and strength) can easily be modified¹¹².

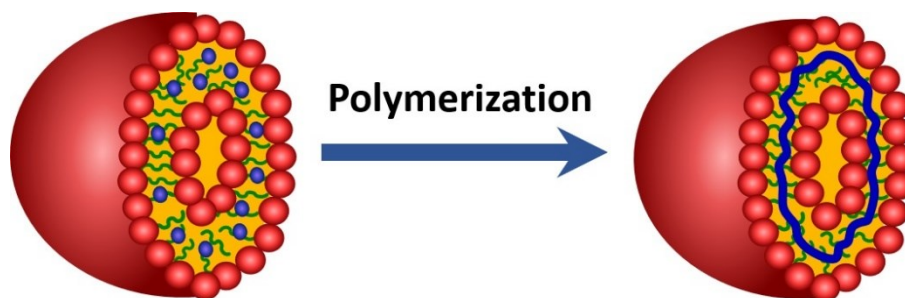


Figure 1.6. Monomer loaded vesicle and polymer stabilized vesicle.

2 Motivation

Vesicles have been important structures formed from lipids or surfactants. These closed bilayer shells attract great attention due to their hollow spherical geometry which allows for their use as nanocarrier systems. Surfactant mixtures of different types such as anionic, cationic or zwitterionic amphiphiles can form vesicles spontaneously without any energy input with an average size between 50-100 nm. These submicron structures can be stabilized by polymerization, or in other words they can be used as templates for the synthesis of polymer nanocapsules.

In recent years, many approaches have been developed for the vesicle templating procedure. Polymerization within the vesicle membrane is a widely used method. This method is categorized in two parts; in the first part polymerizable surfactants and amphiphilic block copolymers are employed, and in the second part hydrophobic organic monomers, i.e. styrene or acrylates, are used for cross-linked polymerization (by having a certain percentage of cross-linker present in the monomer mixture) to provide an enhanced stability^{102,113}. The latter is an effective way where the vesicle template is not involved directly in the reaction, but at the same time shapes the finally formed polymer network.

Although it is a convenient approach for controlling the final structure, it is challenging with respect to the polymerization process. One of the important issues observed is the phase separation in the bilayer whereby polymerization led to the formation of parachute-like structures¹⁰³. Consequently, products with unintended morphologies can likely be formed. Additionally, another problem is the rough polymerization reaction conditions such as high temperature or the need of organic solvents and their direct effects on self-assembled architecture, therefore the final product.

The aim of this PhD work was to address these open questions and to provide a powerful, straightforward method of stabilization via polymerization at mild reaction conditions. Therefore, we choose to template a well-defined vesicle system by inserting hydrophobic monomers, i.e. styrene and acrylates with different chain lengths, into the membrane. Afterwards the structures were fixated by UV-initiated polymerization under very mild conditions, eventually generated monodisperse hollow spherical polymer nanocapsules.

Thus, the vesicle system of choice consisted of nonionic tetradecyldimethylamine oxide (TDMAO) and anionic lithium perfluorooctylsulfonate (LiPFOS), which had been studied

earlier, was chosen as template. It was shown that due to the synergistic interaction between the surfactant pairs, vesicles are spontaneously formed, since the head groups are interacting attractively and reducing the joint head group area¹¹⁴. Stability and size of these vesicles can be controlled by addition of Pluronic copolymers ($\text{EO}_n\text{-PO}_m\text{-EO}_n$) where L35 attaches on the rim, stabilizes the structures in a way preventing them to converge. As a consequence small, monodispersed and kinetically long-time stabilized vesicle are formed with a low polydispersity PDI of ~ 0.05 ¹¹⁵.

In the present study, we used these well-defined, monodisperse vesicles of a TDMAO/LiPFOS mixture with molar ratio of 55:45 in the presence of 1 mol % Pluronic L35, as a suitable template for the cross-linked polymerization to produce polymer nanocapsules. For this aim, hydrophobic organic monomers, which can effectively be inserted into the vesicle membrane, were introduced into the vesicle membrane. For determining the effect of various monomers with different hydrophobicity, styrene, butyl-, dodecyl-, isooctyl- and hexyl acrylate monomers were used and their concentration as well as the ratio of cross-linkers were varied. Concurrent loading was chosen as the plausible way for dissolving the water-insoluble monomers entirely and preventing the ageing of the vesicles. Therefore, monomers were initially dissolved in the micellar 50 mM TDMAO / 0.5 mM L35 stocks. Their influence on the primer micellar aggregates was of the key importance in the formation of vesicles. Secondly, TDMAO/L35/monomer stocks were mixed with 50 mM LiPFOS solutions with the molar ratio of 55:45, leading to monomer loaded vesicles. Latterly, the structural changes of the vesicles upon incorporation of the different monomers and the cross-linkers were examined structurally and morphologically. These monomer-loaded vesicles were fixated by UV-initiated polymerization ([Figure 2.1](#)) in water at 18°C. Effect of polymerization on the bilayer membrane and the degree of cross-linking were examined for optimization and enhancing the

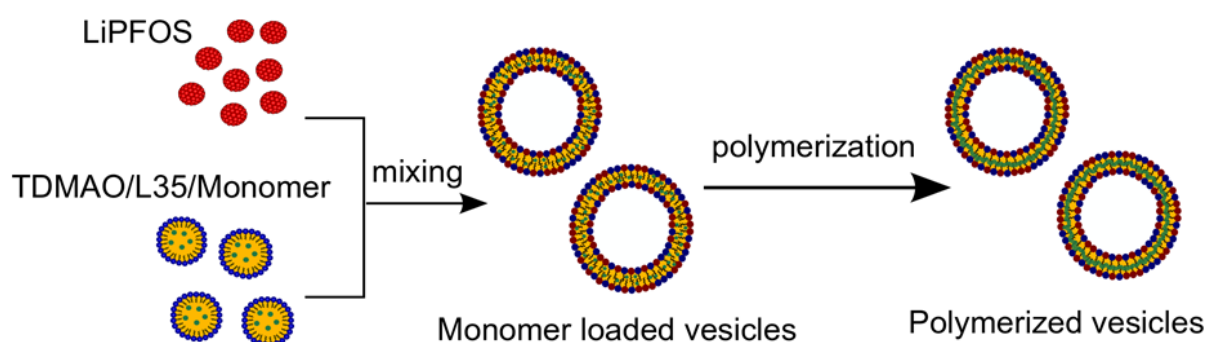


Figure 2.1. Schematic representation of the general synthesis approach.

encapsulation efficiency of the finally formed nanocapsules which was tested via loading with calcein as a water-soluble fluorescence dye.

The thesis and the obtained results are organized in the chapters as follows:

Chapter 3: Materials and methods

The materials and methods used in this study with the experimental preparation of samples and polymerization methods are explained.

Chapter 4: TDMAO/L35/Styrene System

[Chapter 4.1](#) describes the unusual behavior of increasing amount of styrene monomer in TDMAO/L35 system and the results from the analyses of turbidity, dynamic and static light scattering, (DLS, SLS), small angle neutron scattering (SANS) measurements.

[In chapter 4.2](#), polymerization of styrene in TDMAO/L35 leading to viscous hybrid system is investigated in terms of viscosity and rheology, small angle neutron scattering (SANS) and NMR measurements.

Chapter 5: TDMAO/L35/LiPFOS/Styrene System

[Chapter 5.1](#) explains loading the styrene monomer into the vesicle template of TDMAO/LiPFOS/L35 and the obtained results regarding its effect on well-defined vesicle system.

[In part 5.2](#), we present the effect of polymerization of styrene in TDMAO/LiPFOS/L35 vesicle membrane.

Chapter 6: The effect of acrylate monomers

[In chapter 6](#), we summarized the effects of acrylate monomers on the studied vesicle systems. Primarily, different chain length of acrylates tested on TDMAO/L35 mixtures in part 6.1 and results are presented. Secondly, (in [chapter 6.2](#)) by mixing this solution with LiPFOS, monomer loaded vesicles are formed and analyzed structurally in detail. Consequently ([part 6.3](#)), the optimized system of TDMAO/LiPFOS/L35/ hexyl acrylate is polymerized and investigated by means of phase behavior, scattering, NMR, neutron spin echo, cryo-TEM methods, and the encapsulation efficiency was tested with fluorescence spectroscopy.

Chapter 7: Summary and Outlook

In [chapter 7](#), results are generally summarized and the key points for stabilizing vesicles via polymerization are indicated. Additionally, future studies about improving this method, such as

its compatibility with biodegradable systems are suggested for future work and discussed in this chapter.

3 Materials and Methods

3.1 Methods

3.1.1 Density

Densities were measured at 25°C by using a capillary oscillating density meter DMA 4500 Anton Paar, based on electronically measuring the oscillation period of a known volume fraction of sample in a U-shaped borosilicate tube with the relation of $\rho = A\tau^2 + B$ where the density ρ is related with the oscillation period τ , A and B are device constants.



Figure 3.1. Capillary oscillating density meter.

3.1.2 Refractivity Measurements

Refractivity measurements have been done with an Abbe 2WJ refractometer at 25°C for 630 nm wavelength and values are averaged for three repeated measurements.

3.1.3 Refractive Index Increment Measurements

Refractive index measurements were performed on the device from Orange Analytics 19" dn/dc on the wavelength of 620 nm. The refractive index increments were derived from concentration series at constant sample composition up to the 100-mM content and used for evaluating the data from turbidity and light scattering measurements. For the higher styrene content, dn/dc values were estimated via:

$$\frac{dn}{dc} = x \cdot \frac{dn}{dc} \text{ styrene} + \frac{(1-x)dn}{dc} \left(\frac{tdmao}{L35} \right) \quad (3.1)$$

Measured values of dn/dc are listed in [Table A1](#), [Table A3](#), [Table A4](#), [Table A5](#) (see Appendix).

3.1.4 Viscosity

Viscosity measurements were performed on calibrated Schott Ubbelohde micro Ostwald viscometers, type I (517 10) and Ic (517 13). Capillary constants are given for I, $0.01151 \text{ mm}^2 \text{ s}^{-2}$ and for Ic, $0.02942 \text{ mm}^2 \text{ s}^{-2}$. Zero shear viscosity η_0 values were calculated from the flow time t of the samples using the equation 3.2 related with density ρ and capillary constants K :

$$\eta_0 = \rho K t \quad (3.2)$$

Flow time t were registered automatically on Ivisc (Lauda-Brinkmann) and are averaged values of six measurements.

3.1.5 Light Scattering

Light scattering is one of the fundamental methods in the characterization of colloids. In principal, it can be described as the redirection of an incident light beam due to its interactions with a sample material. When the electromagnetic radiation interacts with the material, it induces an oscillation of the electrons in the molecule and leads a secondary radiation which is the scattering from the sample ([Figure 3.2](#)).

In scattering experiments, intensity over time is dependent on the magnitude of the scattering vector, q , which is angle dependent and given by $q = \left(\frac{4\pi n}{\lambda}\right) \sin\left(\frac{\theta}{2}\right)$ where n is the refractive index, λ the wavelength, and θ is the scattering angle.

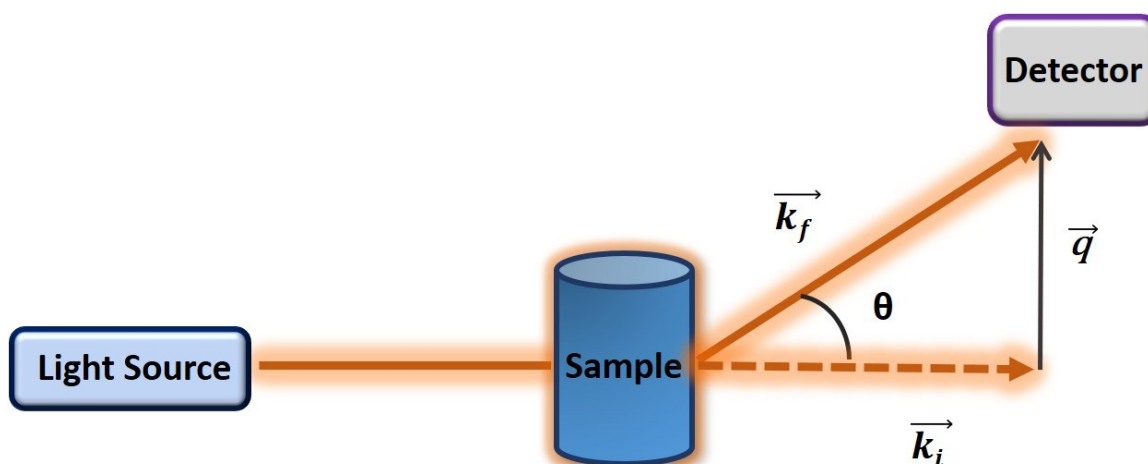


Figure 3.2. Schematic representation of light scattering experimental setup.

3.1.5.1 Dynamic Light Scattering

Dynamic light scattering (DLS) is based on the time dependence of fluctuations of the scattering intensity. The collective diffusion coefficient can be observed due to the fluctuations of particles undergoing Brownian motion. In such scattering experiment, [Figure 3.2](#) light passes through a scattering volume and is scattered due to inhomogeneities. The intensity is measured and detected at a certain angle by a photomultiplier from the correlation function of the photon count rate of the detector. Thus, dynamic information about the particles can be obtained during the measurement. In particular, DLS allows to determine the particle radius using the scattered light to measure the rate of diffusion of the particles and polydispersity.

The intensity autocorrelation function $g^2(\tau)$ for a given delay time τ (termed as t at DLS curves given thereafter) is obtained by:

$$g^2(\tau) = \frac{\langle I(t)I(t + \tau) \rangle}{\langle I(t) \rangle^2} \quad (3.3)$$

Where $I(t)$ and $I(t + \tau)$ are the intensities of the scattered light at times t and $(t + \tau)$.

Based on the Siegert relation the intensity autocorrelation function $g^2(\tau)$ can be converted to the field autocorrelation function $g^1(\tau)$ via:

$$g^2(\tau) = 1 + B|g^1(\tau)|^2 \quad (3.4)$$

The field correlation function decays exponentially in the solutions for monodisperse particles: $g^1(\tau) = e^{-\Gamma\tau}$ where the decay rate is $\Gamma = Dq^2$. For polydisperse samples $g^1(\tau)$ is presented as a sum of a distribution of decay rates $G(\Gamma)$.

The diffusion coefficient of the particles can be determined from the intensity correlation function $g^2(\tau)$. By plotting $g^2(\tau)-1$ as a function of τ , data shows an exponential decay and fitting the exponential decay one can obtain the diffusion coefficient D . Using the Stokes-Einstein relation hydrodynamic radius R_h can be estimated via:

$$R_h = \frac{k_B T}{6\pi\eta D} \quad (3.5)$$

In the equation T is the temperature, η the viscosity, k_B the Boltzmann constant, and D the diffusion coefficient.

As mentioned above, for polydisperse systems $g^1(\tau)$ is given as a sum of a distribution of decay rates $G(\Gamma)$. *Cumulant method* is one precise way to characterize the decay rates in such a case, which determines the size and polydispersity extending the logarithm of $g^1(\tau)$ with regards to

cumulants of the distribution ¹¹⁶. In this work, intensity correlation functions with monomodal decays have been analyzed with cumulant method via the second order to the function:

$$\ln[g^1(\tau)] = -\Gamma\tau + \frac{\mu_2}{2}\tau^2 - \frac{\mu_3}{6}\tau^3 \quad (3.6)$$

R_h the hydrodynamic radius can be calculated from the cumulant analysis using [equation 3.5](#) and also the polydispersity index can be calculated from second order fitting: $PDI = \frac{\mu_2}{\Gamma^2}$.

Light Scattering measurements were performed using an ALV/CGS-3 Compact Goniometer with an ALV/LSE-5004 multiple tau digital correlator equipped with a He-Ne laser with the wavelength of = 632.8 nm. All experiments were done in a thermostated bath at 25±0.1 °C using cylindrical sample cells with a diameter of 8 mm placed in toluene bath. The intensity autocorrelation function $g^2(\tau)$ was obtained by averaging three repeat measurements at different angles (30, 40, 50, 60, 70, 80, 90, 100, 110 and 120°) and performed on all samples at 25 °C. Static light scattering (SLS) measurements were performed using the same setup as employed for in Dynamic light scattering (DLS).

3.1.5.2 Static Light Scattering

Static light scattering (SLS) analyses the time-averaged scattering intensity as a function of the angle. In SLS one normalizes the time-average scattered intensity with incoming light. SLS provides critical information about the radius of gyration R_g , which is a measure of the size of an object of arbitrary shape and can be obtained from the Guinier approximation ²⁸, and molecular weights M_w of the aggregates.

The absolute intensities can be obtained by using the [equation 3.7](#). normalizing the measured intensities of the samples with the solvent and toluene as a standard, then correcting them with the Rayleigh ratio of toluene $R_{toluene}(q)$ toluene as reference, $1.34 \times 10^{-5} \text{ cm}^{-1}$ at 632 nm ¹¹⁷. Finally for the cylindrical cells, this value is corrected with the Herman & Levinson factor $(n_{toluene}/n_{solvent})^2$ ^{118,119}.

$$I(q) = \frac{I_{sample}(q) - I_{solvent}(q)}{I_{toluene}(q)} R_{toluene}(q) \left(\frac{n_{toluene}}{n_{solvent}} \right)^2 \quad (3.7)$$

The forward scattering $I(0)$ is extrapolated by fitting the Guinier approximation on scattering curves whereby the weight average molecular weights, M_w can be determined ¹²⁰:

$$M_w = \frac{I(q=0)}{Kc_g} \quad (3.8)$$

K in the equation is the optical constant given with the formula as:

$$K = \frac{4(\pi n_0 \left(\frac{dn}{dc}\right))^2}{N_A \lambda_0^4} \quad (3.9)$$

Where dn/dc_g is refractive index increment and c_g is the weight concentration of sample content.

3.1.6 Small Angle Neutron Scattering

Small angle neutron scattering (SANS) is one of the most important characterization methods for microstructural investigations on various materials. SANS allows investigations on the nanoscale and determines the morphology of particle systems for average particle sizes or shapes. Small angle scattering was first discovered by Guinier in 1930s during X-ray diffraction experiments and 30 years later SANS experiments were developed with the work of Stuhrmann on contrast variation experiments^{121,122}. Neutrons are produced by two types of sources, first steady-state reactors where neutrons are produced by fission processes and secondly spallation sources, where heavy nuclides are subjected to spallation by protons arriving from a high-power accelerator, often working in pulse mode. Being non-destructive, neutrons do not alter or destroy the materials therefore SANS has a great contribution in several areas of the basic and applied research, for instance in polymer science, biology and materials science^{123–125}. Fundamentally the scattering length density, which is a measure of the scattering power of a material, differences between isotopes especially hydrogen and deuterium, is the main basis of this method¹²⁶.

As described above the scattering length density is the decisive parameter in SANS. For each sample mixture, SLD values were calculated according to the equation 3.10 using the Scattering Length Density Calculator of the NIST web page¹²⁷.

$$SLD = \frac{\sum_{i=1}^n b_i}{v_m} \quad (3.10)$$

b_i is the sum of scattering length contributions from each species of n atoms in the molecule and divide by the molecular volume, v_m . The scattering length density of aggregates in the model fits was calculated as an average of all SLDs of components and weighted by the corresponding volume fractions.

In a statically isotropic system, the amplitude scattered by different particles is given as:

$$A(q) = \int_v \rho(r) e^{-iqr} dr \quad (3.11)$$

In the equation $\rho(r)$ is the distribution of length densities in the particle related with the composition. For averaging the fluctuations $\rho(r)$ can be split in two parts $\rho(r) = \langle \rho \rangle + \delta\rho(r)$ and [equation 3.11](#) is modified to $A(q) = \int_V \delta\rho(r)e^{-iqr} dr$, for $q>0$ average term is null. The measured intensity per unit volume is the absolute square of the amplitude and defined as:

$$I(q) = \frac{A(q)A^*(q)}{V} = \frac{1}{V} \int_V \int_V \delta\rho(r)\delta\rho(r') e^{-iq(r-r')} dr dr' \quad (3.12)$$

For a two-phase system ρ becomes to ρ_p and ρ_s then [equation 3.12](#) evolves to:

$$I(q) = \frac{1}{V} (\rho_p - \rho_s)^2 \int_{V_p} \int_{V_p} e^{-iq(r-r')} dr dr' = \frac{1}{V} \Delta\rho^2 \int_{V_p} \int_{V_p} e^{-iq(r-r')} dr dr' \quad (3.13)$$

The scattering length density difference of particle and matrix is the $\Delta\rho$ and for N of particle number

$$I(q) = \frac{V_p^2}{V} N_p \Delta\rho^2 [F(q)]^2 \quad (3.14) \quad F(q) = \frac{1}{V_p} \int_{V_p} e^{-iqr} dr \quad (3.15)$$

And equation is reorganized to:

$$I(q) = \phi V_p \Delta\rho^2 P(q), \quad P(q) \text{ is particle form factor} \quad (3.16)$$

Additionally, the interference of neutrons scattering from different particles is termed as structure factor S(q). In the isotropic solutions S(q) is defined by:

$$S(q) = 1 + 4\pi N_p \int_0^\infty [g(r) - 1] \frac{\sin(qr)}{qr} r^2 dr \quad (3.17)$$

$g(r)$ is the pair correlation function of the scattering objects. While the form factor term is describing the shape and size of the scattering object, structure factor determines the correlation between particle mass centres. [Equation 3.16](#) is rewritten as

$$I(q) = \phi V_p \Delta\rho^2 P(q) S(q) \quad (3.18)$$

A typical example setup of neutron scattering instrument can be seen in [Figure 3.3](#). After the production of neutrons from the reactor source, the required wavelength is selected by a velocity selector. Since neutrons cannot be easily focused, the coming neutron beam is collimated in the next part and defined with an aperture depending on the cell geometry which is providing a

better focus on the sample cell. Later on, the beam interacting with the sample has been scattered and detected at certain distances, which is called as sample to detector distance (SD). The choice of configuration in terms of wavelength, collimation and detector combinations, is important to address the need of information at different q -ranges.

In this study, SANS experiments were performed on 2 different instruments. For all measurements, quartz cuvettes with path lengths of 1 or 2 mm were used as sample cells and measured at 25 °C. For simulation and modelling of the data SASfit software was used ¹²⁸.

Details are described below.

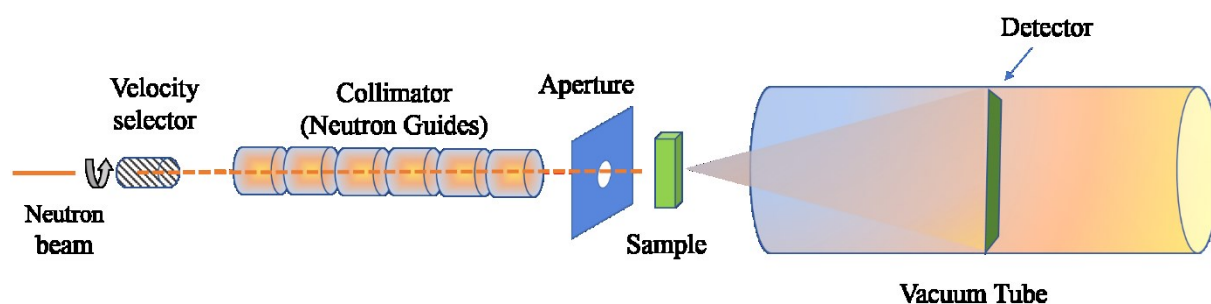


Figure 3.3. Schematic representation of neutron scattering instrument general setup.

KWS 1, Germany: Measurements were performed on the instrument KWS 1, FRM II, Jülich Center for Neutron Science (JCNS) at MLZ, Munich, Germany ¹²⁹. Scattering intensities were measured with a position-sensitive ⁶Li scintillation detector of Anger type has 128 x 128 pixels with a 5.25 x 5.25 mm special resolution. A 50 x 50 mm beamstop is located in the middle of detector with a small window for a ³He counter, which determines the intensity of the direct beam for transmission measurements. Measurements were done at a wavelength of 0.6 nm, the spread of wavelength in our case was given by a FWHM (full width at half maximum) of 9 %, and three sample-detector distances of 1.2, 7.7, and 19.7 m with corresponding beam collimation lengths of 8.0, 8.0, and 20.0 m respectively. Transmissions were measured at 8 m distance with the attenuated direct beam. Water was used as standard to determine the absolute intensities and detector efficiency. Data reduction was done using the QtiKWS software developed by JCNS ¹³⁰ and as background the scattering of the empty cell was subtracted.

D11, France: Spectra were recorded using instrument D11 at the Institute Laue Langevin (ILL) in Grenoble, France ¹³¹ on a 2-dimensional ³He-detector. A wavelength of 0.6 nm (FWHM of 9%), three sample-detector distances of 1.2, 8.0, and 39.0 m with corresponding beam collimation lengths of 5.5, 8.0, and 40.5 m were employed, respectively. Transmissions were

measured at 8.0 m distance with the attenuated direct beam. Data reduction was done using the Lamp software developed by ILL¹³². Background the scattering of the empty cell was subtracted and sample transmissions and dead-times were considered. Scattering of H₂O in a 1 mm cuvette was used for obtaining the absolute units.

3.1.6.1 Model Independent Analysis

The scattering vector is reciprocal length of the sample and radiation source. Simply, in a small angle scattering curve, q scale can be described by three ranges, which are low, middle and large q . Thus, we consider gaining information of bigger structures at small q values while for smaller structures, they arise from the large q regime. Depending on the intensity decay, $I(q) \propto q^{-\alpha}$, structural geometries of the aggregates can be described and [Figure 3.4](#) illustrates the geometrical assumptions. In the intermediate q , one predicts for $\alpha = 2$ discs of two dimensions

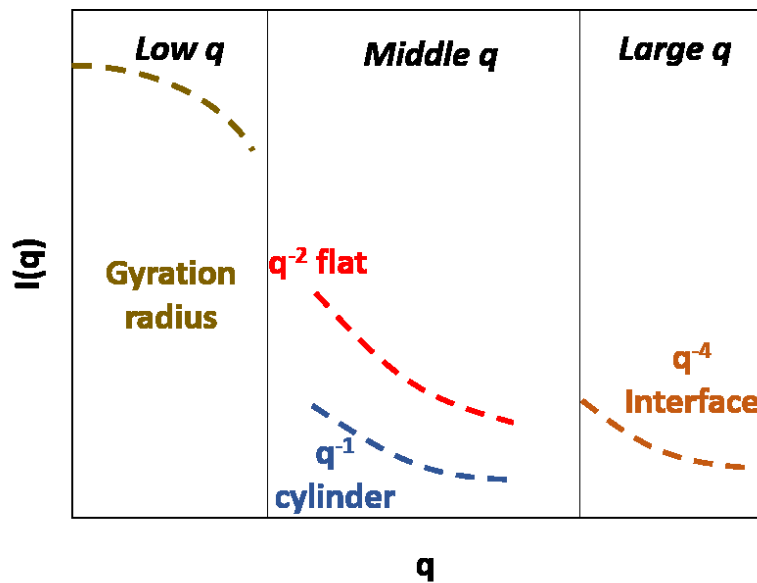


Figure 3.4. Schematic representation of neutron scattering instrument general setup.

and $\alpha = 1$ cylinders of one dimension.

Guinier Approximation is applied independently from the particle structure at very low q . In the range of $qr < 1$, $P(q)$ form factor is generalized to a form which described by the forward scattering $I(0)$ and the radius of gyration R_g ¹³³:

$$P(q) \sim \phi V_p \exp\left(-\frac{(qR_g)^2}{3}\right), \quad (3.19a) \quad \lim_{q \rightarrow 0} I(q) = I_0 \exp\left(-\frac{(qR_g)^2}{3}\right) \quad (3.19b)$$

R_g , can be obtained from the slope of a plot of $\ln(I(q))$ vs q^2 . The radius of gyration of a homogenous sphere of radius R is: $R_g^2 = \frac{3}{5}R^2$, for the thin spherical shell of radius R , $R_g^2 = R^2$ and for a cylinder with R radius and length of l , $R_g^2 = \frac{R^2}{2} + \frac{l^2}{12}$ ¹²⁶. It also has to be kept in mind that Guinier approximation is limited to low angles ($qR_g \ll 1$) and valid when the interparticle interactions are negligible¹³⁴.

Porod Law is valid for two-phase systems with sharp interfaces. When the q vector is larger than the curvature of interfaces, the interfaces appear flat and intensity is proportional to the surface area, S . Due to the Porod limit at high q range, intensity decays with q^{-4} ¹³⁵.

$$I(q) = 2\pi S \Delta\rho^2 q^{-4} \quad (3.20)$$

Kratky-Porod Plot is derived from the intermediate- q Guinier approximation and used for different geometries in the form of^{134,136}:

$$I(q) = I(0)q^{-\alpha} \exp(-q^2\beta) \quad (3.21)$$

α has different forms such as 0 for spherical particles, -1 for rod-like and -2 for flat bilayer. While β is the space average radius of gyration and β is $R_g^2/3$ for spherical particles, R_t^2 for flat bilayers. As described above in the part of Guinier approximation, R_g differs for different radii and thicknesses. For flat bilayers with thickness t , $R_t^2 = t^2/12$ and intermediate q Guinier approximation has the form of:

$$I(q) = I(0)q^{-2} \exp\left(\frac{-q^2 t^2}{12}\right) \quad (3.22)$$

When we plot the $\ln(q^2 I(q))$ vs q^2 middle q range give a straight line with the slope $-t^2/12$, thus membrane thickness can be extracted from the slope.

3.1.6.2 Model Dependent Analysis

Scattering intensity described above with the [Equation 3.18](#) has two important parameters which are termed as form and structure factor. While the form factor $P(q)$ describes the interference of neutrons scattered from different parts of the same object; structure factor, $S(q)$ represents the interference of neutrons scattered from different objects meaning interparticle interactions and for very dilute systems $S(q) = 0$. The form factor, $P(q)$ describes the size and shape of the scattering object and can be derived for common geometries for instance spheres

or spherical shells from analytical expressions. Following part presents the form factor expressions of different geometries applied for modelling the scattering curves in the present work.

3.1.6.2.1 Form factor of sphere

The form factor of homogenous spheres and globular objects with radius of R is given as ¹³⁷:

$$P(q, R) = [F(q, R)]^2, F(q, R) = \left[3 \frac{\sin(qR) - (qR)\cos(qR)}{(qR)^3} \right] \quad (3.23)$$

3.1.6.2.2 Form factor of cylinders

The form factor P(q) for cylinder with length L and radius R is given as ¹³⁸:

$$I_{cyl} = 16(\pi R^2 L)^2 \Delta SLD_s^2 \int_0^1 \left[\frac{J_1(qR\sqrt{1-x^2})}{q^2 R} \frac{\sin\left(\frac{qLx}{2}\right)}{\sqrt{1-x^2}Lx} \right]^2 dx \quad (3.24)$$

where J_1 is the first order Bessel function of the first type.

3.1.6.2.3 Form factor of spherical shell

Spherical shell is described with R_0 as inner radius, R_1 as outer radius (giving $D = R_1 - R_0$ as a shell thickness), and ΔSLD_i is the scattering length density difference between shell and matrix. It has to be noted that the mean vesicle radius, R_{ves} was defined as the sum of R_0 and D , i. e. the outer vesicle radius.

$$P(q, R_i, \Delta SLD_i) = \left(\sum_{i=0}^1 F(q, R_i, \Delta SLD_i) \right)^2 \quad (3.25)$$

$$F(q, R_i, \Delta SLD_i) = \frac{4}{3} \pi R_i^3 \Delta SLD_i \left(3 \frac{\sin(qR_i) - qR_i \cos(qR_i)}{(qR_i)^3} \right) \quad (3.26a)$$

The scattering intensity was calculated by an integrating over the contained distribution of particle sizes as described with a log-normal distribution.

$$I = {}^1N \int_0^\infty L_N(R_0, R_{ves}, \sigma) P(q, R_0, D, \Delta SLD_i) dR_0 + I_{inc} \quad (3.26b)$$

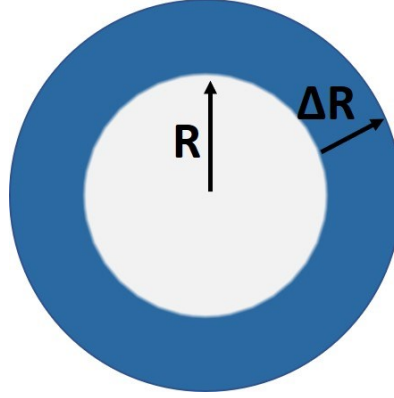


Figure 3.5. Spherical shell model.

3.1.6.2.4 Log-normal size distribution

Since our system consists of different aggregate types, for a detailed understanding we employed different form factors of different geometries taking into consideration their polydispersity by assuming a log-normal distribution function which was described as:

$$L_N(R_0, R_{ves}, \sigma) = \frac{1}{R_0 \sigma \sqrt{2\pi}} \exp\left(-\frac{(\ln(R_0) - (R_{ves} - D))^2}{2\sigma^2}\right) \quad (3.27)$$

σ is the variance. Additionally, in the SASfit software¹²⁸, the volume fractions f_p has been implemented in the log-normal size distribution by integrating over the particle volume V_p :

$$f_p = \int_0^\infty L_N(r, \mu, \sigma) V_p(r) dr \quad (3.28)$$

Volume fractions of samples Φ , were calculated from the total concentration of amphiphilic materials compounds used in each sample C_{tot} multiplied by the sum of the molar mass M_i and the density ρ_i of each component i :

$$\Phi = C_{tot} \sum \frac{M_i}{\rho_i} \quad (3.29)$$

3.1.6.2.5 Instrumental resolution

The experimental smearing was accounted in the intensities I , by the resolution function assuming a Gaussian function ¹³⁹:

$$I(q) = \frac{1}{\sqrt{2\pi}\sigma q(q)} \int_{-\infty}^{+\infty} \exp\left(-\left[\frac{q' - q}{\sqrt{2\pi}\sigma q(q)}\right]^2\right) I(q') dq' \quad (3.30)$$

The standard deviation $\sigma(q)/q$ was taken into account for the instrument resolution via:

$$\left(\frac{\sigma(q)}{q}\right)^2 = \left(\frac{\sigma(\lambda)}{\lambda}\right)^2 + \left(\frac{\sigma(\theta)}{\theta}\right)^2 \quad (3.31)$$

q is defined as the magnitude of scattering wave vector $q = (4\pi/\lambda)\sin(\theta/2)$ with θ being the scattering angle. In [equation 3.30](#) first contribution is the q dependent wavelength spread $\Delta q_\lambda = (\Delta\lambda/\lambda) q$ and was related to the FWHM (full width at half maximum).

3.1.6.2.6 Structure factor

In [equation 3.18](#) $S(q)$ defines the inter-particle interaction. We used the structure factor of hard sphere to describe the scattering curves. It can be solved in the Percus–Yevick approximation as closure relation to solve the Ornstein-Zernike equation to yield an analytical expression ¹⁴⁰. Here the $S(q)$ determines a pair interaction potential $U(r)$ with the repulsion radius r .

$$U(r) = \begin{cases} \infty, & 0 < r < \sigma \\ 0, & r > \sigma \end{cases}, \quad S_{HS}(q, R_{HS}, f_p) = \frac{1}{1 + 24f_p \frac{G(q, R_{HS}, f_p)}{R_{HS}q}} \quad (3.32)$$

The expansion of the structure factor can be explained as

$$G(q) = \alpha \frac{\sin A - A \cos A}{A^2} + \beta \frac{2A \sin A + (2 - A^2) \cos A - 2}{A^3} + \gamma \frac{-A^4 \cos A + 4[(3A^2 - 6) \cos A + (A^3 - 6A) \sin A + 6]}{A^5} \quad (3.33)$$

$$\alpha = \frac{(1 + 2f_p)^2}{(1 - f_p)^4}, \quad \beta = -6f_p \frac{(1 + \frac{f_p}{2})^2}{(1 - f_p)^4}, \quad \gamma = \frac{f_p \alpha}{2} \text{ and } A = 2R_{HS}q \quad (3.33a)$$

Practically this approximation depends on the hard sphere radius R_{HS} and hard sphere volume fraction f_p . In our system the cylindrical particles occupy larger hard sphere volume. We considered the R_{HS} a sum of the particle diameter and two hydrophilic chain lengths (-EO₁₁-) of L35 attached on the aggregate. According to de Gennes approximation, the area occupied by single PEO chain was calculated before with assuming the PEO chains of L35 form mushroom-

like conformations when they attach on the surface of the aggregate^{115,141}. The interactions were determined by fitting this model.

3.1.7 Neutron Spin-Echo Spectroscopy (NSE)

Neutron spin echo is a type of time-of-flight spectrometer whereby one can determine the energy changes along with the scattering. Although it is an inelastic neutron scattering method invented by Mezei^{142,143}, it differs from other conventional techniques in the way of measuring singular incident and scattered neutron velocities considering the Larmor precession of the nuclear neutron spin in a magnetic field. This spin vector works like an internal clock which relates the individual neutron to its velocity, and by this way one measures directly the velocities before and after the scattering.

In general, while the incident neutron beam (generally with a wavelength interval of 10-20% width) is polarized through the guide direction, it is subjected with a spin flip of $\pi/2$ which leads the polarization to a vertical direction via Larmor precession. However, because of the different neutron velocities thereof the flight times, the final beam reaching to the sample loses the polarization. When the beam hits the sample, it passes through a π flipper and goes towards the second precession field, which thereafter is applied for aligning the position of different spin via another $\pi/2$ flipper. Finally, it restores the initial polarization again. [Figure 3.6](#) represent a general scheme of neutron spin echo spectrometer.

This technique allows decoupling the energy resolution of the experiment from the monochromaticity of the beam, which allows to detect energy transfers as small as a few nanoelectronvolts¹⁴⁴. This provides highest energy resolution and differently it measures the intermediate scattering function $S(q,t)$ which makes it useful to investigate the dynamic measurements, and slow relaxations. The scattering functions are related to the coherent or incoherent intermediate scattering function by Fourier transformation¹⁴⁴ and by this way the dynamic structure function $S(q,\omega)$, can be converted to $S(q,t)$:

$$S(q, \omega) = \int \exp(i\omega t) S(q, t) dt \quad (3.34)$$

The spin manipulations of the NSE spectrometer serve to detect miniscule energy transfers during scattering in a way that finally yields the intermediate scattering function which is related to the time-dependent coordinates of the nuclei in the system¹⁴⁵:

$$S(q, t) = \frac{1}{N} \sum_{i,j}^N \exp(-iq(r_i(0) - r_j(t))) \quad (3.35)$$

Details of the neutron spin echo method can be found in the literature ^{142,146–148}.

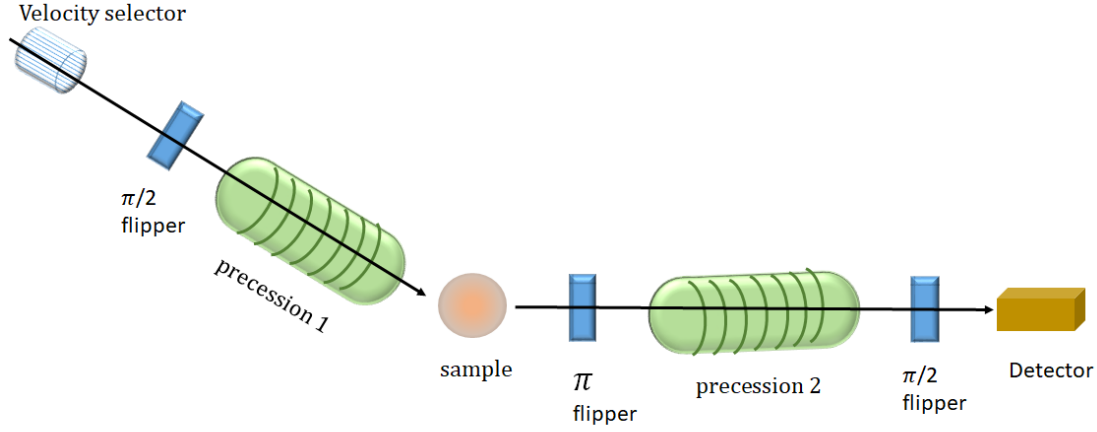


Figure 3.6. Schematic representation of neutron spin echo instrument general setup.

The NSE experiments in this thesis were performed on the instrument IN15 of the ILL, which provides highest resolution with longest Fourier time worldwide, at Grenoble (France). Samples are measured in quartz cuvettes (Hellma) with path lengths of 1 mm and measured at 25 °C. The Fourier time was ranging up to 532 ns by varying the wavelength of 14, 10 and 6 Å thereof covering a q -range from 0.014 to 0.14 1/Å.

3.1.8 Cryogenic Transmission Electron Microscopy (cryo-TEM)

Transmission electron microscopy (TEM) measures the structures in real space providing a high resolution of submicron structures. Fundamentally, an electron beam is focused on the vitrified sample while the light passes through it, the transmitted beam forms the image of the aggregate. TEM consists of illumination and imaging part. The first part consists of an electron source where electrons are emitted from a heated filament, and the electron density can be controlled via an applied voltage. A high voltage field accelerates the emitted electrons through the condenser lens. The imaging part provides the representation of the sample under high vacuum to prevent the electron gas interaction. This part is formed from objective, projector lens and corresponding apertures, the phosphor viewing screen and the photographic film. When the transmitted electron beam is focused on the objective lens, an image forms on the phosphor image screen and with the help of the generated light, image can be seen.

Since this technique needs specific preparations for instance on a grid made of copper, gold or nickel, it does not allow to image samples in their native environment. Thus, cryogenic Transmission Electron Microscopy (cryo-TEM) has been developed for investigating the nanostructured materials in aqueous solutions.

3.1.8.1 Sample Preparation

Cryo-TEM images were taken from two different measurements. Imaging of the polymerized vesicle sample was performed at Technion, Haifa (Israel). Here, the samples were prepared in controlled environment vitrification system (CEVS) at 25°C and humidity at saturation to prevent evaporation from the specimen. Prior to specimen preparation, the grids were plasma etched in a PELCO EasiGlow glow-discharger (Ted Pella Inc., Redding, CA) to increase their hydrophilicity. Inside the CEVS chamber, a carbon-coated perforated polymer film, supported on a 200 mesh TEM grid was held by tweezers. A drop of the sample was placed on the film and blotted by a filter paper-covered metal strip to remove excess solution and form a thin film of liquid. The specimen was then vitrified by quickly plunging it into liquid ethane at its freezing point. After vitrification, the sample is kept in liquid nitrogen until transfer into the TEM for imaging. Imaging was performed using a FEI Tecnai T12 G2 transmission electron microscope. The microscopes are equipped with LaB6 electron gun and operates at 120kV. Specimens were equilibrated in the microscope below -178 °C in Gatan 626 cryo-holders and imaged using a low-dose imaging procedure to minimize electron-beam radiation damage (where the electron exposure in a recorded micrograph is less than 1000 nm. A Gatan US1000 high-resolution cooled-CCD camera recorded the images at exposure time of 1 second using the DigitalMicrograph software package.

Images of the unpolymerized sample were taken at TEM laboratory of MLZ (JCMS) Munich, Germany. Similar as described above, the specimen was vitrified by plunging the sample into liquid ethane and prior to vitrification it was maintained at 20 °C and 80% relative humidity. Here, the sample is deposited on holey carbon grids and grids were replaced to a Gatan 910 multi-specimen holder.

3.1.9 Rheology

Rheological properties of self-assembling systems provide crucial information for their potential applications as new materials ^{149–151}. In general, dilute surfactant systems usually behave as Newtonian fluid, which has a linear relationship between shear stress and shear rate,

thus the viscosity remains constant and related to the concentration and shape of aggregates. In contrast, for non-Newtonian fluids the viscosity of the fluid changes when shear is applied.

Some surfactant solutions show more complicated rheological behaviour being elastic and viscous at the same time and depending on the shear rate. Oscillatory measurements provide detailed information about the viscoelastic properties by determining storage (elastic) modulus G' and loss (viscous) modulus G'' . The two moduli can be described by the Maxwell model¹⁵²:

$$G'(\omega) = \frac{\omega^2 \tau_R^2}{1 + \omega^2 \tau_R^2} G_0 \quad \text{and} \quad G''(\omega) = \frac{\omega \tau_R}{1 + \omega^2 \tau_R^2} G_0 \quad (3.36)$$

Rheological measurements were performed using a Malvern Bohlin Gemini 200 HR nano rheometer. Measurements were done at 25°C with the cone-plate- geometry at the cone angle of 4° and the cone diameter of 40 mm. The gap size between cone and plate was set to 150 μm. A pre-shear of 1 s⁻¹ was given to the sample for 30 seconds, subsequently the sample was left to rest for 3 minutes before measurements. For the shear experiments, shear rate was varied from 1 – 70 s⁻¹ and the experimental data was analysed with Carreau-Yasuda model ([equation 3.37](#))¹⁵³:

$$\eta = \eta_0 [1 + (\tau \dot{\gamma})^a]^{\frac{n-1}{a}} \quad (3.37)$$

η_0 is the zero-shear viscosity, the relaxation time τ , the constant a , and n is the power law exponent (for $n < 1$ one observes shear thinning). The relation ([equation 3.38](#)) between zero shear viscosity and relaxation time leads to the shear modulus G_0 , corresponding the plateau of loss modulus G' .

$$G_0 = \frac{\eta_0}{\tau} \quad (3.38)$$

From the oscillatory experiments, the viscoelastic response of polymerized sample was obtained by means of the loss (G') and storage (G'') modulus; therefore, a frequency sweep was applied between 0.006-10 Hz.

3.1.10 Nuclear Magnetic Resonance Spectroscopy (NMR)

Polymerization was followed by using ¹H NMR for confirming the full conversion of monomer with vanishing the proton signals of monomers. A Bruker Avance II 400 spectrometer operating at 400 MHz was used to recording the spectra. As the solvent, D₂O was used to obtain the chemical shifts and Tetramethylsilane (TMS) was used as reference agent.

3.1.11 UV-vis Spectrometry

UV-vis spectroscopy has been used to measure the transmissions of the samples for obtaining the turbidity values. Measurements were performed on a Varian Cary 50 UV-vis spectrophotometer. Rectangular Hellma quartz cuvettes with a thickness $d =$ of 1 mm were used for measurements and data was scanned over a range of 350-800 nm wavelength. For each sample, measurements were repeated three times at 25 °C.

3.1.11.1 Turbidity and Transmission

Turbidity values are calculated from the transmission T observed from UV-vis measurements according to the equation:

$$\tau = -\frac{\ln(T)}{d} \quad (3.39)$$

The following relations define the relation between the transmission and the molecular weight of the aggregates:

$$M_{\text{weff}} = \frac{\tau}{K * c_g} \quad (3.40)$$

$$K = \frac{32\pi^3 n_o^2 \left(\frac{dn}{dc_g}\right)^2}{(3N_{\text{av}}\lambda^4)} \quad (3.41)$$

Here, λ is the wavelength, n the refractive index of the solvent, N_{Av} is the Avogadro constant, c the weight concentration of the samples, dn/dc_g the refractive index increment, and ρ the density of the aggregates.

3.1.12 Fluorescence Spectroscopy

Fluorescence is the emission of light by a substance (fluorophores) which is absorbing light. When the species are absorbing photons of sufficiently high energy, they become excited from the ground electronic state to an excited electronic state. After staying short time in this excited state, the molecule returns to its stable ground state with transferring its energy in the form of emitting light of longer wavelength than that of the initial light. Typical fluorophores are mostly aromatic molecules. Most important characteristics of a fluorophore is the lifetime and quantum yield. The lifetime of the fluorophore is the duration of the excited state of the fluorophore before returning to its ground state. Moreover, the quantum yield is the ratio of the number of emitted photons to the number of absorbed photons.

Quenching is a process that reduces the fluorescence intensity of a substance. Different molecular interactions such as molecular rearrangements, complex formation, energy transfer, or collision can be result with quenching. Molecular oxygen¹⁵⁴, metal ions^{155,156} are common quenchers have been used widely in the literature. Stern-Volmer equation 3.42 describes the collisional quenching theoretically¹⁵⁷:

$$\frac{F_0}{F} = 1 + k_q\tau_0[Q] = 1 + K_D[Q] \quad (3.42)$$

Where F_0 and F are the fluorescence intensities before and after the addition of quencher, respectively, k_q is the bimolecular quenching constant, τ_0 is the lifetime of the fluorophore and Q is the concentration of the quencher. K_D is the Stern-Volmer constant which signs the sensitivity of the fluorophore to the quencher. Depending of the variety of quenchers, the fluorophore-quencher combinations can be determined for a desired aim.

Steady-state fluorescence measurements were performed using a fluorescence spectrophotometer Hitachi FL 4500. Fluorescence intensities were recorded in the region from 490 to 600 nm with an excitation wavelength of 495 nm and an emission wavelength of 515 nm in the scan mode of emission. The excitation and emission slits were set at 2.5 nm and scan speed was chosen as 240 nm/min. For each sample, measurements repeated three times (in 10 mm × 10 mm × 45 mm quartz cell) at 25 °C.

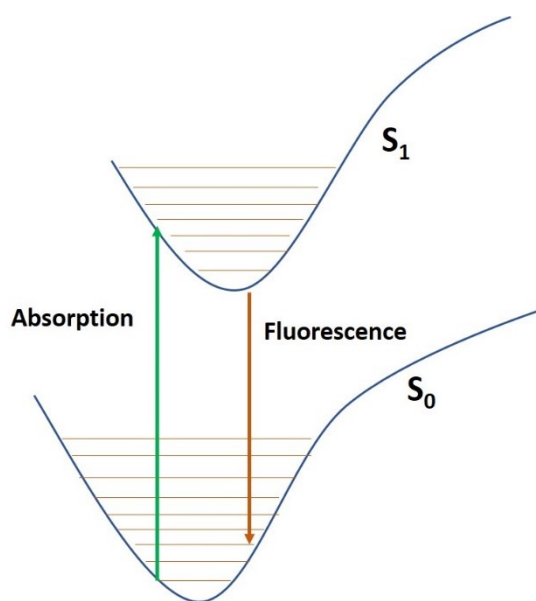


Figure 3.7. Absorption and emission of light schematically for two shifted potential energy surfaces.

3.2 Materials and Experimental

3.2.1 Chemicals

[Table 3.1](#) present the surfactants used in this thesis, and details will be explained below.

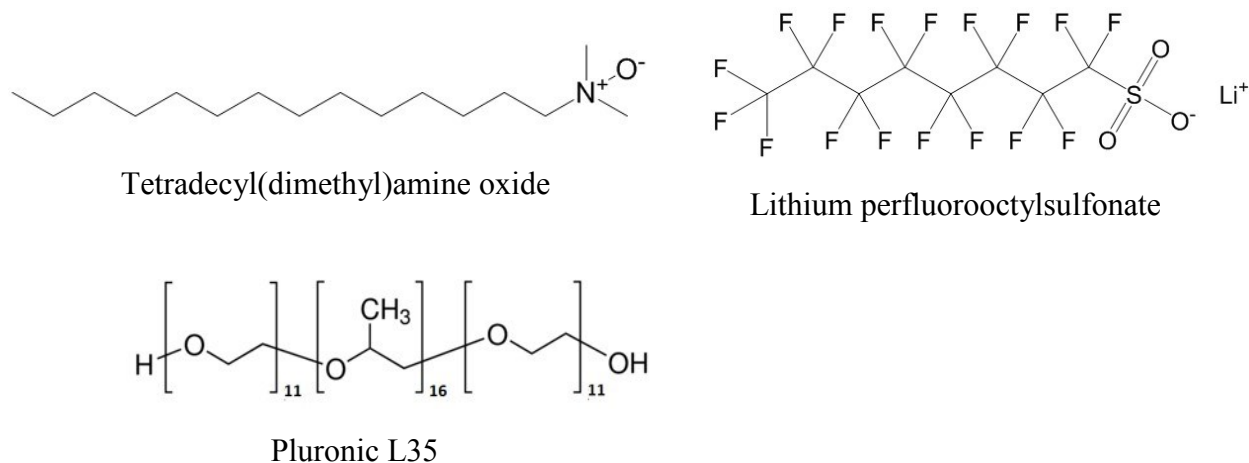


Figure 3.8. Chemical structures of surfactants used in this study.

Tetradecyl(dimethyl)amine oxide (TDMAO, cmc = 0.12 mM) was kindly provided by Stepan company (Illinois, USA) as a 25% TDMAO solution in water named as Ammonyx M. This solution was freeze-dried and used without any further purification. Pluronic L35 (L35, EO₁₁PO₁₆EO₁₁, M_w = 1900 g/mol, on average but as a polymer being polydisperse with respect to its molecular composition) was kindly given by BASF SE (Ludwigshafen, Germany). Lithium perfluorooctylsulfonate (LiPFOS, cmc = 6.3 mM) was purchased from TCI Europe

Table 3.1. Surfactants used in this thesis, with their common name, abbreviation, molecular formula, molecular weight, density and scattering length densities.

Compounds	Synonym	Molecular formula	M _w / (g/mol)	ρ / (g/ml) at 25°C	SLD / (10 ¹⁰ cm ⁻¹)
Tetradecyl dimethylamine oxide	TDMAO	C ₁₆ H ₃₅ NO	257.146	0.897	-0.197
Lithium perfluorooctane sulfonate	LiPFOS	C ₈ F ₁₇ SO ₃ Li	506.06	1.86	3.71
Pluronic L35	L35	C ₉₂ H ₁₈₆ O ₃₈	1900	1.06	0.458
D ₂ O	D ₂ O	D ₂ O	20.03	1.1	6.35

(purity > 96%). Samples for small-angle neutron scattering (SANS) experiments were prepared using D₂O (D content > 99.9 %) from Eurisotop company (France). All the stock solutions used in this work were prepared by dissolving the proper mass amount of the compounds either in Millipore or D₂O.

Additionally, compounds used for polymerization reactions such as monomers, cross-linkers and photo-initiators are tabulated in [Table 3.2](#). In details, styrene (C₈H₈, >99% GC, contains 0.005% 4-tert-butylcatechol as stabilizer), hexyl acrylate (98%, contains 100 ppm hydroquinone as inhibitor), dodecyl acrylate (technical grade 90%, contains 60-100 ppm monomethyl ether hydroquinone as inhibitor), isooctyl acrylate (>90%, contains 75-125 ppm monomethyl ether hydroquinone as inhibitor,) monomers, 1,6-hexanediol diacrylate (technical grade 80%, 100 ppm monomethyl ether hydroquinone as inhibitor), and divinylbenzene (technical grade 80%, 1000 ppm p-tert-butylcatechol as inhibitor) as cross-linking agents were all purchased from Sigma-Aldrich. All monomers and cross-linkers were washed through inhibitor remover column before usage and stored dark in the fridge. Therefore, flash columns with 20 cm height and 3 cm diameter size were produced in-house, filled with initiator remover (Sigma Aldrich- CAS:311332) up to 5 cm height. While monomers were washing through it, the column was covered with aluminum folio and worked in the dark.

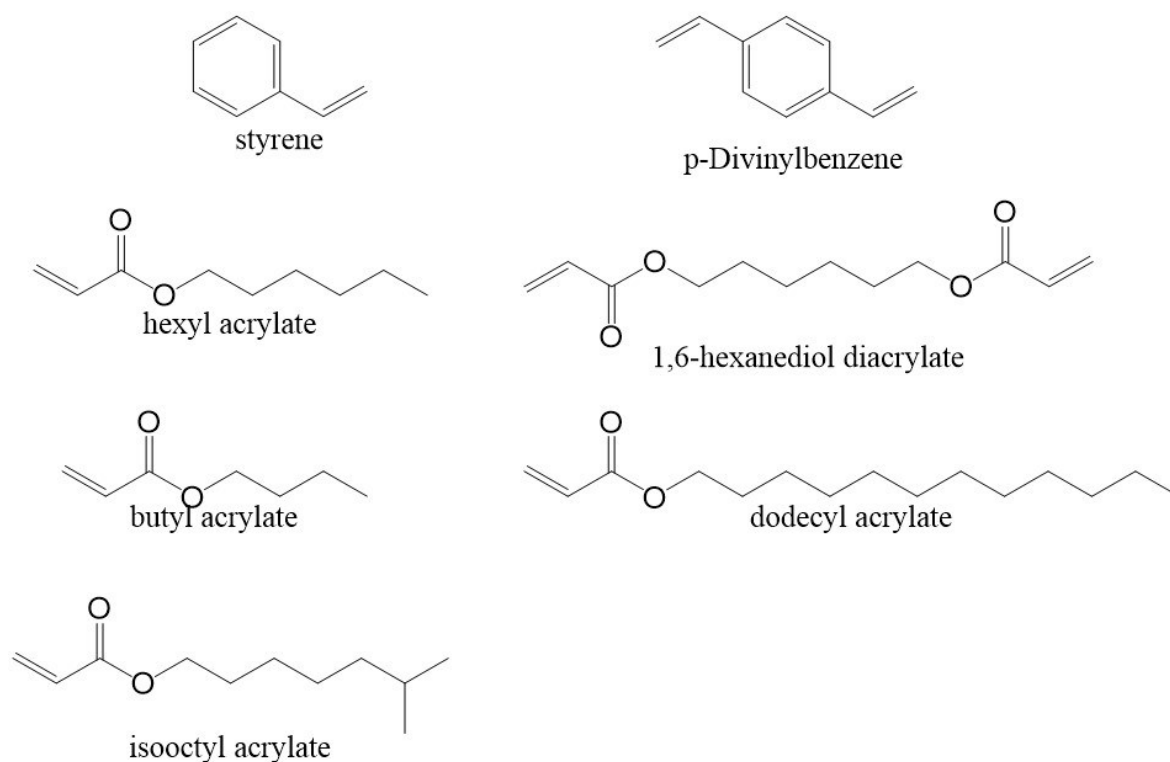


Figure 3.9. Chemical structures of monomers and cross-linkers used in this study.

Benzoyl peroxide, 2,2-Dimethoxy-2-phenylacetophenone (99%) and Azoisobutyronitrile (98%) were used as water insoluble photo-initiator ([Figure 3.10](#)) and received from Sigma-Aldrich. These compounds were used without further purification.

Additionally, calcein (λ_{ex} 470 nm; λ_{em} 509 nm at pH 7.4) was used as water-soluble fluorescence dye and Cobalt (II) chloride (anhydrous) as the quenching agent. Both were purchased from Sigma-Aldrich.

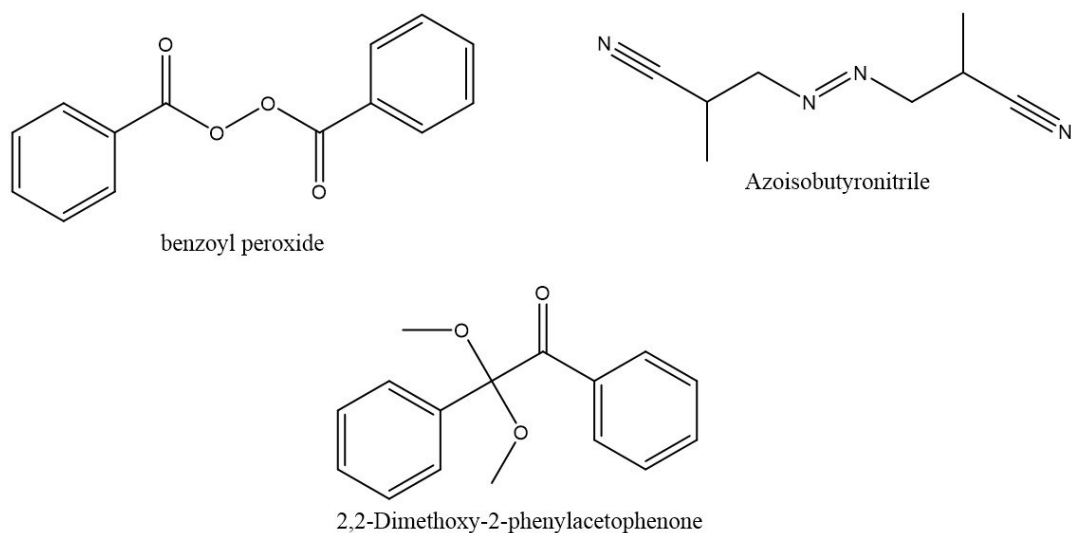


Figure 3.10. Chemical structures of photo-initiators used in polymerization reactions in this study.

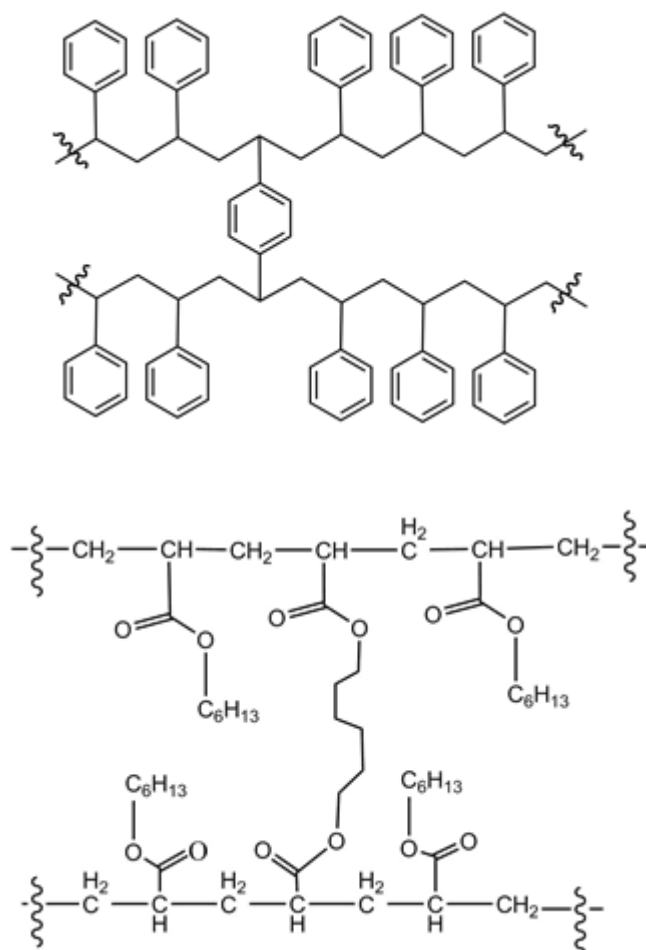


Figure 3.11. Structural presentation of top) poly(styrene-co-divinylbenzene); bottom) poly(hexyl acrylate-co-1,6-hexanediol diacrylate).

Table 3.2. Monomers, cross-linkers, photo-initiators used in this thesis, with their common names, abbreviations, molecular formula, molecular weights, density, water solubility and scattering length densities.

Compounds	Synonym	Molecular formula	M_w / (g/mol)	/(g/ml) at 25 C	Water Solubility/at 25 C (g/L)	SLD / (10^{10}cm^{-1})
Styrene	-	C_8H_8	104.15	0.906	0.3	1.21
Divinylbenzene	DVB	$\text{C}_{10}\text{H}_{10}$	130.19	0.914	0.052	1.224
Hexyl acrylate	HA	$\text{C}_{10}\text{H}_{10}$	156.22	0.888	0.4	0.397
1,6-hexanediol diacrylate	HDODA	$\text{C}_{12}\text{H}_{18}\text{O}_4$	226.27	1.01	<0.1	0.623
Butyl acrylate	BA	$\text{C}_7\text{H}_{12}\text{O}_2$	128.17	0.89	0.01	0.554
Dodecyl acrylate	Lauryl acrylate	$\text{C}_{15}\text{H}_{28}\text{O}_2$	254.41	0.86	0.0015	0.144
Isooctyl acrylate	IOA	$\text{C}_{11}\text{H}_{20}\text{O}_2$	184.28	0.88	0.001	0.286
Benzoyl peroxide	BPO	$\text{C}_{14}\text{H}_{10}\text{O}_4$	242.23	1.33	<1	2.60
2,2-Dimethoxy-2-phenylacetophenone	DMPA	$\text{C}_{16}\text{H}_{16}\text{O}_3$	256.3	1.122	insoluble	1.68
Azobisisobutyronitrile	AIBN	$\text{C}_8\text{H}_{12}\text{N}_4$	164.21	1.1	<0.1	1.84

3.2.2 Sample Preparation

The basic model system in our work composed of nonionic TDMAO, pluronic L35 (1 mol % with respect to TDMAO) and anionic LiPFOS surfactants. Vesicles were formed from these mixtures with the final concentrations of 27.5 mM TDMAO / 0.275 mM L35 / 22.5 mM LiPFOS.

TDMAO/L35/Monomer

Dissolving the hydrophobic monomers into the vesicle membrane was the challenging issue during this study since the outside media was water. To prevent aging and provide better dissolving, concurrent loading was efficient. Therefore, concurrent loading of monomers was chosen in which case monomers (in the case of polymerization, details will be described below) were dissolved in 50 mM TDMAO / 0.5 mM L35 stocks prior to vesicle preparation. 50 mM TDMAO / 0.5 mM L35 stocks / varying concentrations of monomers were prepared in millipore water or in D₂O for SANS experiments. Samples were equilibrated by stirring for 3 days at room temperature in the dark.

TDMAO/L35/Monomer/LiPFOS

Concurrent monomer loaded vesicles were prepared by mixing monomer loaded TDMAO / L35 stock solutions described above with 50 mM LiPFOS stocks at the molar ratio of 55:45. Consequently, monomer loaded vesicles with the final concentration of 27.5 mM TDMAO / 0.275 mM L35 / 22.5 mM LiPFOS / different monomer concentrations were freshly prepared before experiments.

Polymerization of vesicles from TDMAO/L35/Monomer/LiPFOS

Polymerized samples were prepared by dissolving 3% mol water-insoluble initiator (varying due to the total monomer concentration) in monomer/cross-linker mixtures. The cross-linker ratio was adjusted to three different values 0.1, 0.2 and 0.4 with respect to the monomer concentrations. These mixtures were added to 50 mM TDMAO / 0.5 mM L35 and homogenized by stirring for 3 days at room temperature in the dark. Then the solution was taken into a three-neck round bottom flask and was degassed with nitrogen for one hour to remove dissolved oxygen from the system ([Figure 3.12](#)). The flask was placed into in-house made thermostated water bath at 18 °C. As mentioned above, the model system had the molar ratio of TDMAO and LiPFOS as 55:45. For the preparation, the calculated amount of 50 mM LiPFOS was taken with the help of syringe and added in one stroke from the side neck into the flask while reaction

mixture was stirring vigorously with a PTFE stir bar. Spectroline Quartz Pencil shape UV lamp with wavelength of 365 nm inserted into the reaction flask from the middle neck up until it is fully submerged in the reaction mixture but does not touch the stirrer. All these steps were done in the dark. After adding the LiPFOS, the reaction mixture was let to stir for 1 minute then immediately the UV lamp was turned on. Reaction was run over the night. Polymerization was followed by NMR and run 15 hours for polymerization of styrene and 18 hours for the case of hexyl acrylate under nitrogen atmosphere with moderately stirring at 18 °C in the dark.

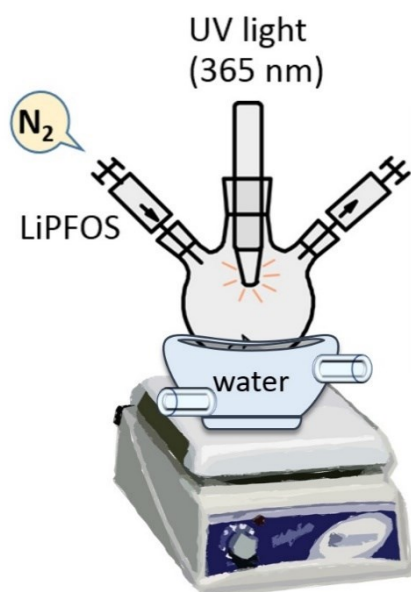


Figure 3.12. Representation of polymerization reaction.

4 TDMAO/L35/Styrene System

Introduction

Surfactants have a tendency for self-assembly in water to spherical or rod-like micelles, or flat bilayers or vesicles depending on the packing parameter described in [chapter 1.1](#)³. Especially, rod-like micelles are of great interest because of their rheological properties and viscoelastic behavior^{27,35} and their potential applications^{149,158,159}.

Therefore, such rod-like systems were studied where they were used as templates and by systematically varying the reaction conditions, the dimension of the final aggregates can be controlled^{160,161}. Due to the ease of styrene's polymerization, its solubilization into the micellar solutions has been preferred usually and studied before¹⁶². Soltero *et al.* examined the polymerization of styrene in wormlike micelles of the cationic CTAT surfactant and concluded the wormlike structures were fixated by polymerization at the same time with the formation of spheroidal polymer particles depending on the concentration¹⁶³. Another study on microemulsion polymerization of styrene stabilized by DTAB in water yielded the formation of small nanolattices instead of bigger polymeric particles¹⁶⁴.

In the present chapter, the effect of styrene monomer on the rod-like micelles consisting of nonionic tetradecyldimethylamine oxid (TDMAO) and Pluronic L35 were investigated. Here, L35 was included in order to stabilize sterically the former self-assembled structures¹¹⁴ and styrene monomer was added in order to serve as starting point for templating via polymerization. The interaction of different additives with micellar TDMAO was studied before and have seen that in the presence of medium chain alcohols such 1-hexanol, leads to the formation of cylindrical aggregates and then to bilayers¹⁶⁵ which can be considered as cosurfactants. These hydrophobic moieties can either insert into the interior of micellar aggregates or become incorporated within the palisade layer of self-assembled structures and by this way the packing parameter can be changed.

In our study, we investigated the structural effect of styrene monomer on the micellar TDMAO/L35 system, where styrene is at the same time hydrophobic and having a cosurfactant character ([Figure 4.1](#)). Our investigations concluded to an unusual finding that styrene promotes a transition from micellar to vesicular structures, i.e., here the cosurfactant character dominates and behaves in a similar fashion as has been observed for medium chain alcohols such as 1-hexanol^{51,166}. This phenomenon was supported and confirmed with light scattering, turbidity,

and small angle neutron scattering techniques. For these self-assembled structures, the effect of subsequent styrene polymerization is explained in [section 4.2](#), and resulted in the formation of rod-like aggregates with corresponding high viscosity in solution.

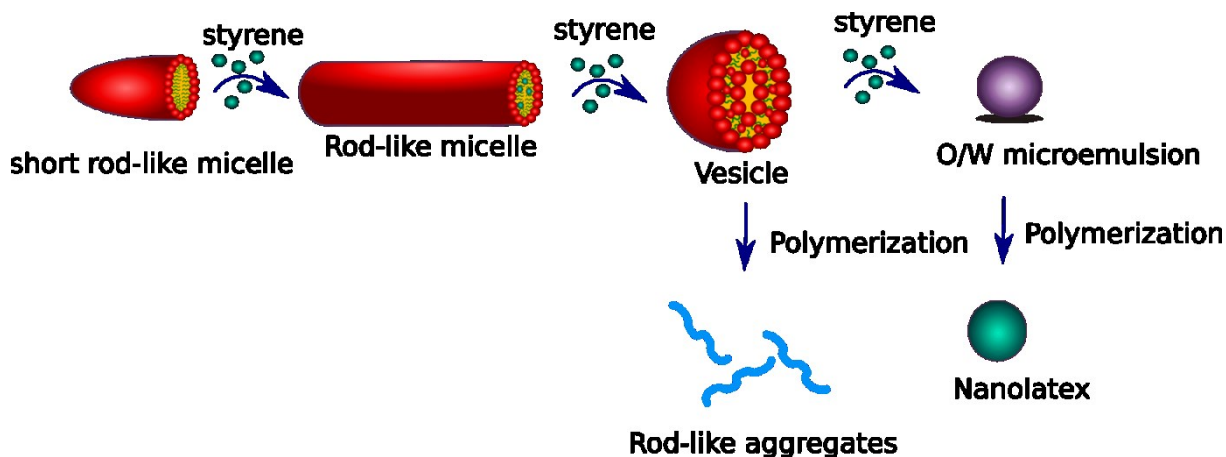


Figure 4.1. Schematic representation of TDMAO/L35/styrene system.

4.1 TDMAO/L35 /Styrene

4.1.1 Phase Behaviour

Co-surfactants have an effect on decreasing the spontaneous curvature of interfaces when they are added to the micellar aggregates. By virtue of their occupied area during the formation of the aggregates, interfacial curvature changes and ends up with different aggregate types and geometries^{167,168}. Basically, system adjusts the two principal curvatures of the micelles to the same as spontaneous curvature with keeping the bending energy as low as possible. With increasing amount of additive, then system shifts from micelles to spheres and rods or to bilayers. These transitions can be simply monitored by phase behaviour of the samples.

In the first step, we investigated the phase behaviour of the system 50 mM TDMAO / 0.5 mM L35 as a function of the concentration of monomer styrene. Styrene has a low water solubility of ~ 3 mM¹⁶⁹ and at the same time high volatility. Thus, when styrene was added into the TDMAO/L35 solution, sample closed firmly, a PTFE magnet added in the bottle and stored in the dark at room temperature. This was repeated for all samples for increasing amount of styrene and stirred continuously for 3 days until the entire monomer was dissolved into the solutions. Finally, after 3 days of stirring they had a homogeneous appearance up to 230 mM styrene concentration. After this point, a two-phase system formed. These systems were followed by

visual inspection after 1 hour, 7 days and 2 weeks after preparation in terms of homogenization and ageing.

Firstly, the 50 mM TDMAO / 0.5 mM L35 sample without styrene formed a visually transparent single-phase solution. When styrene was introduced into the system the transparent, single phase, isotropic micellar solutions (L_1) remained up to 50 mM styrene concentration as seen in [Figure 4.2](#). From 50 to 120 mM styrene content, system shifted to another phase. The samples in this range had a bluish tinge, which is typically an indication of the presence of vesicles (L_{ves})^{170,171}. This bluish appearance is because of the scattered light by the bigger aggregates¹⁷². Additionally, vesicle formation in this intermediate styrene range was confirmed by scattering methods as well.

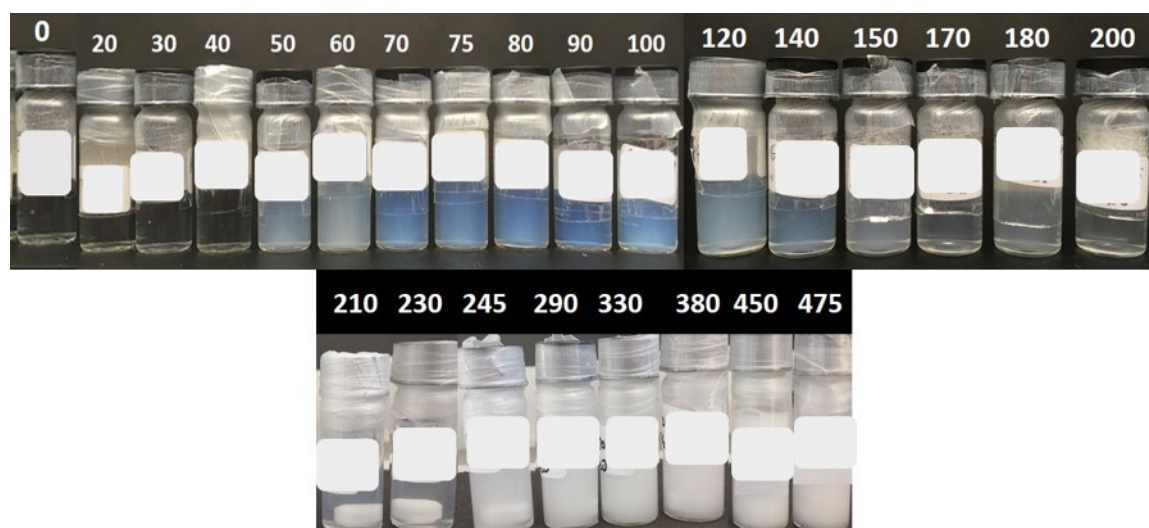


Figure 4.2. Sample photographs of 50 mM TDMAO / 0.5 mM L35 / styrene mixtures (20 mM – 475 mM content) at 25 °C.

Secondly, between 120 - 230 mM monomer content, the bluish appearance of previous range was replaced by a less turbid phase, which may be assigned as L_1 -phase, simply an O/W microemulsion. With the addition of more styrene, formed vesicles were ruptured and evaluated into microemulsion droplets. Moreover, for higher than 230 mM styrene content, the turbidity increased drastically to white, milk-like appearance. The presence of 2 phase region was started around 240 mM, the undissolved monomer separated into an upper phase within a few hours (2Φ), while shaking the samples made the whole sample white turbid again.

We measured the UV-transmissions of the samples 1 hour and 1 week after preparation and the turbidity values were calculated from these experiments. [Figure 4.3](#) shows turbidity as a function of styrene concentration. The first part (L_1), seen in the figure corresponds to the

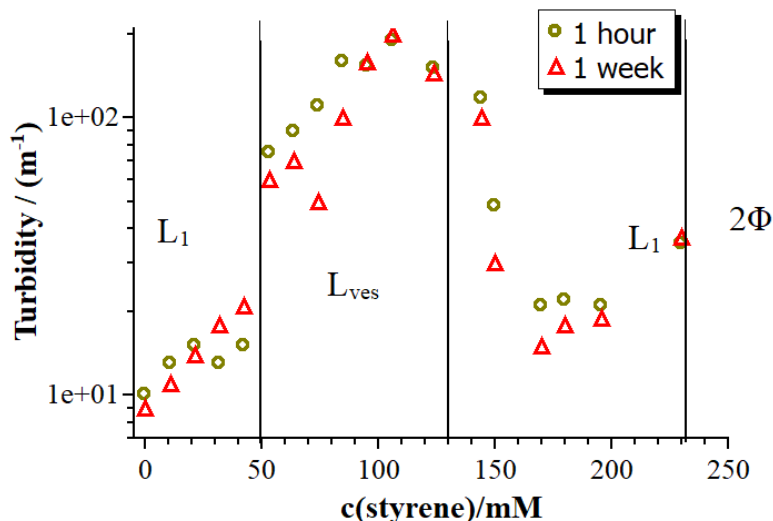


Figure 4.3. Turbidity ($\lambda=632$ nm) as a function of styrene concentration in 50 mM TDMAO / 0.5 mM L35/ styrene mixtures at 25°C. (green circles): after 1 hour of mixing; (orange triangle): after 1 week of mixing.

transparent micellar regime as describe above. The turbidity of the micellar solutions increases very slightly with introducing styrene into the system, however, for the 50 to 120 mM styrene content a sharp increase in the turbidity values is observed. Styrene, here, has an effect on shifting the packing parameter and induces the transition from micelles to vesicular aggregates.

Later on, with the addition of more monomer to the system, turbidity decreases again to the similar values observed in the first L_1 phase, confirming the return to the O/W microemulsion phase. Measurements were repeated after 1 week from preparation, and we obtained similar results meaning samples remained stable, almost unchanged.

4.1.2 Light Scattering

Dynamic and static light scattering analyses reveal more detailed information about the nascent structures and the structural transitions. Varying the amount of styrene, we determined the hydrodynamic radius R_h , polydispersity index PDI, and molecular weight M_w of the aggregates.

The autocorrelation functions of the samples seen in [Figure 4.4](#) indicate an apparent shift to the longer relaxation times. The relaxation processes of the curves are mainly monomodal however, the decay time below 50 mM styrene increases significantly, thereby indicating a growth of the micelles. Above 50 mM, the characteristic time increases, and the curves become more stretched. This implies slower particle diffusion i.e., the presence of bigger particles in the system with broader size distribution confirms the formation of vesicles with high polydispersity.

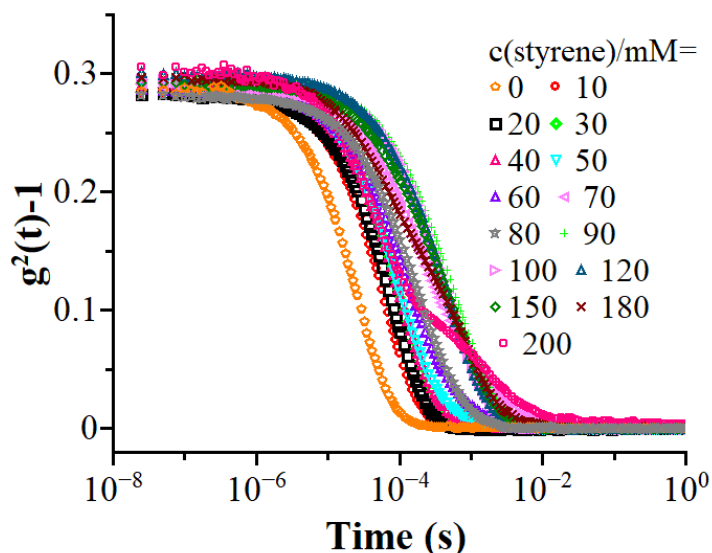


Figure 4.4. Intensity autocorrelation function $g^2(t)$ measured at $\theta = 90^\circ$ of 50 mM TDMAO / 0.5 mM L35 / styrene mixtures at 25°C .

Upon further increase of the styrene concentration, one shifts back to a monomodal fast decay for 90 to 150 mM. However, between 150 and 200 mM monomer amount, curves become stretched, but now having shorter characteristic times. At 200 mM concentration the characteristic behavior of scattering curve changes completely and having bimodal behavior at this point. The second mode appears at the concentration close to where the phase behavior starts to shift from microemulsion (L_1) to 2-phase region (2Φ).

Dynamic light scattering of the samples was measured at seven different angles $30, 45, 60, 75, 90, 105$ and 120° . The cumulant method was used to analyze the scattering curves for obtaining the average aggregate size and polydispersity index of their distribution. For the sample without styrene, a hydrodynamic radius, R_h of 3.1 nm was observed and with introducing monomer into the system this value increased to 6-7 nm. Clearly, this is because of the swelling of micelles by loading with monomers which ends up in a more elongated cylindrical structure. For more than 50 mM styrene, hydrodynamic radii for vesicle reach a value of 70 nm together high polydispersity. The loaded micelles show polydispersity indices of 0.1-0.2, while for the vesicles values of ~ 0.2 are observed. [Figure 4.5 \(left\)](#) shows the evolution of hydrodynamic radii of the aggregates of TDMAO/L35 solutions with different amounts of dissolved styrene for repeated measurements of 1 week and 2 weeks after preparation. Below 50 mM styrene concentration, small aggregates with hydrodynamic radius of 6-8 nm were formed. However, for 50 to 120 mM styrene concentration R_h increased drastically. Evidently, this increase of the size confirms the transition from smaller structures to relatively big ones, in this case from

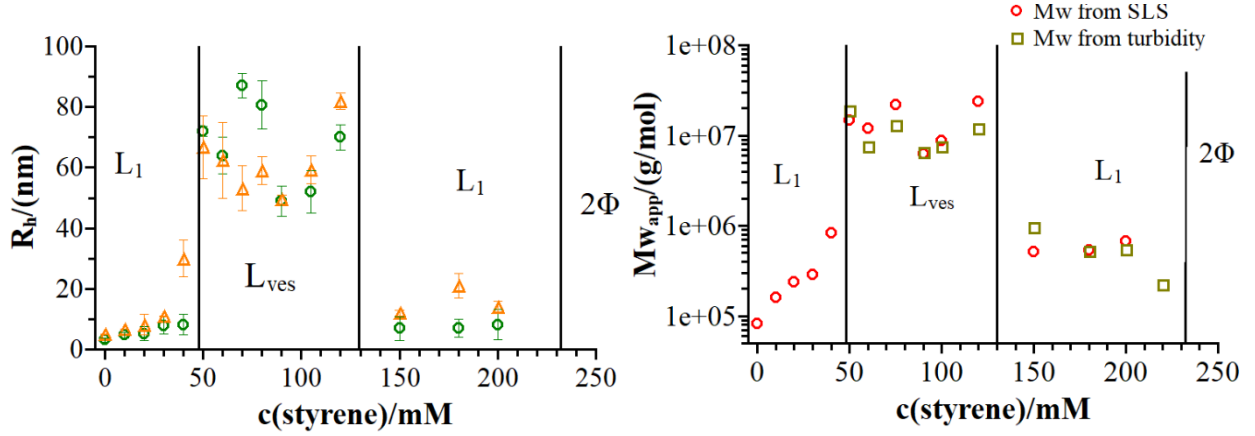


Figure 4.5. **(left):** Hydrodynamic radii, R_h , of aggregates in 50 mM TDMAO / 0.5 mM L35 / styrene solutions at 25°C. (R_h from cumulant method: orange circle: 1-week, purple triangle: 2 weeks after preparation). **(right):** Molecular weight, M_w , of aggregates in 50 mM TDMAO / 0.5 mM L35 / styrene solutions at 25°C.

micelles to vesicles. For more than 120 mM styrene, hydrodynamic radii become smaller again to 5-6 nm confirming the disruption of vesicular aggregates to the small droplets.

As an alternative way to determine the effective diffusion coefficients, we obtained them from the initial slopes of the scattering curves. Therefore, we replotted (Figure 4.6) the autocorrelation functions $\ln((g^2/t)-1)$ vs time and from the initial slopes ($t = 0-0.06$ ms), we obtained the effective diffusion coefficient via:

$$g^2(t) - 1 = A \exp(-2Dq^2t) \quad (4.1)$$

$$\ln(g^2(t) - 1) = \ln A - 2Dq^2t \quad (4.2)$$

Plots showing the correlation functions of the samples above 50 mM styrene do not decay linearly which is the sign of high polydispersity. Collaboratively, the polydispersity values from cumulant method seen in Table 4.2 are in good agreement with being ~ 0.2 .

For comparison of the results from the DLS and SANS analyses, we calculate the theoretical diffusion coefficients using the size parameters obtained from SANS with the equation:

$$D = kT(\ln(p) + \gamma)/3\pi\eta L \quad (4.3)$$

where η is the solvent viscosity, and $\gamma = 0.312 + \frac{0.565}{p} + \frac{0.1}{p^2}$, $p = L/2R$, L being the length of the cylinder and R is the radius¹⁷³.

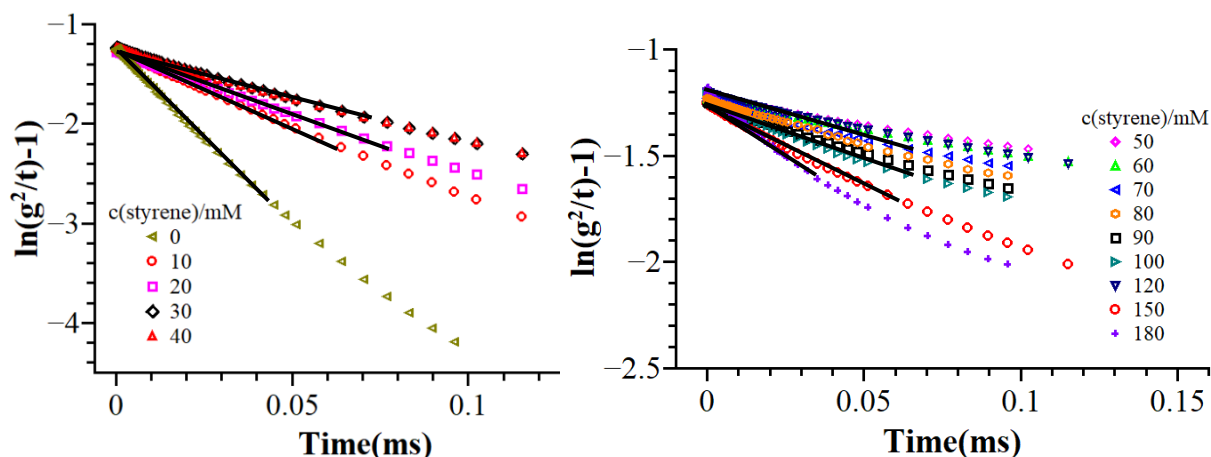


Figure 4.6. Autocorrelation functions $g^2(t)$ measured at $\theta = 90^\circ$ of 50 mM TDMAO / 0.5 mM L35 / styrene mixtures at 25°C (solid lines: linear fit).

Diffusion coefficients from initial slopes, cumulant method, and theoretically calculated D_0 from the obtained SANS parameters are listed in [Table 4.1](#). As seen in the table, values are decreasing along with the increase of styrene concentration. The slower diffusion of the particles indicates the formation of bigger particles. For the first L_1 phase, diffusion coefficient values are in the range of $\sim 10^{-11} \text{ m}^2\text{s}^{-1}$, however for the vesicle phase, L_{ves} , corresponding 50 mM -120 mM styrene concentration diffusion coefficient values decreases to the order of $\sim 10^{-12} \text{ m}^2\text{s}^{-1}$, which is much smaller than expected for micelles¹⁷⁴. Furthermore, for the samples with more than 120 mM styrene, diffusion coefficient values started to increase and reached to

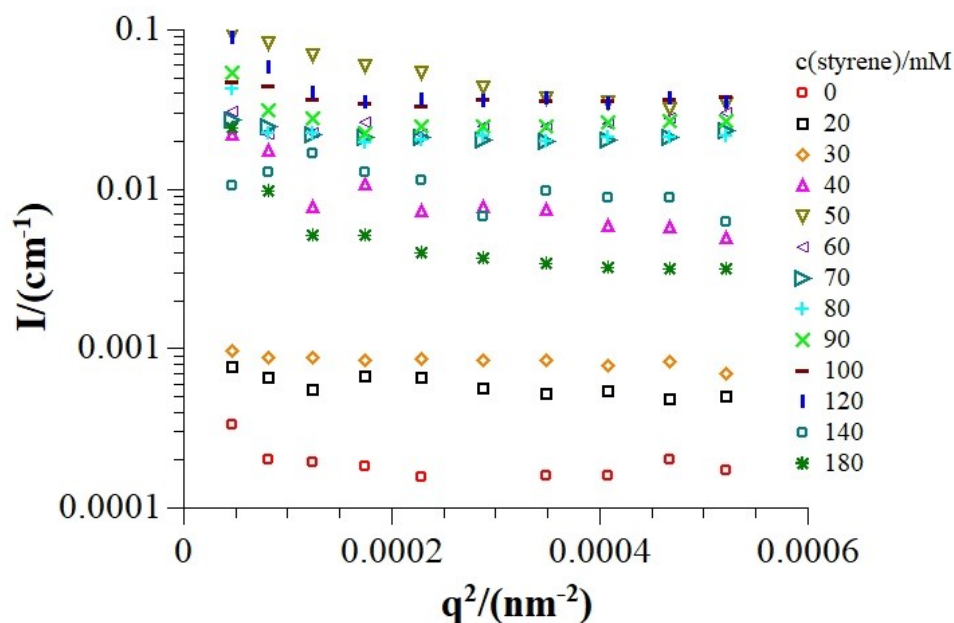


Figure 4.7. Intensity vs q^2 for 50mM TDMAO/0.5mM L35/styrene mixtures at 25°C , Guinier plots of the SLS data.

the order of $\sim 10^{-11} \text{ m}^2\text{s}^{-1}$ again which is in the same range as for the L_1 phase, indicating the presence of smaller aggregates.

Table 4.1. Diffusion coefficient values deduced from: D_{eff} : linear fits from initial slopes of figure 4.6, D_{eff} : from cumulant analyses, and D : theoretically calculated values by using the size parameters observed from SANS analyses.

Styrene amount (mM)	D_{eff} (m^2/s) from initial slope	D_{eff} (m^2/s) from cumulant	D (m^2/s) from SANS
0	4.05×10^{-11}	5.6×10^{-11}	6.8×10^{-11}
10	5.59×10^{-11}	5.6×10^{-11}	3.5×10^{-11}
20	1.92×10^{-11}	3.0×10^{-11}	2.6×10^{-11}
30	1.53×10^{-11}	2.6×10^{-11}	2.3×10^{-11}
40	1.47×10^{-11}	1.9×10^{-11}	1.8×10^{-11}
50	4.02×10^{-12}	5.1×10^{-12}	-
60	7.44×10^{-12}	7.5×10^{-12}	-
70	4.9×10^{-12}	3.9×10^{-12}	-
80	6.1×10^{-12}	5.1×10^{-12}	-
90	1.29×10^{-11}	9.0×10^{-12}	-
100	8.87×10^{-12}	7.9×10^{-12}	-
120	5.21×10^{-12}	5.9×10^{-12}	-
150	4.82×10^{-11}	5.2×10^{-11}	-
180	3.62×10^{-11}	4.9×10^{-11}	-
200	3.36×10^{-11}	3.7×10^{-11}	-

From the static light scattering (SL) measurements, the absolute intensities $I(q)$, were obtained and plotted against q^2 (Figure 4.7). Scattering curves were fitted with the Guinier approximation: $I(q) = I_0 \exp\left(-\frac{(R_g q)^2}{3}\right)$ to extrapolate the forward scattering $I(q=0)$.

Deduced absolute intensities were used for the calculation of apparent molecular weights via equation 3.8 and listed in Table 4.2. Similarly, the molecular weights, M_w of the turbid samples was calculated from equation 3.40 relating it to the turbidity measurements, and they are compared to SLS results in Figure 4.5 (right). Due to the increase in size, molecular weight increases until the end of vesicular regime up to 120 mM styrene content. For higher styrene concentrations, the molecular weights decreased according to the formation of droplets of smaller sizes. Results are summarized in Table 4.2.

To compare the outcome from the scattering analyses, we calculate the theoretical radii of vesicles considering the membrane thicknesses gained from SANS analyses therefore estimating the vesicular volume for the aggregate densities (see Appendix 9.1.3). We observe

that the results are rather close to the radii obtained from light scattering, confirming the accuracy of the analyses. Similarly, theoretical lengths of the micelles were determined and are presented in [Table 4.2](#).

Table 4.2. Results from the SLS and DLS measurements of 50 mM TDMAO / 0.5 mM L35 and added styrene mixtures at 25°C. Given are the hydrodynamic radius R_h from the cumulant method, $R_{ves,th}$ theoretically calculated vesicle radius from M_w , l_{th} theoretically calculated cylinder length from M_w , polydispersity index PDI, the apparent molecular weight $M_{w,app}$, and aggregation number N_{agg} (of TDMAO molecules).

Styrene amount (mM)	R_h (nm)	$R_{ves,th}$ (nm)	l_{th} (nm)	PDI	$M_{w,app}$ (g/mol)	N_{agg} from SLS
0	3.11	-	7.23	0.1	7.17×10^4	262
10	4.77	-	23.3	0.12	1.9×10^5	879
20	5.25	-	30.2	0.15	2.0×10^5	886
30	7.9	-	45.8	0.16	2.9×10^5	1370
40	8.2	-	56.5	0.25	8.4×10^5	4230
50	72.0	89.6	-	0.38	1.1×10^7	58100
60	64.2	68.2	-	0.43	8.2×10^6	45200
70	87.3	89.1	-	0.40	1.6×10^7	92800
80	80.7	77.5	-	0.41	1.4×10^7	88100
90	49.2	45.3	-	0.28	6.3×10^6	37100
100	52.3	50.5	-	0.19	8.8×10^6	51800
120	70.1	-	-	0.27	2.4×10^7	99700
150	6.9	-	-	0.21	5.5×10^5	3570
180	7.1	-	-	0.18	5.9×10^5	3960
200	8.2	-	-	0.17	6.5×10^5	4430

4.1.3 Small Angle Neutron Scattering (SANS)

For a more detailed characterization of nanostructures and complementary to the investigation by light scattering, we analysed these aggregates by small angle neutron scattering. SANS measurements were performed on the instrument KWS1 Jülich Center for Neutron Science (JCNS) at MLZ, Munich, Germany, at a wavelength of 0.6 nm, with a FWHM (full width at half maximum) of 9 %, and three sample-detector distances of 1.2, 7.7, and 19.7 m with corresponding beam collimation lengths of 8.0, 8.0, and 20.0 m respectively. Transmissions were measured at 8 m distance with the attenuated direct beam. These experiments were done in D₂O as solvent for having a better contrast. Samples with various amounts of styrene monomer mixed with 50 mM TDMAO / 0.5 mM L35 were measured at 25 °C.

[Figure 4.8](#) shows the general view for the neutron scattering curves of samples with increasing amount of styrene. At first glance, one observes initially the scattering of small micelles that grow in size with higher scattering intensity along with the increasing styrene content. These samples in the range of L₁ phase up to 50 mM show rod-like shape of TDMAO/L35 micelles and for pure TDMAO, the presence of short rod-like micelles was shown by SANS before ¹⁷⁵.

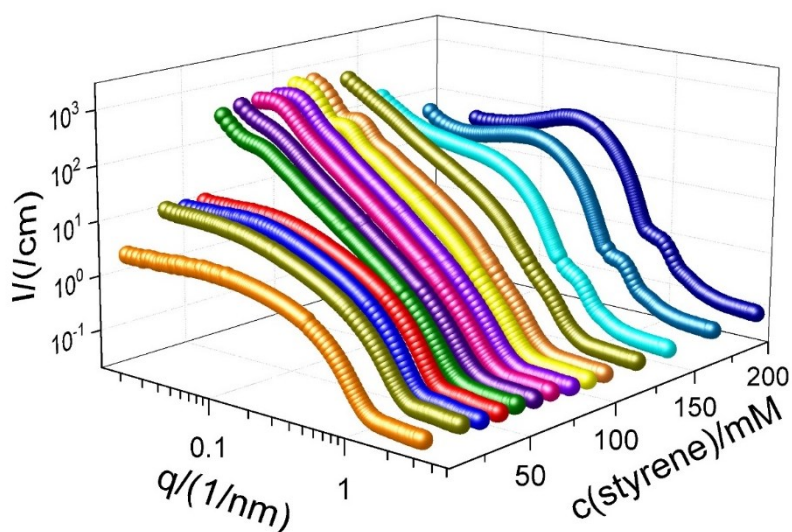


Figure 4.8. SANS intensity patterns of 50 mM TDMAO / 0.5 mM L35 and increasing amount of styrene mixtures at 25°C. (styrene contents (mM): red:0, dark blue:20, magenta:30, green:40, navy:50, violet:60, purple:70, wine:80, dark yellow:90, blue:100, light blue:120, gold:140, light green:170, light magenta: 200).

With increasing styrene content, we noticed that the q^{-1} behavior extends to lower q thereby indicating an elongation of these structures, being in good agreement with the light scattering results (see [Table 4.2](#)). At 50 mM styrene amount, a rather abrupt change of the scattering pattern

takes place, the intensity becomes much larger and a q^{-2} scaling is observed in the middle q region between 0.1 to 0.7 nm^{-1} , which is the signature of formation of bilayers. This characteristic behavior remains similar between 50 to 140 mM styrene content evidencing the formation of vesicles which clearly has been induced by the styrene likewise cosurfactants¹⁶⁶. Similar behavior has been seen before for the addition of medium chain alcohols as cosurfactants to TDMAO¹⁷⁶.

Table 4.3. Results from the SANS analysis of 50 mM TDMAO / 0.5 mM L35 and different styrene content at 25 °C: Φ : Volume fraction, R_1 : Radius of cylindrical micelles, l : Length of the cylinders, R_{ves} : Mean vesicle radius, D : Bilayer thickness, PDI: Polydispersity index of radius (R_1 , R_2 , R_{ves}) distribution; R_2 : Radius of spheres; N_{agg} : aggregation number (App. 9.2), M_w : Molecular weight of aggregates. For styrene amounts of 0-40 mM, parameters arise from the cylindrical model, for 50-100 mM from spherical shell model; for 140-200 mM content from the sphere model.

Styrene amount (mM)	Φ Volume Fraction	R_1 (nm)	l (nm)	R_{ves} (nm)	D (nm)	PDI	R_2 (nm)	M_w (g/mol)	N_{agg}
0	0.0124	1.93	5.79	-	-	0.12	-	3.72×10^4	136
20	0.0144	1.90	28.7	-	-	0.14	-	1.79×10^5	798
30	0.0157	2.05	38.6	-	-	0.15	-	2.80×10^5	1330
40	0.0161	2.21	44.6	-	-	0.14	-	3.78×10^5	1901
50	0.0171	-	-	70.0	2.82	0.19	-	9.52×10^6	50300
60	0.0181	-	-	80.2	2.88	0.22	-	9.72×10^6	53500
70	0.0191	-	-	80.5	2.97	0.28	-	1.08×10^7	63470
80	0.0199	-	-	72.4	3.00	0.30	-	1.00×10^7	57200
90	0.0209	-	-	49.6	3.20	0.21	-	5.42×10^6	32800
100	0.0217	-	-	55.1	3.36	0.17	-	6.99×10^6	43400
120	0.0238	-	-	-	3.21	0.28	-	-	-
140	0.0258	-	-	-	-	0.18	5.48	3.77×10^5	2530
150	0.0265	-	-	-	-	0.16	5.75	4.36×10^5	2970
180	0.0293	-	-	-	-	0.15	6.00	4.95×10^5	3510
200	0.0314	-	-	-	-	0.15	6.27	5.65×10^5	4092

As seen in the [Figure 4.8](#), the drastic increase of intensity at low q implies the formation of larger objects in the system. Additionally, for the samples between 70 and 100 mM styrene we observed oscillations denoting more well-defined structures, i.e. vesicles with well-defined radii of 50-60 nm. Above 120 mM styrene content, the scattering pattern changes qualitatively, with lowering the intensity at low q regime. These curves point out the presence of spherical droplets with radii of ~ 6 nm eventuated from the form factor minimum around $q = 0.75 \text{ nm}^{-1}$.

SANS curves were analyzed by applying different geometrical models described [in section 3.1.6.2](#) to the curves as can be seen in [Figure 4.9](#). In more details, we applied a cylindrical model to TDMAO/L35 sample without monomer, and results indicate the presence of small rod-like aggregates with a length of 5.8 nm and a radius of 1.9 nm as initial structure. We should consider that these values are shorter than previously observed for pure TDMAO¹⁷⁵. This can be explained in the way that two PEO chains of Pluronic L35 and its bulky head group stabilizes more curved structures, i. e., shorter rods. Therefore, the system ends up such shorter rod-like particles.

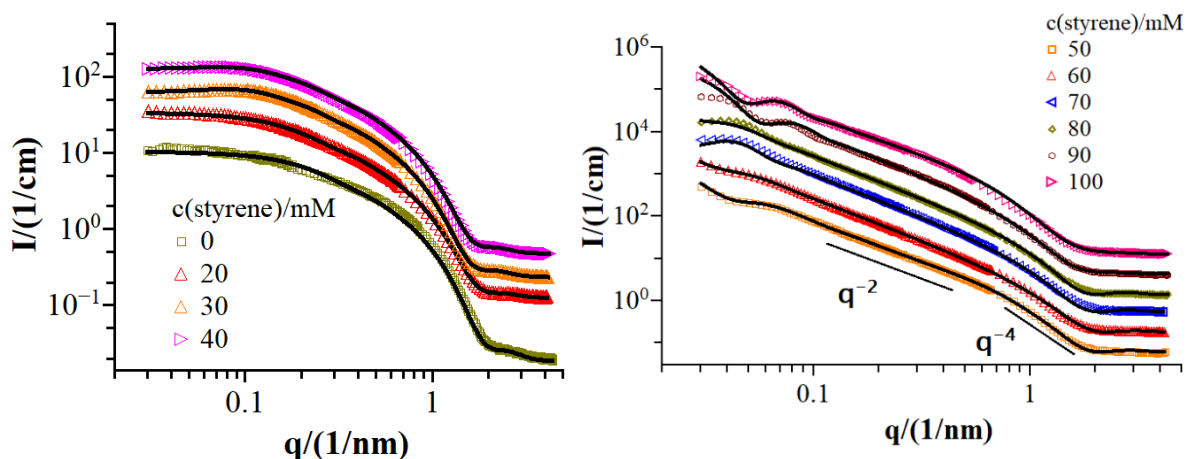


Figure 4.9. SANS curves of 50 mM TDMAO / 0.5 mM L35 / styrene mixtures at 25°C. (solid black line: fitted data). For clarity subsequent data sets were multiplied each with a scale factor of 3.

As it can be predicted from looking at the curves in [Figure 4.9](#), when styrene is introduced into the system, structures start to be elongated. For the sample with 20 mM styrene, an increase of the length to 28 nm and a radius of 2.02 nm is obtained from modelling the curve with cylindrical geometry. Same model was applied for 30 and 40 mM styrene amounts, and the length of the aggregates already reaches to an average value of 40 nm with a radius of 2.2 nm in combination with the structure factor of hard spheres, as our system composed from uncharged particles which may interact via steric repulsion, was fitted to the experimental data (see [section 3.1.6.2.6](#)).

In the system the cylindrical particles occupy larger hard sphere volume. The hard sphere radius, R_{HS} , was fixed to the sum of the radius of one particle and two hydrophilic chain lengths (-EO₁₁-) of L35 attached on the aggregate which basically stabilize the particle according to de Gennes approximation, the area occupied by single PEO chain was calculated before with assuming the PEO chains of L35 form mushroom-like conformations when they attach on the surface of the aggregate^{115,177}. Considering the steric hindrance of PEO chains from two particles approaching to each other, the length of the two PEO chains were added to the hard sphere radius. Therefore,

R_{HS} becomes a sum of the radius and two chain lengths. The interactions were determined by fitting with this model and the variables are summarized in [Table 4.4](#).

Table 4.4. Parameters for structure factor fit of hard sphere interaction.

Styrene amount (mM)	$R_{HS}/(\text{nm})$	f_p
30	10	0.054
40	10	0.061
180	11	0.175
200	11	0.185

In [Figure 4.9](#), samples with styrene beyond 50 mM concentration reveal the q^{-2} behavior at middle q regime, indicating clearly the formation of bilayers¹⁷⁸. Except the deviation at low q , a shell model agrees with a high polydispersity of ~ 0.2 for the radius and a thickness around 3-3.3 nm. Systematical analysis of these curves shows that the size of the particles increases until 90 mM styrene concentration along with high polydispersity, however above 90 mM the oscillations at low q become more visible, and the polydispersity drops to a value of ~ 0.1 .

The samples in this range of styrene concentration (50-120 mM) are the most interesting part of this chapter. The evolution from micelles to vesicular structures initiated only by styrene monomer is confirmed by SANS measurements. The size parameters, radii, bilayer thickness,

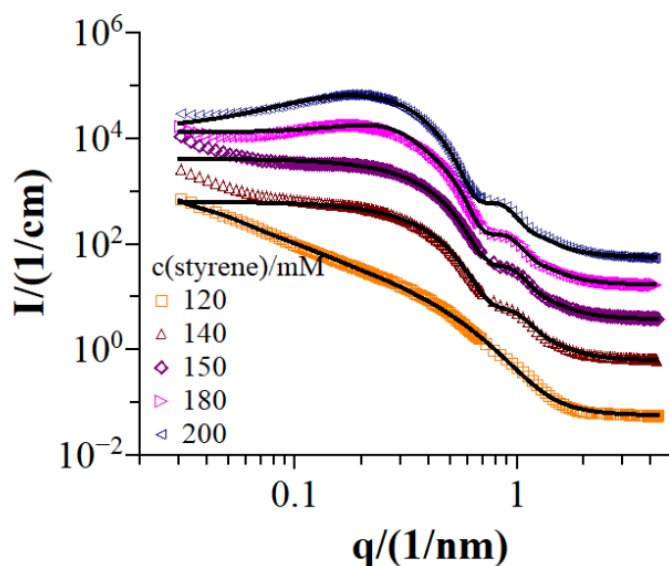


Figure 4.10. SANS curves of 50 mM TDMAO / 0.5 mM L35 / styrene mixtures at 25°C. (solid black line: fitted data). For clarity subsequent data sets were multiplied each with a scale factor of 3.

polydispersity index, aggregation numbers and molecular weights obtained from the spherical shell model are summarized in [Table 4.3](#).

The Kratky-Porod plot is an alternative representation of the SANS curves from that one can obtain the one-dimensional radius of gyration R_g , which is related to the bilayer thickness D using $R_g^2 = \frac{D^2}{12}$,^{134,136}. Therefore, $\text{Ln}[I(q)q^2]$ vs q^2 plots were fitted with: $I(q)q^2 = I(0)\exp\left(-\frac{q^2 R_g^2}{1}\right)$ for samples with styrene concentration between 50-100 mM ([Figure A1](#) and [A2](#)). The values from both approaches are in good agreement and results are given in [Table 4.5](#) (for the Kratky-Porod plots see [Appendix 9.1.4](#)).

For the sample containing 120 mM styrene, the SANS curve shows a more complicated pattern which is mainly indicating that spherical aggregates start to show up together with the previously formed bilayers. The spherical shell model does not fully agree with this curve, nevertheless as much as it could be fitted on the curve we were able to obtain the value for the polydispersity of radius (R_{ves}) which jumps to ~ 0.3 . However, defining a radius was not possible from these curves since the sample contains a mixture of different aggregate types.

Table 4.5. Calculated Thickness for the bilayer from of spherical-shell model and Kratky-Porod approximation.

Styrene amount (mM)	D/(nm) Spherical shell	D/(nm) Kratky-Porod
50	2.82	2.72
60	2.88	2.87
70	2.97	2.94
80	3.00	3.01
90	3.20	3.32
100	3.36	3.45

Upon the addition of still more styrene, the spherical droplets become more pronounced and a disappearance of the bilayers is evident as seen from the vanishing q^{-2} slope at middle q . This is also visible from the [Figure 4.10](#), droplet radius changes slightly from 5.5 to 6.3 nm. At the same time a correlation peak becomes dominant. Therefore, here a hard sphere structure factor was applied to describe the curves of the samples with 180 and 200 mM styrene with keeping the R_{HS} of 11.5 nm which is relevance for the measured data due to the calculation of volume fractions ([Table 4.4](#)).

Consequently, SANS provides a full picture of the aggregates formed in the presence of styrene with TDMAO and L35 surfactants. It can be understood and confirmed from these experiments that styrene induces the formation of bilayers like cosurfactants and by increasing its amount, structural transition occurs starting from cylindrical micelles to spherical droplets.

4.2 Polymerization of the TDMAO/L35/Styrene System

In this part, we investigate whether the styrene containing samples can be fixated by a photo-initiated radical polymerization and how the polymerization does affect the vesicle system with respect to phase behavior, small angle neutron scattering and in particular rheological properties. The completeness of the polymerization reaction was verified by NMR and the obtained polymerized samples characterized with respect to their properties and structure.

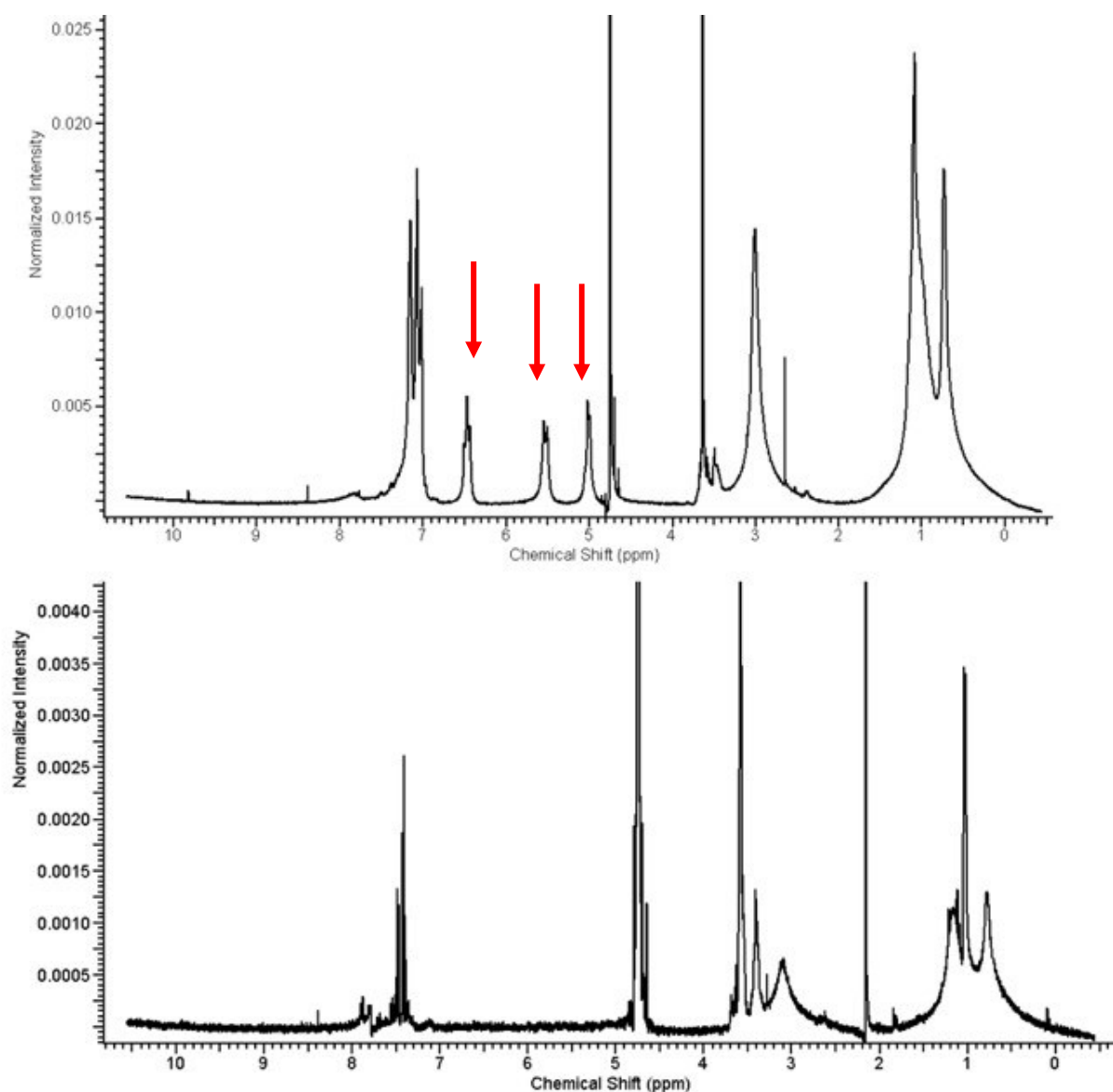


Figure 4.11. $^1\text{H-NMR}$ spectra of unpolymerized (top) and polymerized (bottom) 50 mM TDMAO / 0.5 mM L35 / 80 mM styrene at 25 °C.

4.2.1 Nuclear Magnetic Resonance (NMR)

Polymerization was followed by using ^1H NMR for confirming the full conversion of monomer. As solvent we used D_2O to obtain the chemical shifts and Tetramethylsilane (TMS) as reference agent. Spectra were recorded on Bruker Avance II 400 spectrometer operating at 400 MHz. Vanishing of the proton signals of double bond at styrene molecule means that the monomer is fully converted to polystyrene. In the [Figure 4.11](#) at the top given the NMR spectrum of the sample before the polymerization, however at the bottom one sees the polymerized sample. The main difference in both is the disappearance of signals at δ 5.02-5.5-6.5 corresponds to CH- of vinyl group. As expected, after polymerization the signals of the vinyl bond are disappearing and the CH_3 signals on the spectrum mainly becoming more pronounced due to the polymerization.

4.2.2 Phase Behaviour

As described above, the most interesting part of TDMAO/L35/styrene system is the vesicle regime, which corresponds to the styrene concentration of 50-100 mM. Therefore, we studied fixating these samples by UV- initiated polymerization. The polymerized system showed a different phase behavior than the systems they



Figure 4.12. Photographs of polymerized samples of 50 mM TDMAO / 0.5 mM L35 / styrene mixtures (50 mM – 80 mM content) at 25 °C.

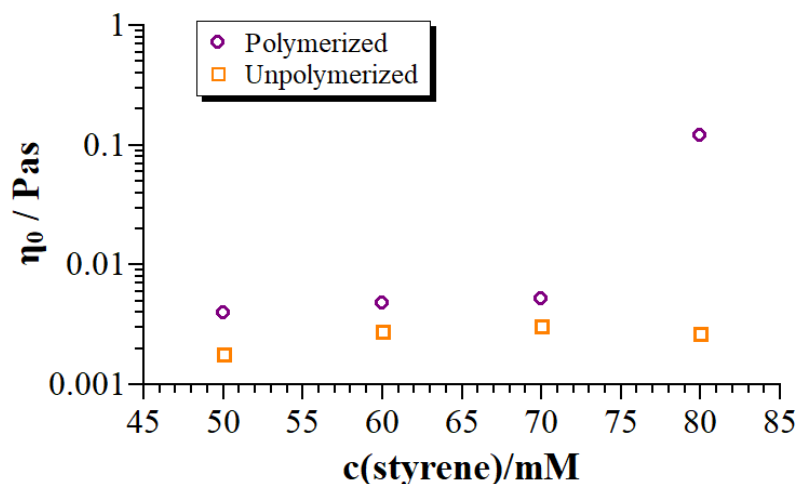


Figure 4.13. Zero-shear viscosity η_0 of 50 mM TDMAO / 0.5 mM L35 / styrene mixtures at 25°C, measured with a capillary viscometer, except for the polymerized 80 mM styrene sample, which was measured with the Gemini 200 HR rheometer.

derived from. For instance, while the vesicle samples were bluish, slightly turbid, and water viscous (see [Figure 4.2](#)), polymerization led to more transparent and differently viscous solutions ([Figure 4.12](#)).

We measured the viscosity of samples before and after polymerization and concluded with the result that in general viscosity increased slightly when compared to the unpolymerized case. However, for the case of the 80 mM styrene sample, the viscosity increased by a factor of 100, [Figure 4.13](#) summarizes the viscosity values for both cases. The high viscosity of this sample can be seen in [Figure 4.15](#), after shaking it, air can be trapped in the sample.

4.2.3 Small Angle Neutron Scattering (SANS)

Because of the fact that the behavior of system changes entirely after polymerization, we investigated the polymerized samples with respect to their detailed structure by means of SANS. These measurements were all done at KWS1 instrument, Munich, with the same experimental set up described in [section 4.1.3](#). In [Figure 4.14](#), we plotted the SANS curves, exhibiting largely different scattering profiles than seen for the unpolymerized samples ([Figure 4.9](#)). The q^{-2} slope at intermediate q range disappears, which means that bilayers are no longer present. The change in the scattering patterns indicates that after polymerization, vesicles are essentially replaced by small ellipsoidal aggregates. Until 80 mM styrene concentration, the length of the aggregates is 11 nm and the radius 2.04 nm. Additionally, a correlation peak at $\sim 0.2 \text{ nm}^{-1}$ becomes more pronounced along with increasing monomer amount. This peak is the sign for a higher ordering of the structures in combination with a repulsive interaction of elongated particles.

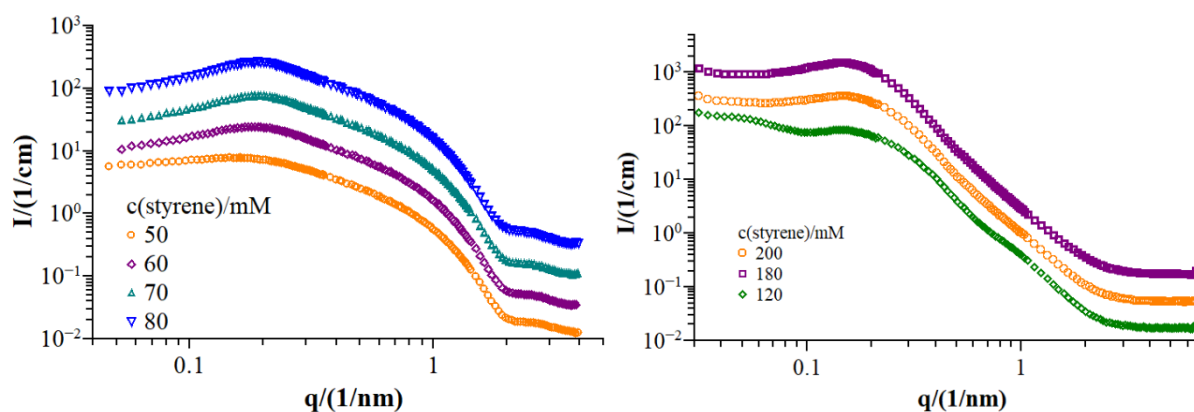


Figure 4.14. SANS intensity patterns of polymerized 50 mM TDMAO / 0.5 mM L35 / styrene mixtures at 25°C.

This structural transition can be explained by the packing parameter concept. Styrene with its double bond is a relatively polar molecule, but after the polymerization the double bond is gone, and the formed polystyrene is mainly hydrophobic. Accordingly, it behaves like an oil and becomes solubilized within the micellar core and this morphological change was characterized by SANS.

For higher styrene concentrations of 120 to 200 mM, which are in the microemulsion phase (for unpolymerized samples [Figure 4.10](#), for polymerized samples [Figure 4.14](#)), polymerization lead to spherical particles with radii of ~ 7 nm having the similar inter-particle interactions. Apparently, the initially formed microemulsion droplets are retained in structure, i. e. one has a case of precise templating.

4.2.4 Rheology

We have described so far that polymerization noticeably disrupts the formed vesicles which are induced with the presence of styrene. As explained in [section 4.2.2](#) phase behavior of the polymerized samples was quite different from unpolymerized ones, losing the characteristic bluish tinge of vesicles and being more viscous. The most interesting sample of the polymerized series is certainly the one with 80 mM styrene, which led to a much more viscous phase ([Figure 4.15](#)) and can be seen on the



Figure 4.15. Photograph of polymerized sample of 50 mM TDMAO / 0.5 mM L35 / 80 mM styrene at 25 °C.

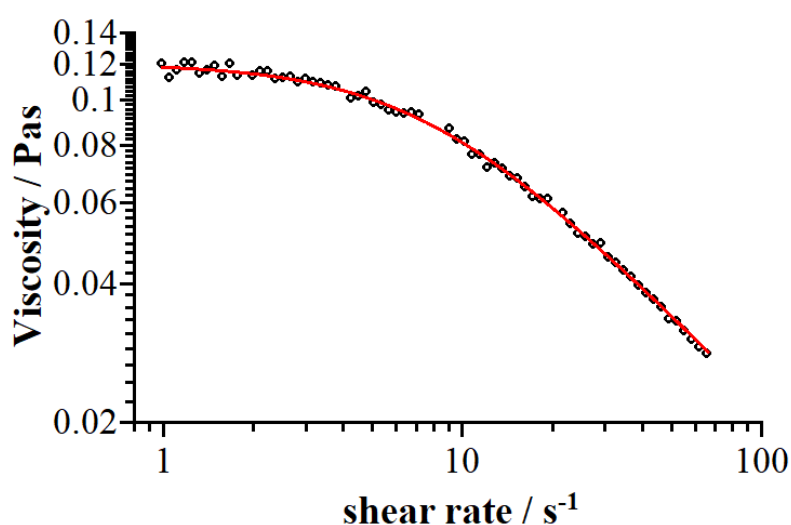


Figure 4.16. Measured shear viscosity of polymerized sample containing 50 mM TDMAO / 0.5 mM L35 / 80 mM styrene as a function of applied shear rate (black circles), solid red line is the model fit of the Carreau-Yasuda model ([equation 3.37](#)).

photo that after shaking the sample, air is trapped. It draws interest in terms of the rheological behavior of the polymerized sample of 80 mM styrene / 50 mM TDMAO / 0.5 mM L35 and this sample was examined in more detail by means of oscillating and shear experiments.

As known, a non-linear relation between shear rate and shear stress implies the behavior of non-Newtonian flows ¹⁷⁹ which is observed for our case as well. The constant shear experiments showed a constant viscosity at low shear rates which was followed by a shear thinning behavior for shear rates above 2 s^{-1} .

[Figure 4.16](#) shows the viscosity as a function of shear rate. The curve was modeled with the Carreau-Yasuda model ([Equation 3.37](#)), to obtain the zero shear viscosity η_0 of 0.12 Pas, and the relaxation time τ of 0.128 s ¹⁵³. By using these observations, we can calculate the shear modulus G_0 being as 0.93 Pa.

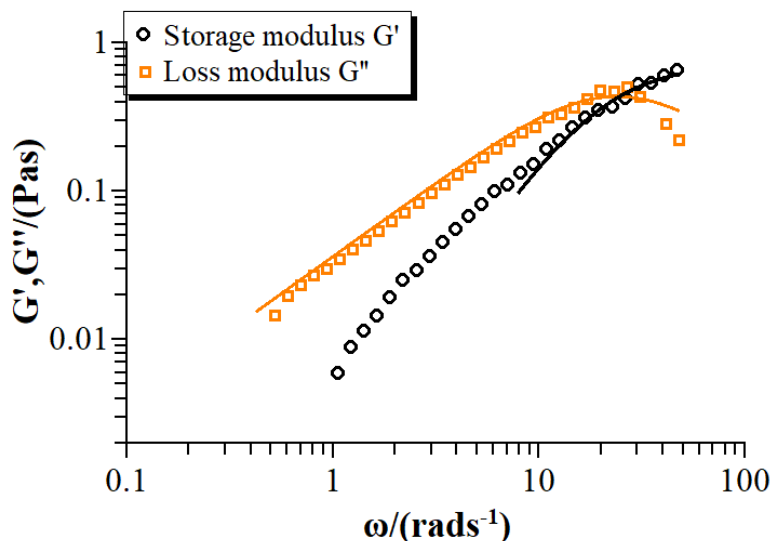


Figure 4.17. Storage G' (black circle) and loss G'' (red square) modulus as a function of angular frequency ω for polymerized sample of 50 mM TDMAO / 0.5 mM L35 / 80 mM styrene, solid lines represents fits from Maxwellian model.

On the other hand, the viscoelastic properties of the sample can be provided by oscillatory measurements in terms of determining storage (elastic) modulus G' and loss (viscous) modulus G'' . These two moduli are plotted as a function of oscillating frequency in [Figure 4.17](#), and from the crossover, where both moduli are equal ($G'=G''$) the relaxation time can be determined via $\tau = \omega^{-1}$. The Maxwell model summarized by [equation 3.36](#) ¹⁵² describes these two parameters and fitted on the curves which shown as solid lines in [Figure 4.17](#).

The Cole-Cole plot is the presentation of G' against G'' providing more information about viscoelastic behavior of the systems¹⁵⁰. For a defined Maxwellian behavior this plot fits on a semicircle and described by the equation: $G''(\omega) = [G'(\omega)G_0 - G'(\omega)^2]^m$ (see [equation 3.36](#))

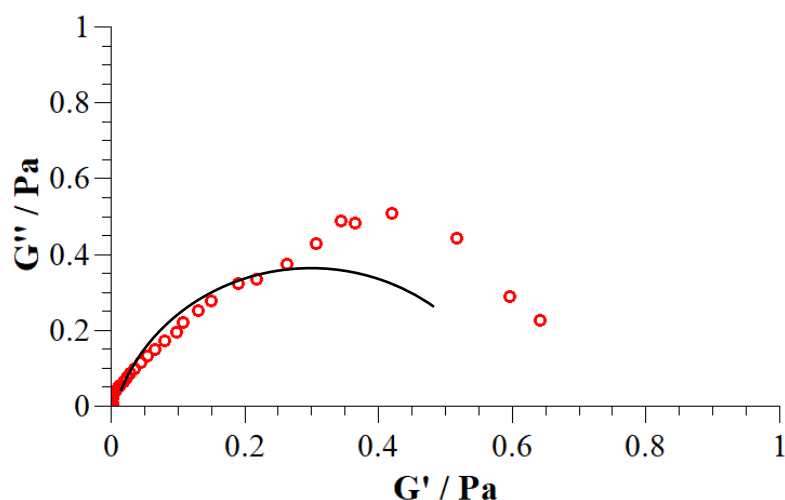


Figure 4.18. Cole-Cole plot of loss modulus vs storage modulus for polymerized sample of 50 mM TDMAO / 0.5 mM L35 / 80 mM styrene.

When we look at the Cole-Cole plot in [Figure 4.18](#), the discrepancies between the measured and fitted data indicates that the Maxwell model is clearly not perfect in this case. This implication seems considerably parallel to the idea revealed before, while most of the entangled rod like micellar structures are showing similar behavior to Maxwell model, polymeric systems with a wide chain length distribution do not comply with it¹⁸⁰. The plateau modulus G_0 and the relaxation time τ_R obtained from steady shear and oscillatory measurements are summarized in [Table 4.6](#) and show very good agreement of both experiments.

Table 4.6. Summarized results obtained from fitting with the Carreau-Yasuda [Equation 3.37](#) and the Maxwell [Equation 3.36](#) models.

	Carreau-Yasuda	G' (ω)	G'' (ω)
G_0/Pa	0.93	0.86	0.73
τ_R/sec	0.128	0.19	0.19
η_0/Pa	0.12	-	-

4.3 Summary

In this chapter we aimed to investigate the effect of styrene, as a common hydrophobic monomer, on the mixture of nonionic surfactants tetradecyldimethylamine oxide (TDMAO) and L35, where the copolymer provides colloidal stabilization in the system. Our main aim was to fixate the self-assembled structures by polymerization, therefore we varied the monomer composition until the solubilization limit was reached. Phase behavior, structural evaluations, then the subsequent polymerization of styrene monomer was studied by means of turbidity, static and dynamic light scattering (SLS, DLS), as well as small-angle neutron scattering (SANS). Because of the interesting viscoelastic properties of polymerized system, we probed the rheological behavior with oscillatory and shear experiments.

First, from the scattering analyses we obtained that with increasing styrene amount, rod-like micelles of TDMAO/L35 evaluate to more elongated micellar structures. Upon further increase of styrene, spontaneously vesicles are forming where styrene plays the similar role as cosurfactants. However, when styrene is in excess, much smaller spherical aggregates are formed. Apparently, this additional styrene can no longer takes part in vesicle formation and does not go the micellar interface but goes to the hydrophobic core. Basically, it solubilizes internally, reaching to the solubilization limit for the ~ 4.5 molar ratio of styrene to surfactants, and accordingly forming small microemulsion droplets (oil-in-water (O/W)). Additionally, visual inspection together with turbidity measurements of the given system confirm these results.

The interesting part of this chapter is that the vesicle regime corresponds the 50 mM to 120 mM styrene amount. As described in [section 1.1](#), here the packing parameter plays the key role in formation of vesicles. Styrene molecules effect the packing parameter not substantially on the head group area but largely on the volume. This means numerically the packing parameter, p , increases. This induces the transition from cylinders to a locally flat geometry and the formation of vesicles ³.

In the second part, we discussed that the polymerization of TDMAO/L35/styrene vesicles lead to the disruption of the bilayers and formation of more elongated aggregates. This structural evaluation is also described by the packing parameter. Styrene is a relatively polar molecule based upon its double bond. However, after the polymerization, the double bond is gone, and the formed polystyrene becomes more hydrophobic. Accordingly, this hydrophobic polymer chains are like oil molecules, which can be solubilized in the micellar core. With the help of SANS we could confirm that this structural conversion ends up with spherical structures with

the radius around ~ 7 nm which means basically the size of the initial microemulsion droplets were retained after polymerization. Importantly, a polymerized sample with 80 mM styrene showed a noticeable viscoelastic behavior that we can explain by the fact of formation of wormlike micelles which are stiffened and permanent in shape due to the polymerization and also investigated from rheological side. This chapter presents and confirms that as a common hydrophobic monomer, styrene takes part in the formation of vesicles with the nonionic TDMAO/L35 surfactant mixture, like the effect of cosurfactant. When it is polymerized, it becomes much more hydrophobic and changes the structure back to the smaller rod-like aggregates. This study presents a new way of vesicle formation by addition of the styrene and fixating the self-assembled structures by subsequent polymerization.

5 TDMAO/LiPFOS/L35/Styrene System

Introduction

Vesicles have great potential for being used as templates within the aim of producing nanocarriers^{112,181} because of their structural feasibility for encapsulation^{3,43,182,183}. They can transport hydrophobic compounds in their lipid shell or hydrophilic moieties in the core. Various studies have shown that their formation and structural properties can be controlled as well as an improved stability, thereby vesicles have a wide application area from biomedicine to electronics¹⁸⁴⁻¹⁸⁸. In addition, these well-defined systems can be formed spontaneously by proper surfactant types^{56,189,190}.

Surfactant mixture of zwitterionic tetradecyldimethylamine oxide (TDMAO) and anionic lithium perfluorooctylsulfonate (LiPFOS) is spontaneously forming monodisperse vesicles with a PDI ~ 0.05 which had been shown previously^{191,192}. This formation is explained due to the synergistic interaction between the surfactant pairs, where the head groups are attractively interacting thereby reducing the joint head group area and therefore inducing vesicle formation. Stability and size of these vesicles can be controlled by addition of Pluronic copolymers ($\text{EO}_n\text{-PO}_m\text{-EO}_n$)^{114,115}. Consequently, small, monodispersed and kinetically long-time stabilized vesicles are formed in their mixtures.

This chapter reveals the effect of styrene monomer on this system with the intention of fixating the vesicles by polymerization. TDMAO/LiPFOS mixture with molar ratio of 55:45 in the presence of 1 mol % Pluronic L35 was employed, since this ratio is yielding the most well-defined vesicles^{114,115}. As chapter 4 defines the effect of styrene on TDMAO/L35 system, with the present part we conclude its role on the essential vesicle system in this context by focusing on the subsequent polymerization of this system and thereby its permanent fixation.

5.1 TDMAO/LiPFOS/L35/Styrene

5.1.1 Phase Behaviour

As a hydrophobic monomer and slightly soluble in water, styrene needs to homogenize into the vesicle bilayer according to our main objective. Its low water solubility, $\sim 3 \text{ mM}$ ¹⁶⁹, makes the homogenization difficult, thus we choose to dissolve the styrene into the TDMAO/L35 solutions prior to vesicle preparation. Chapter 4 has described the behaviour of styrene during the dissolution into the 50 mM TDMAO / 0.5 mM L35 solutions. Mixing them with LiPFOS leads to formation of vesicles loaded with styrene monomer.

In this step we investigate 27.5 mM TDMAO / 0.275 mM L35 / 22.5 mM LiPFOS / styrene mixtures, for varying amounts of styrene. These samples were created by blending the 50 mM TDMAO / 0.05 mM L35 / various styrene (prepared 3 days prior to vesicle formation) mixtures and 50 mM LiPFOS together at room temperature in the molar ratio of 55:45 (TDMAO:LiPFOS).

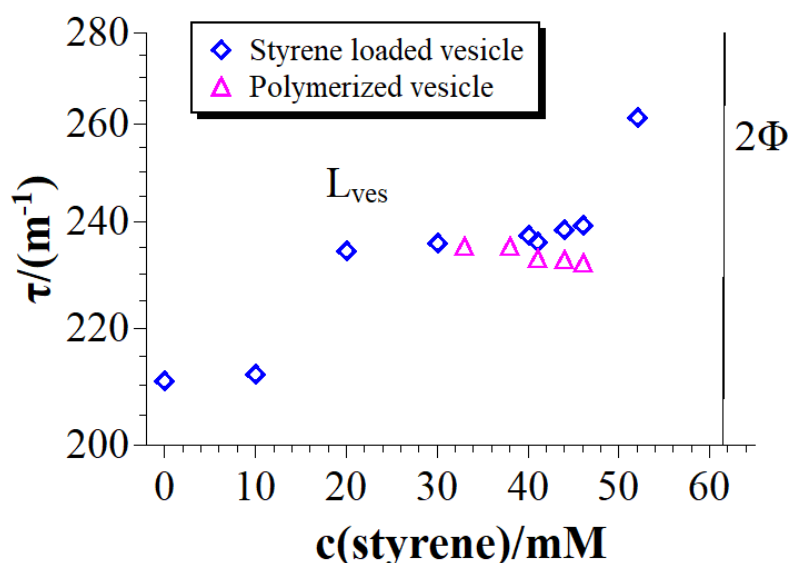


Figure 5.1. Turbidity τ ($\lambda=632 \text{ nm}$) as a function of styrene concentration in 27.5 mM TDMAO / 0.275 mM L35 / 22.5 mM LiPFOS (red diamond); polymerized samples of 27.5 mM TDMAO / 0.275 mM L35 / 22.5 mM LiPFOS (blue triangle) at 25 °C. Measurements were done after 1 hour of both sample preparation and polymerization.

We gained information on the styrene solubilization, stability and the potential aging process of the aggregates by turbidity measurements parallel to visual inspection. The TDMAO/L35 samples with dissolved styrene were closed firmly and stirred for 3 days in order to dissolve the monomer entirely in the solutions at 25 °C. Later on, vesicles were prepared by mixing

these solutions with 50 mM LiPFOS at aforementioned ratio. After mixing both solutions, the vesicle phase, L_{ves} , directly was characterized by the bluish appearance as seen in [Figure 5.2](#)^{171,176}. From 0 mM to 65 mM styrene amount, samples had the same slightly turbid appearance, no precipitation or phase separation was observed. However, for more than 65 mM styrene amount, this sight changed drastically. Apparently, system was saturated with styrene monomer, becoming very turbid view and an excess of the monomer was phase separated at the top of the solution within an hour (2Φ).



Figure 5.2. Sample photograph after 1 hour of preparation 27.5 mM TDMAO / 0.275 mM L35 / 22.5 mM LiPFOS with increasing amount of styrene mixtures from 0 to 65 mM at 25 °C.

[Figure 5.1](#) shows the turbidity values calculated by UV-transmission measurements of TDMAO/L35/LiPFOS vesicles with ascending amount of styrene. When the bare vesicles without styrene and the styrene loaded vesicle samples are compared, it can be seen from the figure that turbidity values are stayed almost the same. This means styrene loading had no disruptive effect on vesicles, simply it became dissolved in the hydrophobic bilayer. On the other hand, after reaching its saturation limit, then turbidity jumps into a higher-level following by a phase separation. These findings are in good agreement with the visual inspection of the samples.

Additionally, the inspection of samples revealed that the bluish-one phase appearance of the samples stayed unchanged for an observation window of one year. After 1 year, samples were phase separated.

5.1.2 Light Scattering

In order to gain more systematic structural information on the effect of styrene, we performed light scattering measurements.

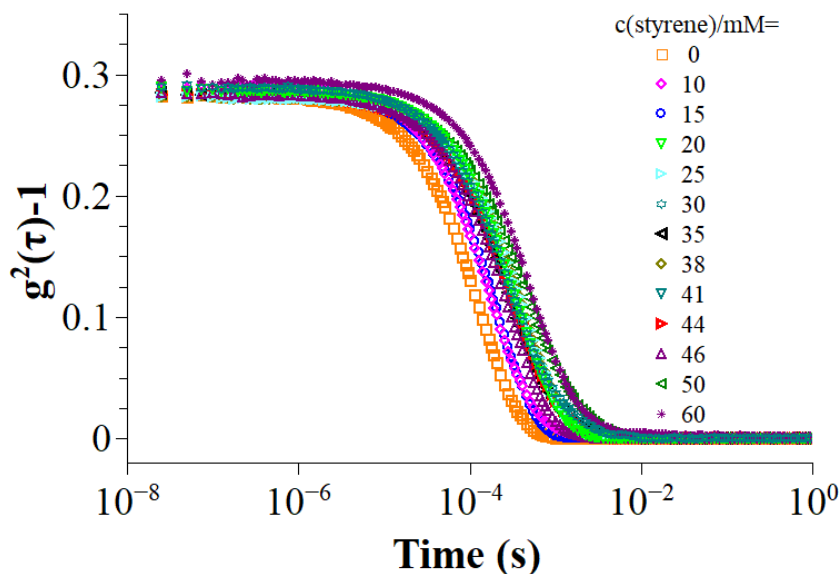


Figure 5.3. Intensity autocorrelation function $g^2(t)$ measured at an angle of 90° of monomer loaded vesicles in 27.5 mM TDMAO / 0.275 mM L35 / 22.5 mM LiPFOS / styrene mixtures at 25 °C.

The size of styrene loaded vesicles was obtained by dynamic light scattering measurement. [Figure 5.3](#) shows the intensity autocorrelation functions of the TDMAO/LiPFOS vesicles with different styrene concentrations measured at the scattering angle of 90° at 25°C. These curves show a monomodal decay for all samples. However, the decay time of the aggregates increases along with styrene concentration. This means the particle diffusion becomes slower implying the formation of bigger particles in the system.

The average vesicle size and polydispersity in a distribution was obtained with the cumulant method. Analyses of the data indicate and confirm that this bluish slightly turbid phase consisted of vesicular aggregates. The obtained hydrodynamic radii from cumulant method after the insertion of styrene into the system is depicted in [Figure 5.4](#) together with gyration radii deduced from static light scattering. Based upon the analyses, vesicle radii increased systematically up to 30 mM styrene amount, then stagnated until 45 mM concentration. Above this point, it increased substantially again until the 2-phase region was reached. Styrene insertion to the bilayer of TDMAO/LiPFOS system, reduces the preferred curvature hence leading to bigger vesicles. Furthermore, styrene loaded vesicles hold a much wider size

distribution than the system without styrene, as seen in [Table 5.1](#), and the PDI value jumps from 0.09 to ~0.3-0.4.

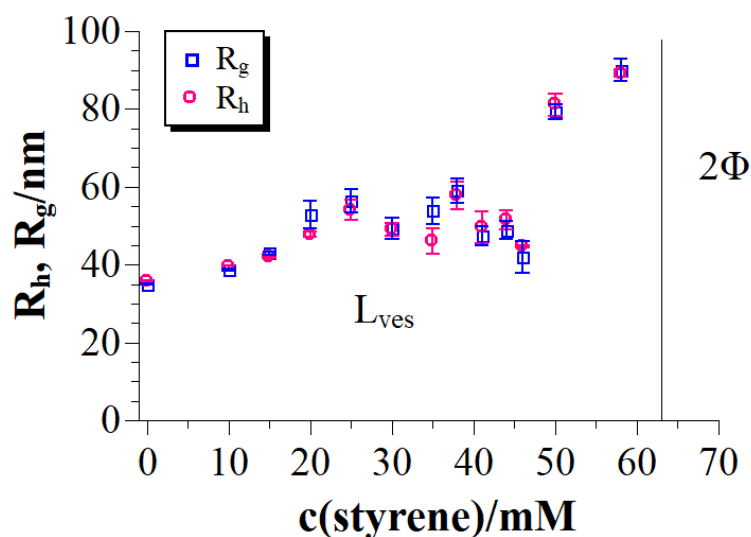


Figure 5.4. Intensity autocorrelation function $g^2(t)$ measured at an angle of 90° of monomer loaded vesicles in 27.5 mM TDMAO / 0.275 mM L35 / 22.5 mM LiPFOS / styrene mixtures at 25°C

In the light of static light scattering measurements, information about the radii of gyration R_g , and molecular weights, M_w of the aggregates can be gained from Guinier approximation (see [section 3.1.5.2](#)). Samples were measured at the same set-up as DLS at 10 different angles ($30, 40, 50, 60, 70, 80, 90, 100, 110$ and 120°). When we look at the R_g , it changes exactly in the same fashion as the hydrodynamic radii seen ([Figure 5.4](#)). For vesicles $R_g = R_{\text{outer}}^{126}$, which is in our case in good agreement and therefore corroborative to the presence of vesicles.

The forward scattering, $I(0)$ values were extrapolated by fitting the scattering curves (in [Figure 5.5](#))¹²⁰ with Guinier approximation, therefore, intensities were plotted against q^2 . Then the M_w was

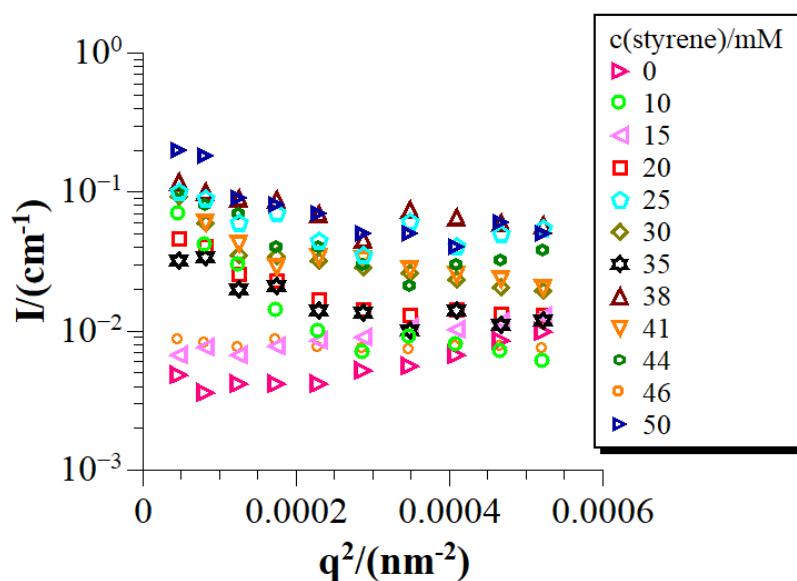


Figure 5.5. Intensity vs q^2 for 27.5 mM TDMAO/0.275 mM L35/22.5 mM LiPFOS/styrene mixtures at 25°C .

determined for the vesicles from the [equation 3.8](#) (Table 5.1). Refractive index increments used in the [equation 3.9](#) were measured and are listed in [Appendix 9.2.1, Table A3](#). [Table 5.1](#) represents R_h hydrodynamic radii, PDI, polydispersity index, (both from DLS), M_w , apparent molecular weights, R_g , radius of gyration values and N_{agg} , the aggregation numbers (from M_w , and with respect to all molecules contained) for styrene loaded vesicles.

Based upon the analyses so far, we prefer to study the styrene concentrations between 30-45 mM in which range the particle size stagnated after the increase, and just before the saturation point of the system to the monomer. Coming part below is describing the samples with mentioned styrene range for a comparative analysis of unpolymerized and polymerized vesicles.

Table 5.1. Results from the SLS and DLS measurements of styrene loaded vesicles of 27.5 mM TDMAO / 0.275 mM L35 / 22.5 mM LiPFOS mixtures at 25°C. Given are the hydrodynamic radius R_h , radius of gyration R_g , theoretically calculated vesicle radius from M_w (from SLS) and thickness (from SANS) $R_{ves,th}$, polydispersity index PDI (from DLS), aggregation number N_{agg} (from M_w , and with respect to all molecules contained) and the apparent molecular weight M_w .

Styrene amount (mM)	R_h (nm)	R_g (nm)	R_{ves} theor. (nm)	PDI	M_{wapp} (g/mol)	N_{agg} from SLS
0	35.6	35.1	30.7	0.09	1.29×10^7	35000
10	39.4	38.8	33.2	0.38	1.80×10^7	54400
15	42.1	43.2	36.7	0.37	2.23×10^7	70300
20	47.7	52.8	42.2	0.42	3.08×10^7	110700
25	54.3	56.4	51.1	0.39	4.46×10^7	163500
30	48.9	49.2	45.7	0.29	3.54×10^7	128000
35	46.2	53.9	47.9	0.44	2.80×10^7	102000
38	57.8	59.1	53.4	0.39	4.82×10^7	180000
41	49.6	47.4	44.2	0.41	3.83×10^7	148000
44	51.5	48.9	41.8	0.43	4.09×10^7	154000
46	44.6	42.1	36.7	0.41	2.67×10^7	100600
50	81.2	79.2	63.9	0.47	6.11×10^7	257000
58	89.1	89.9	67.4	0.45	6.52×10^7	273000

5.1.3 Small Angle Neutron Scattering (SANS)

Small angle neutron scattering curves were recorded on instrument D11 at the Institute Laue Langevin (ILL) with the wavelength of 0.6 nm (FWHM of 9%), three sample-detector distances of 1.2, 8.0, and 39.0 m with corresponding beam collimation lengths of 5.5, 8.0, and 40.5 m respectively.

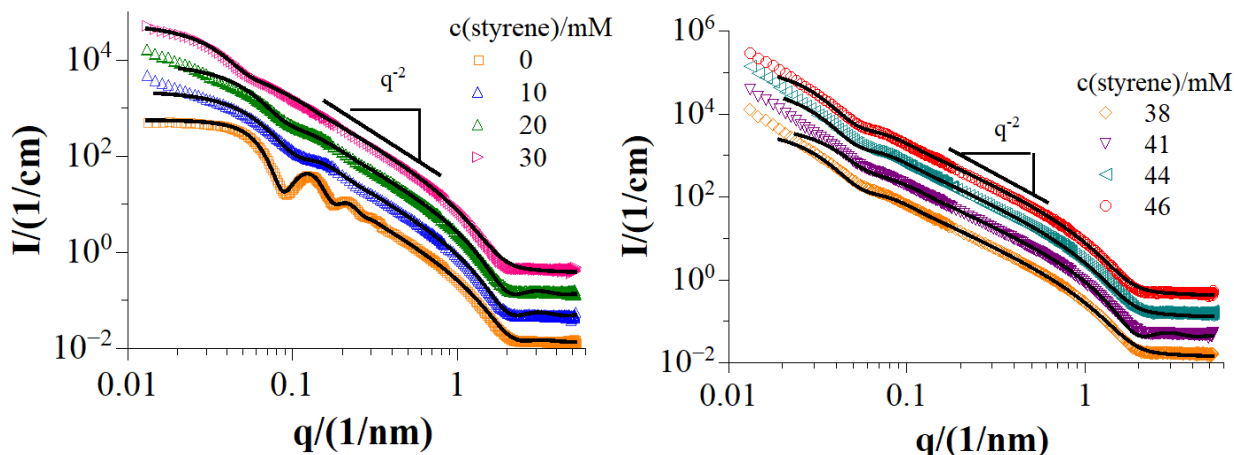


Figure 5.6. SANS curves of 27.5 mM TDMAO / 0.275 mM L35 / 22.5 mM LiPFOS / styrene mixtures at 25 °C. (Colored lines: measured data; solid black line: fitted data). For clarity subsequent data sets were multiplied each with a scale factor of 3.

All the samples were prepared freshly in D₂O prior to SANS measurements. Styrene amount was varied over in the same range described so far. Measured data were fitted using a form factor of a spherical shell geometry yielding a vesicle radius for neat system around 32.5 nm and a membrane thickness of 2.73 nm. These results are in good agreement with the values observed for the same system in the previous work^{114,115}.

Scattering data of the styrene loaded vesicle samples are presented in [Figure 5.6](#). What is more apparent at first look is that, the significant oscillations at low q ($0.08\text{--}0.09\text{ nm}^{-1}$), become flattened with incorporating styrene into the system. This means the narrow size distribution of the formed particles becomes wider, namely the polydispersity index is increased. Nevertheless, the q^{-2} slope observed in the middle q region, in the range of $0.2\text{ to }0.8\text{ nm}^{-1}$, is the signature of the bilayers and this behavior remains similar for all the samples.

Upon addition of styrene into the vesicles, in the beginning the position of the first minima shifts to the lower q , indicating clearly an increase of the vesicle size. Looking at the scattering curves of higher styrene concentrations, the intensity at low q increases drastically, evidencing the presence of larger particles in the sample.

In detail, the modeled curves in [Figure 5.6](#) exhibit an interesting behavior for the samples below 30 mM styrene amount. Here, the vesicle size slightly decreases from 32.5 nm to 26 nm with the insertion of styrene into the system. For 10 mM sample, this is different from light scattering result, where bigger and more polydisperse vesicles were observed. This difference can be due to the light scattering method is sensitive to the collective diffusion in the sample. However, above this point, similar trend was obtained. Vesicles start to grow to the radius of ~45 nm, together with an increase of the bilayer thickness to ~2.9 nm by means of the incorporation of the styrene within the bilayer. The polydispersity reaches a value of ~0.3 confirming the light scattering results ([Table 5.1](#)).

Additionally, M_w , molecular weights were calculated by using the vesicle radii and bilayer thickness obtained from SANS analyses. When we compare the result listed in [Table 5.2](#) with M_w from SLS ([Table 5.1](#)), both results are in good agreement.

Table 5.2. Results from the SANS analysis of 27.5 mM TDMAO / 0.275 mM L35 / 22.5 mM LiPFOS and styrene mixtures at 25°C. Given are the vesicle radius R_{ves} ($R_{ves}=R+\Delta R$), polydispersity index PDI, aggregation number N_{agg} , molecular weight M_w , bilayer thickness D ($D=\Delta R$) from spherical shell model, bilayer thickness D ($D=\Delta R$) from Kratky- Porod analysis (see [Appendix 9.2.2](#) and [Figure A4-A5](#), and the volume fractions Φ of dispersed material.

Styrene amount (mM)	Φ Volume Fraction	R_{ves} (nm) SANS	PDI	D/nm Spherical shell	D/nm Kratky Porod	M_w (g/mol)	N_{agg}
0	0.0144	35.2	0.10	2.73	2.78	1.32×10^7	35000
10	0.0156	26.1	0.29	2.71	2.77	1.56×10^7	47100
20	0.0169	28.9	0.31	2.70	2.80	1.75×10^7	59000
30	0.0182	46.1	0.34	2.72	2.84	2.80×10^7	112000
38	0.0188	46.4	0.31	2.84	2.87	2.75×10^7	109000
41	0.0191	46.7	0.29	2.92	2.94	2.94×10^7	115000
44	0.0196	48.3	0.30	2.94	2.95	3.03×10^7	120500
46	0.0202	47.9	0.33	2.95	2.97	3.00×10^7	118800

The aggregation number N_{agg} were calculated for surfactant by using the formula:

$$N_{agg} = V \cdot \rho \cdot \frac{N_A}{M_{wi}} \quad (5.1)$$

where V is the volume, N_A Avogadro's number, ρ is the density, and M_{wi} is a sum of the molecular weight of components due to the molar fractions x , in each sample. Results are listed in [Table 5.2](#).

5.2 Polymerization of the TDMAO/LiPFOS/L35/Styrene System

So far, in the previous part the well-defined TDMAO/LiPFOS/L35 vesicles were loaded with styrene monomer and investigated by systematically varying the monomer amount. The scope of this part is to elucidate the fixating process of these styrene loaded vesicles with photo-initiated radical polymerization by means of several methods such as turbidity measurements, static light scattering (SLS), dynamic light scattering (DLS), small angle neutron scattering (SANS) and by nuclear magnetic resonance (NMR) technic. Particularly we choose the monomer range of 30-45 mM for further polymerization step, which can be explained with the basis of dynamic light scattering measurements in [section 5.1.2](#). As described in aforementioned part, monomer loaded vesicles in this range showed a stagnated size evolution. The size of the vesicles in this monomer range are more stable, therefore, aimed to be used for polymerization.

5.2.1 Phase Behaviour

Cross-linked polymerized samples of 27.5 mM TDMAO / 22.5 mM LiPFOS / 0.275 mM L35 with styrene concentration varying from 35 mM to 46 mM / 0.1 molar ratio of DVB as cross-linker (with respect to the monomer concentration) showed similar visual appearance as before polymerization. The bluish, slightly turbid view of vesicles retained after polymerization. No phase separation, coagulation or precipitation as observed. [Figure.5.7](#) depicts the sample photos taken after 1 hour from the end of the polymerization which was proceeded for 15 hours.

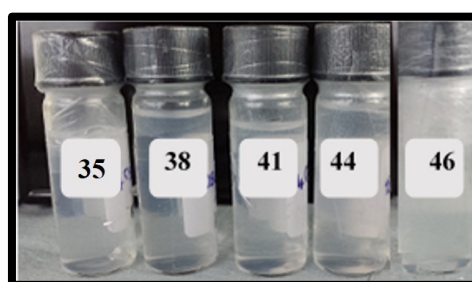


Figure 5.7. Sample photograph after 1 hour from the end of polymerization for 27.5 mM TDMAO / 0.275 mM L35 / 22.5 mM LiPFOS / varying amount of styrene mixtures (with 0.1 molar ratio of cross-linker with respect to the styrene amount) at 25 °C.

Turbidities of the polymerized samples were obtained in the same way as unpolymerized ones via measuring the transmissions then converting them to the turbidity values via the [equation 3.39](#). The values are presented in the same plot together with the values for unpolymerized

samples in [Figure 5.1](#). Although both results are almost in the same range, a very slight drop in turbidities for polymerized samples with styrene amount more than 40 mM, is recognizable. Presumably, it could be the result of the fact that polystyrene has low refractive index and therefore the contrast decreases. Another assumption is due to the polymerization, the dissolved styrene in the mixture arranges. Both lead to a slight decrease in turbidity for high monomer concentrations. However, it has to be noted that the visual appearance of the samples remained after the polymerization, which is an indication of preserving the vesicle structures.

5.2.2 Light Scattering

Light scattering is a powerful way to compare the structural variation and size distribution for both cases. [Figure 5.8](#) presents time dependent autocorrelation functions of the scattered light intensities for polymerized samples measured at the scattering angle of 90° and performed at 25°C .

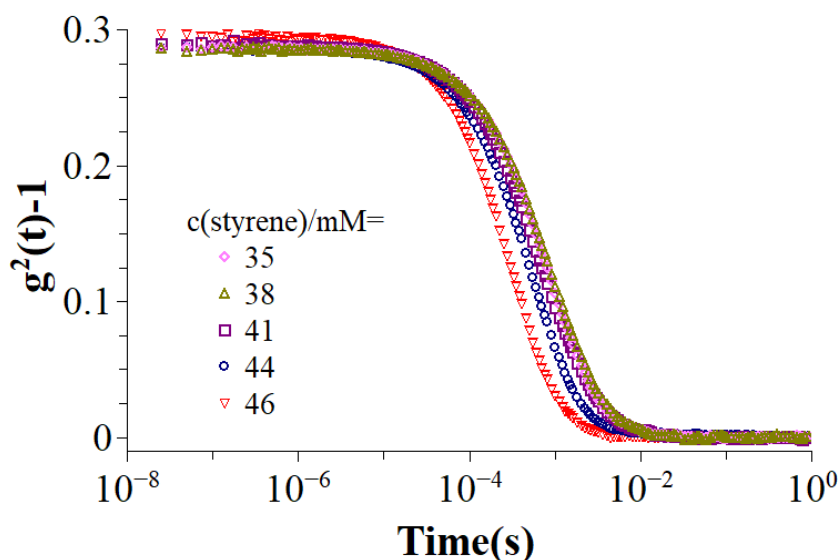


Figure 5.8. Intensity autocorrelation function $g^2(t)$ measured at an angle of 90° of polymerized vesicles in 27.5 mM TDMAO / 0.275 mM L35 / 22.5 mM LiPFOS / styrene and 0.1 ratio of cross-linker mixtures at 25°C .

At first look, they seem all monomodal and the decay times are close to each other. However, in detail one can see the autocorrelation curves of the polymerized samples shifted to the slightly shorter decay times when monomer amount increases.

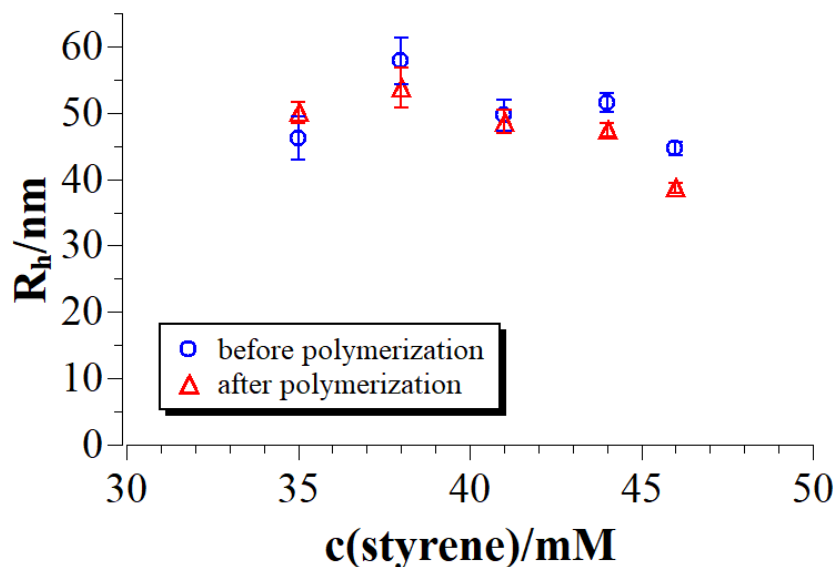


Figure 5.9. Hydrodynamic radii before and after polymerization of vesicles in 27.5 mM TDMAO / 0.275 mM L35 / 22.5 mM LiPFOS / styrene and 0.1 ratio of cross-linker mixtures at 25 °C.

The analysis of the measured data with cumulant method allows the determination of the average particle diameter and size distribution. According to the analyses, the high polydispersity of the unpolymerized samples in [section 5.1.2](#) remains in the same range. Hydrodynamic radii are depicted in [Figure 5.9](#) together with the R_h of unpolymerized vesicles. The values show a very slight increase for each polymerized sample in the similar trend as in the unpolymerized case. It can be noted that during the polymerization process, the radius of the vesicles was retained around 40-60 nm. This implies that these small vesicles can successfully be fixed in the templating process by polymerization.

Table 5.3. Results from the SLS and DLS measurements of polymerized vesicles of 27.5 mM TDMAO / 0.275 mM L35 / 22.5 mM LiPFOS mixtures at 25 °C. Given are the hydrodynamic radius R_h , radius of gyration R_g , theoretically calculated vesicle radius from M_w (from SLS) and thickness (from SANS) $R_{ves\ theor.}$, polydispersity index PDI (from DLS), and the apparent molecular weight $M_{w,app}$.

Styrene amount (mM)	R_h (nm)	R_g (nm)	$R_{ves\ theor.}$ (nm)	PDI	$M_{w,app}$ (g/mol)
35	50.1	47.3	52.6	0.41	4.43×10^7
38	52.3	54.3	58.2	0.42	4.67×10^7
41	48.2	46.3	52.0	0.35	4.01×10^7
44	47.4	54.0	53.1	0.37	3.98×10^7
46	38.7	43.3	40.7	0.30	2.85×10^7

Additionally, from the static light scattering measurements, the information on molecular weights and radius of gyration was provided. Thereby, we calculated the theoretical vesicle radii from molecular weights obtained by SLS with assuming the bilayer thicknesses from small angle neutron scattering measurements. Results listed in [Table 5.3](#), show good agreement with the hydrodynamic radii from DLS confirming the accuracy of the templating process.

5.2.3 Small Angle Neutron Scattering (SANS)

For the aim of small angle neutron scattering measurements, polymerization reactions took place in D₂O as solvent. Measurements were done in the similar set up as for unpolymerized samples and data were analysed in the same manner. [Figure 5.10](#) illustrates the neutron scattering curves of polymerized vesicles with 0.1 molar ratio of cross-linker. Noticeably, these curves show similar scattering patterns as unpolymerized ones, holding the q^{-2} slope is in the middle q region of 0.2 to 0.8 nm⁻¹, indicating the presence of bilayer structures. This means that polymerization did not have a destructive effect on the monomer-loaded vesicles, conversely it sustained the preformed structures by stabilizing their structures.

When we look at the curves closely, as a result of the polymerization, the form factor minima which is around 0.06-0.07 nm⁻¹ first shifted to higher values (0.04-0.05 nm⁻¹), and afterwards tended to go to smaller q again. This means the vesicles ended up with smaller radii and also a higher polydispersity which is noticeable from the more flattened form factor minimum.

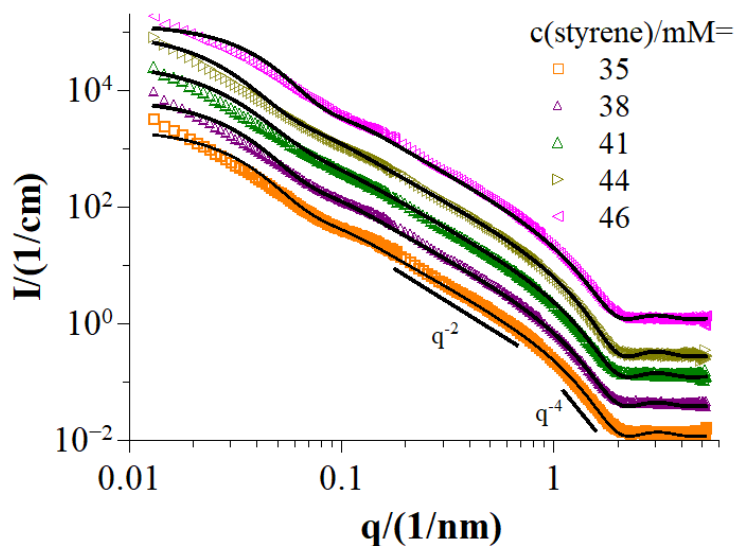


Figure 5.10. SANS curves of cross-linked polymerized samples of 27.5 mM TDMAO / 0.275 mM L35 / 22.5 mM LiPFOS / styrene mixtures at 25°C. (Colored lines: measured data; solid black line: fitted data). For clarity subsequent data sets were multiplied each with a scale factor of 3.

These curves were fitted with a spherical-shell model similarly as unpolymerized samples and yielded values in the same range changing from 36 to 43 nm in radius for varying styrene concentrations. Structural parameters obtained for polymerized vesicles are summarized in [Table 5.4](#). As seen from the analyses, the bilayer thicknesses of the cross-linked polymerized samples did not change, indicating a robust cross-linked polymer shell was formed within the bilayers. This interesting finding was analyzed precisely further by the help of Kratky-Porod plots (see Appendix 9.2.2, Figure A6). The thicknesses deduced from both analyses differ somewhat from each other, however revealing basically the accuracy of the analyses and are summarized in [Table 5.4](#).

Table 5.4. Results from the SANS analysis of cross-linked polymerized samples of 27.5 mM TDMAO / 0.275 mM L35 / 22.5 mM LiPFOS / styrene mixtures at 25 °C. Given are the vesicle radius R_{ves} , polydispersity index PDI, molecular weight M_w , bilayer thickness D from spherical shell model, bilayer thickness from Kratky- Porod analyses (see [Appendix 9.2.2](#) and [Figure A6](#)), and calculated thickness for the polystyrene shell.

Styrene amount (mM)	R_{ves} (nm) SANS	PDI	D/nm Spherical shell	D/nm Kratky Porod	Polymer shell thickness	M_w (g/mol)
35	38.8	0.37	2.81	2.87	1.18	2.72×10^7
38	43.1	0.38	2.82	2.84	1.24	3.14×10^7
41	44.9	0.39	2.82	2.87	1.30	3.48×10^7
44	40.8	0.41	2.83	2.90	1.39	2.83×10^7
46	33.2	0.40	2.84	2.92	1.50	2.11×10^7

5.2.4 Nuclear Magnetic Resonance (NMR)

Polymerization was confirmed with ^1H NMR measurements. The conversion of monomer and the end of polymerization was determined with vanishing the proton signals of the double bond of the styrene molecule. A Bruker Avance II 400 spectrometer operating at 400 MHz was used to record the spectra. D_2O was used as solvent and tetramethylsilane (TMS) was used as reference agent.

[Figure 5.11](#) shows the ^1H -NMR spectra of vesicles before and after the polymerization. Signals at δ 5.0-5.5 and δ 6.47 (C-H of vinyl group) are visible before polymerization while after polymerization, these signals had disappeared ([Figure 5.11](#) bottom). This evidently shows the full conversion of styrene monomers to the polystyrene.

Additionally, proton signals of the aromatic group appear between δ 7.0-7.8 vanishes or became reduced, and the peak integrals of the aromatic group decreased by half (compared to the proton signals of the surfactant molecule between δ 3.0-3.7). This can be explained by the fact that polymerization within the hydrophobic bilayer of the vesicles restricts the motion of the formed polymeric network protons therefore their signals are no longer visible or pronounced.

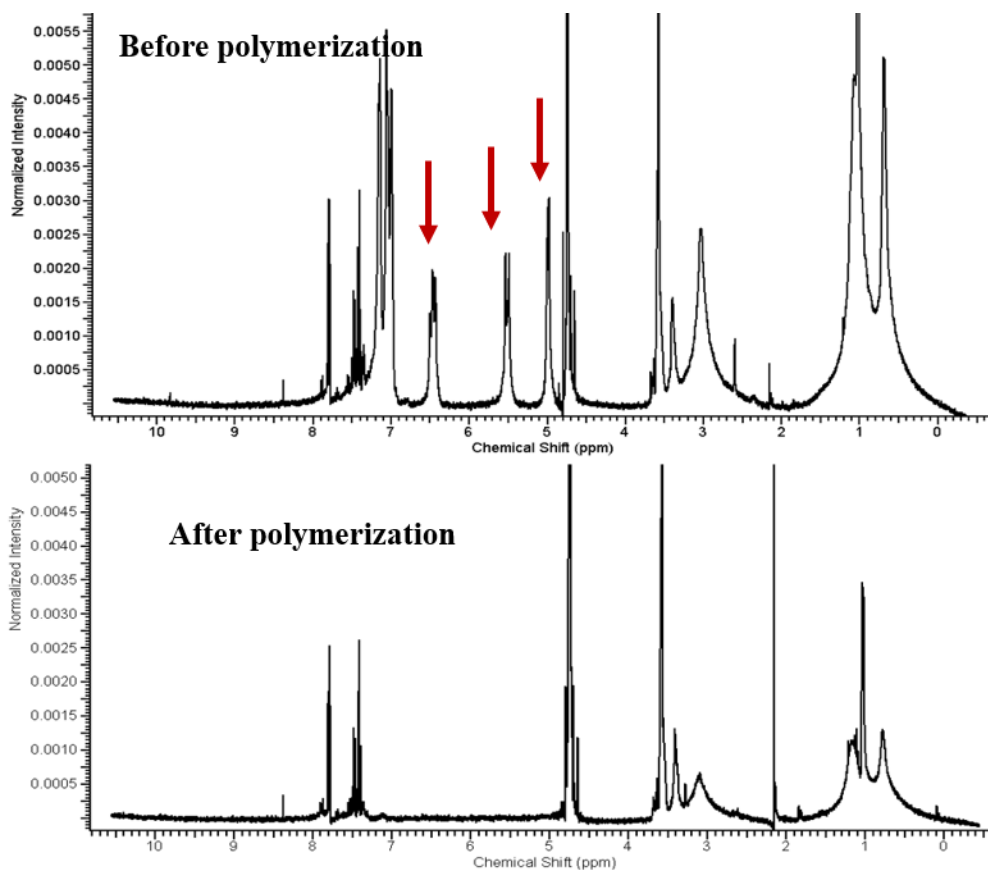


Figure 5.11. ¹H-NMR spectra of vesicles before and after cross-linking polymerization at 25 °C. The molar ratio of divinylbenzene to styrene was 0.1 with a total concentration of monomer of 35 mM. Red arrows: signals of the vinylic protons.

5.3 Summary

Kinetically stable, monodisperse vesicles consisted from zwitterionic TDMAO and anionic LiPFOS surfactants with the presence of Pluronic L35 copolymer, were used as model system for fixation by polymerization. Such polymer stabilized vesicles are important structures due to their geometrical feasibility for encapsulation which allows them for being used as nanocarriers.

In this chapter, we performed the concurrent loading of styrene monomer into the hydrophobic vesicle bilayer and accordingly its polymerization. In the first part, monomer loading capacity of vesicles were investigated for increasing monomer concentrations with the help of turbidity, static and dynamic light scattering (SLS, DLS), and small-angle neutron scattering (SANS) measurements. Scattering experiments provided information on the presence of vesicles due to the monomer loading, at the same time demonstrated remarkable increase of the size and polydispersity index. In [chapter 4](#), we showed that styrene monomer has an effect on forming vesicles already only with TDMAO/L35 surfactants, like a typical cosurfactant. Adding the LiPFOS surfactant, the model vesicle system was retained. However, styrene loading caused a drastic shift from monodisperse to polydisperse structures. The reason of this sharp change can be explained with the fact that styrene as a cosurfactant, may speed up the equilibration.

Second part explained the effects and results of polymerization on vesicles. In general, vesicles became slightly smaller in comparison to unpolymerized ones. Vesicles were structurally and morphologically retained after polymerization. Scattering measurements, in particular SANS experiments, show that vesicle formation was not affected by polymerization and showed identical scattering patterns either before or after polymerization. The increase of polydispersity due to the styrene loading stayed similar for polymerized vesicles as well, however, is still in the range of theoretical polydispersity value which is calculated for equilibrium vesicles¹⁹³.

This chapter elaboratively revealed that a model, well-defined vesicle system can be used as template for fixation by polymerization under mild reaction conditions and structures successfully retain their initial form after polymerization. By this way, it is possible to produce polymeric nanocapsules in the size range of 40-100 nm in a straightforward way which enables for further investigations with different monomers, cross-linkers to different vesicle systems.

6 The Effect of Acrylate Monomers

Introduction

Polymerization is an effective way for fixating vesicles that results in the formation of polymeric nanocapsules. These nanostructures can be used as nanocarriers in different research areas from material science to the nanomedicine ^{87,88,194}. Stabilization of the vesicles by inserting hydrophobic monomers into their bilayers and subsequently polymerizing them, should increase the bilayer rigidity and should reduce its permeability. Thereby one would exert control over these important properties of these shell-structured colloids. Therefore, different studies have been made in recent years in terms of solubilizing traditional hydrophobic monomers in the bilayer to produce hollow polymer nanocapsules ^{86,106,195–197}.

Although the polymerization is a convenient approach, it can have several challenges. It was shown before that due to the polymerization, a phase separation can take place in the bilayer with formation of parachute-like structures ¹⁰³. Additionally, polymerization mostly needs high temperature or using organic solvents, which can have crucial effects on the final structure.

In this chapter, we examine acrylate monomers of different alkyl chain lengths with different hydrophobicity to determine appropriate conditions for an effective templating and polymerization for the further formation of polymer nanocapsules. As the polymerization will take place within the few nanometer wide hydrophobic bilayer, the most important points to take into account are the chain length and hydrophobicity of the acrylate monomers. Accordingly, we varied the hydrophobicity of the acrylate monomers in a systematic fashion by using butyl, hexyl, isooctyl and dodecyl acrylate.

The core vesicle system consisted of nonionic tetradecyldimethylamine oxide (TDMAO), Pluronic L35 and anionic lithium perfluorooctylsulfonate (LiPFOS) surfactant ^{114,115,192}, has been concurrently loaded with alkyl acrylates, and templated via polymerization under quite mild conditions, where the reaction was taking place in water at 18 °C (the polymer surfactant L35 was included in this formulation in order to bring in additional steric stabilization for the formed colloidal assemblies). For dissolving the water-insoluble monomer and preventing vesicle aging, concurrent loading was preferred, and primarily varying amount of hydrophobic monomer as well as the cross-linker were dissolved in micellar TDMAO/L35 solutions. In the first part of this chapter, the effect of acrylate monomers on TDMAO/L35 micelles is described. The second part presents the investigation on the formation of acrylate monomer loaded

TDMAO/L35/LiPFOS vesicles and their characterization. In the last part, particularly the effect of hexyl acrylate monomer on the model vesicle system and its polymerization in the bilayer were studied. Later on, the encapsulation efficiency of the final hollow polymer nanocapsule product was studied by using calcein as a water-soluble fluorescence dye.

6.1 TDMAO/L35/Acrylate System

In this section, we investigate the dissolution behaviour of different acrylate monomers, i.e. butyl acrylate, hexyl acrylate, isooctyl acrylate and dodecyl acrylate in 50 mM TDMAO / 0.5 mM L35 mixtures. Different amounts of monomer were dissolved in samples of constant concentration of TDMAO/L35 mixture and stirred for 3 days in the dark. Sample vials were closed firmly for preventing any evaporation of the monomer.

6.1.1 Phase Behaviour

As a first step, the phase behaviour of surfactant solutions of constant concentration was studied for dissolving increasing amounts of monomer. Starting from the short chain alkyl acrylates, we studied the dissolution of butyl acrylate. [Figure 6.1](#) depicts the sample photos after 3 days of stirring. Since butyl acrylate has a high water solubility of ~ 1.4 g/L¹⁹⁸, the mixtures up to 130 mM butyl acrylate concentration could dissolve in micelles and formed transparent single micellar phase L₁. For high butyl acrylate concentration of 180 mM, the system became saturated with monomer and a more turbid, oily phase separated from solution.

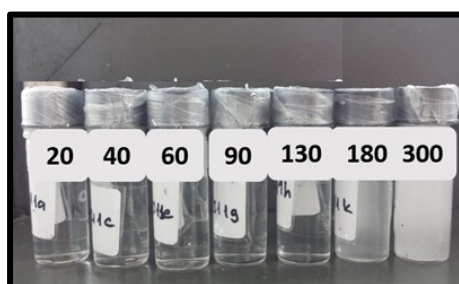


Figure 6.1. Sample photograph after 3 days of stirring 50 mM TDMAO / 0.5 mM L35 / varying amounts of butyl acrylate mixtures at 25 °C.

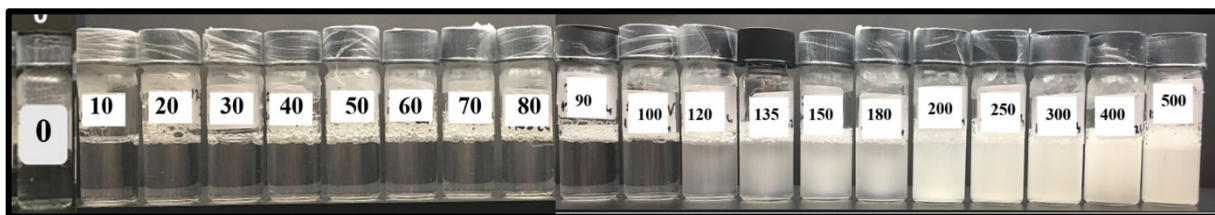


Figure 6.2. Sample photograph after 3 days of stirring 50 mM TDMAO / 0.5 mM L35 / varying amounts of hexyl acrylate at 25 °C.

Hexyl acrylate is another acrylate monomer having a medium chain length and an intermediate water solubility of 0.4 g/L¹⁹⁹ which is appropriate for the polymerization within the hydrophobic vesicle membrane amongst other acrylate monomers (Figure 6.2). Our investigations showed that hexyl acrylate can dissolve in TDMAO micelles up to 120 mM concentration. Above this point, the micellar phase shifts to a turbid phase indicating that an emulsion of monomer droplets is formed. For higher than 200 mM hexyl acrylate amount, samples were turbid with a whitish appearance and separated into 2 phases within an hour (2Φ).

A third monomer that we studied was; isooctyl acrylate. Its solubility in micellar solution differed from butyl and hexyl acrylate due to the low water solubility of ~ 0.01 g/L at 25 °C²⁰⁰. Samples (Figure 6.3 top) up to 90 mM monomer concentration, showed a clear single phase of micellar solutions, L_1 . Afterwards samples turned to white turbid solutions and the excess of monomer phase separated after one hour at the top of the vial (2Φ).



Figure 6.3. Sample photograph after 3 days of stirring 50 mM TDMAO / 0.5 mM L35 / varying amounts of top: isooctyl acrylate, bottom: dodecyl acrylate mixtures at 25 °C.

The fourth monomer was dodecyl acrylate with a water solubility of $\ll 0.01$ g/L at 25°C ²⁰¹. The solubility of dodecyl acrylate monomer in TDMAO micelles was quite low, and a micellar L_1 phase was only observed up to 75 mM concentration. Then for higher monomer amounts, samples immediately turned to white turbid solutions, and phase separated at the top in an hour (2Φ), as seen before for the case of isooctyl acrylate.

As known from the previous works^{115,202}, TDMAO/L35/LiPFOS vesicle has a bilayer thickness of ~ 2.7 nm. Therefore, hexyl acrylate which has a medium chain length in comparison with other acrylates, was preferred to use for further polymerization. Apart from that, its water solubility is in the moderate range, thus this monomer can still be mixed in the solution and at the same time effectively being entrapped into the hydrophobic membrane. Moreover, hexyl acrylate enables to work in a wide concentration range for further vesicle formation and subsequent polymerization.

6.1.2 Light Scattering

To confirm that the monomers incorporate in vesicles as suggested above, the acrylate/TDMAO/L35 mixtures were characterized by dynamic light scattering. The increasing hydrodynamic radius upon increasing the monomer amounts was followed for all acrylate monomers to find optimal conditions for subsequent polymerization.

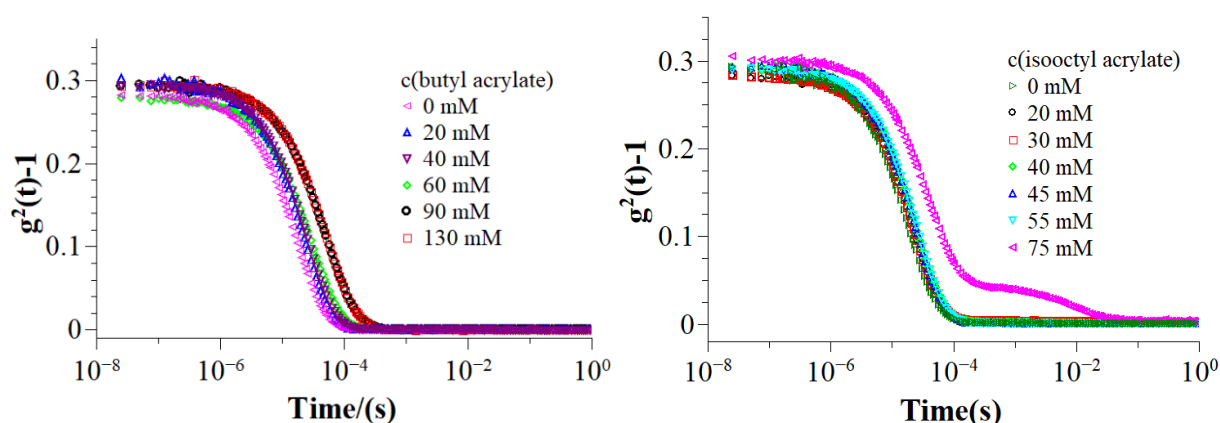


Figure 6.4. Intensity autocorrelation function $g^2(t)$ measured at an angle of 90° of 50 mM TDMAO / 0.5 mM L35 / (left) butyl acrylate (right) isooctyl acrylate mixtures at 25°C .

In the butyl acrylate case, intensity correlation functions were all monomodal (Figure 6.4 left). With introducing the monomer into the system, the decay time stayed nearly constant for monomer amounts up to 90 mM. For 90 and 130 mM amount it slightly shifted to higher decay

times, corresponding to the increasing size of micelles. Similar trend can be seen from the phase behaviour confirming it.

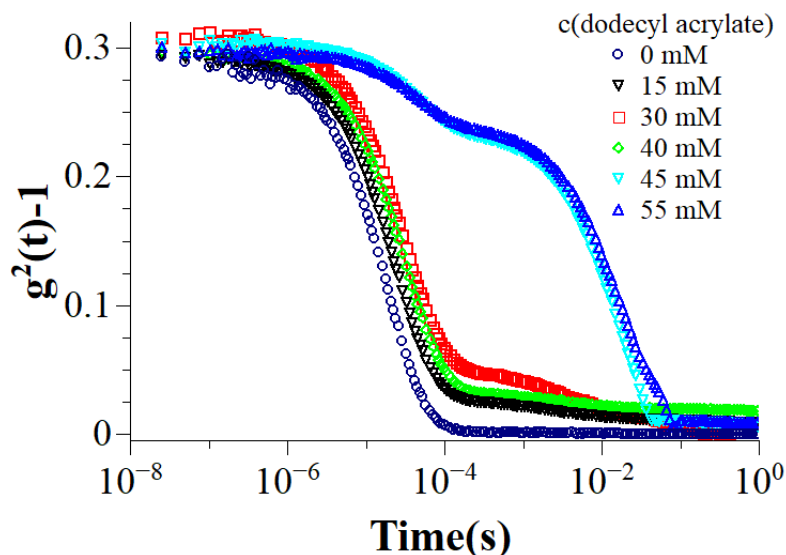


Figure 6.5. Intensity autocorrelation function $g^2(t)$ measured at an angle of 90° of 50 mM TDMAO / 0.5 mM L35 / dodecyl acrylate mixtures at 25°C .

The presence of isoctyl acrylate did not have significant effects on changing the scattering behaviour up to 55 mM concentration. Monomodal curves with fast decay time are depicted in [Figure 6.4](#) (right) and hydrodynamic radius varied from 3.9 to 5.5 nm (see [Table 6.3](#)). However, at 75 mM monomer concentration, the curve looked completely different, being bimodal and shifting to the higher decay time. As a comparison to the previous [part 6.1.1](#), 75 mM is the boundary concentration where the sample appearance changes (see [Figure 6.3](#)). Clearly, DLS confirms the shift from L_1 phase of monomer dissolved micelles and presence of bigger aggregates, presumably emulsion droplets of undissolved excess monomer.

DLS analysis of samples with dodecyl acrylate monomer shown in [Figure 6.5](#), revealed different characteristic than others. Dodecyl acrylate's very low water solubility²⁰¹ made it difficult to dissolve in TDMAO/L35 micelles, therefore different sizes of ~ 4.2 to 6.8 nm (see [Table 6.2](#)) were observed from the intensity correlation curves and none of them was monomodal. In general, this trend of lowered solubilisation with increasing chain length/hydrophobicity of oil molecules is typically observed in surfactant systems^{203,204}.

As expected from the visual inspection, hexyl acrylate monomer showed more consistent behaviour in micellar solutions (Figure 6.6). Autocorrelation curves for increasing amounts of monomer, looked almost similar. As for the butyl acrylate monomer, the decay time stayed almost constant up to 80 mM monomer content, however later on with increasing monomer addition, it noticeably shifted to slower decay time. In all cases, the monomodal decay for the samples confirms that between 10-100 mM hexyl acrylate addition to 50 mM TDMAO / 0.5 mM L35 samples, only the micellar L_1 phase exists.

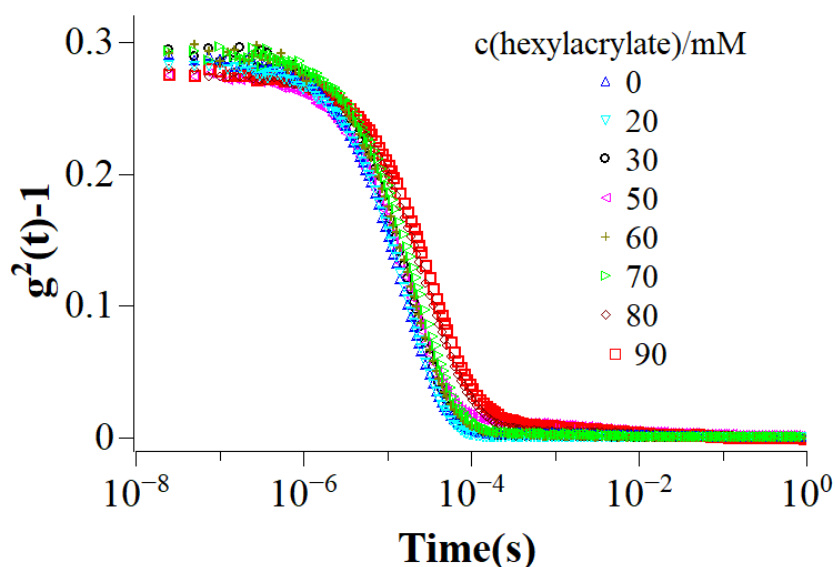


Figure 6.6. Intensity autocorrelation function $g^2(t)$ measured at an angle of 90° of 50 mM TDMAO / 0.5 mM L35 / hexyl acrylate mixtures at 25°C .

The curves were analysed with the cumulant method (see section 3.1.5.1) for correlation times from $(10^{-5}-10^{-1})$ s (Eq. 3.6), and weighted with using the errors, in order to obtain the hydrodynamic radii and polydispersity index. Cumulant analyses of DLS measurements for hexyl acrylate/TDMAO/L35 mixtures demonstrated the size of the micelles varied over the range of 3.1 nm to 4.8 nm along with monomer addition. As 50 mM TDMAO / 0.5 mM L35 forms short rod-like micelles (see chapter 4), we calculated the theoretical length of the micelles assuming the similar geometry from the molecular weights, Mw_{app} , which are deduced by SLS, and end up in a range of 7.3 to 8.1 nm depending on the monomer amount. Results are listed in Table 6.1. Another important point gained from light scattering is the information of polydispersity. As seen in Table 6.1 that unlike styrene monomer (see section 4.1.2), hexyl acrylate/TDMAO/L35 micelles show low PDI values, are being more monodisperse.

Table 6.1. Results from the SLS and DLS measurements of 50 mM TDMAO / 0.5 mM L35 / hexyl acrylate mixtures at 25 °C. Given are the hydrodynamic radius R_h : from the cumulant method, l_{th} : theoretically calculated cylinder length from M_w , polydispersity index PDI, the apparent molecular weight $M_{w,app}$, and aggregation number N_{agg} (with respect to all molecules contained).

Hexyl acrylate amount (mM)	R_h (nm)	l_{th} (nm)	PDI	$M_{w,app}$ (g/mol)	N_{agg} from SLS
0	3.1	7.34	0.12	7.21×10^4	275
20	3.2	7.26	0.13	7.34×10^4	250
30	3.4	7.21	0.14	7.64×10^4	275
50	4.0	7.34	0.12	8.21×10^4	301
60	4.3	7.37	0.17	9.38×10^4	350
70	4.7	7.29	0.16	1.31×10^5	460
80	4.8	8.10	0.18	1.45×10^5	550
90	4.8	8.06	0.15	2.07×10^5	746

6.1.3 Small Angle Neutron Scattering (SANS)

In order to obtain further detailed insight into the structural analyses upon addition of the different acrylate monomers to the micellar TDMAO/L35 solution, SANS experiments were performed for increasing addition of monomer with longer alkyl chain and low water solubility. Since butyl acrylate does not meet the expectation with rather short chain and high water solubility, only dodecyl-, isooctyl- and hexyl acrylate monomers were analysed in terms of small angle neutron scattering experiments. SANS experiments performed at KWS1 (Munich), at 0.6 nm wavelength (with FWHM of 10 %), and three sample-detector distances of 1.2, 7.7, and 19.7 m with corresponding beam collimation lengths of 8.0, 8.0, and 20.0 m respectively.

Neutron scattering curves of TDMAO/L35 mixtures with dodecyl acrylate monomer are presented in [Figure 6.7](#). We described in [section 4.1.3](#), that 50 mM TDMAO / 0.5 mM L35 mixture without monomer presents short-rod like micelles with a radius of 1.9 nm and length ~6 nm.

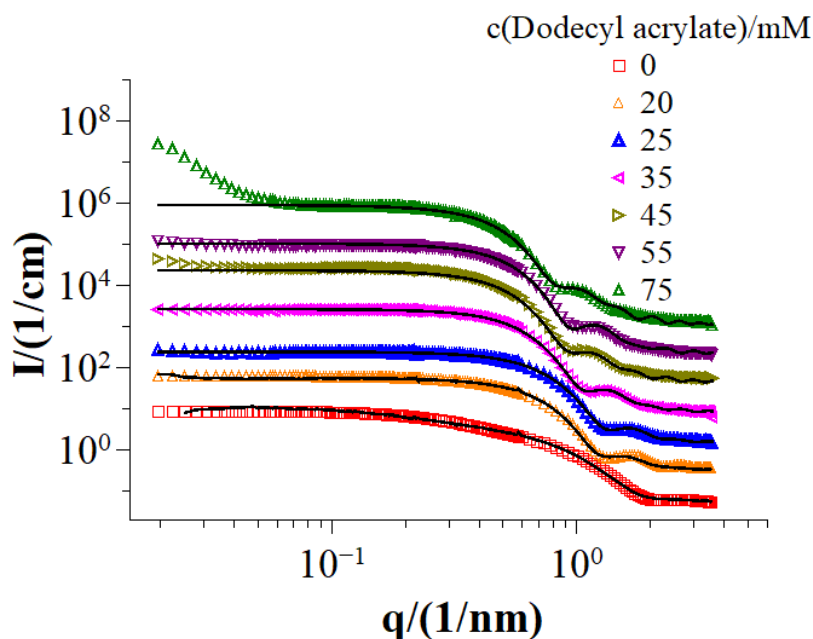


Figure 6.7. SANS curves of 50 mM TDMAO / 0.5 mM L35 / dodecyl acrylate mixtures at 25 °C. (Colored lines: measured data; solid black line: fitted data (for monomer amounts of 0-25 mM: cylindrical model and for 35-75 mM: spherical model was employed)). For clarity, subsequent data sets were multiplied each with a scale factor of 5.

With the addition of dodecyl acrylate, one observes similar short-rod like aggregates with an increase of the size.

Table 6.2. Results from the SANS analysis of 50 mM TDMAO / 0.5 mM L35 / dodecyl acrylate mixtures at 25°C. Given are the Φ : Volume fraction, R: cylinder radius, L: cylinder length, PDI: Polydispersity index of radius distribution, M_w : Molecular weight of aggregates, N_{agg} : aggregation number (with respect to all molecules contained), R_h : Hydrodynamic radius obtained from DLS via cumulant analysis, R_{sphere} : theoretically calculated spherical radius (from R and L obtained by SANS), $R_{swelling}$: theoretically calculated droplet radius from the swelling law assuming all the monomer goes into the micellar core.

c(dodecyl acrylate) / mM	Φ Volume fraction	R (nm)	L (nm)	PDI	M_w (g/mol)	N_{agg} from SANS	R_h (nm)	R_{sphere} (nm)	$R_{swelling}$
0	0.0150	1.97	6.02	0.12	3.91×10^4	143	3.10	2.60	2.76
20	0.0210	2.84	6.40	0.10	7.47×10^4	283	3.83	3.39	3.85
25	0.0227	2.78	6.72	0.12	6.03×10^4	230	4.02	3.40	4.08
35	0.0248	4.11	-	0.13	1.26×10^5	483	4.49	-	4.60
45	0.0284	4.51	-	0.16	1.98×10^5	770	-	-	5.16
55	0.0291	4.45	-	0.15	1.73×10^5	673	-	-	5.45
75	0.0359	5.20	-	0.14	2.49×10^5	983	-	-	6.76

For monomer content up to 35 mM, we applied a cylindrical model with a log-norm distribution of the radius to the scattering curves. Analyses indicated that the radius increased from 1.9 to 2.8 nm and the length from 6 to 6.7 nm upon the addition of monomer and have seen that the polydispersity is around ~ 0.1 , which is lower than the case of styrene (PDI ~ 0.14). SANS curves of the samples with monomer concentration higher than 35 mM were analysed applying a spherical model with log-normal distribution of radius, which can expediently define the formed microemulsion droplets as indicated in the previous part by light scattering and turbidity increase. With the addition of 75 mM monomer, the radius of the droplet reaches 5.2 nm. At the same time for this sample one observes a marked increase of scattering intensity at low q which indicates the presence of emulsion droplets. The results obtained from both models are presented in [Table 6.2](#). For samples with monomer amount of 0-25 mM, we theoretically calculated spherical radius R_{sphere} (by using the parameters R and L obtained from SANS) and compare them with R_h from DLS measurements in the same table. Results indicate that R_h (from DLS) is slightly different from theoretically calculated radius R_{sphere} . It has to be noted that the values of R_h determined from DLS can be expected being different since one obtains the collective diffusion of particles (DLS curves in [Figure 6.5](#) show non-monomodal behaviour) in DLS measurements.

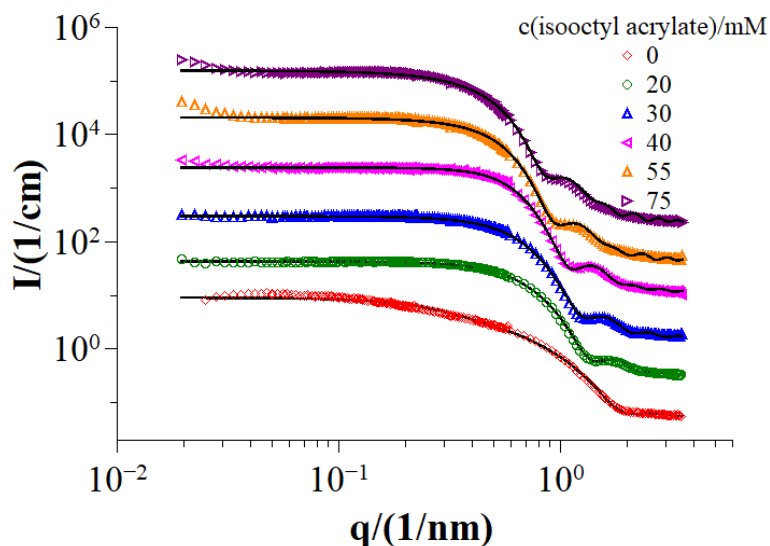


Figure 6.8. SANS curves of 50 mM TDMAO / 0.5 mM L35 / isooctyl acrylate mixtures at 25 °C. (Colored lines: measured data; solid black line: fitted data (for monomer amounts of 0-20 mM, cylindrical model and for 30-75 mM, spherical model was employed)). For clarity subsequent data sets were multiplied each with a scale factor of 5.

Accordingly, assuming that all the added monomer locates into the micellar core, one ends up a theoretical swelling radius, R_{swelling} . We calculated R_{swelling} via $R = 3 * \left[\left(\frac{V_s}{a_h} \right) + \left(\frac{V_m}{a_h} \right) * \left(\frac{n_m}{n_s} \right) \right]$, with a_h is the head group area, V_s and V_m are the volumes of surfactant and monomer, and n_s and n_m are the numbers of surfactant and monomer molecules, respectively. These values are listed together with the sphere radius, R_{sphere} from SANS and hydrodynamic radius R_h from DLS, in [Table 6.2](#). The values for the swelling radius and experimental values are close to each other up to 25 mM monomer content, which indicates almost all of the added monomer goes into the micellar core. For concentrations higher than 35 mM, values started to deviate. The experimental values are lower than the theoretical swelling radius. This means that monomer cannot anymore penetrate into the micelles. The excess of the monomer forms emulsion droplets in the outside medium, which leads the scattering intensity increase at low q regime in [Figure 6.7](#).

Similarly, samples with isooctyl acrylate monomer exhibit SANS curves with same scattering patterns as dodecyl acrylate. SANS curves for lower monomer content up to 30 mM were interpreted with a cylindrical model, revealing an increase of the radius from 1.97 to 2.6 nm. For concentrations higher than 20 mM isooctyl acrylate monomer, a spherical model was applied with log normal distribution of the radius to determine the size parameters of the microemulsion droplets ([Table 6.3](#)). Scattering curves of isooctyl acrylate mixtures ([Figure 6.8](#)) have the same intensity rise at small q for the samples above 40 mM monomer amount, however

Table 6.3. Results from the SANS analysis of 50 mM TDMAO / 0.5 mM L35 / isooctyl acrylate mixtures at 25°C. Given are the Φ : Volume fraction, R: cylinder radius, L: cylinder length, PDI: Polydispersity index of radius distribution, M_w : Molecular weight of aggregates, N_{agg} : aggregation number (with respect to all molecules contained), R_h : Hydrodynamic radius obtained from DLS via cumulant analysis, R_{sphere} : theoretically calculated spherical radius (from R and L obtained by SANS), R_{swelling} : theoretically calculated droplet radius from the swelling law assuming all the monomer goes into the micellar core.

c(isooctyl acrylate) / mM	Φ Volume fraction	R (nm)	L (nm)	PDI	M_w (g/mol)	N_{agg} from SANS	R_h (nm)	R_{sphere} (nm)	R_{swelling}
0	0.0150	1.97	6.02	0.12	3.91×10^4	143	3.10	2.60	2.76
20	0.0195	2.62	6.21	0.11	6.21×10^4	250	3.94	3.17	3.58
30	0.0210	3.43	-	0.15	8.12×10^4	336	3.96	-	3.99
40	0.0235	3.92	-	0.13	1.25×10^5	533	4.22	-	4.38
55	0.0271	4.56	-	0.14	1.95×10^5	861	4.50	-	5.04
75	0.0300	5.02	-	0.14	2.79×10^5	1260	5.51	-	5.74

not as drastic as dodecyl acrylate samples. As expected from the observations of the previous parts, isooctyl acrylate monomer has a better solubility in the micellar aggregates when comparing with dodecyl acrylate monomer therefore we assume it dissolves in the TDMAO/L35 micelles. Accordingly, when we compare the swelling radius R_{swelling} , and experimental radius in [Table 6.3](#), values are rather close and for high monomer concentration the deviation is relatively small. This implies that for isooctyl acrylate case considerable amount of monomer locates into the micelles in comparison to dodecyl acrylate monomer.

Lastly, we investigated the effect and solubilisation of hexyl acrylate monomer in the micellar TDMAO/L35 aggregates. [Figure 6.9](#) shows the scattering intensity of the samples for increasing monomer amount. Similar to the other two acrylate monomers presented so far, hexyl acrylate has the neutron scattering curves with same patterns. The analysis of the curves indicate that micelles were elongated from 1.97 to 2.7 nm ([Table 6.4](#)). For monomer amounts above 30 mM the same model as for the other acrylate monomers, i.e. a spherical model with the log-norm distribution of the radius was applied and pointed out the increase of the droplet size from 3.4 to 4.4 nm. Unlike the other long chain acrylate monomers, hexyl acrylate samples in general did not show a significant intensity increase at small q regime. This implies and confirms that up to 75 mM hexyl acrylate concentration, monomer can easily be dissolved in the micelles and is not present in form of additional bigger aggregates. In the same table, we have included the values of swelling radius R_{swelling} , assuming all the added monomer located into the micelles. By comparison of the results from other acrylate monomers from [Table 6.2](#) and [Table 6.3](#), these

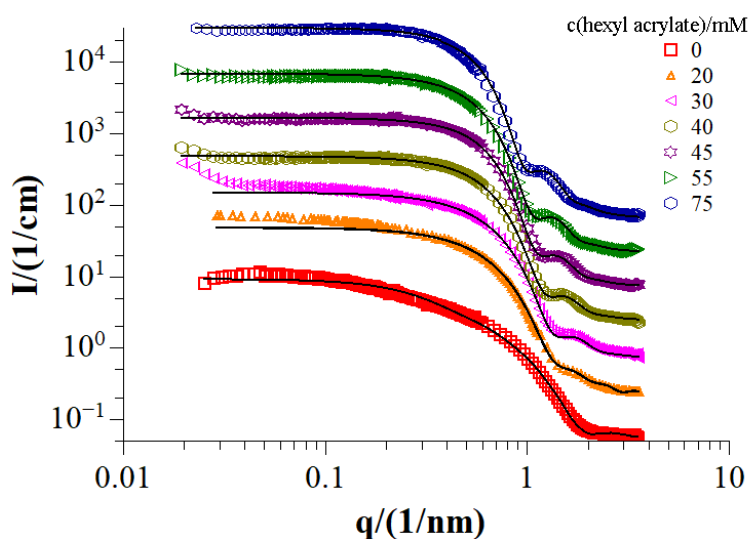


Figure 6.9. SANS curves of 50 mM TDMAO / 0.5 mM L35 / hexyl acrylate mixtures at 25 °C. (Colored lines: measured data; solid black line: fitted data (for monomer amounts of 0-30 mM, cylindrical model and for 40-75 mM, spherical model was employed)). For clarity subsequent data sets were multiplied each with a scale factor of 3.

values are almost identical to the experimental radius. This indicates that, TDMAO/L35 micelles can solubilize high concentrations of hexyl acrylate monomer, and only less amount of monomer remains insoluble into the outside media.

Table 6.4. Results from the SANS analysis of 50 mM TDMAO / 0.5 mM L35 / hexyl acrylate mixtures at 25°C. Given are the Φ : Volume fraction, R: cylinder radius, L: cylinder length, PDI: Polydispersity index of radius distribution, M_w : Molecular weight of aggregates, N_{agg} : aggregation number (with respect to all molecules contained), R_h : Hydrodynamic radius obtained from DLS via cumulant analysis, R_{sphere} : theoretically calculated spherical radius (from R and L obtained by SANS), $R_{swelling}$: theoretically calculated droplet radius from the swelling law assuming all the monomer goes into the micellar core.

c(hexyl acrylate) / mM	Φ Volume fraction	R (nm)	L (nm)	PDI	M_w (g/mol)	N_{agg} from SANS	R_h (nm)	R_{sphere} (nm)	$R_{swelling}$
0	0.015	1.97	6.02	0.12	3.9×10^4	143	3.10	2.60	2.76
20	0.018	2.54	6.79	0.11	7.1×10^4	297	3.20	3.20	3.45
30	0.021	2.69	6.94	0.10	7.7×10^4	340	3.40	3.35	3.83
40	0.022	3.42	-	0.12	8.4×10^4	380	-	-	4.09
45	0.023	3.77	-	0.12	9.6×10^4	450	4.0	-	4.28
55	0.025	3.96	-	0.11	1.2×10^5	590	4.3	-	4.61
75	0.028	4.36	-	0.12	1.7×10^5	852	4.7	-	5.30

Eventually small angle neutron scattering results exhibit a general trend that the structures become bigger with the insertion of hydrophobic acrylate monomers into the micelles. Starting from rod-like micelles, structures evolved to that of spheres, i. e. microemulsion droplets are formed. From the Porod approximation, one can determine the surface to volume ratio of the particle due to the monomer addition via $\lim_{q \rightarrow \infty} I(q)q^4 = 2\pi\Delta SLD^2 \left(\frac{S}{V}\right)$ where S/V is the specific surface of the system^{205–207}. When we plot the $I(q)q^4$ vs q^4 , it reaches a limit for large q values and this value is proportional to the specific surface S/V of the system. Thereby, we can investigate the effect of the additive on the micellar structure in a precise way. The $I(q)q^4$ vs q^4 plots (so called Porod-Debye plots) are presented in [Appendix 9.3.3.3](#). The specific surface S/V was obtained from the intercept of these curves and plotted as function of monomer surfactant ratio in [Figure A18](#). Firstly, we deduced an increase due to the addition of monomer. Subsequently the value remains constant and for high monomer amounts it slightly decreases. The first increase is due to the monomer incorporation into the interfacial area of the micelle

and then monomer goes to the interior of the aggregate, which is the sign of rod to sphere transition.

In particular, hexyl acrylate could incorporate within TDMAO/L35 micelles in wide range of monomer concentration and final structures showed low PDI values and were well-defined. Thus, hexyl acrylate can be used as a model monomer which is appropriate for further polymerization in the vesicle membrane effectively.

6.2 TDMAO/LiPFOS/L35/Acrylate Monomers

In this section we study the effect of acrylate monomers on our vesicle template system. For that mixtures of 50 mM TDMAO / 0.5 mM L35 with increasing amounts of acrylate were mixed with 50 mM LiPFOS solutions (with the molar ratio of 0.55:0.45). In that way monomer loaded vesicles were prepared and characterized with the aim of determining optimized conditions for subsequent polymerization reactions.

6.2.1 Phase Behaviour

TDMAO / L35 / LiPFOS vesicles loaded with acrylate monomers were studied regarding the phase behaviour after mixing the two micellar stock solutions. Vesicle phases are generally slightly turbid, and have a characteristic bluish tinge. The photo seen in [Figure 6.10](#) top, is the dodecyl acrylate samples, which presented the described vesicle appearance up to 40 mM monomer concentration (L_{ves}). With increasing monomer amount, the turbidity increased



Figure 6.10. Sample photograph after 1 hour of preparation of 27.5 mM TDMAO / 0.275 mM L35 / 22.5 mM LiPFOS top: dodecyl acrylate bottom: isooctyl acrylate mixtures at 25 °C.

drastically and later on, the excess of the monomer separated building a second phase to the top of the vial in a few hours (2Φ).

In the same figure bottom picture displays the samples with isooctyl acrylate monomer. Here the vesicle phase (L_{ves}) only appeared for very low monomer concentrations below 20 mM, afterwards samples had very turbid appearance and, as in the dodecyl acrylate case, phase separation occurred in a few hours.



Figure 6.11. Sample photograph after 1 hour of preparation of 27.5 mM TDMAO / 0.275 mM L35 / 22.5 mM LiPFOS hexyl acrylate mixtures at 25 °C.

The formation of hexyl acrylate loaded vesicles can be perfectly seen at [Figure 6.11](#) from the presence of usual vesicle view (L_{ves}) for samples below 25 mM hexyl acrylate concentrations. For the samples with high monomer amount than 25 mM, turbidity increased noticeably, and for even further monomer concentrations, samples turned to white and an excess monomer phase separated in an hour ([Figure 6.12](#)).

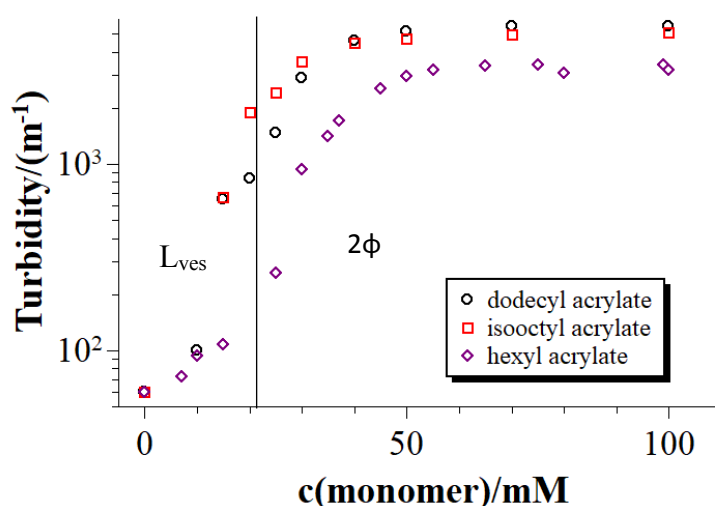


Figure 6.12. Turbidity τ ($\lambda=632$ nm) as a function of monomer concentration in 27.5 mM TDMAO / 0.275 mM L35 / 22.5 mM LiPFOS at 25 °C. Measurements were done after 1 hour from sample preparation.

6.2.2 Light Scattering

First, monomer loaded vesicles were studied with static and dynamic light scattering (SLS, DLS) in terms of gaining structural information of the size and size distribution. Measurements were done in 1 hour after the preparation at 7 angles (30, 45, 60, 75, 90, 105 and 120°) at 25 °C.

Autocorrelation functions of the samples with dodecyl acrylate monomer (Figure 6.13, left) show in general monomodal decay. The fast decay in the autocorrelation functions observed for TDMAO/L35/acrylate monomers was described in section 6.1.2 (Figures 6.4, 6.5 and 6.6) indicating the presence of small micelles. Here the decay time shifted to higher values compared to the micellar case due to the formation of vesicles as expected, which confirms the increase of particle size. In detail, the scattering behaviour obtained by DLS (Figure 6.13 left) reveals that by introducing the dodecyl acrylate monomer, vesicles became smaller. The decay time shifted very slightly to the larger values upon the addition of more monomer. From the phase study of dodecyl acrylate loaded vesicles, we have seen that L_{ves} extends up to 40 mM monomer concentration. Above 40 mM, vesicle system was saturated with monomer. High turbidity of these samples (see Figure 6.10) causes multiple scattering, which does not allow analysing their light scattering behaviour precisely.

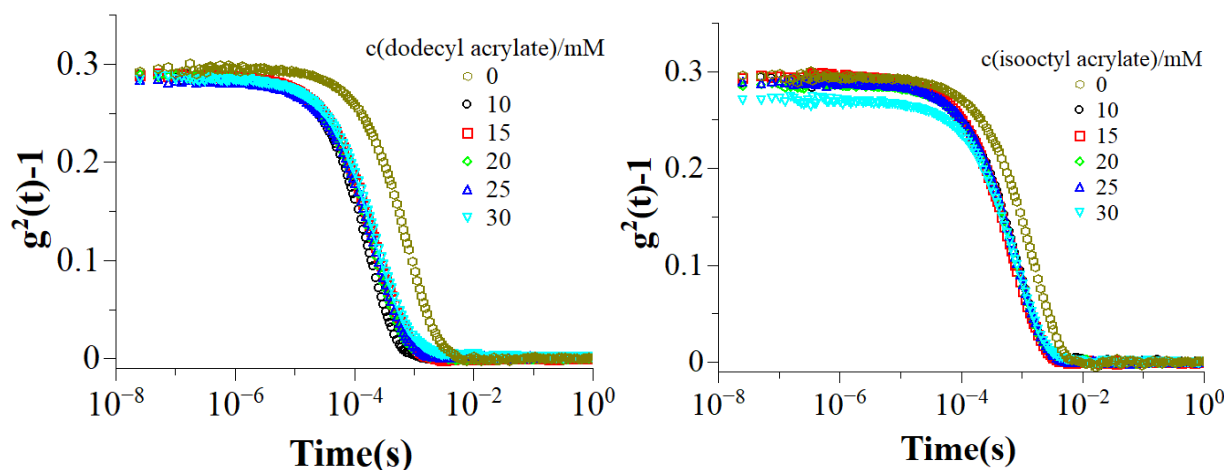


Figure 6.13. Intensity autocorrelation function $g^2(t)$ measured at an angle of 90° of 27.5 mM TDMAO / 0.275 mM L35 / 22.5 mM LiPFOS (left) dodecyl; (right) isoctyl acrylate mixtures at 25 °C.

Similarly, autocorrelation functions of the isoctyl acrylate loaded vesicles (Figure 6.13 right) shifted to smaller decay times along with increasing the monomer amount. However, it is not as drastic as in dodecyl acrylate case, indicating here isoctyl acrylate loaded vesicles are still

slightly bigger. The L_{ves} phase boundary for isooctyl acrylate was ~ 25 mM concentration (see [Figure 6.10](#)).

DLS measurements of hexyl acrylate monomer proved the presence of vesicles as for the other acrylate monomers. Here ([Figure 6.14](#)) the size evolution is evident from the shortening of the decay times. Similar as the longer chain acrylates, the size becomes smaller. Analyses of the scattering curves via cumulant method yielded first a decrease of the vesicle radius from 36 to 20 nm. However, with further increasing monomer amount, the radius shifted slightly to 27 nm. For hexyl acrylate, we determined the vesicle phase L_{ves} below 25mM.

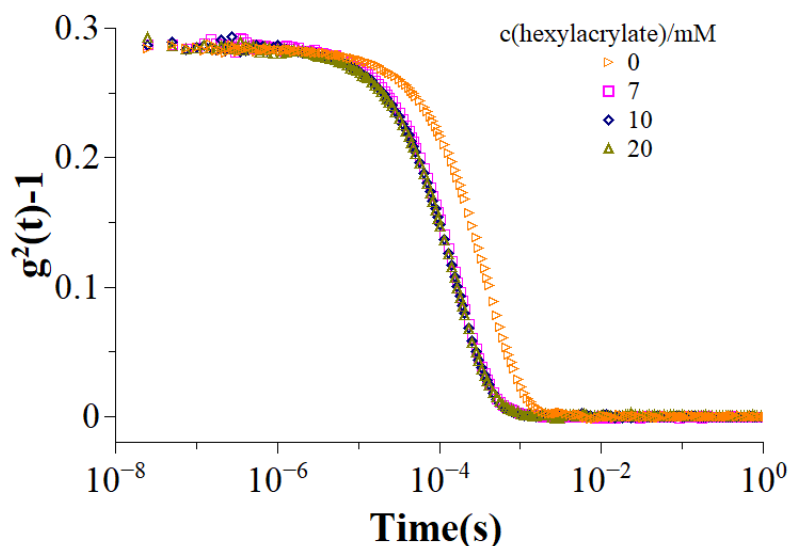


Figure 6.14. Intensity autocorrelation function $g^2(t)$ measured at an angle of 90° of 27.5 mM TDMAO / 0.275 mM L35 / 22.5 mM LiPFOS / hexyl acrylate mixtures at 25 °C.

Static light scattering analyses were performed at the same setup as DLS. From the intensities, we calculated the radius of gyration, R_g and molecular weights of the monomer loaded vesicles. Similar as described in [section 5.1.2](#), the molecular weights were calculated from the [equation 3.8](#) using the refractive index increments (see [Appendix 9.3.3.1](#), [Table A5](#)) in the [equation 3.9](#). In [table 6.5](#), the R_h values determined from DLS analyses are compared with radius of gyration, R_g deduced by SLS. As known from the literature, $R_g \cong R_{ves}$ for vesicles¹²⁶ and the results agreed well for L_{ves} phase (< 25 mM). Furthermore, we theoretically determined vesicle radius $R_{ves,theor}$, from the molecular weight obtained by SLS (considering the bilayer thickness from SANS) and are in good agreement with R_h .

Table 6.5. Results of the SLS and DLS measurements of 27.5 mM TDMAO / 0.275 mM L35 / 22.5 mM LiPFOS / hexyl acrylate mixtures at 25 °C. Shown are the hydrodynamic radius R_h , radius of gyration R_g , polydispersity index PDI (from DLS), apparent molecular weight M_w (from SLS) and N_{agg} aggregation number (with respect to all molecules contained), $R_{ves,theor}$: theoretically calculated vesicle radius from M_w (from SLS) and thickness (from SANS).

c(hexyl acrylate) / mM	R_h (nm)	R_g (nm)	PDI	$M_{w,app}$ (g/mol)	N_{agg} from SLS	$R_{ves,theor}$ (nm)
0	36.6	38.6	0.09	1.73×10^7	39300	32.5
7	20.5	21.8	0.13	9.9×10^6	25700	24.4
10	23.7	18.3	0.14	1.2×10^7	33500	27.3
20	26.6	21.1	0.18	1.4×10^7	37500	29.2

6.2.3 Small Angle Neutron Scattering (SANS)

So far, the effect of acrylate monomers on the vesicle formation and information about structural changes during the monomer loading were obtained from turbidity and light scattering measurements. Further insight to the structural progression was gained with SANS measurements for different acrylate monomers of increasing amounts. SANS experiments were performed at KWS1 (Munich), at a wavelength of 0.6 nm, the spread of wavelength was given by a FWHM (full width at half maximum) of 10 %, and three sample-detector distances of 1.2,

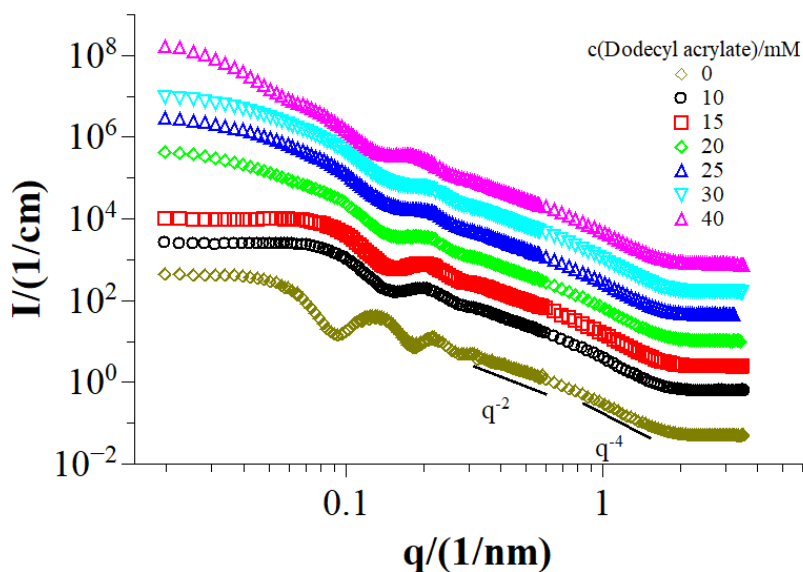


Figure 6.15. SANS curves of 27.5 mM TDMAO / 0.275 mM L35 / 22.5 mM LiPFOS / dodecyl acrylate mixtures at 25 °C. (Colored lines: measured data; solid black line: fitted data with spherical shell model). For clarity subsequent data sets were multiplied each with a scale factor of 3.

7.7, and 19.7 m with corresponding beam collimation lengths of 8.0, 8.0, and 20.0 m respectively.

Previous studies of our template vesicle system consisted from 27.5 mM TDMAO / 0.275 mM L35 / 22.5 mM LiPFOS demonstrated a vesicle radius of 36 nm with PDI of 0.055¹¹⁴. In a similar manner, we investigated the model system with SANS and obtained 36.3 nm for the vesicle radius and 0.06 for polydispersity index, which are very close to the literature values (see [Table 6.8](#)).

First, we studied the effect of dodecyl acrylate monomer on the vesicle system with small angle neutron scattering. [Figure 6.15](#) depicts the SANS measurements of monomer loaded vesicles as a function of dodecyl acrylate concentration at 25 °C. From the curves, one observes an explicit form factor bump around $q = 0.17 \text{ nm}^{-1}$, which corresponds to a mean vesicle radius of ~18-19 nm. The linear decay at intermediate q range ($0.3\text{-}0.8 \text{ nm}^{-1}$) revealed a slope of q^{-2} and at high q ($1.15\text{-}1.7 \text{ nm}^{-1}$) one of q^{-4} , together confirming the presence of bilayers. Additionally, for the samples above 20 mM, intensity increased noticeably at low q regime pointing out the presence of bigger particle along with the vesicles in the system. Another implication from the curves is the less pronounced form factor peaks at high monomer concentrations, which is related with the size distribution of the formed aggregates.

Table 6.6. Results from the SANS analysis of 27.5 mM TDMAO / 0.275 mM L35 / 22.5 mM LiPFOS / dodecyl acrylate mixtures at 25°C. Given are Φ : Volume fraction, vesicle radius R_{ves} ($R_{\text{ves}}=R+D$), polydispersity index PDI, bilayer thickness D from spherical shell model, bilayer thickness from Kratky-Porod analyses (see section 3.1.6.1 and Appendix 9.3.1), D_{swelling} : theoretically calculated bilayer thickness from the swelling law assuming all the monomer incorporated within the bilayer, molecular weight M_w , and N_{agg} aggregation number (with respect to all molecules contained).

c(dodecyl acrylate) / mM	Φ Volume fraction	R_{ves} (nm)	PDI	D/nm Spherical shell	D/nm Kratky Porod	D_{swelling} /nm	M_w (g/mol)	N_{agg} from SANS
0	0.0145	36.3	0.06	2.68	2.72	-	1.83×10^7	48300
10	0.0176	20.9	0.21	2.89	2.91	3.19	7.35×10^6	20900
15	0.0186	21.0	0.21	2.88	2.90	3.36	6.97×10^6	20100
20	0.0197	21.3	0.22	2.89	2.91	3.54	1.52×10^7	44800
25	0.0217	21.5	0.24	2.94	3.03	3.88	1.93×10^7	61100
30	0.0221	21.9	0.24	2.93	3.06	3.94	2.16×10^7	65800
40	0.0258	23.4	0.21	2.91	3.10	4.56	2.62×10^7	79300

The scattering curves were analyzed by using a spherical shell model applying a log-normal distribution of radius. Our investigations resulted that the vesicle radius decreased from 36 nm to 20 nm when we introduced the dodecyl acrylate monomer to the system. For 40 mM the radius increased slightly to 22-23 nm with the addition of more monomer, however different size of particles started to show up and therefore the polydispersity index also increased slightly. In general, the PDI is much higher for the monomer-loaded vesicles than for the pure one.

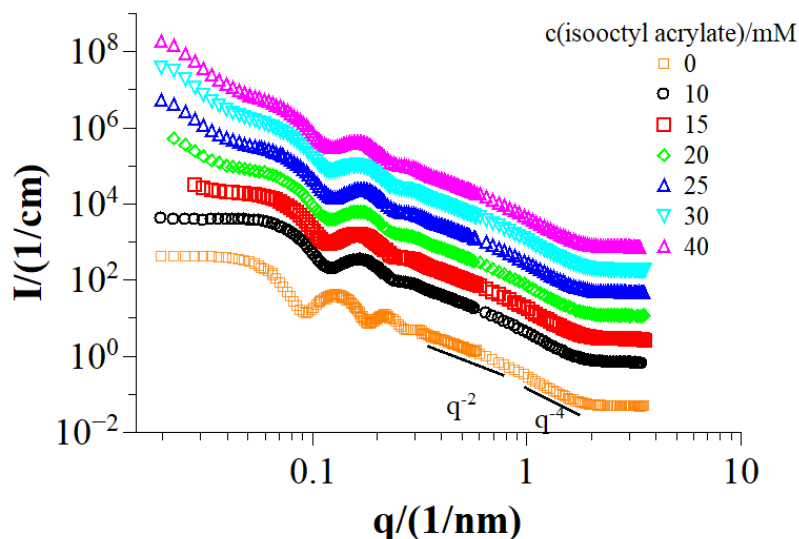


Figure 6.16. SANS curves of 27.5 mM TDMAO / 0.275 mM L35 / 22.5 mM LiPFOS / isooctyl acrylate mixtures at 25 °C. (Colored lines: measured data; solid black line: fitted data with spherical shell model). For clarity subsequent data sets were multiplied each with a scale factor of 3.

The model vesicle system has a bilayer thickness of 2.7 nm and our model yielded a thickness of 2.9 nm irrespective of the monomer content (Table 6.6). For a better understanding, we determined the bilayer swelling assuming all of the monomer is incorporated within the bilayer and the interfacial area remains unchanged. Thereby, the swelling bilayer thickness, D_{swelling} , was theoretically calculated and included in the same table. For low monomer concentrations theoretical values are rather close to the experimentally deduced ones. Especially for high monomer concentrations, the discrepancy is high. In general, this deviation can be explained with the loading capacity of the bilayer. After some time vesicle bilayer is saturated with the monomer thereof, the excess of the monomer starts forming bigger droplets in the outside media. This results in an increase of intensity at low q regime.

On the other hand, our assumption above is based on the unchanged interfacial area, which considers all the monomer are located in the middle part of the bilayer. In such a case, bilayer thickness increases drastically while the overall size does not change too much. On the contrary,

when monomer is distributed homogenously within the bilayer, the thickness stays constant but the overall size increases²⁰⁸. With the help of Porod-Debye plots (described in [section 6.1.3](#)) we determined the specific surface S/V of these samples ([Figure 6.18b](#)). The first increase of S/V up to 20 mM concentration reveals that monomer is located close to the head groups of surfactant pairs. Then along with the monomer addition it slightly shifts to the hydrophobic part of the bilayer which leads to the decrease of surface volume ratio, S/V .

Isooctyl acrylate showed similar scattering properties ([Figure 6.16](#)) in vesicle solutions as dodecyl acrylate. The slope of q^{-2} (at q range of 0.35-0.80 nm^{-1}) and q^{-4} (at high q range of 1.20-1.6 nm^{-1}) confirmed the vesicle formation was successful at the same time with the monomer insertion. Scattering curves were analyzed with the spherical shell model, similar as dodecyl acrylate. In this case, we obtained the vesicle radius of 23 nm. Upon the addition of monomer, the vesicle radius did not show a significant increase. On the other hand, we observed the expansion of the bilayer thickness from 2.7 to 2.95 nm. Similar as above, D_{swelling} was calculated and compared with the experimental thickness values in [Table 6.7](#). Differently, the thickness of the isooctyl acrylate vesicles are increasing in a systematic way, while for dodecyl acrylate it deviates depending on the monomer addition.

Table 6.7. Results from the SANS analysis of 27.5 mM TDMAO / 0.275 mM L35 / 22.5 mM LiPFOS / isooctyl acrylate mixtures at 25°C. Given are Φ : Volume fraction, vesicle radius R_{ves} ($R_{\text{ves}}=R+D$), polydispersity index PDI, bilayer thickness D from spherical shell model, bilayer thickness from Kratky- Porod analyses (see section 3.1.6.1 and Appendix 9.3.2), D_{swelling} : theoretically calculated bilayer thickness from the swelling law assuming all the monomer incorporated within the bilayer, molecular weight M_w , and N_{agg} aggregation number (with respect to all molecules contained).

c(isooctyl acrylate) / mM	Φ Volume fraction	R_{ves} (nm)	PDI	D/nm Spherical shell	D/nm Kratky Porod	D_{swelling} /nm	M_w (g/mol)	N_{agg} from SANS
0	0.0145	36.3	0.06	2.68	2.72	-	1.83×10^7	48300
10	0.0168	26.2	0.16	2.79	2.84	3.10	1.25×10^7	36400
15	0.0176	26.6	0.16	2.82	2.89	3.24	1.41×10^7	44300
20	0.0190	26.7	0.15	2.83	2.90	3.48	1.48×10^7	44400
25	0.0199	26.2	0.17	2.95	3.09	3.64	1.37×10^7	43250
30	0.0210	26.8	0.18	2.93	3.05	3.79	1.54×10^7	52800
40	0.0226	26.9	0.18	2.95	3.08	4.11	1.70×10^7	55900

The specific surface area (S/V) of isooctyl acrylate loaded vesicles, presented in the same plot with other monomers in [Figure 6.18b](#), shows same trend as dodecyl acrylate monomer. Surface volume ratio (S/V) increases with increasing monomer amount until 20 mM concentration. The decrease above this point indicates the surface area of bilayer does not change in parallel with the volume growth. Namely, monomer does not localize anymore into the interfacial area of the bilayer and large amount of it moves in the interior part of the membrane.

In the last step, we examined the hexyl acrylate behavior in the vesicle formation with SANS experiments. Scattering curves ([Figure 6.17](#)) were analyzed by using the same model above as spherical shell with log-normal distribution of the radius. The individual fit parameters from the model are presented in [Table 6.8](#). Similar to other acrylate monomers, we observed a decrease in vesicle radius to from 36 nm to 23-24 nm when the monomer was introduced. We had observed the hydrodynamic radius of 20-26 nm from light scattering measurements for these samples, which confirms that both results are identical. Interestingly, in contrast to other acrylate monomers, here we obtained low polydispersity values of ~ 0.1 for hexyl acrylate loaded vesicles. The bilayer thickness varied in the range of 2.7 to 2.9 systematically within the addition of monomer. For further comparison, the thickness gained from plotting $\ln(q^2 I(q))$ vs q^2 yielded the values around 2.80 nm (see [appendix 9.3.3.2](#)).

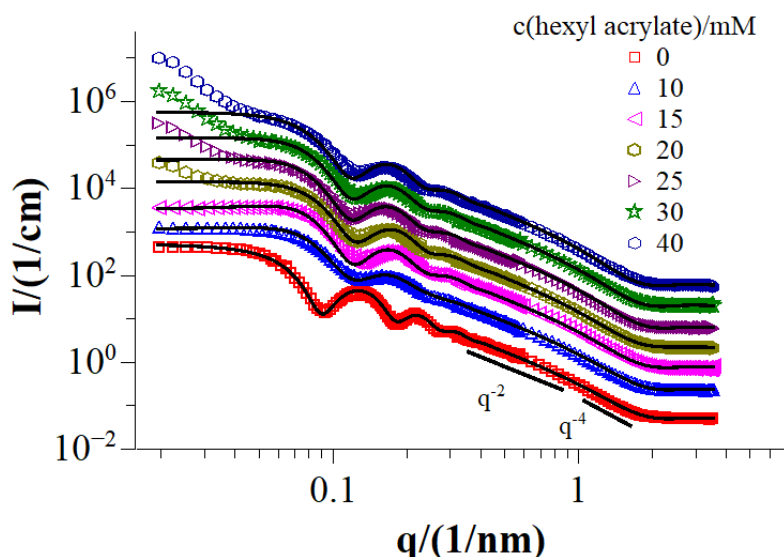


Figure 6.17. SANS curves of 27.5 mM TDMAO / 0.275 mM L35 / 22.5 mM LiPFOS / hexyl acrylate mixtures at 25 °C. (Colored lines: measured data; solid black line: fitted data with spherical shell model). For clarity subsequent data sets were multiplied each with a scale factor of 3.

Table 6.8. Results from the SANS analysis of 27.5 mM TDMAO / 0.275 mM L35 / 22.5 mM LiPFOS / hexyl acrylate mixtures at 25°C. Given are Φ : Volume fraction, vesicle radius R_{ves} ($R_{ves}=R+D$), polydispersity index PDI, bilayer thickness D from spherical shell model, bilayer thickness from Kratky- Porod analyses (see section 3.1.6.1 and Appendix 9.3.3.2), $D_{swelling}$: theoretically calculated bilayer thickness from the swelling law assuming all the monomer incorporated within the bilayer, molecular weight M_w , and N_{agg} aggregation number (with respect to all molecules contained).

c(hexyl acrylate) / mM	Φ Volume fraction	R_{ves} (nm)	PDI	D/nm Spherical shell	D/nm Kratky Porod	$D_{swelling}$ /nm	M_w (g/mol)	N_{agg} from SANS
0	0.0145	36.3	0.06	2.68	2.72	-	1.83×10^7	48300
10	0.0165	24.8	0.10	2.69	2.52	3.00	1.03×10^7	34000
15	0.0175	25.6	0.11	2.75	2.66	3.18	1.05×10^7	35200
20	0.0183	25.9	0.12	2.77	2.70	3.30	1.08×10^7	35700
25	0.0190	26.1	0.16	2.81	2.83	3.41	1.09×10^7	36800
30	0.0198	26.3	0.17	2.87	2.91	3.55	1.23×10^7	44000
40	0.0214	26.5	0.18	2.92	2.95	3.82	1.34×10^7	47000

The reduction of the initial size along with the monomer addition can be explained with the rearrangement of surfactants to form a new and more favored equilibrium structure of small vesicles. On the other hand, swelling of the vesicles is also possible and was shown before with CTAB/SDBS vesicles, which grew when styrene monomer was added¹⁰⁶. Similarly in our study, acrylate laden TDMAO/L35/LiPFOS vesicles grew along with increasing the monomer concentration. We calculated the increase of the size regarding to the bilayer thickness assuming the added volume of the monomer located into the hydrophobic bilayer. The mass of a vesicle with bilayer thickness of $t + 2b$ (t is the thickness of the alkyl chain and b is the thickness of the head group region) was calculated via: $m_v = \frac{4\pi M_w (R_{ves}^2 + (R_{ves} - t - 2b)^2)}{a_h N_A}$ where M_w is the average molecular weight of the surfactants: $M_w = \chi_{TDMAO} M_{TDMAO} + \chi_{L35} M_{L35} + \chi_{LiPFOS} M_{LiPFOS}$; χ_i is the mole fraction and M_i is the molecular weight, a_h is the average area per head group for the surfactant mixture, R_{ves} is the outer vesicle radius, and N_A is the Avogadro's number. The volume of the hydrophobic chain region is $V_0 = \frac{4\pi}{3} [(R_{ves} - b)^3 - (R_{ves} - t - b)^3]$. Upon the addition of monomer, we assume the volume of the bilayer changes as: $dV = f m_v / \rho$, here ρ is the monomer density and f is the weight fraction of monomer to surfactant in each sample. When the monomer only locates in the hydrophobic chain region, the thickness of this region

should then increase by a factor of $\sim\left(1 + \frac{dV}{V_0}\right)^{1/3}$. Accordingly, then the radius of the monomer loaded vesicle (theoretically calculated swelling radius) can be written as: $R = (R_{ves} - b)\left(1 + \frac{dV}{V_0}\right)^{1/3} + b$. The thickness t was taken from the neat TDMAO/L35/LiPFOS vesicles. For a_h we assumed a value of 0.5 nm^2 and for b 0.3 nm^2 .

In [Figure 6.18a](#), outer vesicle radii R_{ves} are presented as a function of monomer concentration which were obtained from the spherical shell model applied to SANS curves and from our calculation assuming all the monomer accommodates into the bilayer thereby the swelling radius of the structures. Vesicle with 10 mM monomer content was taken as reference, and then swelling radii were calculated for other samples. For 15 mM monomer, both values are in good agreement. However, later the difference between both models suggest that monomer does not only incorporate into hydrophilic part of the bilayer but also swells into the interior part, thereby we end up an almost stagnated bilayer thickness. This assumption is corroborated with determining the specific surface area change of the system. [Figure 6.18b](#) expresses the surface volume ratio S/V of the system, which increases systematically as a function of the monomer amount. As distinct from the other acrylate monomers, it rises gently until 30 mM hexyl acrylate amount. This implies here the monomer is distributed more homogenously in the interfacial and

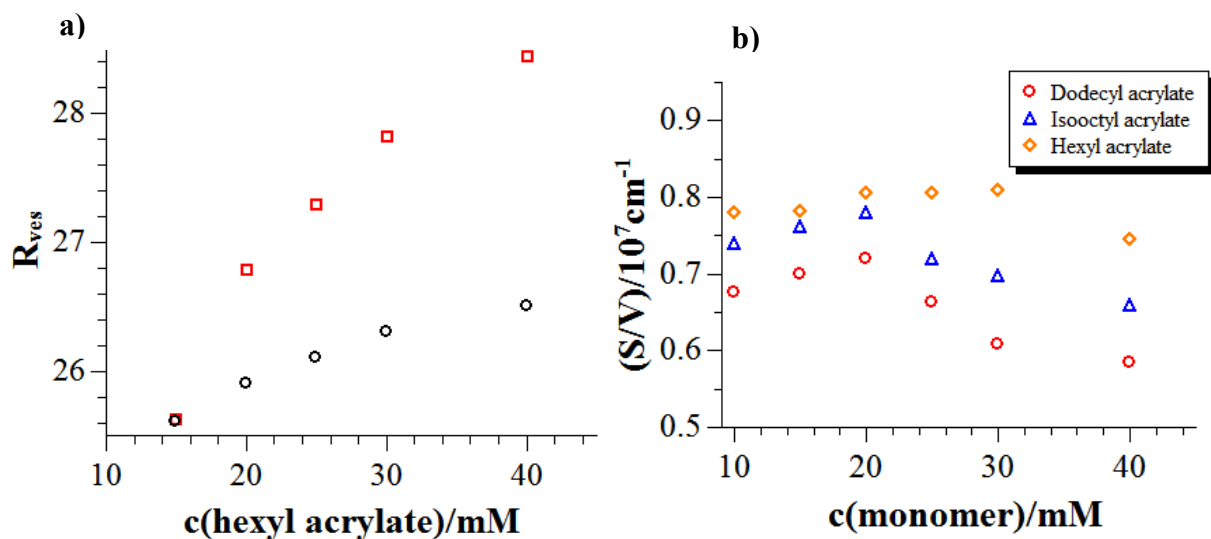


Figure 6.18. **a)** Outer vesicle radius R_{ves} (of 27.5 mM TDMAO / 0.275 mM L35 / 22.5 mM LiPFOS / hexyl acrylate vesicles black circle: obtained from SANS experiments, red square: theoretically calculated swelling radius R by assuming all monomer was taken into the bilayer. **b)** The specific surface area (S/V) as the function of monomer concentration for dodecyl-, isooctyl-, and hexyl acrylate.

interior areas of the bilayer. However, above 30 mM it tends to stay in the interior part, consequently does not change the surface area S , but enhances the volume V .

As our main focus is to stabilize the model vesicle system by polymerization, the results of hexyl acrylate case comply with the idea of retaining the well-defined vesicle system. When we compare all acrylate cases, the progression of the system is more stable and allows working in a wide concentration range of monomer. Since the model system consisted of small, unilamellar well-defined vesicles, the results yielded from the hexyl acrylate case fitted ideally.

6.3 Polymerization of the TDMAO/LiPFOS/L35/Hexyl Acrylate System

These studies were done for gaining an insight into the detailed control of polymer nanocapsule formation and for optimizing the conditions for stabilization of the vesicles by polymerization, as it is relevant for potential future application such as their use as delivery vehicles.

From the studied systems above, the hexyl acrylate system was chosen for further polymerization. First, its phase behavior is more promising in comparison to the other acrylates that allows to study in a wide concentration range. Secondly, its chain length is moderate enough to fit in the few nanometer wide hydrophobic bilayer. Besides that, its loading into the vesicles does not have significant change on the formation of well-defined vesicles. One can afterwards still effectively retain small, unilamellar highly monodisperse monomer loaded vesicles than other acrylate monomers. Therefore, it is appropriate for further polymerization in the vesicle membrane. Initially, the vesicle system was varied over 10 to 30 mM monomer concentrations and the samples within this monomer range polymerized. Then for monomer concentrations of 15, 20 and 25 mM three molar cross-linker ratios of 0.1, 0.2 and 0.4 were employed, with respect to the total monomer concentrations. Samples were polymerized via UV-initiated polymerization for 18 hours at 15 °C and the reaction was ended by removing the nitrogen atmosphere and having oxygen quench the reaction (for details see [section 3.2.2](#)).

6.3.1 Phase Behaviour

In this study polymerization was done as an effective way for fixation of the vesicle system. Thereof, we expect not to see any difference between the unpolymerized and polymerized samples in terms of visual appearance, size and structural progression. [Figure 6.19](#) displays the polymerized vesicle solutions without cross-linker. Sample photos were taken after 1 hour from the end of the reaction. Comparing with the unpolymerized vesicles ([Figure 6.11](#)), polymerized samples retained the typical vesicle tinge consisting of bluish turbid appearance. Samples showed no precipitation, separation or any other phase alteration and stayed stable for 1 month. Later than 1 month, presumably some polymer chains settled down and formed a very

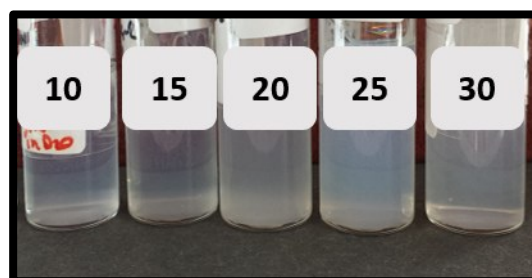


Figure 6.19. Photos of polymerized 27.5 mM TDMAO / 0.275 mM L35 / 22.5 mM LiPFOS / hexyl acrylate mixtures taken 1 hour after the end of polymerization. (Labels: monomer concentrations in mM).

small smoky cloudy phase which can be easily dispersed into the solution by simply shaking. The formed polymer chains are not bound to a certain vesicle and will over a longer time simply associate.

Additionally, we tested the cross-linked polymerized samples of hexyl acrylate. [Figure 6.20](#) displays the sample photos after 1 hour from the end of polymerization reactions. These samples were varied with respect to the cross-linker/monomer ratios. For instance, for 15 mM total monomer concentration the cross-linker (1, 6-hexanediol diacrylate) molar ratio was varied over 0.1, 0.2 and 0.4 with respect to the hexyl acrylate amount but keeping the total concentration constant. As seen from the sample photo, they all look identical to the unpolymerized vesicle solution. The only difference encountered was for the highest cross-linker content with 0.4 molar ratio for 20 and 25 mM samples. These cross-linked polymerized samples were more turbid than others. However, in general all cross-linked polymerized samples were homogenous, uniform and none of them showed phase separation or precipitation. Unlike the uncross-linked polymerized vesicles described above they did not show the smoky polymer phase in the course of time. This can be explained such that by cross-linking one can expect to just have one cross-linked polymer molecule in the vesicle shell, which then cannot diffuse out of it.

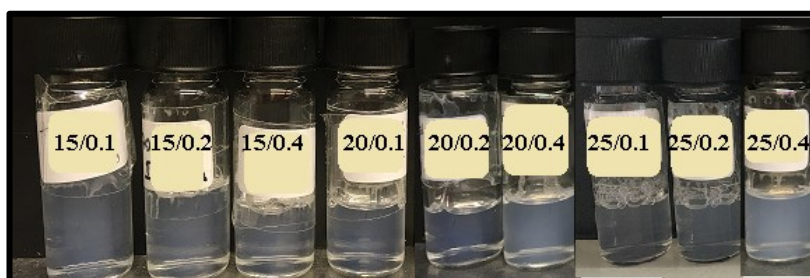


Figure 6.20. Sample photo of cross-linked polymerized 27.5 mM TDMAO / 0.275 mM L35 / 22.5 mM LiPFOS / hexyl acrylate / 1, 6-hexanediol diacrylate mixtures after 1 hour from the end of polymerization. (Labels: total monomer concentration in mM/cross-linking ratio).

6.3.2 Nuclear Magnetic Resonance (NMR)

Nuclear magnetic resonance (NMR) can provide crucial information and ^1H NMR experiments were done before and after the polymerization. For NMR the preparation of the monomer loaded vesicles and subsequent polymerization was done in deuterium oxide (D_2O), and the

measurements were performed with a Bruker Avance II 400 spectrometer operating at 400 MHz was used to record the spectra and tetramethylsilane (TMS) was used as reference agent.

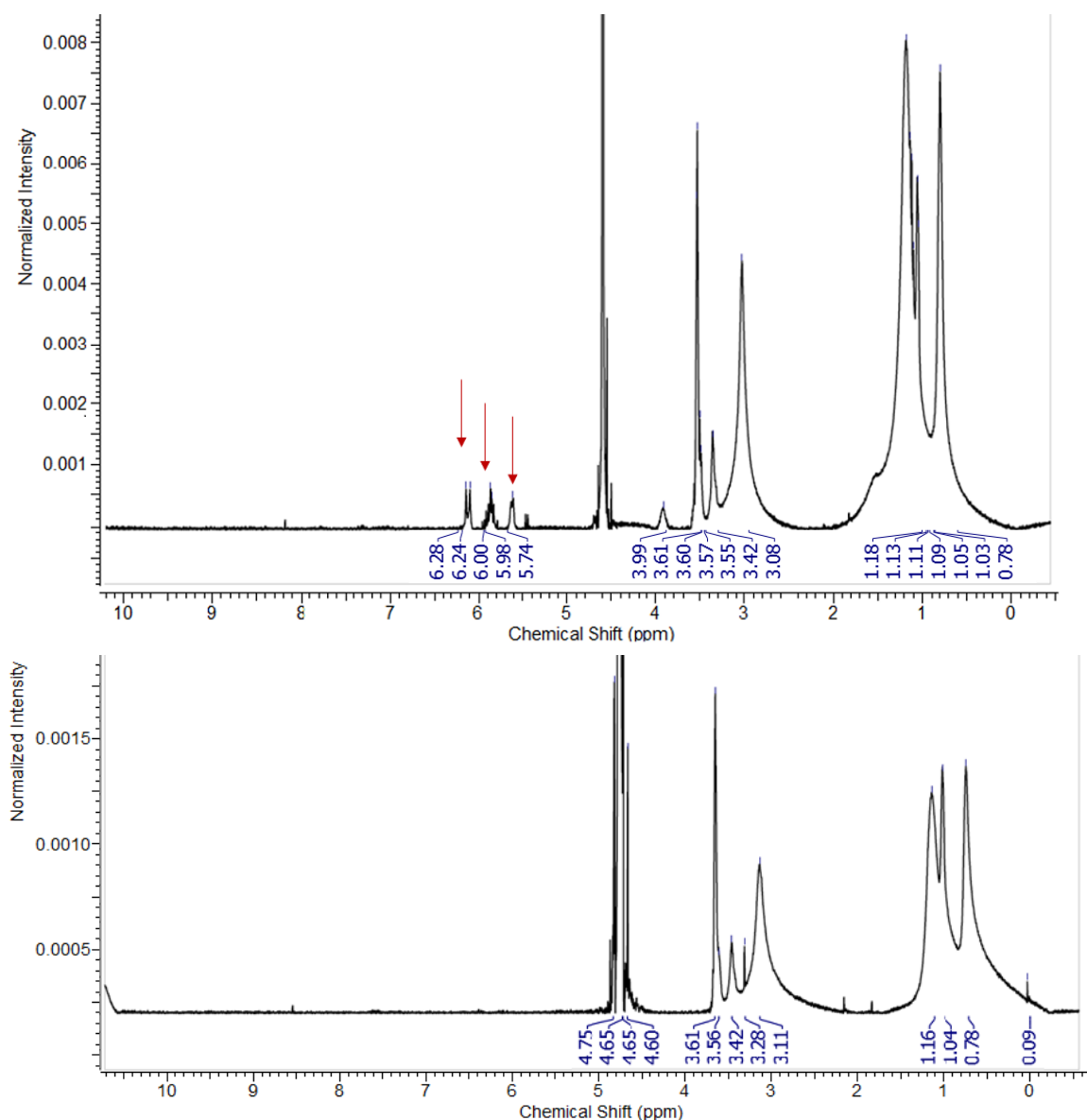


Figure 6.21. ¹H-NMR spectra of vesicles before (top) and after (bottom) cross-linking polymerization at 25 °C. The molar ratio of 1, 6-hexanediol diacrylate to hexyl acrylate was 0.1 with a total concentration of monomer of 35 mM. The signals of the vinylic protons are marked with red arrows.

Polymerization confirmed the complete conversion of monomer via the vanishing proton signals of the vinyl bond on acrylate molecule. Figure 6.21 shows the ¹H NMR spectra for hexyl acrylate loaded vesicles (consisted of 27.5 mM TDMAO / 0.275 mM L35 / 0.025 mM LiPFOS) before (top) and after polymerization (bottom). Disappearance of the 3 signals at δ 5.8, 6 and 6.3 (C-H vinyl groups) implies the full conversion from monomer to polyhexyl acrylate. After

polymerization the peak intensity of the signals at δ 3.6, 3.1, and 0.78 decreased by a ratio of 0.4, and at δ 3.4, and 1.1 decreased by half. The restricted motion of polymer protons is the main reason of this decrease or having less pronounced peaks.

6.3.3 Light Scattering

From the visual inspection of polymerized samples in the previous section it was assumed that the vesicle structures were retained successfully after the polymerization reaction. For more quantitative information, we investigated the polymerized samples by light scattering method in order to obtain realistic detailed structural information and for confirming the assumptions. In [Figure 6.22](#) the autocorrelation functions of polymerized samples are presented. The scattering curves on the left side of the figure belong to the polymer samples without cross-linker. The hydrodynamic radii and polydispersity values of these polymerized vesicles were obtained by fitting the scattering curves with cumulant method and parameters from the model are listed in [Table 6.9](#).

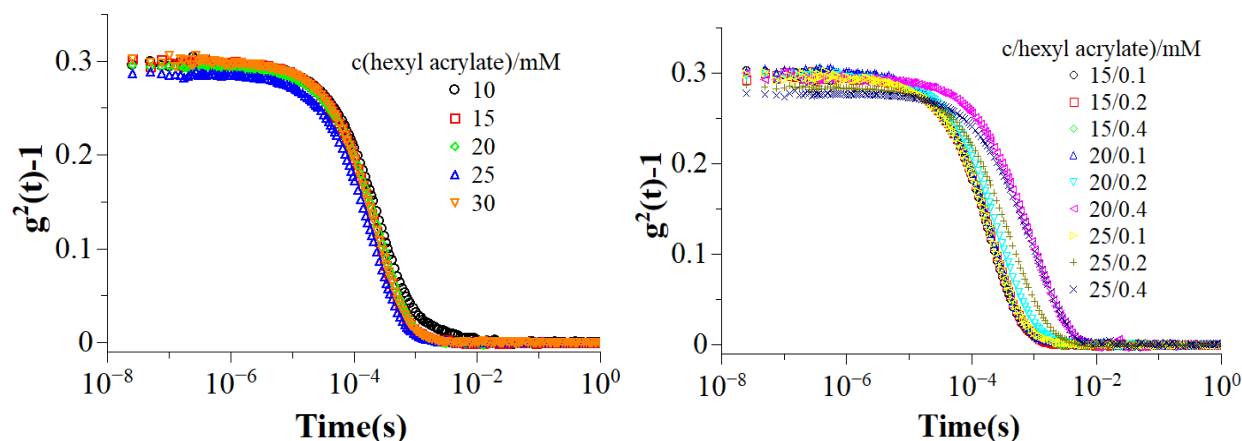


Figure 6.22. Intensity autocorrelation function $g^2(t)$ measured at an angle of 90° of left) polymerized vesicles of 27.5 mM TDMAO / 0.275 mM L35 / 22.5 mM LiPFOS / hexyl acrylate; right) cross-linked polymerized vesicles of 27.5 mM TDMAO / 0.275 mM L35 / 22.5 mM LiPFOS / hexyl acrylate / 1, 6-hexanediol diacrylate mixtures at 25 °C.

When comparing the vesicle size before and after the polymerization, light scattering yielded a small but noticeable increase in vesicle radii along with the polymerization. While before vesicles had a radius of ~23 nm, after the polymerization this value increased to ~27-29 nm depending on the monomer concentration. At the same time, polymerized vesicles showed a somewhat higher polydispersity and the PDI increased from 0.1 to 0.16-0.2, increasing with the monomer amount.

Table 6.9. Results from the SLS and DLS measurements of polymerized samples of 27.5 mM TDMAO / 0.275 mM L35 / 22.5 mM LiPFOS / hexyl acrylate mixtures at 25 °C. Given are the hydrodynamic radius R_h , radius of gyration R_g , polydispersity index PDI (from DLS), apparent molecular weight M_w (from SLS) and N_{agg} aggregation number (with respect to all molecules contained).

c(hexyl acrylate) / mM	R_h (nm)	R_g (nm)	PDI	M_{wapp} (g/mol)
10	28.7	22.8	0.16	1.7×10^7
15	27.9	28.0	0.19	1.5×10^7
20	29.7	29.2	0.21	2.4×10^7
25	25.4	24.9	0.20	1.1×10^7
30	26.2	30.5	0.22	1.4×10^7

On the right side of [Figure 6.22](#), we present the autocorrelation curves of cross-linked polymerized samples of hexyl acrylate loaded vesicles. Mostly these curves have similar scattering properties to the curves on the left side. Only for the samples containing 20 and 25 mM hexyl acrylate and having a 0.4 molar ratio of 1, 6-hexanediol diacrylate curves shifted to the right, meaning the formation of bigger particles with slower decay times. This result is in good agreement with the visual appearance of the samples seen in [Figure 6.20](#).

Cumulant analysis of the scattering curves of cross-linked polymerized samples confirmed this increase in size with yielding radii of 30.2 and 33.7, respectively ([Table 6.10](#)). In [Table 6.10](#) one observes a very good agreement between the size changes observed via R_h and R_g and the M_{wapp} seen in SLS. Unlike the uncross-linked polymerized samples above, cross-linked polymerized vesicles have smaller sizes for low cross-linking ratios and low polydispersity

index. This change can be explained by the effect of cross-linking. Cross-linked polymer chains entrapped in the vesicle membrane, basically tighten the particle and make them more robust.

Table **6.10**. Results from the SLS and DLS measurements of cross-linked polymerized samples of 27.5 mM TDMAO / 0.275 mM L35 / 22.5 mM LiPFOS / hexyl acrylate / 1, 6-hexanediol diacrylate mixtures at 25 °C. Given are the hydrodynamic radius R_h , radius of gyration R_g , polydispersity index PDI (from DLS), apparent molecular weight M_w (from SLS) and N_{agg} aggregation number (with respect to all molecules contained).

c(hexyl acrylate) / mM	R_h (nm)	R_g (nm)	PDI	M_{wapp} (g/mol)
15/0.1	22.6	23.2	0.16	1.5×10^7
15/0.2	23.5	28.0	0.18	1.6×10^7
15/0.4	23.9	24.5	0.20	1.8×10^7
20/0.1	28.1	28.0	0.23	2.2×10^7
20/0.2	28.4	28.5	0.20	2.2×10^7
20/0.4	30.2	31.5	0.21	2.6×10^7
25/0.1	24.0	26.7	0.22	1.9×10^7
25/0.2	27.3	26.2	0.22	2.1×10^7
25/0.4	33.7	29.7	0.26	3.4×10^7

6.3.4 Small Angle Neutron Scattering (SANS)

Figure 6.23 shows the small angle neutron scattering intensity as a function of the magnitude of the scattering vector q of polymerized vesicles with 50 mM total surfactant concentration and for increasing amount of monomer. Measurements were performed at KWS1 (Munich) with the same setup and configuration as unpolymerized vesicles described in section 6.2.3 for a direct comparison. From the scattering curves, initially one can see that they are identical to the scattering curves of unpolymerized samples represented in Figure 6.17 (for comparison see Appendix 9.3.3.4). The form factor minima are around $\sim 0.1 \text{ nm}^{-1}$ and the linear slope of q^{-2} at intermediate q range and q^{-4} at high q range are visible from the scattering curves.

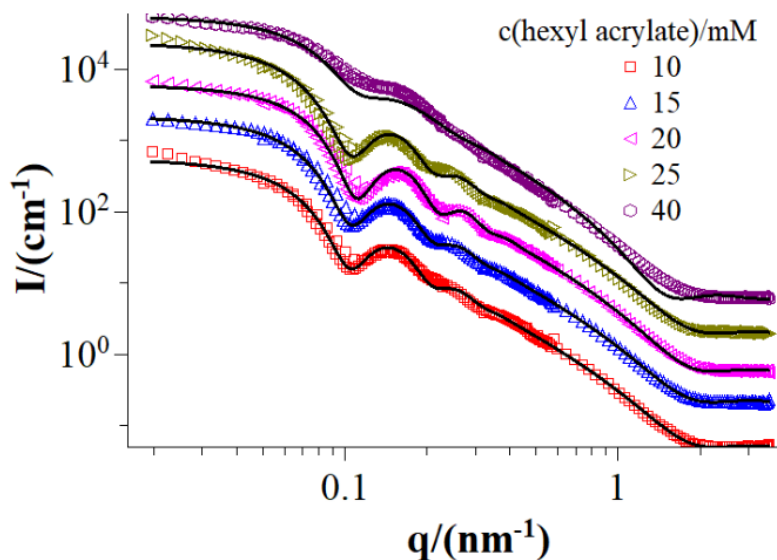


Figure 6.23. SANS curves of polymerized samples of 27.5 mM TDMAO / 0.275 mM L35 / 22.5 mM LiPFOS / hexyl acrylate mixtures at 25 °C. (Colored lines: measured data; solid black line: fitted data). For clarity subsequent data sets were multiplied each with a scale factor of 3.

For a detailed analysis of structural improvement after the polymerization, we applied the same spherical shell model explained earlier with the log-normal distribution of the radius to the scattering curves (Figure 6.23). For monomer concentrations lower than 40 mM, scattering patterns did not show a remarkable change and a constant PDI (Table 6.11). For 40 mM, the form factor minimum is much less pronounced and the PDI increases to 0.26. When we compare the bilayer thickness before and after the polymerization, the bilayer of the polymerized vesicles is expanded slightly from 2.7 to 2.8 nm depending on the monomer concentration.

Table 6.11. Results from the SANS analysis of polymerized samples of 27.5 mM TDMAO / 0.275 mM L35 / 22.5 mM LiPFOS / hexyl acrylate mixtures at 25°C. Given are Φ : Volume fraction, vesicle radius R_{ves} , polydispersity index PDI, bilayer thickness D from spherical shell model, bilayer thickness from Kratky-Porod analyses (see [Figure A15](#)), theoretically calculated polymer shell thickness, and molecular weight M_w .

hexyl acrylate amount (mM)	R_{ves} (nm) SANS	PDI	D/nm Spherical shell	D/nm Kratky Porod	Polymer shell thickness /nm	M_w (g/mol)
10	29.8	0.14	2.79	2.83	0.13	1.26×10^7
15	29.6	0.15	2.81	2.87	0.17	1.22×10^7
20	28.7	0.15	2.83	2.89	0.23	1.17×10^7
25	29.6	0.15	2.85	2.91	0.38	1.24×10^7
40	26.3	0.26	3.21	3.10	0.60	1.28×10^7

The cross-linked polymerized vesicles are another important system to be investigated by neutron scattering in order to gain information on the effect of cross-linking to the vesicle stabilization. The scattering curves of these samples displayed in [Figure 6.24](#) showed similar scattering properties as the monomer loaded vesicles. Their size slightly changed due to the cross-linking ratio and are presented in [Table 6.12](#). The thickness of the formed polymer shell

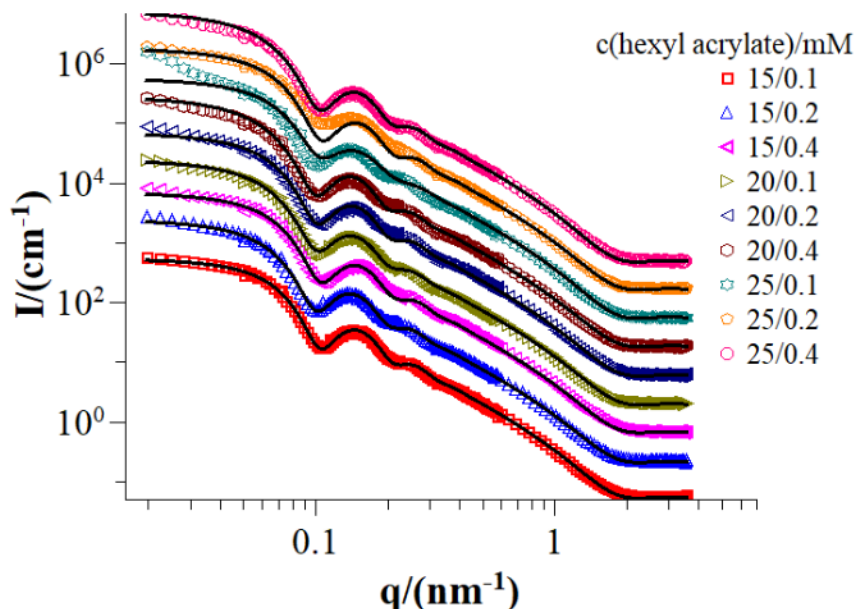


Figure 6.24. SANS curves of cross-linked polymerized samples of 27.5 mM TDMAO / 0.275 mM L35 / 22.5 mM LiPFOS / hexyl acrylate / 1, 6-hexanediol diacrylate mixtures at 25 °C. (Colored lines: measured data; solid black line: fitted data). For clarity subsequent data sets were multiplied each with a scale factor of 3.

in the vesicle membrane was calculated theoretically, details are explained in [appendix 9.2.5](#). When one compares it with the bilayer thickness obtained from SANS analysis, especially for low monomer concentrations, we ended up reasonable values that can fit in the bilayer range ([Figure 6.25](#)). However, for high monomer amounts results differ from each other. Calculated polymer shell is higher than the experimental values. This means above 20 mM concentration, the added monomer could not entirely insert and therefore polymerize into the vesicle membrane. For a detailed understanding, from the Porod analyses ($I(q)q^4$ vs q^4) we determined the specific surface S/V of the polymerized samples and plotted as a function of monomer concentration (see [Figure A19](#)). It was found that specific surface, S/V , changes very slightly for 10 to 25 mM monomer amount, however then it decreases for 40 mM. The decrease at 40 mM content can be attributed to the formed polymer chain locate mostly in the middle hydrophobic part of the bilayer.

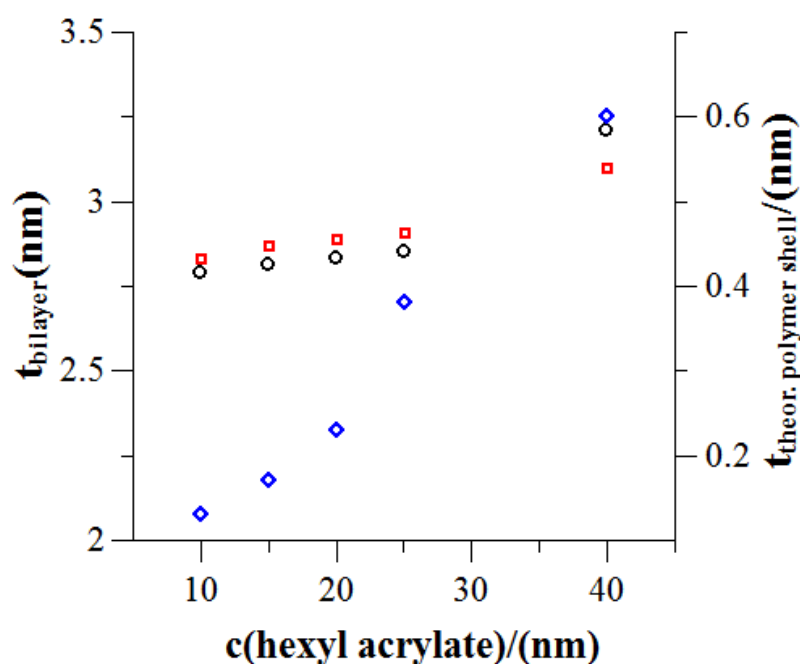


Figure 6.25. Thickness (t) as function of monomer concentration for polymerized samples of 27.5 mM TDMAO / 0.275 mM L35 / 22.5 mM LiPFOS / hexyl acrylate mixtures. *Red square*: bilayer thickness obtained from Kratky-Porod analysis; *black circle*: bilayer thickness obtained from SANS model; *blue diamond*: theoretically calculated polymer shell thickness.

Moreover, when polymerized samples are compared with the unpolymerized ones, they retained the low PDI values in the range of 0.11 to 0.14. This confirms the effectiveness of the method on stabilization of the vesicle templates via polymerization resulting monodisperse, and well-defined nanocapsules.

Table 6.12. Results from the SANS analysis of cross-linked polymerized samples of 27.5 mM TDMAO / 0.275 mM L35 / 22.5 mM LiPFOS / hexyl acrylate / 1, 6-hexanediol diacrylate mixtures at 25°C. Given are Φ : Volume fraction, vesicle radius R_{ves} , polydispersity index PDI, bilayer thickness D from spherical shell model, bilayer thickness from Kratky-Porod analyses (see [Figure A16](#)), theoretically calculated polymer shell thickness, and molecular weight M_w .

hexyl acrylate amount (mM)	R_{ves} (nm) SANS	PDI	D/nm Spherical shell	D/nm Kratky Porod	Polymer shell thickness/nm	M_w (g/mol)
15/0.1	30.0	0.14	2.82	2.83	0.22	1.21×10^7
15/0.2	30.4	0.15	2.81	2.85	0.24	1.29×10^7
15/0.4	29.8	0.14	2.75	2.81	0.20	1.17×10^7
20/0.1	30.1	0.15	2.78	2.87	0.22	1.29×10^7
20/0.2	30.9	0.14	2.80	2.89	0.23	1.30×10^7
20/0.4	31.2	0.14	2.94	2.90	0.24	1.40×10^7
25/0.1	29.4	0.14	2.82	2.86	0.38	1.05×10^7
25/0.2	30.1	0.18	2.83	2.87	0.44	1.09×10^7
25/0.4	30.3	0.14	2.81	2.80	0.35	1.24×10^7

6.3.5 Cryogenic Electron Microscopy (Cryo-TEM)

An effective way to gain further structural and morphological insights can be done by cryo-TEM experiments on the vesicle samples before and after polymerization. In [Figure 6.26](#) cryo-TEM images of unpolymerized and cross-linked polymerized vesicles are represented. These samples consisted from 27.5 mM TDMAO / 0.275 mM L35 / 22.5 mM LiPFOS with 20 mM total monomer concentration and 0.1 molar ratio of cross-linker with respect to the total monomer amount. Images were taken separately before and after polymerization. The image on the left side belong to the monomer loaded vesicles before polymerization and was taken at TEM laboratory of MLZ (JCNS) at Munich, Germany. Samples were deposited on holey carbon grids. The other image on the right side was performed at Technion, Haifa (Israel) using a FEI Tecnai T12 G2 transmission electron microscope. The details on sample preparation can be found in [section 3.1.8](#).

The Cryo-TEM images illustrate that both the monomer loaded vesicles and their subsequently polymerized species have spherical shape. A vesicle radius of approximately 25 nm is obtained from the images. Nevertheless, different size of particles seen on the images indicate a certain size distribution of the unpolymerized and polymerized vesicles and the polydispersity deduced

is in good agreement with that from the scattering results. We substantially observed small vesicles with radii in the range of 22 - 35 nm.

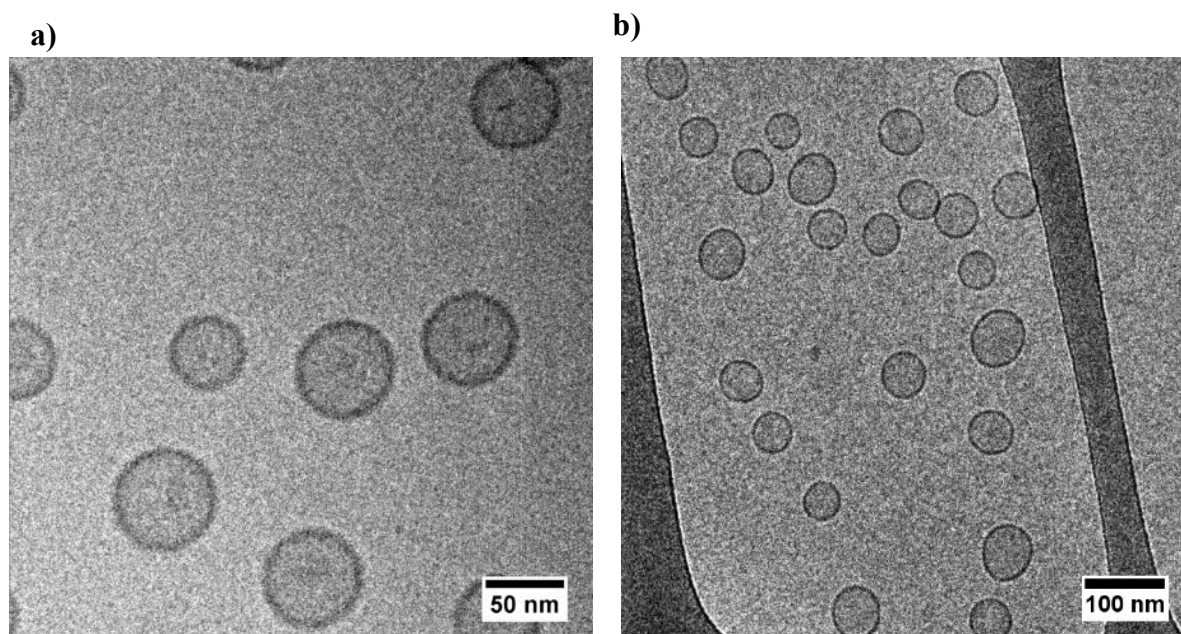


Figure 6.26. Cryo-TEM Images of vesicle system consisted from a) unpolymerized sample of 27.5 mM TDMAO / 0.275 mM L35 / 22.5 mM LiPFOS / 20 mM hexyl acrylate / 0.1 molar ratio of 1, 6-hexanediol diacrylate; b) cross-linked polymerized sample of 27.5 mM TDMAO / 0.275 mM L35 / 22.5 mM LiPFOS / 20 mM hexyl acrylate / 0.1 molar ratio of 1, 6-hexanediol diacrylate.

The most important result pointed out from the Cryo-TEM measurements is the evidence of the stabilization of vesicular structures by polymerization. When we compare both images before and after the polymerization, they look almost identical in terms of shape, size and size distribution. In detail, parameters such as size and polydispersity index as well as the bilayer thickness of the vesicle were be obtained from the images. [Figure 6.27](#) shows the size distribution of vesicles determined from different cryo-TEM images taken before and after polymerization of ~200 vesicles. When we compare the two distributions, radius of 26 nm is more pronounced for unpolymerized vesicles however after polymerization this value shifted slightly to 29 nm. This observation is in accordance with what is observed from SANS and light scattering (R_{ves} : outer radius), that along with the polymerization vesicle radius increased very slightly from 26 nm to 30 nm for the sample composition of 27.5 mM TDMAO / 0.275 mM L35 / 22.5 mM LiPFOS / 20 mM hexyl acrylate / 0.1 molar ratio of 1, 6-hexanediol diacrylate.

The unpolymerized vesicles revealed a monodisperse system with PDI value of 0.093, while afterwards along with the polymerization PDI increased to 0.11. It should be noted that these values are very close to the size and distribution parameters determined from scattering methods (for SANS analysis experimental resolution was accounted).

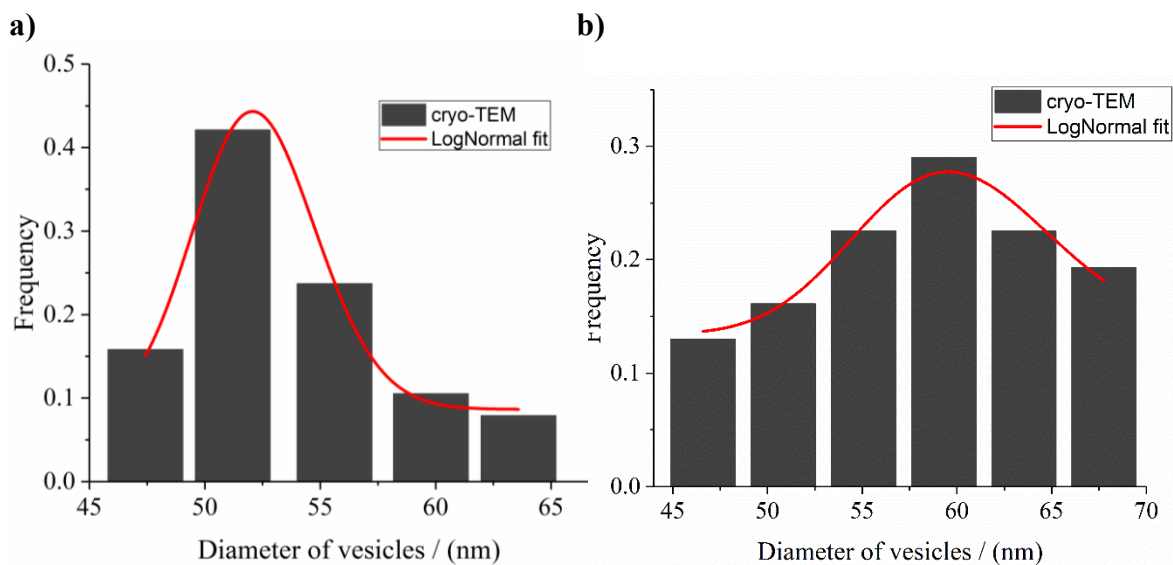


Figure 6.27. Number averaged vesicle size distribution histogram obtained from the analyses of ~200 vesicles from cryo-TEM images of a) unpolymerized sample of 27.5 mM TDMAO / 0.275 mM L35 / 22.5 mM LiPFOS / 20 mM hexyl acrylate / 0.1 molar ratio of 1, 6-hexanediol diacrylate; b) cross-linked polymerized sample of 27.5 mM TDMAO / 0.275 mM L35 / 22.5 mM LiPFOS / 20 mM hexyl acrylate / 0.1 molar ratio of 1, 6-hexanediol diacrylate. The solid lines show the Log-Normal (same function used in SANS analyses) distribution of the data.

Additionally, bilayer thickness is another parameter that can be gained from cryo-TEM images. For unpolymerized vesicles, an average value of 2.82 nm and for polymerized ones 2.84 nm of thickness were calculated. These values are all in very good agreement with results gained from other methods above (see [Table 6.8](#), [Table 6.9](#), [Table 6.11](#) and [Table 6.12](#)). Consequently, results from cryo-TEM analyses are in very good agreement with those of the other methods and demonstrate the morphological picture of the studied systems in a very remarkable way, especially confirming the structural stabilization of vesicles by polymerization.

6.3.6 Neutron Spin Echo (NSE)

Neutron spin echo is an effective and versatile method to study the membrane dynamics of vesicles which can focus on very small length scales. Since the vesicle bilayer enables the loading of different moieties, hydrophobic agents, and in our case monomers, their stability and viscoelastic properties are of crucial importance. The bilayer thicknesses obtained from small angle neutron scattering measurements show the general behavior of the membrane along with the monomer loading. However, in more detail, membrane fluctuations due to the monomer loading and its subsequent polymerization play a key role to understand the membrane stability. Therefore, we investigated these structures with NSE method complimentary to SANS and light scattering measurements.

Basically, vesicle bilayers show undulation movements which are related to the bending rigidity of the membrane and accordingly the mean bending modulus κ and the Gaussian modulus $\bar{\kappa}$ ⁵⁷. NSE makes it possible to determine the bending modulus κ via $S(q,t)$ which is the intermediate scattering function gained from the measurements. $S(q,t)$ as described by²⁰⁹:

$$S(q, t) = \exp(-D(q)q^2t)((1 - A(q)) + A(q)S_{und}(q, t)) \quad (6.1)$$

where $S_{und}(q, t)$ describes the undulation movement of membrane, $D(q)$ is the translational diffusion coefficient $D(q) = D_0/S(q)$ while D_0 is for infinite dilutions related with Stokes-Einstein [equation 3.5](#).

As known from the literature, membrane dynamics can be analyzed with different models. Simply they all derive from Helfrich bending Hamiltonian⁵⁷. The difference arises from how these models are considering the undulation. For small microemulsion spheres, Milner-Safran model describe the motions by applying single exponentials to $S_{und}(q, t)$ by counting in only the longest undulation which is simply the sphere radius. Therefore this approach is only limited to small spheres which has the form factor minima in the high q range^{210,211}.

On the other hand, Zilman-Granek model has been developed to determine the case of vesicles predicting an integration over all undulation wave vectors between the length scale of the vesicle and lower cut-off molecular length scale²¹²⁻²¹⁴. Due to this model $S_{und}(q, t)$ is described as, $S_{und}(q, t) = \exp(-(\Gamma_{ZG}q^3t)^{\frac{2}{3}})$ which decays with a stretched exponential. The Γ_{ZG} (GammaZG) in the equation is described by $= 0.025\gamma\sqrt{\frac{k_B T}{\kappa} \frac{k_B T}{\eta}}$. Here the parameters are $\gamma \approx$

$1 - \frac{3k_B T}{(4\pi\kappa)\ln(q\xi)} \approx 1$ for $\kappa/k_B T \gg 1$. In the end, the relation between the bending modulus κ and the Γ_{ZG} for Zilman-Granek is given as $\Gamma_{ZG} \propto 1/\sqrt{\kappa}$.

In this work we investigated 4 different samples with the neutron spin echo (NSE) method.

- Sample 1 was the bare vesicles (27.5 mM TDMAO / 0.275 mM L35 / 22.5 mM LiPFOS)
- Sample 2 was the 20 mM hexyl acrylate loaded vesicles (unpolymerized mixture of 27.5 mM TDMAO / 0.275 mM L35 / 22.5 mM LiPFOS / 20 mM hexyl acrylate)
- Sample 3 was cross-linked polymerized vesicles of 15 mM monomer concentration (27.5 mM TDMAO / 0.275 mM L35 / 22.5 mM LiPFOS / 15 mM hexyl acrylate / 0.1 molar ratio of 1, 6-hexanediol diacrylate (with respect to the total monomer amount))
- Sample 4 was cross-linked polymerized vesicles of 20 mM monomer concentration (27.5 mM TDMAO / 0.275 mM L35 / 22.5 mM LiPFOS / 20 mM hexyl acrylate / 0.1 molar ratio of 1, 6-hexanediol diacrylate (with respect to the total monomer amount)).

We applied the Zilman-Granek method for data analysis to examine the membrane dynamic.

[Figure 6.28](#) represents the measured NSE data applying a stretch exponential function to the curves. Model derived from the [equation 6.1](#) taking into account the $S_{und}(q, t)$ and as seen

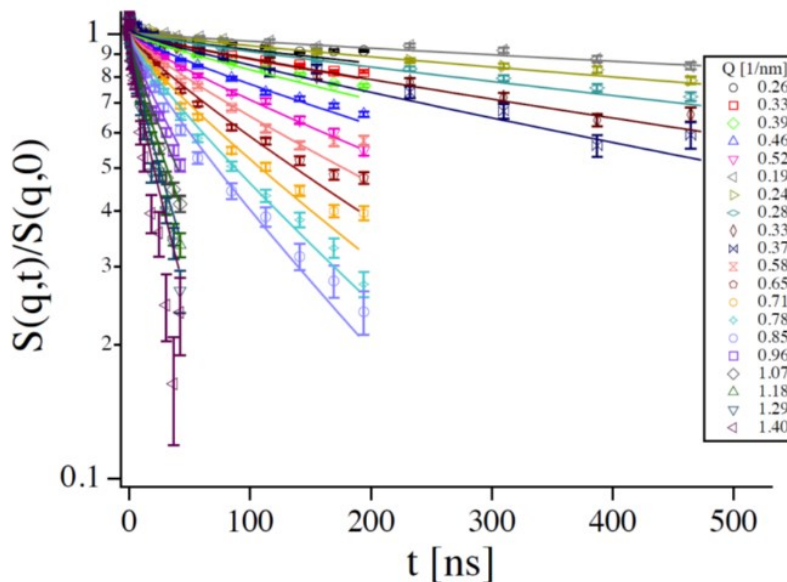


Figure 6.28. $S(Q,t)$ of bare vesicles consisted from 27.5 mM TDMAO / 0.275 mM L35 / 22.5 mM LiPFOS. Solid lines are the fits of Zilman-Granek model.

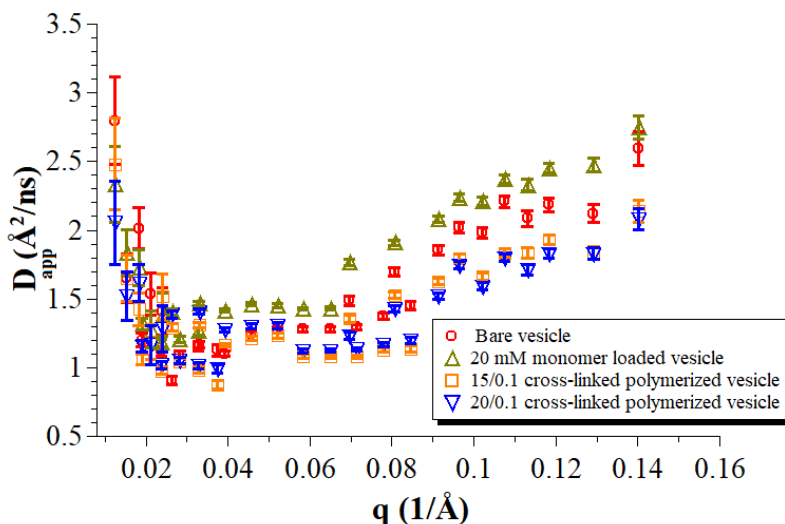


Figure 6.29. Apparent diffusion coefficient D_{app} of samples obtained from fitting the equation $S(Q, t) = \exp(-D_{app}Q^{2t})$ to the NSE data.

from the figure it agreed well with the curves. In [Appendix 9.3.3.5](#) further curves are presented for other samples, fitted with the same model and showing similar decays (Figure [A25](#), [A26](#) and [A27](#)).

In [Figure 6.29](#) the apparent diffusion coefficient values, D_{app} are presented and showing in general similar trends for all samples. However, in detail the monomer insertion into the bilayer has a different effect on dynamic behavior of the membrane. [Sample 2](#) consisted of monomer loaded vesicles has higher D_{app} values than bare vesicles ([sample 1](#)) meaning by inserting monomer, membrane became softened. On the other hand, cross-linking polymerization ([sample 3](#) and [4](#)) leads to a noticeable toughening of the membrane which is inherently expected and can be seen from the low D_{app} data.

Additionally, with the Zilman-Granek model the bending rigidity of the membrane can be determined via the relation $\Gamma_{ZG} \propto 1/\sqrt{\kappa}$. However, it is known that obtaining absolute κ values with Zilman-Granek model poses some inherent difficulties^{144,215,216}. Different assumptions were suggested in this regard and successfully deduced more realistic values of κ ^{217,218}. In a similar way as done in previous investigations, here we corrected the κ values simply using an effective solvent viscosity $\eta_{eff} = 3\eta$ ^{219–221}. Similar to results above, monomer loaded vesicles have the least rigid membrane and this may be explained such that here functions as a cosurfactant that is incorporated within the bilayer (also leading to a slight thinning of it). In contrast after polymerization significantly higher values of κ are observed and this stiffening of the membrane can be directly associated with the polymerization of the contained cross-

linking monomer. The formed polymer shell apparently leads to a stiffening of the membrane, as one would also have expected.

Table 6.13. Bending rigidity $\kappa/[K_B T]$ of the bilayer as obtained from NSE measurements. Sample descriptions are listed above (see [page 124](#)).

Vesicles	$\kappa/[K_B T]$
Sample 1	6.63
Sample 2	4.65
Sample 3	8.48
Sample 4	8.37

6.3.7 Encapsulation Efficiency

Investigations on enhancing the stability of vesicles have crucial importance in regard to their applications in controlled release of encapsulated drugs or any other agents. It is well-known that these hollow spherical structures can widely be used for the aim of delivery depending on their structural properties. Within this frame, different studies have been done to understand the encapsulation capacity of liposomes or different vesicle types such as cationic vesicles or polymeric vesicles^{222,223} and entrapment of fluorescence dyes^{224,225}, drugs^{50,68,226} or glucose²²⁷ has been studied intensively. For that purpose, different spectroscopic or microscopic methods were applied for determining their entrapment and release ability, such as fluorescence spectroscopy, confocal imaging or cross-correlation spectroscopy^{182,225}.

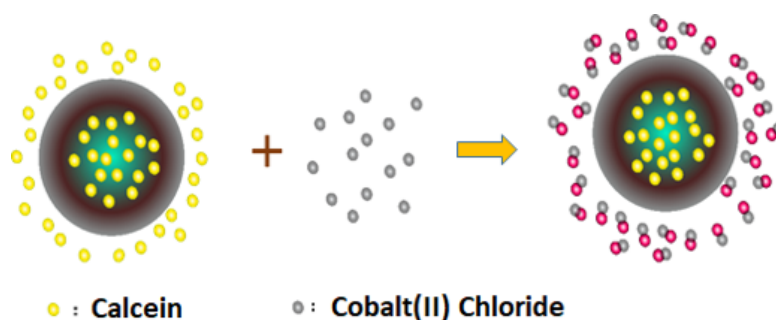


Figure 6.30. Schematic presentation of calcein entrapment in vesicles and quenching function of cobalt (II) ions.

In this part of the work, we studied the encapsulation properties and membrane permeability of polymer stabilized vesicles, in particular cross-linked polymerized vesicles, and compared them with bare vesicles of TDMAO/LiPFOS/L35. Calcein as a water-soluble fluorescence agent, was used for determining the encapsulation capacity of the vesicles. It is known that calcein is soluble in water and self-quenches at higher concentrations²²⁸. Our strategy (see [Figure 6.30](#)) was based on determining the encapsulation efficiency of vesicles by loading their hydrophilic core with calcein dye below self-quenching concentrations. When the system reaches the equilibrium state (fluorescence intensity was measured regularly until remaining constant), cobalt (II) chloride was added to the solution for quenching the untrapped calcein molecules in the bulk media. Thereby, only the fluorescence intensity of entrapped dye can be detected afterwards.

For all experiments, 1 μM concentration of calcein was added to each sample, and later the same amount of cobalt (II) chloride. We tested the entrapment of calcein in two different ways (see [Figure 6.31](#)), as a first attempt dissolving it into the stock solutions (TDMAO/L35 or LiPFOS stocks) prior to polymerization and in the second way it was added after the end of the polymerization. In the first way, calcein was added before the formation of vesicles, which also means before polymerization. Therefore, it needs to be dissolved either in TDMAO/L35 or in LiPFOS solutions. When we added 1 μM concentration of dye in TDMAO/L35 stock solution, calcein's fluorescence intensity remained unchanged as expected. However, interestingly when it was dissolved in LiPFOS solution, intensity dropped down. To avoid this somehow quenching effect of LiPFOS, we dissolved the dye in TDMAO/L35 stock and subsequently

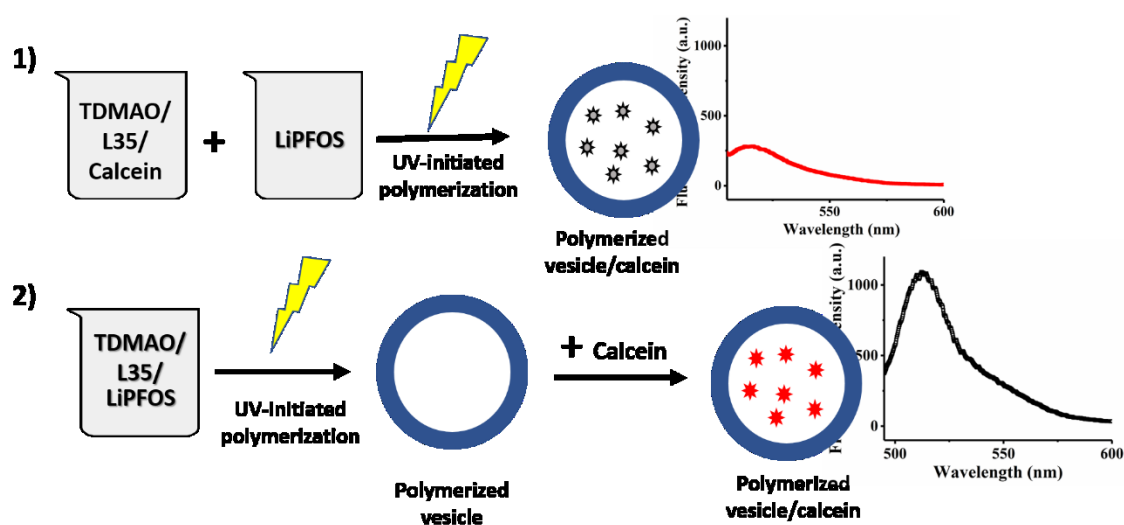


Figure 6.31. Different routes for calcein encapsulation into the vesicles.

mixed this solution with LiPFOS. Right after that, polymerization was started. At the end of the reaction, we still observed that fluorescence intensity of calcein decreased drastically in the absence of cobalt ions. This can happen for different reasons, the dye can be quenched or react with the radicals during the reaction. Therefore, the second method, where we added the dye directly to the freshly polymerized vesicles, was chosen for further analyses.

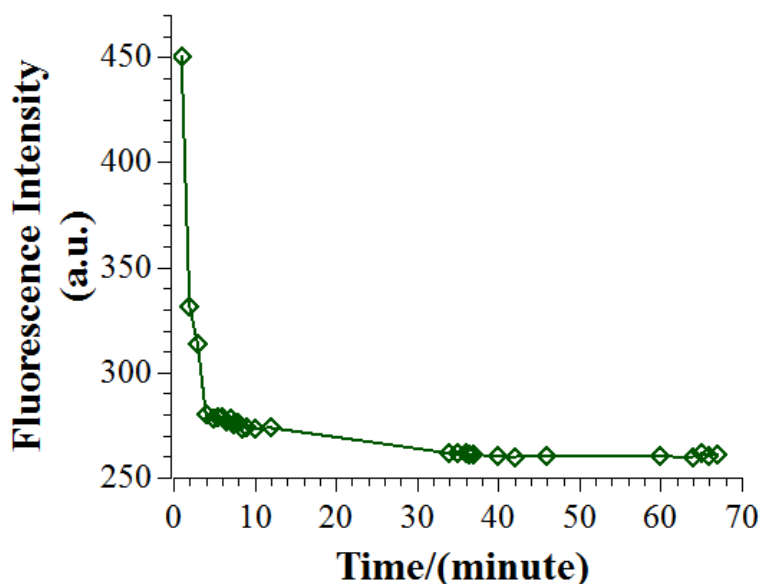


Figure 6.32. Dynamics of Co^{+2} quenching calcein of polymerized vesicle, measured at 25 °C.

At the end of polymerization, 1 μM concentration of calcein was added and equilibrated by slowly mixing in the dark at room temperature until the fluorescence intensity remained unchanged after ~ 1 hour (of 4 ml sample volume). This means while dye was transferring from the outside medium through the polymerized bilayer into the vesicle core, its intensity was fluctuating due to the different reasons such as collision or adsorption. Later on, 1 μM cobalt (II) chloride was added to the solution and fluorescence was measured continuously. In [Figure 6.32](#) we present the dynamics of Co^{+2} quenching calcein in polymerized vesicles. In the presence of cobalt (II) chloride, free calcein in the outside media was quenched and intensity decreased very fast in 4-5 minutes. Then intensity went down slowly until it remained constant in 30 minutes. Since the calcein dye was in equilibrium in the solution, we assume Co^{+2} ions diffused through the membrane in 30 minutes and some of the dye quenched during this time period. However, after 30 minutes we observed only the fluorescence from the encapsulated dye that was not quenched anymore with Co^{+2} ions.

The encapsulation efficiency of vesicles was calculated via the quenching ratio: $= \frac{F_\alpha}{F_\beta}$. F_α is the quenched fluorescence intensity of 1 μM pure calcein (at pH=9.9, which is measured for vesicle solutions) after cobalt chloride was added and F_β is the fluorescence intensity of 1 μM pure calcein (at pH=9.9) itself. Fluorescence of vesicles (pure or polymerized) with calcein is defined as $F_{calcein,ves}$ and after adding cobalt chloride to them the intensity is termed as $F_{quench,ves}$. If all calcein molecules combined with cobalt ions, the fluorescence intensity of vesicles would be decreased to a theoretical value of $F_{theo,ves}$ and $F_{theo,ves} = F_{calcein,ves} * \gamma$. Accordingly, encapsulation efficiency is: $EE = \frac{F_{quench,ves} - F_{theo,ves}}{F_{calcein,ves} - F_{theo,ves}} * 100\%$.

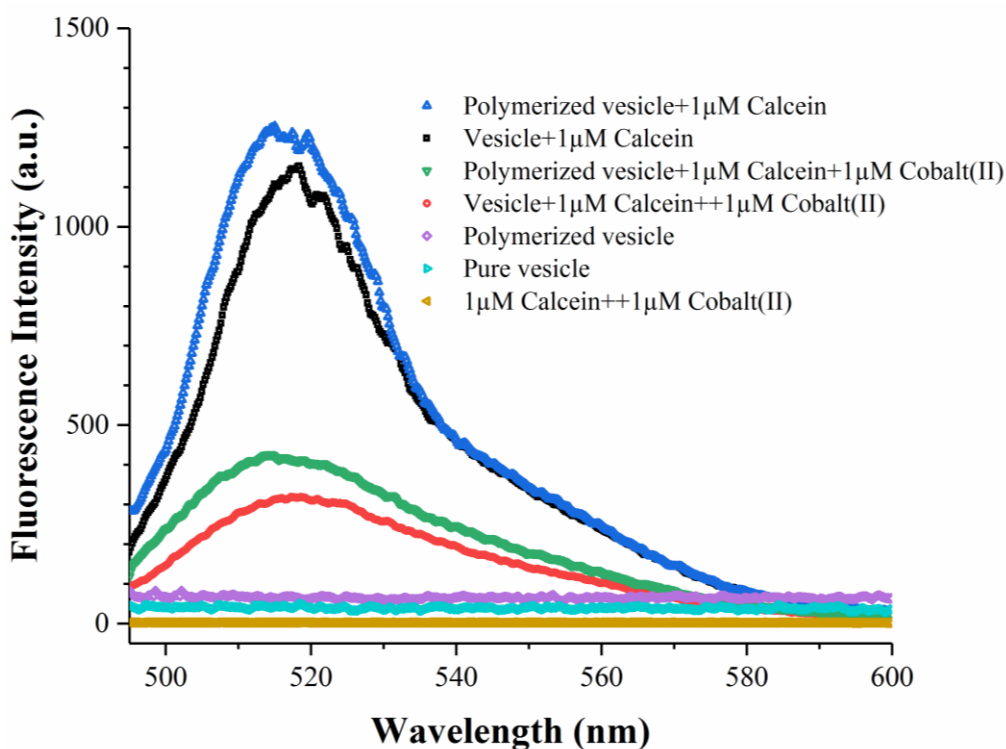


Figure 6.33. Fluorescence intensities measured at 25 °C. $t = 61$ min for samples without Co^{+2} , and $t = 30$ min for samples with Co^{+2} .

In [Figure 6.33](#) we present the measured fluorescence intensities of different sample types. The parameters and conditions of the measurements are described in [section 3.1.12](#). As expected, pure vesicles (27.5 mM TDMAO / 0.275 mM L35 / 22.5 mM LiPFOS) and polymerized vesicles (27.5 mM TDMAO / 0.275 mM L35 / 22.5 mM LiPFOS / 15 mM hexyl acrylate / 0.2 molar ratio of 1, 6-hexanediol diacrylate (with respect to hexyl acrylate concentration)) without calcein were not fluorescent, as seen in the same figure. For comparison, fluorescence intensities of pure and polymerized vesicles were measured after addition of 1 μM calcein to each. Subsequently, 1 μM cobalt (II) added to both solutions and the intensities after quenching

reduced to 200-380 (a.u). From the intensity and related equations above we calculated the encapsulation capacities. As a consequence, it was found that while cross-linked polymerized vesicles can entrap 35 % of calcein, pure vesicles can encapsulate 18 % of it. This means basically polymerization stiffens the vesicle membrane, prevents the release of dye through the outside media, therefore enhances the encapsulation efficiency of vesicles.

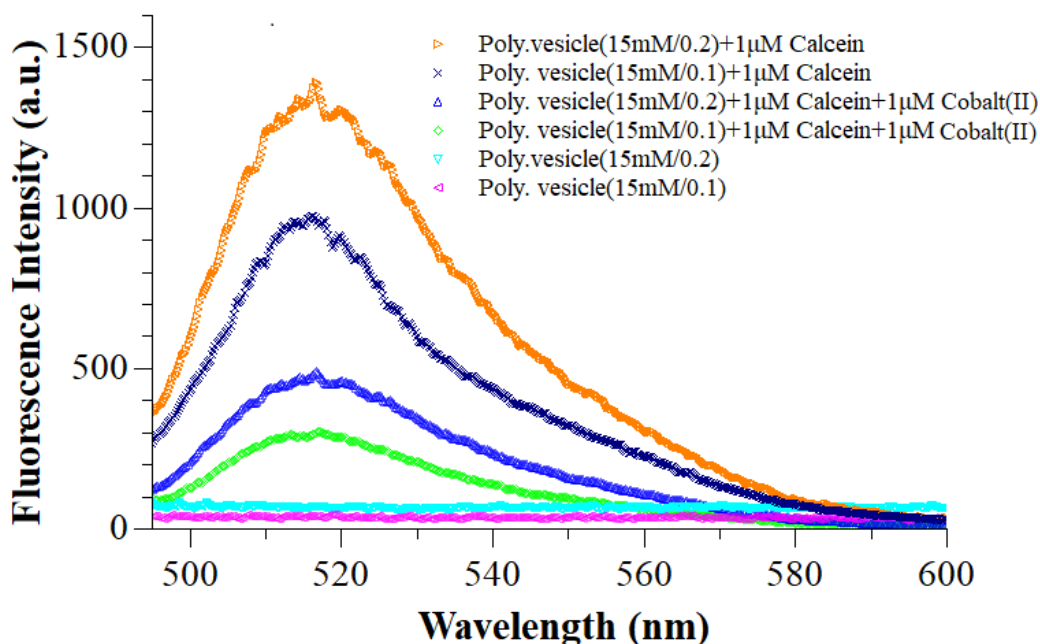


Figure 6.34. Fluorescence intensities measured at 25 °C. $t = 61$ min. for samples without Co^{+2} , and $t = 30$ min for samples with Co^{+2} .

As a second attempt, we compared the effect of cross-linking ratio on entrapment capacity as well. Total monomer concentration of 15 mM was varied for 0.1 and 0.2 molar ratio of cross-linker (with respect to hexyl acrylate concentration). The results displayed in [Figure 6.34](#) revealed that the polymerized vesicle with 0.1 molar ratio of cross-linker can encapsulate 25 % of calcein dye while the polymerized vesicles with higher cross-linker amount of 0.2 molar ratio can entrap 35 % of calcein. These results agree with previously presented encapsulation efficiency values of surfactant vesicles^{32,182,229}.

Overall, investigation on encapsulation efficiency of TDMAO/L35/LiPFOS vesicles and their polymer stabilized types have shown that, polymerization led to an effective increase on encapsulation capacity. The encapsulation capacity of polymer-stabilized vesicles is at least twice as high as pure vesicles. This can be explained by the fact that due to the polymerization, membrane wall becomes more robust, limiting the transportation of dye in and out and

controllably encapsulates it into the nanocapsule. On the other hand, increasing the cross-linker ratio from 0.1 to 0.2 strengthens the polymer network formed into the vesicle membrane and therefore changes the encapsulation capacity proportionally. Additionally, it should also be considered that dye can be adsorbed to the bilayer¹⁸². In either case, dye is sequestered in such a way efficiently.

6.4 Summary

Due to the flexibility of their alkyl chain and the low water solubility, acrylate monomers were suggested to have better compatibility for dissolving into the hydrophobic vesicle membrane. With this idea, acrylates with different chain lengths and associated with different water solubility, were employed to prepare monomer loaded vesicles. Butyl-, hexyl-, isooctyl-, and dodecyl acrylate monomers were dissolved in TDMAO/L35 solutions prior to the preparation of vesicles and they were soluble in micellar solutions at characteristic ratios depending on their structural properties. The monomer dissolved micellar aggregates were monitored by light and small angle neutron scattering (SANS) measurements and resulted in the transition from the cylindrical micelles to the spherical droplet with the increase of monomer concentration.

As second step, micellar solutions of TDMAO/L35/acrylate monomer were added to LiPFOS solution with the aim of forming vesicles. Scattering experiments indicated that acrylates loaded vesicles were formed successfully being smaller in size (radius ~ 26 nm) than bare vesicles and retaining the low polydispersity of 0.09-0.1. The structural transition from micellar to vesicular aggregates were remarkably observable from SANS analyses by means of the changes in scattering patterns ([Figure 6.35](#)).

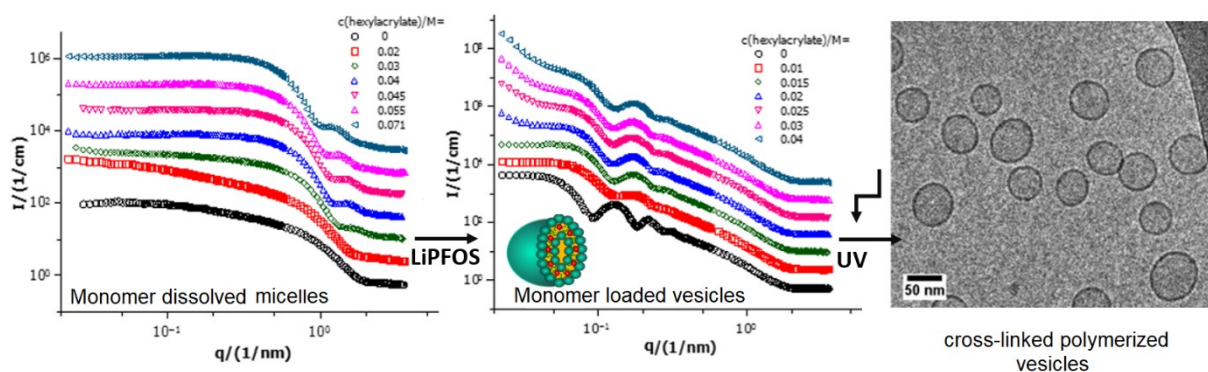


Figure 6.35. Schematic representation of structural transition from hexyl acrylate dissolved TDMAO/L35 micelles to hexyl acrylate loaded TDMAO/L35/LiPFOS vesicles and their cross-linked polymerized types.

In the last part of this section, the effect of polymerization of hexyl acrylate loaded vesicles was comprehensively investigated. It can be said that among other acrylates, hexyl acrylate was best suited to become incorporated into the hydrophobic membrane as it showed the largest concentration range for the vesicle phase. Results demonstrated that after polymerization, vesicles were effectively stabilized around the radii of ~ 29 nm, and structural integrity could be kept successfully. Especially the low PDI of the vesicles could be retained. With the help of

neutron spin echo measurements, we monitored the membrane fluctuations and it was shown that polymerization lead to a substantial increase of the membrane rigidity. Lastly, the encapsulation efficiency (EE) of bare and polymer stabilized vesicles were compared via loading them with a fluorescence dye, calcein. While the EE of polymerized vesicles was 35%, bare vesicles had a value of 18%, and with increasing the cross-linking ratio from 0.1 to 0.2, EE increases to 1.5 times more. In summary, polymerization not only stabilized the vesicles but also improved their membrane permeability. This means that, with the association of polymerization, vesicles can suitably be used in delivery systems or other potential future applications.

7 Summary and Outlook

In this work, we aimed to provide an effective way for stabilizing a well-defined vesicle system which could potentially be used as nanocarrier for different application areas from detergency to electronics^{32,184,185,230}. Polymerization is a key method within this context and has been used in many studies to improve the vesicle structure by inserting hydrophobic monomeric moieties into their bilayer and subsequently fixating them by polymerization^{97,196,231,232}. This strengthens the vesicle architecture providing a polymer shell interior of the hydrophobic vesicle membrane and thereby enhances the entrapment capacity and reduces the permeability of vesicle membrane.

Although it is a straightforward method, different problems have been encountered during the studies. A very known issue reported by Jung is about phase separation^{103,108}. In dioctadecyldimethylammonium bromide (DODAB) vesicles, a phase separation in the bilayer occurred due to the styrene polymerization and the formed structures showed a so called parachute-like shape¹⁰³. These structures lost their original shape of hollow spherical geometry and deviates substantially in structure, thereby being of little use as templated structures. In addition, polymerization often needs high temperatures or organic solvents which poses other limits to the method.

This thesis offers an alternative way avoiding these problems. In particular, we were interested in stabilizing a well-defined vesicle system via UV-initiated polymerization. Spontaneously formed TDMAO/L35/LiPFOS monodisperse vesicles are interesting structures as templates for further applications such as drug delivery^{114,115,233} and were studied before and after their fixation by polymerization. For this purpose, we inserted monomers with different chemical properties into the vesicle system and they were then reacted by UV-initiated polymerisation. Choosing an appropriate monomer, was the most important point because of its vital effect on the formation of vesicle template and its compatibility with the membrane. Therefore, common monomers which can polymerise easily and accurately, such as styrene and alkyl acrylates with different alkyl chain lengths were employed.

Monomers can be inserted into the vesicle bilayer via concurrent or diffusion loading ways¹¹¹. In order to prevent aging problem of vesicles and having entirely homogenous system, we chose concurrent loading where monomer was loaded simultaneously with the formation of the

bilayer. Thus, monomer was dissolved in 50 mM TDMAO / 0.5 mM L35 solution prior to the formation of vesicles. We varied the monomer concentration in a systematic fashion in order to obtain the loading capacity of hydrophobic micellar core or vesicle bilayer.

In the first part of the thesis ([Chapter 4](#)), TDMAO/L35 micelles were treated with styrene monomer. Interestingly, we ended up with the finding that styrene had a dual function of being both hydrophobic and having a cosurfactant character due to its relatively high polarity²³⁴. Investigations revealed a structural transition from rod-like micelles to vesicles only with the presence of styrene monomer as was observed before for medium chain alcohols^{51,166}. Namely, the generation of vesicles is linked to dissolving a certain amount of styrene into the amphiphilic palisade layer, thereby acting as a cosurfactant. Polymerization transformed the polar styrene to less polar polystyrene and this led to a corresponding change of the packing parameter again and highly viscous rod-like structures were formed. For still higher styrene content in TDMAO /L35 mixtures microemulsion droplets are formed as here the further added styrene can no longer become incorporated into the amphiphilic monolayers and then acts as an oil that becomes solubilized into the micellar cores. Polymerization led to the formation of nanolatices of identical size, which means that here templating works perfectly well. The entire structural progression was examined with turbidity, UV-vis, light and small angle neutron scattering, NMR and rheology measurements

For our model vesicle system based on 27.5 mM TDMAO / 0.275 mM L35 / 22.5 mM LiPFOS formulation, the effect of styrene on this template was addressed in the second part of the work ([Chapter 5](#)). Monomer loaded vesicles were prepared by mixing the styrene dissolved TDMAO/L35 solutions with 50 mM LiPFOS in the molar ratio of 55:45. Visual observation and turbidity measurements demonstrated no significant phase change due to increasing the amount of styrene. To gain a better insight scattering experiments were applied and we obtained that vesicle morphology was retained after monomer loading, however their size and polydispersity increased significantly. As our main goal was to stabilize the vesicles by polymerization, we were successfully able to retain the monomer loaded vesicles with their initial size and polydispersity²⁰².

In a similar way, acrylate monomers were studied intensively in the last part ([Chapter 6](#)). The solubilisation behaviour of butyl-, dodecyl-, hexyl-, and isooctyl acrylate monomers were tested firstly in TDMAO/L35 micelles, following that monomer loaded vesicles were prepared by mixing with LiPFOS as identically described above. Possessing a short alkyl chain and therefore having high water solubility, butyl acrylate was differing from the other acrylates.

Oppositely, isooctyl and dodecyl acrylates could hardly have solubilized in the micellar TDMAO/L35/water solutions. Detailed structural information of this process has been studied with mostly scattering experiments. On the other hand, hexyl acrylate monomer facilitated a very good compliance either with micellar aggregates or vesicular bilayer. Its hydrophobicity, and chain length made it a perfect prototype that can easily be located in the bilayer but retaining the thickness of ~ 2.8 nm, which means that it has to act similar to a cosurfactant, becoming incorporated within the amphiphilic palisade layer. Another important point to be considered in the polymerization part, is a proper cross-linker possessing the same chemical structure as monomer. 1, 6-hexanediol diacrylate was used for this aim. Hexyl acrylate dissolved micelles and their further vesicular progression were monitored by turbidity, light and small angle neutron scattering, cryo-TEM, neutron spin echo and NMR techniques. Particularly, the change of the SANS patterns indicated a clear transition from micelles to vesicular structures. Our results demonstrated a decrease in vesicle size from 35 nm to 29 nm with increasing the amount of hexyl acrylate in the hydrophobic shell and the monodisperse size distribution remains. Furthermore, cryo-TEM measurements confirmed that no morphological changes occurred either before or after polymerization. This means hexyl acrylate monomer was a perfectly suitable choice in regard to stabilize the former vesicular structure via polymerization in all aspects. Finally, the encapsulation efficiencies of the pure, and polymerized vesicles were compared by loading a fluorescence dye calcein into the core of the hollow spheres. These experiments confirm nicely that polymerization leads to a much more robust shell that correspondingly makes the transport of molecules out of the vesicles more difficult, i. e. by polymerization one can control the release properties of these nanocapsules.

To summarize, our work in this thesis presents a new point of view for the preparation of monodisperse polymeric hollow spherical nanoparticles in a straightforward way. Its ease for application and advantages makes it a good alternative for the production of delivery agents. Future work in this area can be directed through its development and application into the biocompatible or biodegradable systems. In the similar manner, their functionalized analogues might provide a very broad application area. Consequently, long term stability of polymer stabilized vesicles is one of the open questions which might be addressed in future studies and can raise their importance in the field of nanocarriers.

8 References

- (1) Tanford. Micelle Shape and Size. *J. Physical Chem.* **1972**, Vol. 76, 3020–3024.
- (2) *Molecular Gels: Materials with Self-Assembled Fibrillar Networks*; Weiss, R. G.; Terech, P. Eds.; Springer: Netherland, **2006**.
- (3) Israelachvili, J. N.; Mitchell, D. J.; Ninham, B. W. Theory of Self-Assembly of Hydrocarbon Amphiphiles into Micelles and Bilayers. *J. Chem. Soc. Faraday Trans. 2 Mol. Chem. Phys.* **1976**, 72, 1525–1568.
- (4) Gradzielski, M.; Bergmeier, M.; Hoffmann, H.; Müller, M.; Grillo, I. Vesicle Gel Formed by a Self-Organization Process. *J. Phys. Chem. B* **2000**, 104 (49), 11594–11597.
- (5) Gradzielski, M.; Grillo, I.; Narayanan, T. Dynamics of Structural Transitions in Amphiphilic Systems Monitored by Scattering Techniques. In *Mesophases, Polymers, and Particles*; Springer: Berlin, Heidelberg, **2004**; pp 32–39.
- (6) Einstein, A. Über Die von Der Molekularkinetischen Theorie Der Wärme Geforderte Bewegung von in Ruhenden Flüssigkeiten Suspendierten Teilchen. *Ann. Phys.* **1905**, 322 (8), 549–560.
- (7) von Smoluchowski, M. Zur Kinetischen Theorie Der Brownschen Molekularbewegung Und Der Suspensionen. *Ann. Phys.* **1906**, 326 (14), 756–780.
- (8) Lemons, D. S.; Gythiel, A. Paul Langevin’s 1908 Paper “On the Theory of Brownian Motion” [“Sur La Théorie Du Mouvement Brownien,” C. R. Acad. Sci. (Paris) 146, 530–533 (1908)]. *Am. J. Phys.* **1997**, 65 (11), 1079–1081.
- (9) Intermolecular and Surface Forces. In *Intermolecular and Surface Forces (Third Edition)*; Israelachvili, J. N., Ed.; Academic Press: Boston, **2011**.
- (10) Li, Q.; Jonas, U.; Zhao, X. S.; Kappl, M. The Forces at Work in Colloidal Self-Assembly: A Review on Fundamental Interactions between Colloidal Particles. *Asia-Pacific J. Chem. Eng.* **2008**, 3 (3), 255–268.
- (11) Ohki, S.; Ohshima, H. Interaction and Aggregation of Lipid Vesicles (DLVO Theory versus Modified DLVO Theory). *Colloids Surfaces B Biointerfaces* **1999**, 14 (1), 27–45.
- (12) S Leikin; V A Parsegian; D C Rau; and R P Rand. Hydration Forces. *Annu. Rev. Phys. Chem.* **1993**, 44 (1), 369–395.
- (13) Pashley, R. M. Hydration Forces between Mica Surfaces in Electrolyte Solutions. *Adv. Colloid Interface Sci.* **1982**, 16 (1), 57–62.
- (14) Pashley, R. M. DLVO and Hydration Forces between Mica Surfaces in Li⁺, Na⁺, K⁺, and Cs⁺ Electrolyte Solutions: A Correlation of Double-Layer and Hydration Forces with Surface Cation Exchange Properties. *J. Colloid Interface Sci.* **1981**, 83 (2), 531–546.
- (15) Pashley, R. M. Hydration Forces between Mica Surfaces in Aqueous Electrolyte Solutions. *J. Colloid Interface Sci.* **1981**, 80 (1), 153–162.
- (16) Laing, M. E.; McBain, J. W. The Investigation of Sodium Oleate Solutions in the Three Physical States of Curd, Gel and Sol. *J. Chem. Soc. Trans.* **1920**, 117 (0), 1506–1528.
- (17) Nägeli, C. Theorie Der Gärung: Ein Beitrag Zur Molekularphysiologie. R. Oldenbourg: München **1879**, p 156.
- (18) Davies, D. G.; Bury, C. R. The Partial Specific Volume of Potassium N-Octoate in Aqueous

- Solution. *J. Chem. Soc.* **1930**, No. 0, 2263–2267.
- (19) Crook, E. H.; Trebbi, G. F.; Fordyce, D. B. Thermodynamic Properties of Solutions of Homogeneous p,t-Octylphenoxyethoxyethanols (OPE1-10). *J. Phys. Chem.* **1964**, *68* (12), 3592–3599.
 - (20) Fox, K. K. Determination of the Monomer-Micelle Exchange Frequency of a Paramagnetic Surfactant. *Trans. Faraday Soc.* **1971**, *67* (0), 2802–2809.
 - (21) Musbally, G. M.; Perron, G.; Desnoyers, J. E. Apparent Molal Volumes and Heat Capacities of Ionic Surfactants in Water at 25°C. *J. Colloid Interface Sci.* **1974**, *48* (3), 494–501.
 - (22) J. H. Clint: Surfactant Aggregation, Blackie Publishing Group, Glasgow, **1992**, ISBN 0-216-92905-9.
 - (23) Lange, H.; Schwuger, M. J. Mizellbildung Und Krafft-Punkte in Der Homologen Reihe Der Natrium-n-Alkyl-Sulfate Einschließlich Der Ungeradzahlgigen Glieder. *Kolloid-Zeitschrift und Zeitschrift für Polym.* **1968**, *223* (2), 145–149.
 - (24) Tanford, C. Theory of Micelle Formation in Aqueous Solutions. *J. Phys. Chem.* **1974**, *78* (24), 2469–2479.
 - (25) Nagarajan, R.; Ruckenstein, E. Theory of Surfactant Self-Assembly: A Predictive Molecular Thermodynamic Approach. *Langmuir* **1991**, *7* (12), 2934–2969.
 - (26) Jang, J.; Lee, K. Facile Fabrication of Hollow Polystyrene Nanocapsules by Microemulsion Polymerization. *Chem. Commun.* **2002**, 1098–1099.
 - (27) Cates, M. E.; Candau, S. J. Statics and Dynamics of Worm-like Surfactant Micelles. *J. Phys. Condens. Matter* **1990**, *2*, 6869–6892.
 - (28) IUPAC. Compendium of Chemical Terminology, 2nd ed. (the “Gold Book”). Compiled by A. D. McNaught and A. Wilkinson. Blackwell Scientific Publications Oxford (1997). XML online corrected version: <http://goldbook.iupac.org> (2006-) created by M. Nic, J. Jira.
 - (29) Nagarajan, R.; Chaiko, M. A.; Ruckenstein, E. Locus of Solubilization of Benzene in Surfactant Micelles. *J. Phys. Chem.* **1984**, *88* (13), 2916–2922.
 - (30) Schulman, J. H.; Stoeckenius, W.; Prince, L. M. Mechanism of Formation and Structure of Micro Emulsions by Electron Microscopy. *J. Phys. Chem.* **1959**, *63* (10), 1677–1680.
 - (31) Fletcher, P. D. I.; Horsup, D. I. Droplet Dynamics in Water-in-Oil Microemulsions and Macroemulsions Stabilised by Non-Ionic Surfactants. Correlation of Measured Rates with Monolayer Bending Elasticity. *J. Chem. Soc. Faraday Trans.* **1992**, *88* (6), 855–864.
 - (32) Uchegbu I. F.; Schaetzlein, A. G.; Tetzlaff, L.; Gray, A. I.; Sludden, J.; Siddique, S.; Moshá, E. Polymeric Chitosan-Based Vesicles for Drug Delivery. *J. Pharm. Pharmacol.* **1998**, *50*, 453–458.
 - (33) Graff, A.; Winterhalter, M.; Meier, W. Nanoreactors from Polymer-Stabilized Liposomes. *Langmuir* **2001**, *17* (3), 919–923.
 - (34) Fendler, J. H. Photochemical Solar Energy Conversion. An Assessment of Scientific Accomplishments. *J. Phys. Chem.* **1985**, *89* (13), 2730–2740.
 - (35) Yang, J. Viscoelastic Wormlike Micelles and Their Applications. *Curr. Opin. Colloid Interface Sci.* **2002**, *7* (5–6), 276–281.
 - (36) Mann, S.; Hannington, J. P.; Williams, R. J. P. Phospholipid Vesicles as a Model System for Biomineralization. *Nature* **1986**, *324*, 565.
 - (37) Hauser, H.; Gains, N.; Müller, M. Interaction of Intestinal Brush Border Membrane Vesicles

- with Small Unilamellar Phospholipid Vesicles. Exchange of Lipids between Membranes Is Mediated by Collisional Contact. *Biochemistry* **1983**, *22*, 4775–4781.
- (38) Imura, T.; Yanagishita, H.; Ohira, J.; Sakai, H.; Abe, M.; Kitamoto, D. Thermodynamically Stable Vesicle Formation from Glycolipid Biosurfactant Sponge Phase. *Colloids Surfaces B Biointerfaces* **2005**, *43* (2), 115–121.
- (39) Sundler, R. Studies on the Effective Size of Phospholipid Headgroups in Bilayer Vesicles Using Lectin-Glycolipid Interaction as a Steric Probe. *Biochim. Biophys. Acta - Biomembr.* **1984**, *771* (1), 59–67.
- (40) Lasic, D. *Liposomes: From Physics to Applications*; Elsevier: Amsterdam, **1993**.
- (41) Lockhoff O. Glycolipids as Immunomodulators: Syntheses and Properties. *Angew. Chemie Int. Ed. English*, **1991**, *30* (12), 1611–1620.
- (42) Kamenka, N.; Chorro, M.; Talmon, Y.; Zana, R. Study of Mixed Aggregates in Aqueous Solutions of Sodium Dodecyl Sulfate and Dodecyltrimethylammonium Bromide. *Colloids and Surfaces* **1992**, *67* (Supplement C), 213–222.
- (43) EW Kaler, AK Murthy, BE Rodriguez, J. Z. Spontaneous Vesicle Formation in Aqueous Mixtures of Single-Tailed Surfactants. *Science (80)*. **1989**, *245* (4924), 1371–1374.
- (44) Yacilla, M. T.; Herrington, K. L.; Brasher, L. L.; Kaler, E. W.; Chiruvolu, S.; Zasadzinski, J. A. Phase Behavior of Aqueous Mixtures of Cetyltrimethylammonium Bromide (CTAB) and Sodium Octyl Sulfate (SOS). *J. Phys. Chem.* **1996**, *100* (14), 5874–5879.
- (45) Chiappisi, L.; Yalcinkaya, H.; Gopalakrishnan, V. K.; Gradzielski, M.; Zemb, T. Catanionic Surfactant Systems—thermodynamic and Structural Conditions Revisited. *Colloid Polym. Sci.* **2015**, *293* (11), 3131–3143.
- (46) Murthy, K.; Easwar, N.; Singer, E. Spontaneous Formation of Monodisperse Vesicles near the Cloud Point of an Aqueous Amphiphilic System. *Colloid Polym. Sci.* **1998**, *276* (10), 940–944.
- (47) LL, B.; KL, H.; EW, K. Electrostatic Effects on the Phase-Behavior of Aqueous Cetyltrimethylammonium Bromide and Sodium Octyl Sulfate Mixtures with Added Sodium-Bromide. *Langmuir* **1995**, *11* (11), 4267–4277.
- (48) Vautrin, C.; Zemb, T.; Schneider, M.; Tanaka, M. Balance of PH and Ionic Strength Influences on Chain Melting Transition in Catanionic Vesicles. *J. Phys. Chem. B*, **2004**, *108* (23), 7986–7991.
- (49) Cha, J. N.; Birkedal, H.; Euliss, L. E.; Bartl, M. H.; Wong, M. S.; Deming, T. J.; Stucky, G. D. Spontaneous Formation of Nanoparticle Vesicles from Homopolymer Polyelectrolytes. *J. Am. Chem. Soc.* **2003**, *125* (27), 8285–8289.
- (50) Limin, Z.; Ganzuo, L.; Zhiwei, S. Spontaneous Vesicle Formation in Aqueous Solution of Zwitterionic and Anionic Surfactant Mixture. *Colloids Surfaces A Physicochem. Eng. Asp.* **2001**, *190* (3), 275–283.
- (51) Gradzielski, M.; Hoffmann, H.; Langevin, D. Solubilization of Decane into the Ternary System TDMAO/1-Hexanol/Water. *J. Phys. Chem.* **1995**, *99* (33), 12612–12623.
- (52) Mayhew, E.; Papahadjopoulos, D.; Rustum, Y. M.; Dave, C. Use Of Liposomes For The Enhancement Of The Cytotoxic Effects Of Cytosine Arabinoside. *Ann. N. Y. Acad. Sci.* **1978**, *308* (1), 371–386.
- (53) Panizza, P.; Roux, D.; Vuillaume, V.; Lu, C.-Y. D.; Cates, M. E. Viscoelasticity of the Onion Phase. *Langmuir* **1996**, *12* (2), 248–252.
- (54) Segota S., Tezak D., Spontaneous Formation of Vesicles. *Adv. Colloid Interface Sci.* **2006**, *121*, 51–75.

- (55) Schomaecker, R.; Strey, R. Effect of Ionic Surfactants on Nonionic Bilayers: Bending Elasticity of Weakly Charged Membranes. *J. Phys. Chem.* **1994**, *98* (14), 3908–3912.
- (56) Gradzielski, M. Vesicles and Vesicle Gels - Structure and Dynamics of Formation. *J. Phys. Condens. Matter* **2003**, *15* (19), R655–R697.
- (57) Helfrich, W. Elastic Properties of Lipid Bilayers: Theory and Possible Experiments. *Z. Naturforsch. C.* **1973**, *28* (11), 693–703.
- (58) Helfrich, W. Lyotropic Lamellar Phases. *J. Phys. Condens. Matter* **1994**, *6* (23A), A79–A92.
- (59) Safran, S. A.; MacKintosh, F. C.; Pincus, P. A.; Andelman, D. A. Spontaneous Vesicle Formation by Mixed Surfactants. In *Trends in Colloid and Interface Science V*; Corti, M., Mallamace, F., Eds.; Steinkopff: Heidelberg, **1991**; pp 3–7.
- (60) Porte, G.; Ligoure, C. Mixed Amphiphilic Bilayers: Bending Elasticity and Formation of Vesicles. *J. Chem. Phys.* **1995**, *102* (10), 4290–4298.
- (61) May, S.; Ben-Shaul, A. Spontaneous Curvature and Thermodynamic Stability of Mixed Amphiphilic Layers. *J. Chem. Phys.* **1995**, *103* (9), 3839–3848.
- (62) Papahadjopoulos, D.; Miller, N. Phospholipid Model Membranes. I. Structural Characteristics of Hydrated Liquid Crystals. *Biochim. Biophys. Acta - Biomembr.* **1967**, *135* (4), 624–638.
- (63) Bangham, A. D.; Horne, R. W. Negative Staining of Phospholipids and Their Structural Modification by Surface-Active Agents as Observed in the Electron Microscope. *J. Mol. Biol.* **1964**, *8* (5), 660–668.
- (64) Bangham, A. D.; Standish, M. M.; Weissmann, G. The Action of Steroids and Streptolysin S on the Permeability of Phospholipid Structures to Cations. *J. Mol. Biol.* **1965**, *13* (1), 253–259.
- (65) A., M. L.; Hu, Z.; Ayazi, S. P. Preparation of Small Unilamellar Vesicles (SUV) and Biophysical Characterization of Their Complexes with Poly-l-lysine-condensed Plasmid DNA. *Biotechnol. Appl. Biochem.* **2010**, *37* (1), 73–81.
- (66) Zasadzinski, J. A. Transmission Electron Microscopy Observations of Sonication-Induced Changes in Liposome Structure. *Biophys. J.* **1986**, *49* (6), 1119–1130.
- (67) Jo, Y.-J.; Kwon, Y.-J. Characterization of β -Carotene Nanoemulsions Prepared by Microfluidization Technique. *Food Sci. Biotechnol.* **2014**, *23* (1), 107–113.
- (68) Nagata, T.; Okada, K.; Takebe, I.; Matsui, C. Delivery of Tobacco Mosaic Virus RNA into Plant Protoplasts Mediated by Reverse-Phase Evaporation Vesicles (Liposomes). *Mol. Gen. Genet. MGG* **1981**, *184* (2), 161–165.
- (69) Otake, K.; Shimomura, T.; Goto, T.; Imura, T.; Furuya, T.; Yoda, S.; Takebayashi, Y.; Sakai, H.; Abe, M. Preparation of Liposomes Using an Improved Supercritical Reverse Phase Evaporation Method. *Langmuir* **2006**, *22* (6), 2543–2550.
- (70) Edwin, D.; B., S. G.; Frank, C.; A., D. S.; Helmuth, M. Novel Hollow Polymer Shells by Colloid-Templated Assembly of Polyelectrolytes. *Angew. Chemie Int. Ed.* **1998**, *37* (16), 2201–2205.
- (71) Diat, O.; Roux, D.; Nallet, F. Effect of Shear on a Lyotropic Lamellar Phase. *J. Phys. II* **1993**, *3* (9), 1427–1452.
- (72) Bergmeier, M.; Gradzielski, M.; Hoffmann, H.; Mortensen, K. Behavior of Ionically Charged Lamellar Systems under the Influence of a Shear Field. *J. Phys. Chem. B* **1999**, *103* (9), 1605–1617.
- (73) Watanabe, K.; Nakama, Y.; Yanaki, T.; Hoffmann, H. Novel Vesicle and Sponge Phase Prepared in Amphoteric Surfactant/Anionic Surfactant/Oleic Acid/Water System. *Langmuir*

- 2001**, *17* (23), 7219–7224.
- (74) Mendes, E.; Narayanan, J.; Oda, R.; Kern, F.; Candau, S. J.; Manohar, C. Shear-Induced Vesicle to Wormlike Micelle Transition. *J. Phys. Chem. B* **1997**, *101* (13), 2256–2258.
- (75) Brady, J. E.; Evans, D. F.; Kachar, B. and Ninham, B. W. Spontaneous Vesicles. *J. Am. Chem. Soc.*, **1984**, *106* (15), 4279–4280.
- (76) Ninham, B. W.; Evans, D.F.; Wei, G. J. The Curious World of Hydroxide Surfactants. Spontaneous Vesicles and Anomalous Micelles. *J. Phys. colloid Chem.* **1983**, *87* (24), 5020–5025.
- (77) Hargreaves, W. R.; Deamer, D. W. Liposomes from Ionic, Single-Chain Amphiphiles. *Biochemistry* **1978**, *17* (18), 3759–3768.
- (78) Gebicki, J. M.; Hicks, M. Ufasomes Are Stable Particles Surrounded by Unsaturated Fatty Acid Membranes. *Nature* **1973**, *243* (5404), 232–234.
- (79) Joannic, R.; Auvray, L.; Lasic, D. D. Monodisperse Vesicles Stabilized by Grafted Polymers. *Phys. Rev. Lett.* **1997**, *78* (17), 3402–3405.
- (80) Kunieda, H.; Nakamura, K.; Olsson, U. and Lindman, B. Spontaneous Formation of Reverse Vesicles. *J. Phys. colloid Chem.* **1993**, *97*, 9525–9531.
- (81) Helfrich, W. Size Distributions of Vesicles : The Role of the Effective Rigidity of Membranes. *J. Phys. Fr.* **1986**, *47* (2), 321–329.
- (82) Jung, H. T.; Coldren, B.; Zasadzinski, J. A.; Iampietro, D. J.; Kaler, E. W. The Origins of Stability of Spontaneous Vesicles. *PNAS* **2001**, *98*, 1353–1357.
- (83) Hentze, H.-P.; Raghavan, S. R.; McKelvey, C. A.; Kaler, E. W. Silica Hollow Spheres by Templating of Catanionic Vesicles. *Langmuir* **2003**, *19* (4), 1069–1074.
- (84) Kostarelos, K.; Tadros, T. F.; Luckham, P. F. Physical Conjugation of (Tri-) Block Copolymers to Liposomes toward the Construction of Sterically Stabilized Vesicle Systems. *Langmuir* **1999**, *15* (2), 369–376.
- (85) Semple, S. C.; Chonn, A.; Cullis, P. R. Influence of Cholesterol on the Association of Plasma Proteins with Liposomes. *Biochemistry* **1996**, *35* (8), 2521–2525.
- (86) Hotz, J.; Meier, W. Polymer Particles by Templating of Vesicles. *Adv. Mater.* **1998**, *10*, 1387–1390.
- (87) Mora-Huertas, C. E.; Fessi, H.; Elaissari, A. Polymer-Based Nanocapsules for Drug Delivery. *Int. J. Pharm.* **2010**, *385* (1–2), 113–142.
- (88) Quintanar-Guerrero, D.; Allémann, E.; Fessi, H.; Doelker, E. Preparation Techniques and Mechanisms of Formation of Biodegradable Nanoparticles from Preformed Polymers. *Drug Dev. Ind. Pharm.* **1998**, *24* (12), 1113–1128.
- (89) Rao, J. P.; Geckeler, K. E. Polymer Nanoparticles: Preparation Techniques and Size-Control Parameters. *Prog. Polym. Sci.* **2011**, *36* (7), 887–913.
- (90) Jeong, Y.-I.; Cho, C.-S.; Kim, S.-H.; Ko, K.-S.; Kim, S.-I.; Shim, Y.-H.; Nah, J.-W. Preparation of Poly(DL-Lactide-Co-Glycolide) Nanoparticles without Surfactant. *J. Appl. Polym. Sci.* *80* (12), 2228–2236.
- (91) Meziani, M. J.; Pathak, P.; Hurezeanu, R.; Thies, M. C.; Enick, R. M.; Sun, Y.-P. Supercritical-Fluid Processing Technique for Nanoscale Polymer Particles. *Angew. Chemie Int. Ed.* **2004**, *43* (6), 704–707.
- (92) Ugelstad, J.; El-Aasser, M. S.; Vanderhoff, J. W. Emulsion Polymerization: Initiation of

- Polymerization in Monomer Droplets. *J. Polym. Sci. Polym. Lett. Ed.*, **1973**, *11* (8), 503–513.
- (93) Landfester, K. Miniemulsion Polymerization and the Structure of Polymer and Hybrid Nanoparticles. *Angewandte Chemie - International Edition*. **2009**, *48*, 4488 – 4507.
- (94) Pavel, F. M. Microemulsion Polymerization. *J. Dispers. Sci. Technol.* **2004**, *25* (1), 1–16.
- (95) Zhang, L.; Eisenberg, A. Multiple Morphologies and Characteristics of “Crew-Cut” Micelle-like Aggregates of Polystyrene-*b*-Poly(Acrylic Acid) Diblock Copolymers in Aqueous Solutions. *J. Am. Chem. Soc.* **1996**, *118* (13), 3168–3181.
- (96) Discher, B. M.; Bermudez, H.; Hammer, D. A.; Discher, D. E.; Won, Y.-Y.; Bates, F. S. Cross-Linked Polymersome Membranes: Vesicles with Broadly Adjustable Properties. *J. Phys. Chem. B*, **2002**, *106* (11), 2848–2854.
- (97) Zhu, Z.; Xu, H.; Liu, H.; González, Y. I.; Kaler, E. W.; Liu, S. Stabilization of Catanionic Vesicles via Polymerization. *J. Phys. Chem. B*, **2006**, *110* (33), 16309–16317.
- (98) Discher, B. M.; Won, Y.-Y.; Ege, D. S.; Lee, J. C.-M.; Bates, F. S.; Discher, D. E.; Hammer, D. A. Polymersomes: Tough Vesicles Made from Diblock Copolymers. *Science*, **1999**, *284* (5417), 1143–1146.
- (99) Ding, J.; Liu, G. Water-Soluble Hollow Nanospheres as Potential Drug Carriers. *J. Phys. Chem. B*, **1998**, *102* (31), 6107–6113.
- (100) Jung, M.; den Ouden, I.; Montoya-Goñi, A.; Hubert, D. H. W.; Frederik, P. M.; van Herk, A. M.; German, A. L. Polymerization in Polymerizable Vesicle Bilayer Membranes. *Langmuir* **2000**, *16* (9), 4185–4195.
- (101) Tundo, P.; Kippenberger, D. J.; Klahn, P. L.; Prieto Nelson, E.; Jao, T. C.; Fendler, J. H. Functionally Polymerized Surfactant Vesicles. Synthesis and Characterization. *J. Am. Chem. Soc.* **1982**, *104* (2), 456–461.
- (102) Murtagh, J.; Thomas, J. K. Mobility and Reactivity in Colloidal Aggregates with Motion Restricted by Polymerization. *Faraday Discuss. Chem. Soc.* **1986**, *81* (0), 127–136.
- (103) Jung, M.; Hubert, D. H. W.; Bomans, P. H. H.; Frederik, P. M.; Meuldijk, J.; van Herk, A. M.; Fischer, H.; German, A. L. New Vesicle–Polymer Hybrids: The Parachute Architecture. *Langmuir* **1997**, *13* (26), 6877–6880.
- (104) Jung, M.; van Casteren, I.; Monteiro, M. J.; van Herk, A. M.; German, A. L. Pulsed-Laser Polymerization in Compartmentalized Liquids. 1. Polymerization in Vesicles. *Macromolecules* **2000**, *33* (10), 3620–3629.
- (105) Hotz, J.; Meier, W. Vesicle-Templated Polymer Hollow Spheres. *Langmuir* **1998**, *14* (5), 1031–1036.
- (106) Morgan, J. D.; Johnson, C. A.; Kaler, E. W. Polymerization of Equilibrium Vesicles. *Langmuir* **1997**, *13* (24), 6447–6451.
- (107) Serrano, J.; Mucino, S.; Millan, S.; Reynoso, R.; Fucugauchi, L. A.; Reed, W.; Nome, F.; Tundo, P.; Fendler, J. H. Polymerized Surfactant Vesicles. Determinations of Rates and Degrees of Polymerization in Vesicles Prepared from Styrene-Containing Surfactants. *Macromolecules* **1985**, *18* (10), 1999–2005.
- (108) Jung, M.; Robinson, B. H.; Steytler, D. C.; German, A. L.; Heenan, R. K. Polymerization of Styrene in DODAB Vesicles: A Small-Angle Neutron Scattering Study. *Langmuir* **2002**, *18* (7), 2873–2879.
- (109) Dergunov, S. A.; Schaub, S. C.; Richter, A.; Pinkhassik, E. Time-Resolved Loading of Monomers into Bilayers with Different Curvature. *Langmuir* **2010**, *26* (9), 6276–6280.

- (110) Mariya D. Kim Sergey A. Dergunov; Pinkhassik, E. Directed Assembly of Vesicle-Templated Polymer Nanocapsules under Near-Physiological Conditions. *Langmuir* **2015**, 31, 2561–2568.
- (111) Kim, M. D.; Dergunov, S. A.; Richter, A. G.; Durbin, J.; Shmakov, S. N.; Jia, Y.; Kenbeilova, S.; Orzabekuly, Y.; Kengpeil, A.; Lindner, E.; et al. Facile Directed Assembly of Hollow Polymer Nanocapsules within Spontaneously Formed Catanionic Surfactant Vesicles. *Langmuir* **2014**, 30 (24), 7061–7069.
- (112) Miksa, B. Recent Progress in Designing Shell Cross-Linked Polymer Capsules for Drug Delivery. *RSC Adv.* **2015**, 5 (107), 87781–87805.
- (113) Ringsdorf, H.; Schlarb, B.; Venzmer, J. Molecular Architecture and Function of Polymeric Oriented Systems: Models for the Study of Organization, Surface Recognition, and Dynamics of Biomembranes. *Angew. Chem., Int. Ed. Engl.* **1988**, 27, 113.
- (114) Bressel, K.; Muthig, M.; Prevost, S.; Gummel, J.; Narayanan, T.; Gradzielski, M. Shaping Vesicles—Controlling Size and Stability by Admixture of Amphiphilic Copolymer. *ACS Nano* **2012**, 6 (7), 5858–5865.
- (115) Bressel, K.; Gradzielski, M. Enhancing the Stability of Spontaneously Self-Assembled Vesicles - the Effect of Polymer Architecture. *Soft Matter* **2015**, 11 (12), 2445–2453.
- (116) Koppel, D. E. Analysis of Macromolecular Polydispersity in Intensity Correlation Spectroscopy: The Method of Cumulants. *J. Chem. Phys.* **1972**, 57 (11), 4814.
- (117) Itakura, M.; Shimada, K.; Matsuyama, S.; Saito, T.; Kinugasa, S. A Convenient Method to Determine the Rayleigh Ratio with Uniform Polystyrene Oligomers. *J. Appl. Polym. Sci.* **2006**, 99 (4), 1953–1959.
- (118) Coumou, D. J. Apparatus for the Measurement of Light Scattering in Liquids: Measurement of the Rayleigh Factor of Benzene and of Some Other Pure Liquids. *J. Colloid Sci.* **1960**, 15 (5), 408–417.
- (119) Hermans, J. J.; Levinson, S. Some Geometrical Factors in Light-Scattering Apparatus. *J. Opt. Soc. Am.* **1951**, 41 (7), 460–465.
- (120) Burchard, W. Solution Properties of Branched Macromolecules. In *Branched Polymers II*; Roovers, J., Ed.; Springer Berlin Heidelberg, **1999**; pp 113–194.
- (121) Guinier, A. La Diffraction Des Rayons X Aux Tres Petits Angles : Applications a l’etude de Phenomenes Ultramicroscopiques. *Ann. Phys. (Paris)*. **1939**, No. 12, 161–237.
- (122) Stuhrmann, H. B. Neutron Small-Angle Scattering of Biological Macromolecules in Solution. *J. Appl. Crystallogr.* **1974**, 7 (2), 173–178.
- (123) Jenkins, P. J.; Donald, A. M. Application of Small-Angle Neutron Scattering to the Study of the Structure of Starch Granules. *Polymer (Guildf)*. **1996**, 37 (25), 5559–5568.
- (124) Melnichenko, Y. B.; Wignall, G. D. Small-Angle Neutron Scattering in Materials Science: Recent Practical Applications. *J. Appl. Phys.* **2007**, 102 (2), 21101.
- (125) Svergun, D. I.; Koch, M. H. J. Small-Angle Scattering Studies of Biological Macromolecules in Solution. *Reports Prog. Phys.* **2003**, 66 (10), 1735.
- (126) Hammouda, B. *Probing the Nanoscale Structures - the SANS Toolbox.*; Gaithersburg, **2008**.
- (127) NIST. Neutron activation and scattering calculator
<https://www.ncnr.nist.gov/resources/activation/>.
- (128) Breßler, I.; Kohlbrecher, J.; Thünemann, A. F. SASfit: A Tool for Small-Angle Scattering Data Analysis Using a Library of Analytical Expressions. *J. Appl. Crystallogr.* **2015**, 48 (5), 1587–1598.

- (129) Feoktystov, A. V.; Frielinghaus, H.; Di, Z.; Jaksch, S.; Pipich, V.; Appavou, M.-S.; Babcock, E.; Hanslik, R.; Engels, R.; Kemmerling, G.; et al. KWS-1 High-Resolution Small-Angle Neutron Scattering Instrument at JCNS: Current State. *J. Appl. Crystallogr.* **2015**, *48* (1), 61–70.
- (130) Pipich, V. QtiKWS www.qtikws.de.
- (131) Lindner, P.; Schweins, R. The D11 Small-Angle Scattering Instrument: A New Benchmark for SANS. *Neutron News* **2010**, *21* (2), 15–18.
- (132) Richard, D.; Ferrand, M.; Kearley, G. J. Analysis and Visualisation of Neutron-Scattering Data. *J. Neutron Res.* **1996**, *4*, 33–39.
- (133) Guinier, A. *X-Ray Diffraction in Crystals, Imperfect Crystals, and Amorphous Bodies*; Courier Corporation, **1994**.
- (134) Walenta, E. Small Angle X-Ray Scattering. Von O. Glatter Und O. Kratky. *Acta Polym.* **1985**, *36* (5), 296.
- (135) Porod, G. Die Röntgenkleinwinkelstreuung von Dichtgepackten Kolloiden Systemen. *Kolloid-Zeitschrift* **1953**, *133* (1), 51.
- (136) Felgin, L. A.; Svergun, D. I. *Structure Analysis by Small-Angle X-Ray and Neutron Scattering*, Plenum Press: New York **1987**.
- (137) Rayleigh, Lord. The Incidence of Light upon a Transparent Sphere of Dimensions Comparable with the Wave-Length. *Proc. R. Soc. London* **1910**, *84* (567), 25–46.
- (138) Benoit H. *Polymers and Neutron Scattering*, 2nd ed.; Clarendon Press: Oxford, **1996**.
- (139) Pedersen, J. S.; Posselt, D.; Mortensen, K. Analytical Treatment of the Resolution Function for Small-Angle Scattering. *J. Appl. Crystallogr.* **1990**, *23* (4), 321–333.
- (140) Wertheim, M. S. Exact Solution of the Percus-Yevick Integral Equation for Hard Spheres. *Phys. Rev. Lett.* **1963**, *10* (8), 321–323.
- (141) Genes, P. G. de. Conformations of Polymers Attached to an Interface. *Macromolecules* **1980**, *13*, 1069–1075.
- (142) Mezei, F. Neutron Spin Echo: A New Concept in Polarized Thermal Neutron Techniques. *Z Phys A Hadron. Nucl.* **1972**, *255*, 146–160.
- (143) Lecture Notes in Physics. In *Neutron spin echo*; Mezei, F., Ed.; Springer-Verlag Berlin Heidelberg, **1980**.
- (144) Hoffmann, I. Neutrons for the Study of Dynamics in Soft Matter Systems. *Colloid Polym. Sci.* **2014**, *292* (9), 2053–2069.
- (145) Monkenbusch, M.; Richter, D. Neutron Spin Echo Spectroscopy. In *Neutrons in Soft Matter*; Wiley-Blackwell, **2011**; pp 147–182.
- (146) Schleger, P.; Alefeld, B.; Barthelemy, J. F.; Ehlers, G.; Farago, B.; Giraud, P.; Hayes, C.; Kollmar, A.; Lartigue, C.; Mezei, F.; et al. The Long-Wavelength Neutron Spin-Echo Spectrometer IN15 at the Institut Laue-Langevin. *Phys. B Condens. Matter* **1997**, *241–243* (Supplement C), 164–165.
- (147) Zemb, T.; Lindner, P. *Neutron, X-Rays and Light. Scattering Methods Applied to Soft Condensed Matter, 1st Edition*; **2002**, North Holland: Delta Series – Elsevier.
- (148) Hoffmann, I. Neutrons for the Study of Dynamics in Soft Matter Systems. *Colloid Polym. Sci.* **2014**, *292* (9), 2053–2069.
- (149) Walker, L. M. Rheology and Structure of Worm-like Micelles. *Curr. Opin. Colloid Interface*

- Sci.* **2001**, *6* (5–6), 451–456.
- (150) Annable, T.; Buscall, R.; Ettelaie, R.; Whittlestone, D. The Rheology of Solutions of Associating Polymers: Comparison of Experimental Behavior with Transient Network Theory. *J. Rheol.* **1993**, *37* (4), 695–726.
- (151) Larson, R. G. Going with the Flow. *Science* **2007**, *318* (5847), 57–58.
- (152) Hoffmann, H. Viscoelastic Surfactant Solutions. In *Structure and Flow in Surfactant Solutions*; ACS Symposium Series, **1994**; pp 2–31.
- (153) Yasuda, K.; Armstrong, R. C.; Cohen, R. E. Shear Flow Properties of Concentrated Solutions of Linear and Star Branched Polystyrenes. *Rheol. Acta* **1981**, *20* (2), 163–178.
- (154) Kautsky, H. Quenching of Luminescence by Oxygen. *Trans. Faraday Soc.* **1939**, *35*, 216–219.
- (155) Hariharan, C.; Vijaysree, V.; Mishra, A. K. Quenching of 2,5-Diphenyloxazole (PPO) Fluorescence by Metal Ions. *J. Lumin.* **1997**, *75* (3), 205–211.
- (156) Holmes, A. S.; Birch, D. J. S.; Suhling, K.; Imhof, R. E.; Salthammer, T.; Dreeskamp, H. Evidence for Donor—donor Energy Transfer in Lipid Bilayers: Perylene Fluorescence Quenching by CO₂⁺ Ions. *Chem. Phys. Lett.* **1991**, *186* (2), 189–194.
- (157) Quenching of Fluorescence. In *Principles of Fluorescence Spectroscopy*; Lakowicz, J. R., Ed.; Springer US: Boston, MA, **2006**; pp 277–330.
- (158) Dreiss, C. A. Wormlike Micelles: Where Do We Stand? Recent Developments, Linear Rheology and Scattering Techniques. *Soft Matter* **2007**, *3* (8), 956–970.
- (159) Shibaev, A. V.; Molchanov, V. S.; Philippova, O. E. Rheological Behavior of Oil-Swollen Wormlike Surfactant Micelles. *J. Phys. Chem. B* **2015**, *119* (52), 15938–15946.
- (160) Gerber, M. J.; Kline, S. R.; Walker, L. M. Characterization of Rodlike Aggregates Generated from a Cationic Surfactant and a Polymerizable Counterion. *Langmuir* **2004**, *20* (20), 8510–8516.
- (161) Gerber, M. J.; Walker, L. M. Controlling Dimensions of Polymerized Micelles: Micelle Template versus Reaction Conditions. *Langmuir* **2006**, *22* (3), 941–948.
- (162) Schulz, P. C.; Minardi, R. M.; Vuano, B. Solubilization of Styrene in the Catanionic System Dodecyltrimethylammonium Hydroxide-n-Dodecanephosphonic Acid. *Colloid Polym. Sci.* **1998**, *276* (3), 278–281.
- (163) Becerra, F.; Soltero, J. F. A.; Puig, J. E.; Schulz, P. C.; Esquena, J.; Solans, C. Free-Radical Polymerization of Styrene in Worm-like Micelles. *Colloid Polym. Sci.* **2003**, *282* (2), 103–109.
- (164) Steytler, D. C.; Gurgel, A.; Ohly, R.; Jung, M.; Heenan, R. K. Retention of Structure in Microemulsion Polymerization: Formation of Nanolatices. *Langmuir* **2004**, *20* (11), 3509–3512.
- (165) Beck, R.; Gradzielski, M.; Horbaschek, K.; Shah, S. S.; Hoffmann, H.; Strunz, P. Phase Behavior, Structure, and Physical Properties of the Quaternary System Tetradecyldimethylamine Oxide, HCl, 1-Hexanol, and Water. *J. Colloid Interface Sci.* **2000**, *221* (2), 200–209.
- (166) Oda, R.; Bourdieu, L.; Schmutz, M. Micelle to Vesicle Transition Induced by Cosurfactant: Rheological Study and Direct Observations. *J. Phys. Chem. B* **1997**, *101* (31), 5913–5916.
- (167) Hoffmann, H. Correlation between Surface and Interfacial Tensions with Micellar Structures and Properties of Surfactant Solutions. In *Progress in Colloid and Polymer Science*; Findenegg, G. H., Ed.; Steinkopff: Darmstadt, **1990**; Vol. 83, pp 16–28.

- (168) Gradzielski, M.; Müller, M.; Bergmeier, M.; Hoffmann, H.; Hoinkis, E. Structural and Macroscopic Characterization of a Gel Phase of Densely Packed Monodisperse, Unilamellar Vesicles. *J. Phys. Chem. B* **1999**, *103* (9), 1416–1424.
- (169) Lane, W. H. Determination of the Solubility of Styrene in Water and of Water in Styrene. *Ind. Eng. Chem. Anal. Ed.* **1946**, *18* (5), 295–296.
- (170) Hoffmann, H.; Thunig, C.; Munkert, U.; Meyer, H.; Richter, W. From Vesicles to the L₃ (Sponge) Phase in Alkyldimethylamine Oxide Heptanol Systems. *Langmuir* **1992**, *8*, 2629–2638.
- (171) Borné, J.; Nylander, T.; Khan, A. Vesicle Formation and Other Structures in Aqueous Dispersions of Monoolein and Sodium Oleate. *J. Colloid Interface Sci.* **2003**, *257* (2), 310–320.
- (172) Brasher, L. L.; Herrington, K. L.; Kaler, E. W. Electrostatic Effects on the Phase-Behavior of Aqueous Cetyltrimethylammonium Bromide and Sodium Octyl Sulfate Mixtures with Added Sodium-Bromide. *Langmuir* **1995**, *11* (11), 4267–4277.
- (173) de la Torre, J. G.; Bloomfield, V. A. Hydrodynamic Properties of Complex, Rigid, Biological Macromolecules: Theory and Applications. *Q. Rev. Biophys.* **1981**, *14* (01), 81.
- (174) Hassan, P. A.; Raghavan, S. R.; Kaler, E. W. Microstructural Changes in SDS Micelles Induced by Hydrotropic Salt. *Langmuir* **2002**, *18* (7), 2543–2548.
- (175) Gorski, N.; Kalus, J. Determination of the Structure of Tetradecyldimethylaminoxide Micelles in Water by Small-Angle Neutron Scattering. *J. Phys. Chem. B* **1997**, *101*, 4390–4393.
- (176) Hoffmann, H.; Thunig, C.; Valiente, M. The Different Phases and Their Macroscopic Properties in Ternary Surfactant Systems of Alkyldimethylamine Oxides, Intermediate Chain n-Alcohols and Water. *Colloids and Surfaces* **1992**, *67* (Supplement C), 223–237.
- (177) Gennes, P. G. de. Conformations of Polymers Attached to an Interface. *Macromolecules* **1980**, *13*, 1069–1075.
- (178) Iampietro, D. J.; Kaler, E. W. Phase Behavior and Microstructure of Aqueous Mixtures of Cetyltrimethylammonium Bromide and Sodium Perfluorohexanoate. *Langmuir* **1999**, *15* (25), 8590–8601.
- (179) Barnes, H.A., Hutton, J.F., and Walters, K. *An Introduction to Rheology*; Elsevier: Amsterdam, The Netherlands, 1989.
- (180) Cates, M. E. Flow Behaviour of Entangled Surfactant Micelles. *J. Phys. Condens. Matter* **1996**, *8* (47), 9167–9176.
- (181) Ai, H.; Gao, J. Size-Controlled Polyelectrolyte Nanocapsules via Layer-by-Layer Self-Assembly. *J. Mater. Sci.* **2004**, *39* (4), 1429–1432.
- (182) Wang, X.; Danoff, E. J.; Sinkov, N. A.; Lee, J. H.; Raghavao, S. R.; English, D. S. Highly Efficient Capture and Long-Term Encapsulation of Dye by Catanionic Surfactant Vesicles. *Langmuir* **2006**, *22* (15), 6461–6464.
- (183) Danoff, E. J.; Wang, X.; Tung, S. H.; Sinkov, N. A.; Kemme, A. M.; Raghavan, S. R.; English, D. S. Surfactant Vesicles for High-Efficiency Capture and Separation of Charged Organic Solutes. *Langmuir* **2007**, *23* (17), 8965–8971.
- (184) De, M.; Ghosh, P. S.; Rotello, V. M. Applications of Nanoparticles in Biology. *Adv. Mater.* **2008**, *20* (22), 4225–4241.
- (185) Jain, P. K.; Lee, K. S.; El-Sayed, I. H.; El-Sayed, M. A. Calculated Absorption and Scattering Properties of Gold Nanoparticles of Different Size, Shape, and Composition: Applications in Biological Imaging and Biomedicine. *J. Phys. Chem. B* **2006**, *110* (14), 7238–7248.

- (186) Soppimath, K. S.; Tan, D. C.-W.; Yang, Y.-Y. PH-Triggered Thermally Responsive Polymer Core-Shell Nanoparticles for Drug Delivery. *Adv. Mater.* **2005**, *17* (3), 318–323.
- (187) Maliakal, A.; Katz, H.; Cotts, P. M.; Subramoney, S.; Mirau, P. Inorganic Oxide Core, Polymer Shell Nanocomposite as a High K Gate Dielectric for Flexible Electronics Applications. *J. Am. Chem. Soc.* **2005**, *127* (42), 14655–14662.
- (188) Guchhait, A.; Pal, A. J. Correlation between Photoinduced Electron Transfer and Photovoltaic Characteristics in Solar Cells Based on Hybrid Core–Shell Nanoparticles. *J. Phys. Chem. C* **2010**, *114* (45), 19294–19298.
- (189) Herrington, K. L.; Kaler, E. W.; Miller, D. D.; Zasadzinski, J. A.; Chiruvolu, S. Phase Behavior of Aqueous Mixtures of Dodecyltrimethylammonium Bromide (DTAB) and Sodium Dodecyl Sulfate (SDS). *J. Phys. Chem.* **1993**, *97* (51), 13792–13802.
- (190) Schmölder, S.; Gräbner, D.; Gradzielski, M.; Narayanan, T. Millisecond-Range Time-Resolved Small-Angle X-Ray Scattering Studies of Micellar Transformations. *Phys. Rev. Lett.* **2002**, *88* (25), 258301–258304.
- (191) Wolf, C.; Bressel, K.; Drechsler, M.; Gradzielski, M. Comparison of Vesicle Formation in Zwitterionic and Catanionic Mixtures of Hydrocarbon and Fluorocarbon Surfactants: Phase Behavior and Structural Progression. *Langmuir* **2009**, *25* (19), 11358–11366.
- (192) Bressel, K.; Muthig, M.; Prévost, S.; Grillo, I.; Gradzielski, M. Mesodynamics: Watching Vesicle Formation in Situ by Small-Angle Neutron Scattering. *Colloid Polym. Sci.* **2010**, *288* (8), 827–840.
- (193) Bergström, M. Reversibly Formed Bilayer Vesicles: Energetics and Polydispersity. In *Trends in Colloid and Interface Science XI*; Rosenholm, J. B., Lindman, B., Stenius, P., Eds.; Steinkopff: Darmstadt, **1997**; pp 214–219.
- (194) Ringsdorf, H.; Schlarb, B.; Venzmer, J. Molekulare Architektur Und Funktion von Polymeren Orientierten Systemen – Modelle Für Das Studium von Organisation, Oberflächenerkennung Und Dynamik Bei Biomembranen. *Angew. Chemie* **1988**, *100* (1), 117–162.
- (195) Kurja, J.; Nolt, R. J. M. Free Radical Polymerization of Styrene in Dioctadecyldimethylammonium Bromide Vesicles. *Polymer (Guildf)*. **1993**, *34* (10), 2045–2049.
- (196) Meier, W. Polymer Nanocapsules. *Chem. Soc. Rev.*, **2000**, *29*, 295–303.
- (197) McKelvey, C. A.; Kaler, E. W.; Zasadzinski, J. A.; Coldren, B.; Jung, H.-T. Templating Hollow Polymeric Spheres from Catanionic Equilibrium Vesicles: Synthesis and Characterization. *Langmuir* **2000**, *16* (22), 8285–8290.
- (198) O’Neil, M. J. (ed.). The Merck Index - An Encyclopedia of Chemicals, Drugs, and Biologicals; Whitehouse Station NJ: Merck and Co., Inc., **2006**; p 253.
- (199) IPCS Inchem <http://www.inchem.org/documents/icsc/icsc/eics1288.htm>.
- (200) ILO-ICSC www.ilo.org/dyn/icsc/showcard.display?p_version=2&p_card_id=1743.
- (201) *Handbook of Detergents, Part D*; Showell, M. S., Ed.; CRC Press: Boca Raton, **2006**.
- (202) Yalcinkaya, H.; Bressel, K.; Lindner, P.; Gradzielski, M. Controlled Formation of Vesicles with Added Styrene and Their Fixation by Polymerization. *J. Colloid Interface Sci.* **2018**, *531*, 672–680.
- (203) Abe, M.; Tokuoka, Y.; Uchiyama, H.; Ogino, K.; Scamehorn, J. F.; Christian, S. D. Expansion of Mixed Anionic—non-Ionic Micelles Caused by Solubilization of Organic Solutes. *Colloids and Surfaces* **1992**, *67*, 37–43.

- (204) Attwood, D.; Currie, L. R. J.; Elworthy, P. H. Studies of Solubilized Micellar Solutions. I. Phase Studies and Particle Size Analysis of Solutions Formed with Nonionic Surfactants. *J. Colloid Interface Sci.* **1974**, *46* (2), 249–254.
- (205) Baglioni, P.; Gambi, C. M. C.; Giordano, R.; Senatra, D. SANS Study of a Fluorinated Water-in-Oil Microemulsion. *J. Mol. Struct.* **1996**, *383* (1–3), 165–169.
- (206) Gorski, N.; Gradzielski, M.; Hoffmann, H. Mixtures of Nonionic and Ionic Surfactants. The Effect of Counterion Binding in Mixtures of Tetradecyldimethylamine Oxide and Tetradecyltrimethylammonium Bromide. *Langmuir* **1994**, *10* (8), 2594–2603.
- (207) Rambo, R. P.; Tainer, J. A. Characterizing Flexible and Intrinsically Unstructured Biological Macromolecules by SAS Using the Porod-Debye Law. *Biopolymers* **2011**, *95* (8), 559–571.
- (208) Richter, A. G.; Dergunov, S. A.; Ganus, B.; Thomas, Z.; Pingali, S. V.; Urban, V.; Liu, Y.; Porcar, L.; Pinkhassik, E. Scattering Studies of Hydrophobic Monomers in Liposomal Bilayers: An Expanding Shell Model of Monomer Distribution. *Langmuir* **2011**, *27* (7), 3792–3797.
- (209) Hoffmann, I.; Hoffmann, C.; Farago, B.; Prévost, S.; Gradzielski, M. Dynamics of Small Unilamellar Vesicles. *J. Chem. Phys.* **2018**, *148* (10), 104901.
- (210) Milner, S. T.; Safran, S. A. Dynamical Fluctuations of Droplet Microemulsions and Vesicles. *Phys. Rev. A* **1987**, *36*, 4371–4379.
- (211) Safran S. A. Fluctuations of Spherical Microemulsions. *J. Chem. Phys.* **1983**, *78*, 2073–2076.
- (212) Hoffmann, I.; Hoffmann, C.; Farago, B.; Prévost, S.; Gradzielski, M. Dynamics of Small Unilamellar Vesicles. *J. Chem. Phys.* **2018**, *148* (10), 104901.
- (213) Zilman, A. G.; Granek, R. Undulations and Dynamic Structure Factor of Membranes. *Phys. Rev. Lett.* **1996**, *77* (23), 4788–4791.
- (214) Zilman, A. G.; Granek, R. Membrane Dynamics and Structure Factor. *Chem. Phys.* **2002**, *284* (1–2), 195–204.
- (215) Monkenbusch, M.; Holderer, O.; Frielinghaus, H.; Byelov, D.; Allgaier, J.; Richter, D. Bending Moduli of Microemulsions; Comparison of Results from Small Angle Neutron Scattering and Neutron Spin-Echo Spectroscopy. *J. Phys. Condens. Matter* **2005**, *17* (31), S2903.
- (216) Komura, S.; Takeda, T.; Kawabata, Y.; Ghosh, S. K.; Seto, H.; Nagao, M. Dynamical Fluctuation of the Mesoscopic Structure in Ternary C12E5-Water-n-Octane Amphiphilic System. *Phys. Rev. E* **2001**, *63* (4), 41402.
- (217) Seifert, U.; Langer, S. A. Viscous Modes of Fluid Bilayer Membranes. *EPL (Europhysics Lett.)* **1993**, *23* (1), 71.
- (218) Farago, B.; Monkenbusch, M.; Goecking, K. D.; Richter, D.; Huang, J. S. Dynamics of Microemulsions as Seen by Neutron Spin Echo. *Phys. B Condens. Matter* **1995**, *213*, 712–717.
- (219) Hoffmann, I.; Heunemann, P.; Farago, B.; Grillo, I.; Holderer, O.; Päch, M.; Gradzielski, M. Structure and Dynamics of Nanoemulsions: Insights from Combining Dynamic and Static Neutron Scattering. *Phys. Rev. E* **2012**, *86* (6), 61407.
- (220) Farago, B.; Monkenbusch, M.; Goecking, K. D.; Richter, D.; Huang, J. S. Dynamics of Microemulsions as Seen by Neutron Spin Echo. *Phys. B Condens. Matter* **1995**, *213–214*, 712–717.
- (221) Komura, S.; Takeda, T.; Kawabata, Y.; Ghosh, S. K.; Seto, H.; Nagao, M. Dynamical Fluctuation of the Mesoscopic Structure in Ternary C12E5-Water-n-Octane Amphiphilic System. *Phys. Rev. E* **2001**, *63* (4), 41402.
- (222) Kaler, E. W.; Herrington, K. L.; Murthy, A. K.; Zasadzinski, J. A. N. Phase Behavior and

- Structures of Mixtures of Anionic and Cationic Surfactants. *J. Phys. Chem.* **1992**, *96* (16), 6698–6707.
- (223) Caillet, C.; Hebrant, M.; Tondre, C. Sodium Octyl Sulfate/Cetyltrimethylammonium Bromide Catanionic Vesicles: Aggregate Composition and Probe Encapsulation. *Langmuir* **2000**, *16* (23), 9099–9102.
- (224) Zhao, G.-X.; Yu, W.-L. Vesicles from Mixed Sodium 10-Undecenoate-Decyltrimethylammonium Bromide Solutions. *J. Colloid Interface Sci.* **1995**, *173* (1), 159–164.
- (225) Rigler, P.; Meier, W. Encapsulation of Fluorescent Molecules by Functionalized Polymeric Nanocontainers: Investigation by Confocal Fluorescence Imaging and Fluorescence Correlation Spectroscopy. *J. Am. Chem. Soc.* **2006**, *128* (1), 367–373.
- (226) Maherani, B.; Arab-Tehrany, E.; Kheiriloom, A.; Geny, D.; Linder, M. Calcein Release Behavior from Liposomal Bilayer; Influence of Physicochemical/Mechanical/Structural Properties of Lipids. *Biochimie* **2013**, *95* (11), 2018–2033.
- (227) Fischer, A.; Hebrant, M.; Tondre, C. Glucose Encapsulation in Catanionic Vesicles and Kinetic Study of the Entrapment/Release Processes in the Sodium Dodecyl Benzene Sulfonate/Cetyltrimethylammonium Tosylate/Water System. *J. Colloid Interface Sci.* **2002**, *248* (1), 163–168.
- (228) Hamann, S.; Kiilgaard, J. F.; Litman, T.; Alvarez-Leefmans, F. J.; Winther, B. R.; Zeuthen, T. Measurement of Cell Volume Changes by Fluorescence Self-Quenching. *J. Fluoresc.* **2002**, *12* (2), 139–145.
- (229) Uchegbu, I. F.; Vyas, S. P. Non-Ionic Surfactant Based Vesicles (Niosomes) in Drug Delivery. *Int. J. Pharm.* **1998**, *172* (1), 33–70.
- (230) Guchhait, A.; Pal, A. J. Correlation between Photoinduced Electron Transfer and Photovoltaic Characteristics in Solar Cells Based on Hybrid Core–Shell Nanoparticles. *J. Phys. Chem. C* **2010**, *114* (45), 19294–19298.
- (231) Jutta, H.; Wolfgang, M. Polymer Particles by Templating of Vesicles. *Adv. Mater.* **1999**, *10* (16), 1387–1390.
- (232) Martin Jung Brian H. Robinson, D. C. S. A. L. G.; Heena, R. K. Polymerization of Styrene in DODAB Vesicles: A Small-Angle Neutron Scattering Study. *Langmuir* **2002**, *18*, 2873–2879.
- (233) Bressel, K.; Prevost, S.; Appavou, M.-S.; Tiersch, B.; Koetz, J.; Gradzielski, M. Phase Behaviour and Structure of Zwitterionic Mixtures of Perfluorocarboxylates and Tetradecyldimethylamine Oxide-Dependence on Chain Length of the Perfluoro Surfactant. *Soft Matter* **2011**, *7* (23), 11232–11242.
- (234) Yalcinkaya, H.; Feoktystov, A.; Gradzielski, M. Formation of Well-Defined Vesicles by Styrene Addition to a Nonionic Surfactant and Their Polymerization Leading to Viscous Hybrid Systems. *Langmuir* **2018**, *34* (31), 9184–9194.

9 Appendix

9.1 Appendix of Chapter 4

9.1.1 Refractive Index Increment

Table A1. Refractive index increments for different concentration of styrene in 50 mM TDMAO / 0.5 mM L35 at 25 °C:

Styrene amount (mM)	dn/dc (ml/g)
0	0.1490
10	0.1498
20	0.1505
30	0.1512
40	0.1517
50	0.1522
60	0.1526
70	0.1530
80	0.1534
90	0.1537
100	0.1540
120	0.1545
140	0.1549
150	0.1551
180	0.1556
200	0.1558

9.1.2 Determination of Aggregation Numbers

Aggregation numbers, N_{agg} , were calculated for surfactant by using the formula:

$$N_{agg} = V \cdot \rho \cdot \frac{N_A}{M_{wi}}$$

where V is the volume, N_A Avogadro's number, ρ is the density, and M_{wi} is a sum of the molecular weight of components due to the molar fractions x , in each sample.

9.1.3 Density of the aggregates

The aggregate densities were derived from the dilution series at constant composition of samples for 0-50 mM. For higher styrene concentrations, values were obtained via:

$$\rho = \frac{\chi_{TDMAO}M_{TDMAO} + \chi_{L35}M_{L35} + \chi_{styrene}M_{styrene}}{\chi_{TDMAO}V_{molTDMAO} + \chi_{L35}V_{molL35} + \chi_{styrene}V_{molstyrene}}$$

χ_i is the mole fraction of the component i in the sample, M_{TDMAO} is the molecular weight, and V_{mol} is the molar volume.

Table A2. The density of the aggregates for samples of 50 mM TDMAO / 0.5 mM L35 / Styrene.

Styrene amount (mM)	d/(g/ml)
0	0.9131
10	0.9126
20	0.9122
30	0.9118
40	0.9114
50	0.9111
60	0.9109
70	0.9106
80	0.9104
90	0.9102
100	0.9100
120	0.9097
140	0.9094
150	0.9093
180	0.9090
200	0.9088

9.1.4 Kratky-Porod Plots

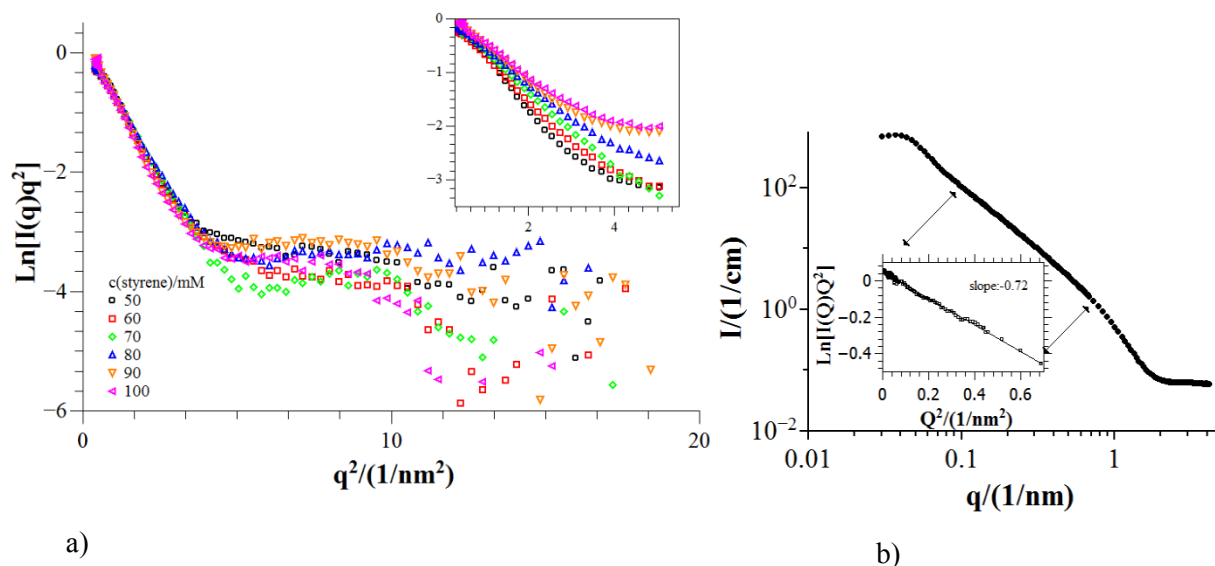
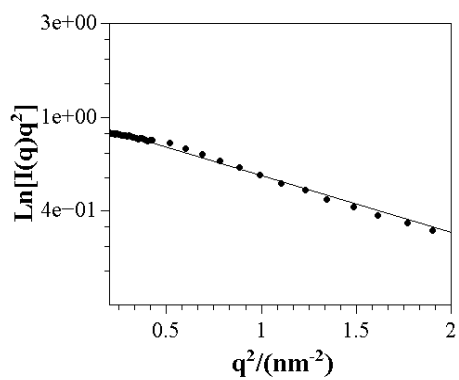
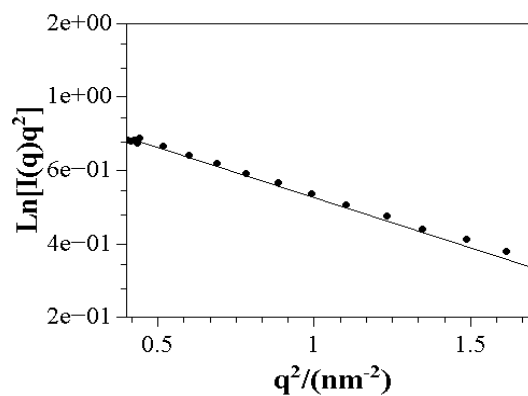


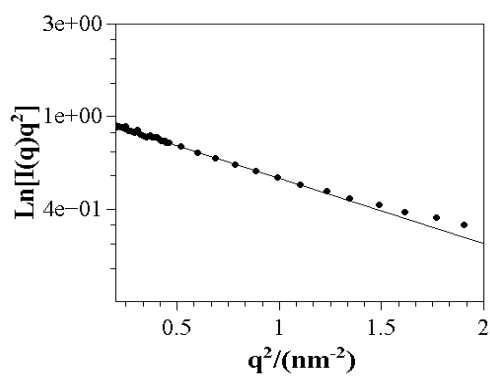
Figure A1. a) Background subtracted Kratky–Porod plots of the scattering curves for 50 mM TDMAO/0.5 mM L35/styrene (50-60-70-80-90-100 mM). b) SANS curve of 50 mM TDMAO / 0.5 mM L35 / 70 mM styrene. Inset shows the Kratky-Porod plot to the q region indicated by arrows. The fitted curves for samples containing 50-60-70-80-90-100 mM styrene concentrations can be seen below.



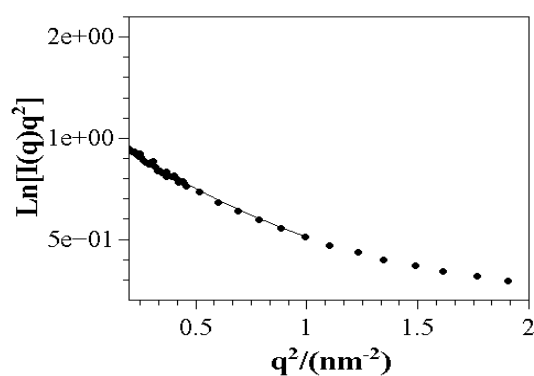
Sample: 50 mM TDMAO / 0.5 mM L35 / 50 mM styrene.



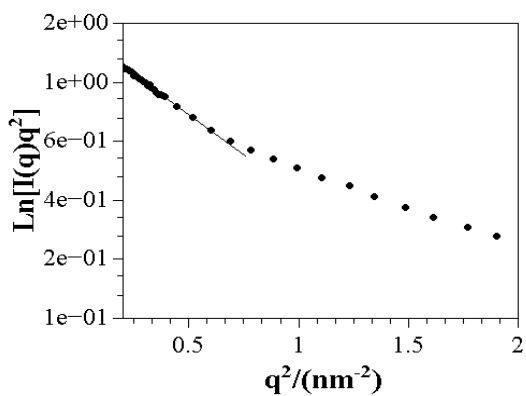
Sample: 50 mM TDMAO / 0.5 mM L35 / 60 mM styrene.



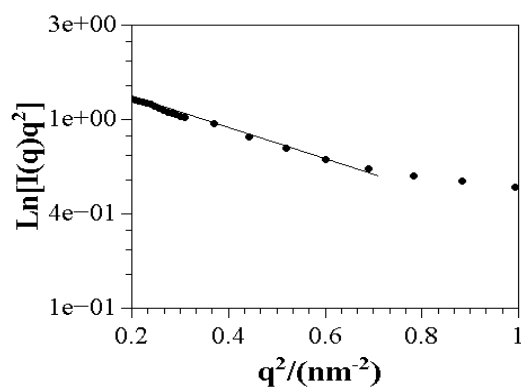
Sample: 50 mM TDMAO / 0.5 mM L35 / 70 mM styrene



Sample: 50 mM TDMAO / 0.5 mM L35 / 80 mM styrene.



Sample: 50 mM TDMAO / 0.5 mM L35 / 90 mM styrene.



Sample: 50 mM TDMAO / 0.5 mM L35 / 100 mM styrene.

Figure A2. The fitted Kratky-Porod curves for samples containing 50-60-70-80-90-100 mM styrene concentrations.

9.1.5 Small Angle Neutron Scattering (SANS) of Polymerized Samples

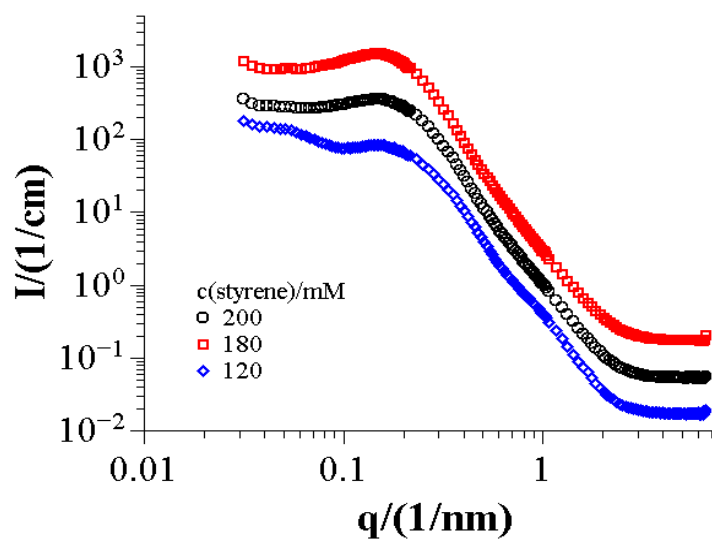


Figure A3. SANS intensity patterns of polymerized 50 mM TDMAO / 0.5 mM L35 / styrene mixtures at 25 °C.

9.2 Appendix of Chapter 5

9.2.1 Refractive Index Increment

Table A3. Refractive index increments for different ratio of styrene to 27.5 mM TDMAO / 0.275 mM L35 / 22.5 mM LiPFOS at 25°C.

Styrene amount (mM)	dn/dc (ml/g)
0	0.0598
10	0.0740
15	0.0795
20	0.0844
25	0.0886
30	0.0925
35	0.0959
38	0.0977
41	0.0995
44	0.1013
46	0.1024
50	0.1044
58	0.1081

9.2.2 Kratky-Porod Plots

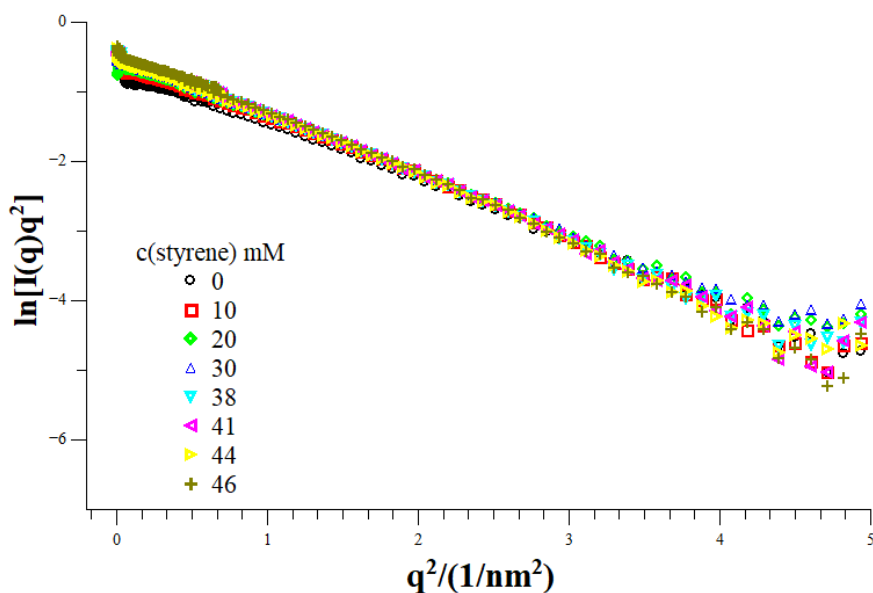


Figure A4. Background subtracted Kratky-Porod plots of the scattering curves for 27.5 mM TDMAO/0.27 mM L35/ 22.5 mM LiPFOS/styrene (0-10-20-30-38-41-44-46 mM).

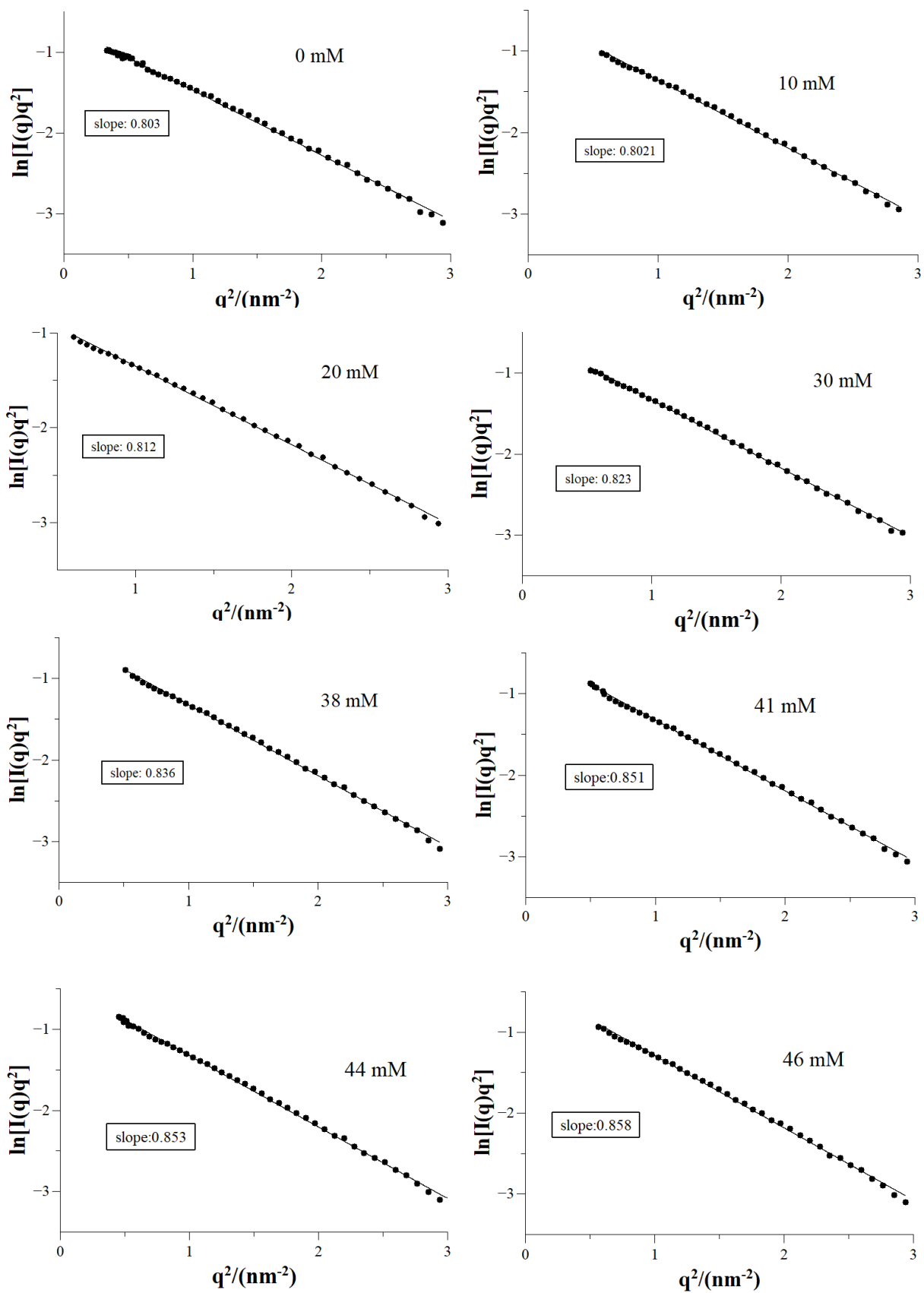


Figure A5. The fitted Kratky-Porod curves for samples containing 27.5 mM TDMAO / 0.275 mM L35 / 22.5 mM LiPFOS / different styrene amounts.

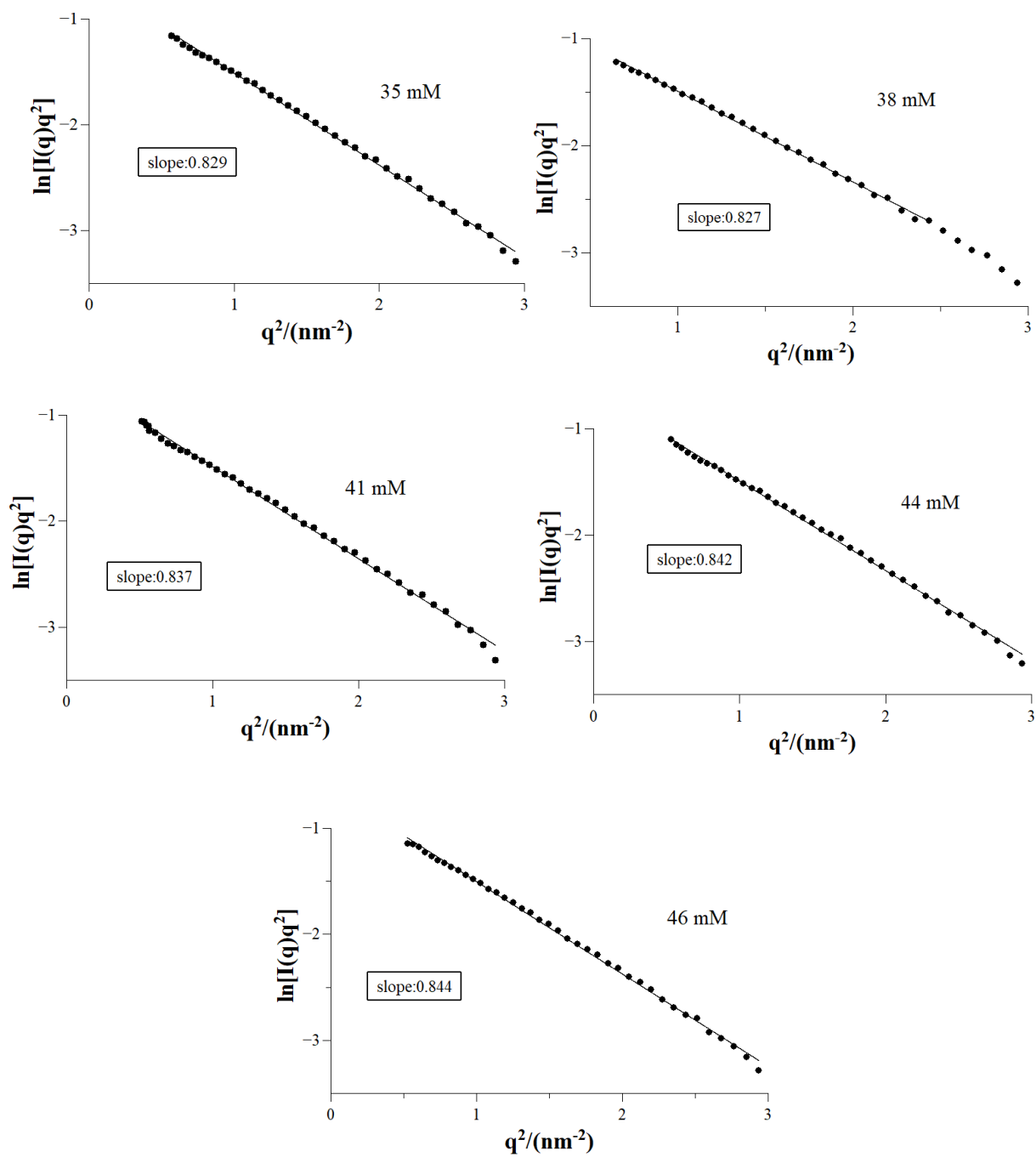


Figure A6. The fitted Kratky-Porod curves for samples of cross-linked polymerized samples containing 27.5 mM TDMAO / 0.275 mM L35 / 22.5 mM LiPFOS / different styrene amounts with 0.1 ratio of cross-linker.

9.2.3 Small Angle Neutron Scattering (SANS) of Samples after 1.5 Years

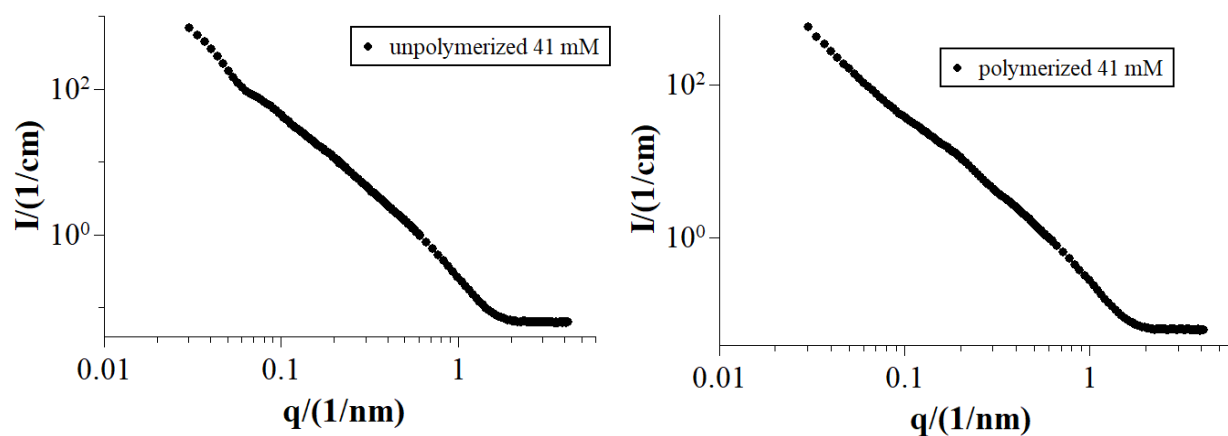


Figure A7. SANS curves of two samples after 1.5 years of preparation. Left: 41 mM styrene loaded vesicle of 27.5 mM TDMAO / 0.275 mM L35 / 22.5 mM LiPFOS, Right: cross-linked polymerized sample of 41 mM styrene / 27.5 mM TDMAO / 0.275 mM L35 / 22.5 mM LiPFOS at 25 °C

9.2.4 Small Angle Neutron Scattering (SANS) of samples before and after polymerization

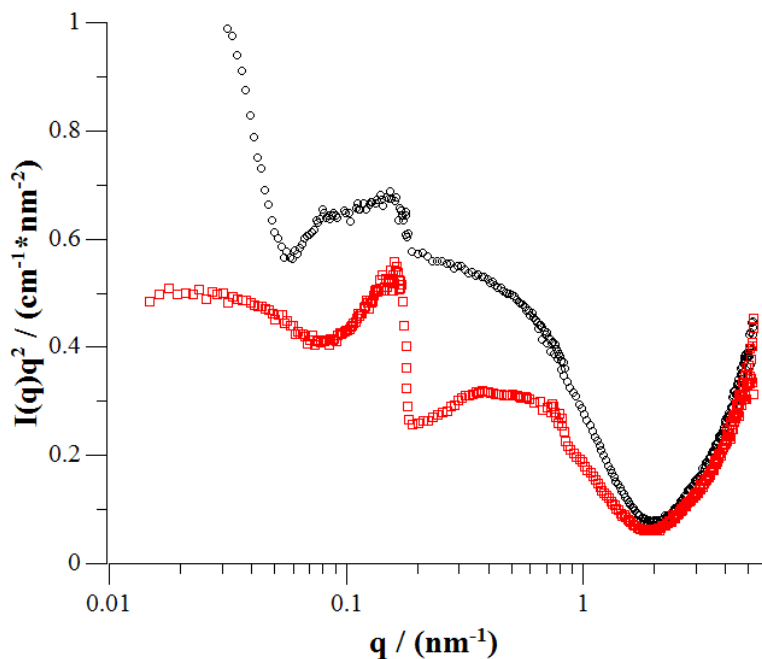


Figure A8. $I(q)q^2$ vs q plot of the SANS data for sample 27.5 mM TDMAO / 0.275 mM L35 / 22.5 mM LiPFOS / 38 mM styrene *black square*: before polymerization, *red circle*: after polymerization.

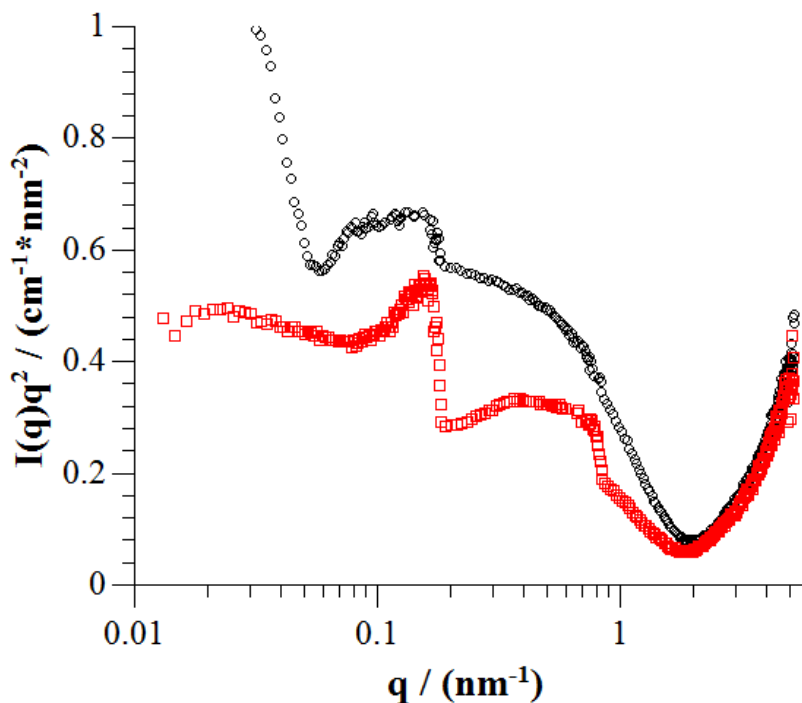


Figure A9. $I(q)q^2$ vs q plot of the SANS data for sample 27.5 mM TDMAO / 0.275 mM L35 / 22.5 mM LiPFOS / 41 mM styrene *black square*: before polymerization, *red circle*: after polymerization.

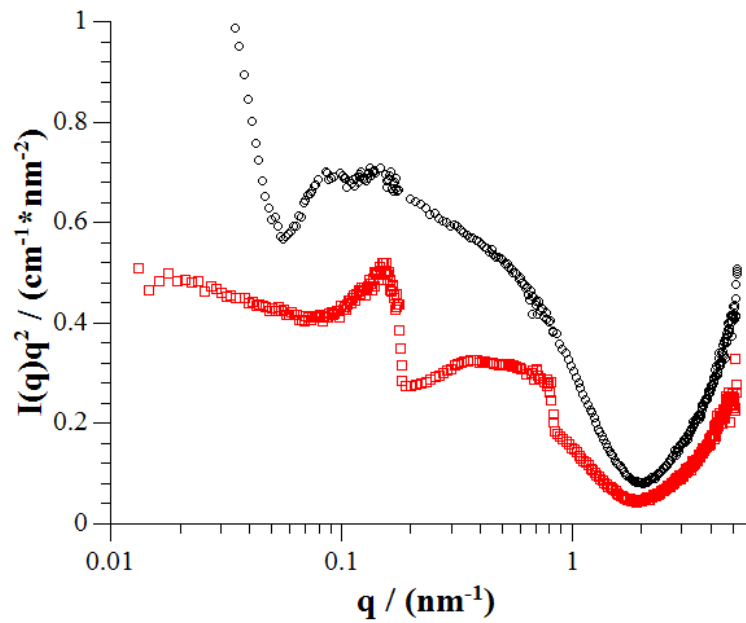


Figure A10. $I(q)q^2$ vs q plot of the SANS data for sample 27.5 mM TDMAO / 0.275 mM L35 / 22.5 mM LiPFOS / 44 mM styrene *black square*: before polymerization, *red circle*: after polymerization.

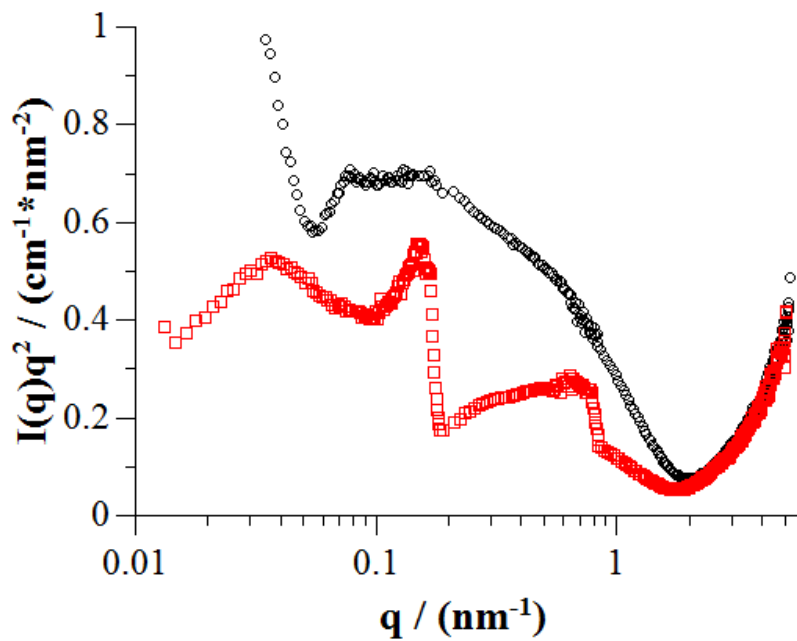


Figure A11. $I(q)q^2$ vs q plot of the SANS data for sample 27.5 mM TDMAO / 0.275 mM L35 / 22.5 mM LiPFOS / 46 mM styrene *black square*: before polymerization, *red circle*: after polymerization.

9.2.5 Calculation of the Polymer Shell Thickness

Assuming a full conversion of monomer, the volume of polystyrene was calculated via:

$$V_{polystyrene} = \frac{N_{agg\ monomer} \cdot MW_{monomer}}{density_{(in\ bulk)} N_A}$$
, then dividing by the surface area for the vesicle

(radius= $R_0 + D/2$, from SANS), the thickness of the polymer shell was theoretically deduced:

$$t_{polystyrene} = \frac{V_{polystyrene}}{4\pi(R_0 + D/2)^2}$$

9.3 Appendix of Chapter 6

9.3.1 Appendix to Studies with Dodecyl Acrylate Monomer

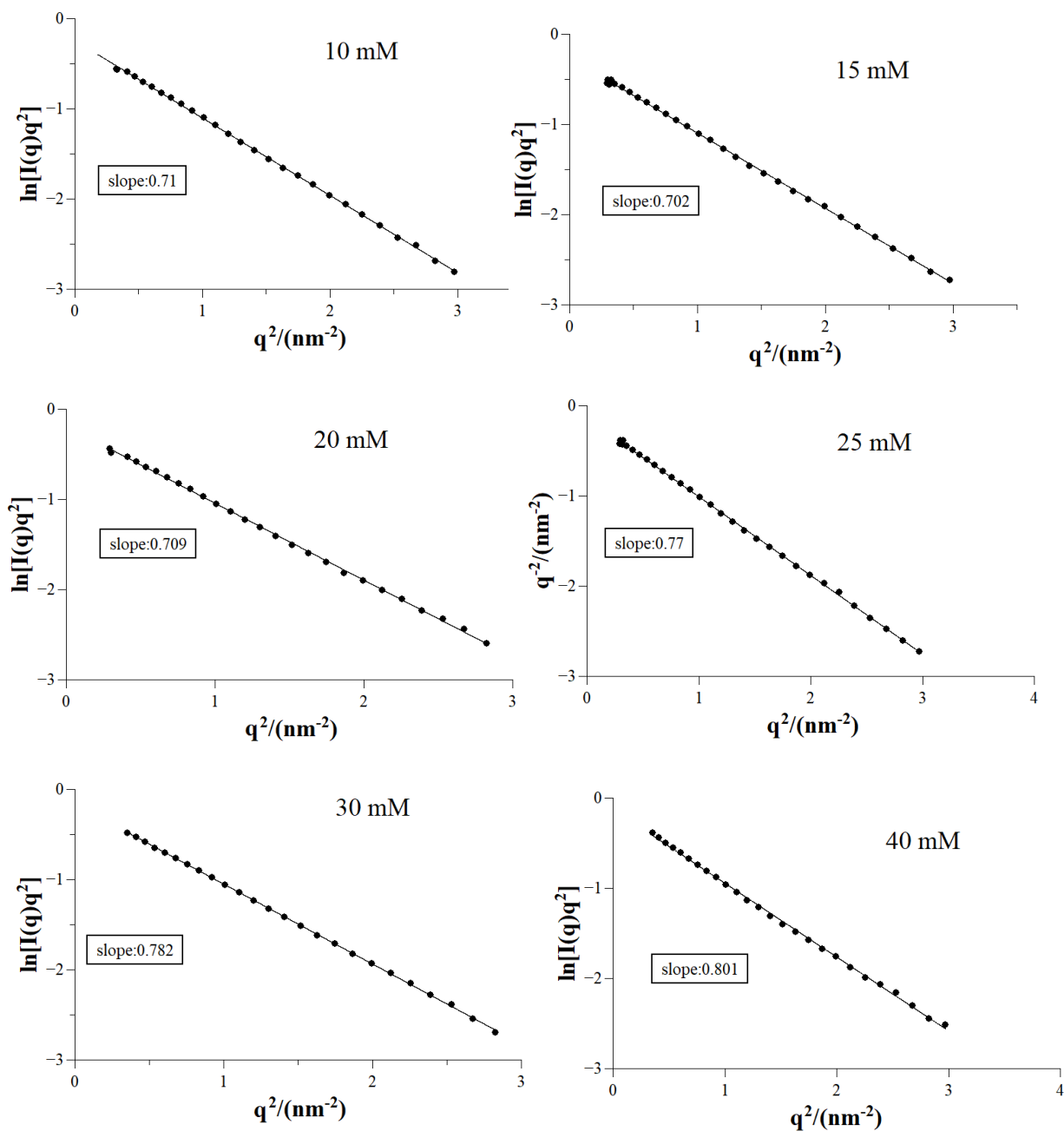


Figure A12. The fitted Kratky-Porod curves for samples containing 27.5 mM TDMAO / 0.275 mM L35 / 22.5 mM LiPFOS / different dodecyl acrylate concentrations.

9.3.2 Appendix to Studies with Isooctyl Acrylate Monomer

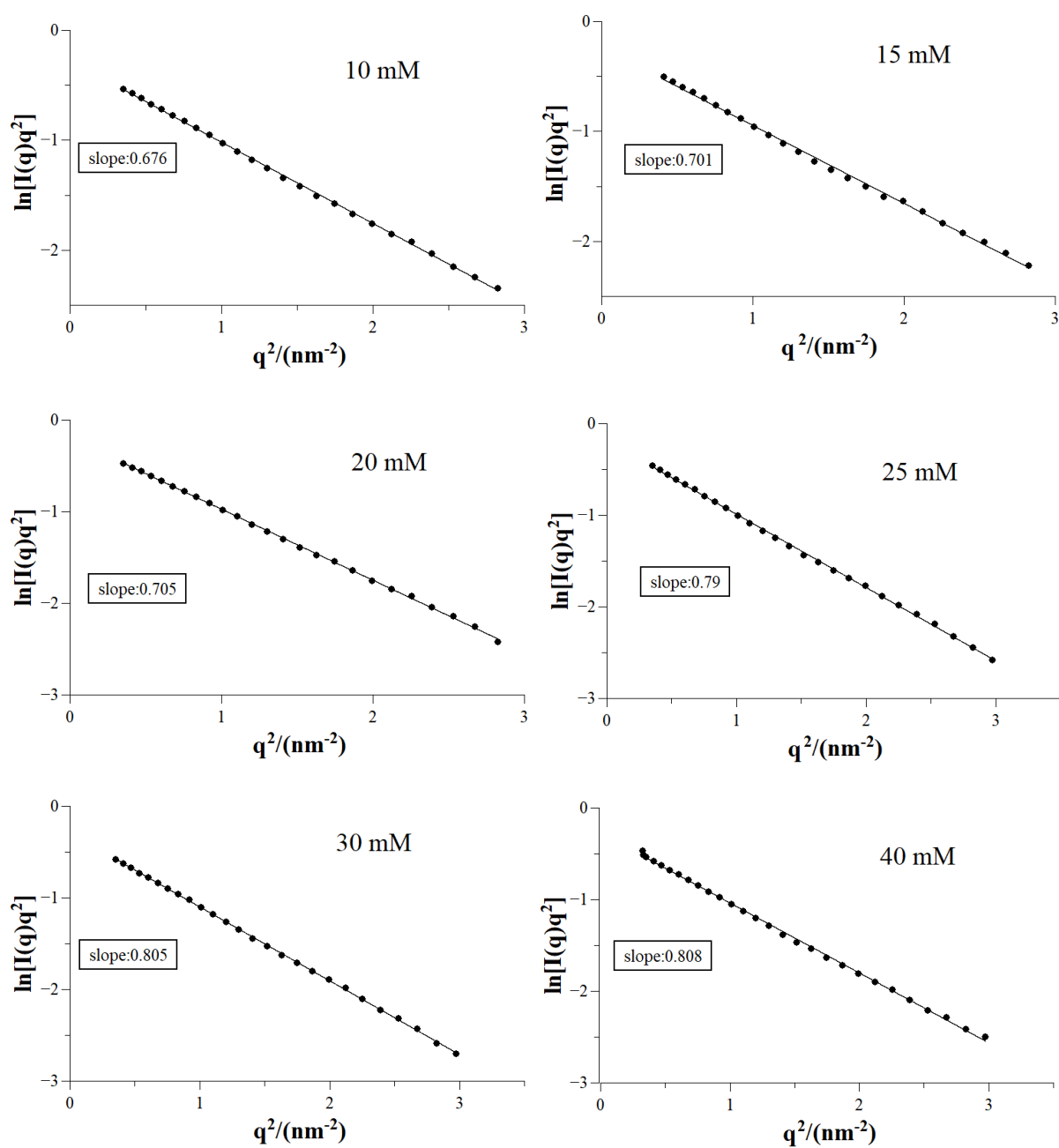


Figure A13. The fitted Kratky-Porod curves for samples containing 27.5 mM TDMAO / 0.275 mM L35 / 22.5 mM LiPFOS / different isooctyl acrylate concentrations.

9.3.3 Appendix to Studies with Hexyl Acrylate Monomer

9.3.3.1 Refractive Index Increment

Table A4. Refractive index increments for different concentration of hexyl acrylate in 50 mM TDMAO / 0.5 mM L35 at 25 °C:

Hexyl acrylate amount (mM)	dn/dc (ml/g)
0	0.1490
20	0.1397
30	0.1361
50	0.1304
60	0.1281
70	0.1260
80	0.1242
90	0.1225

Table A5. Refractive index increments for different ratio of hexyl acrylate to 27.5 mM TDMAO / 0.275 mM L35 / 22.5 mM LiPFOS at 25°C.

Hexyl acrylate amount (mM)	dn/dc (ml/g)
0	0.0598
7	0.0632
10	0.0644
20	0.0679
25	0.0694
30	0.0707

9.3.3.2 Kratky-Porod Plots

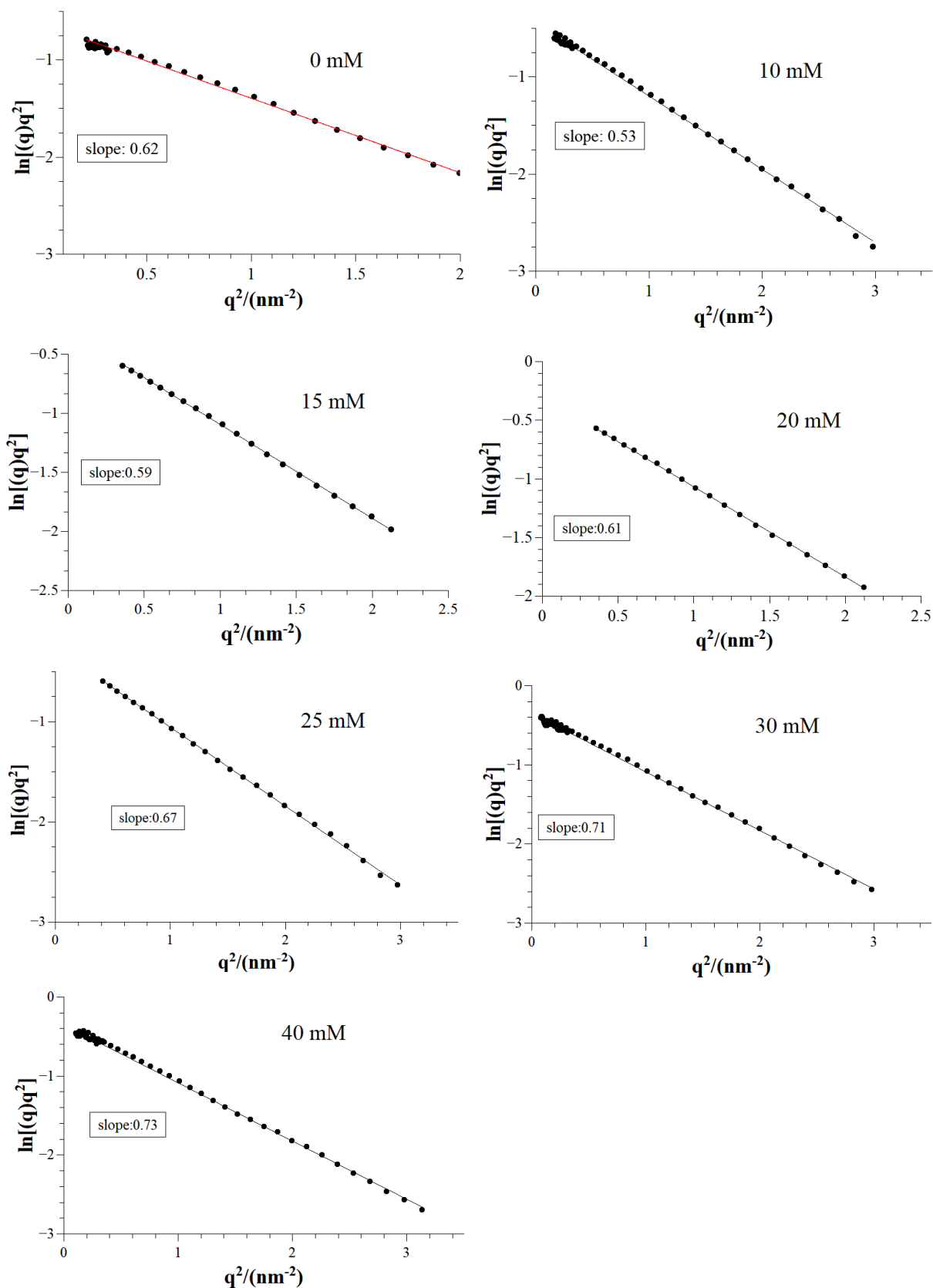


Figure A14. The fitted Kratky-Porod curves for samples containing 27.5 mM TDMAO / 0.275 mM L35 / 22.5 mM LiPFOS / different hexyl acrylate concentrations.

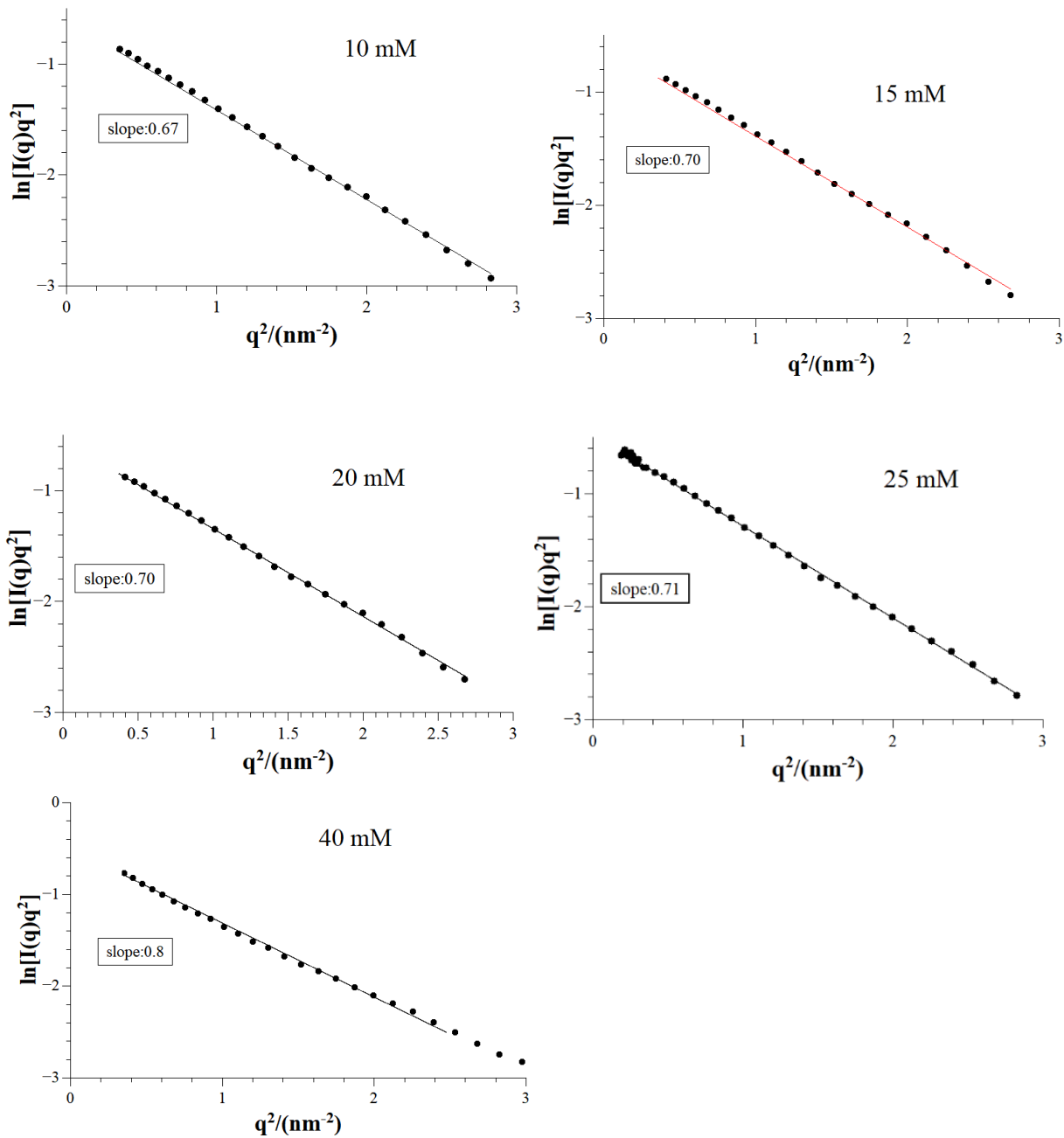


Figure A15. The fitted Kratky-Porod curves for polymerized samples containing 27.5 mM TDMAO / 0.275 mM L35 / 22.5 mM LiPFOS / different hexyl acrylate concentrations.

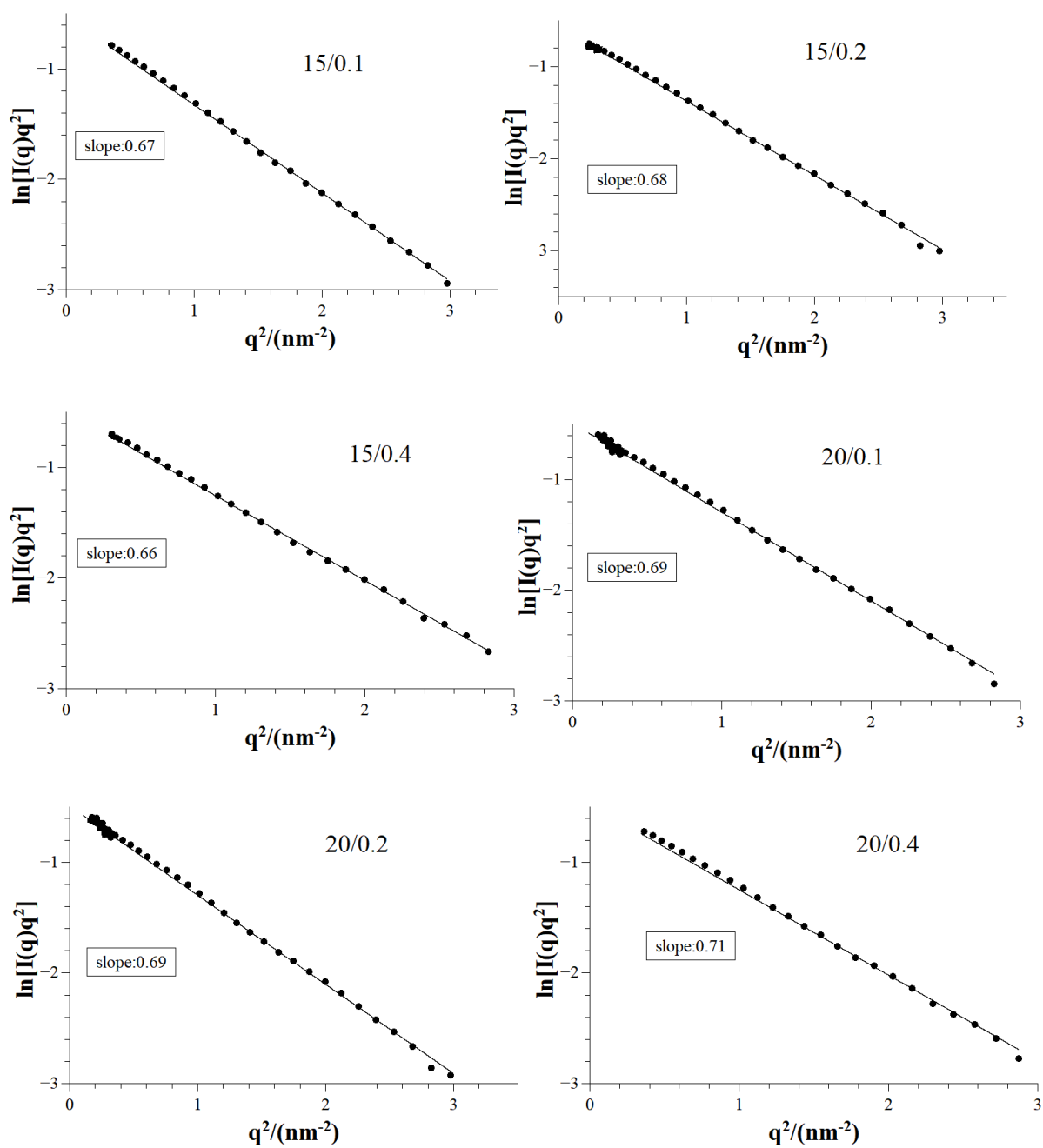


Figure A16. The fitted Kratky-Porod curves for cross-linked polymerized samples containing 27.5 mM TDMAO / 0.275 mM L35 / 22.5 mM LiPFOS / different hexyl acrylate concentrations for different cross-linker ratios.

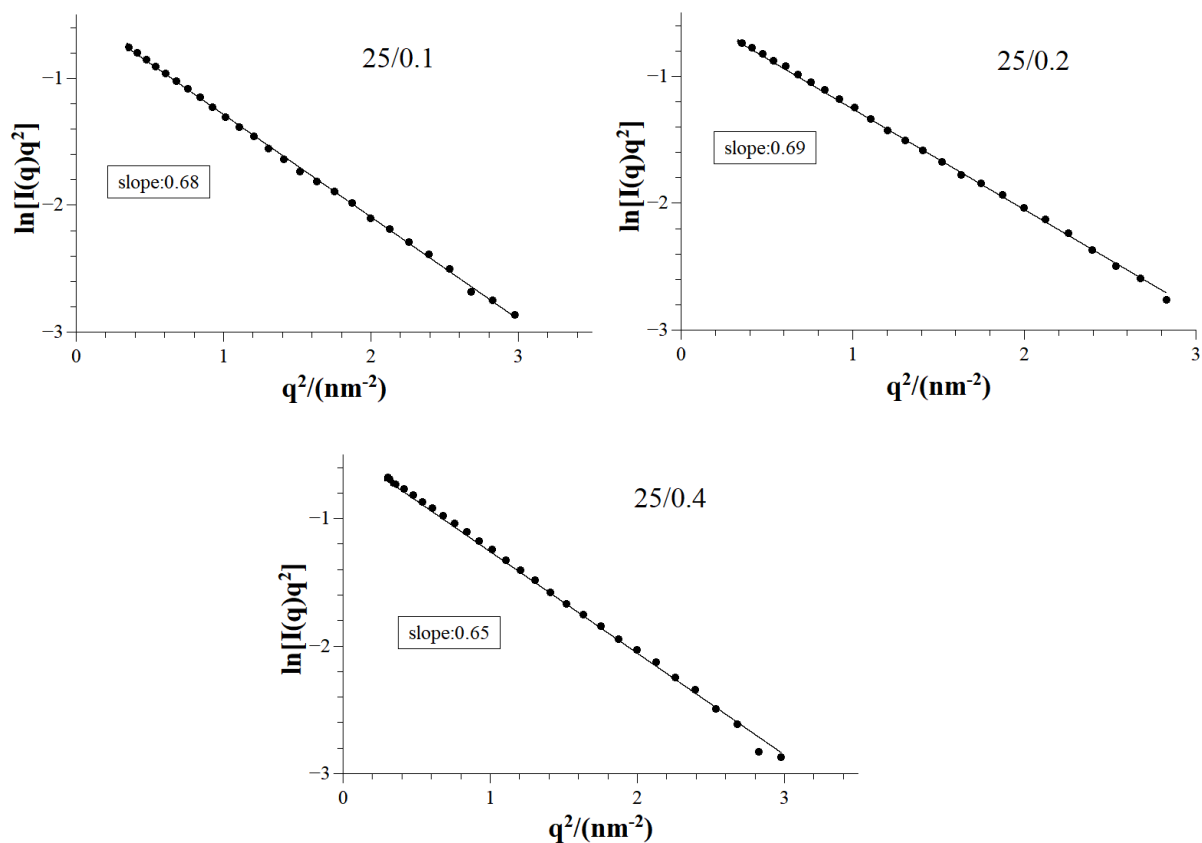


Figure A16 (continue). The fitted Kratky-Porod curves for cross-linked polymerized samples containing 27.5 mM TDMAO / 0.275 mM L35 / 22.5 mM LiPFOS / different hexyl acrylate concentrations for different cross-linker ratios.

9.3.3.3 Porod-Debye Plots

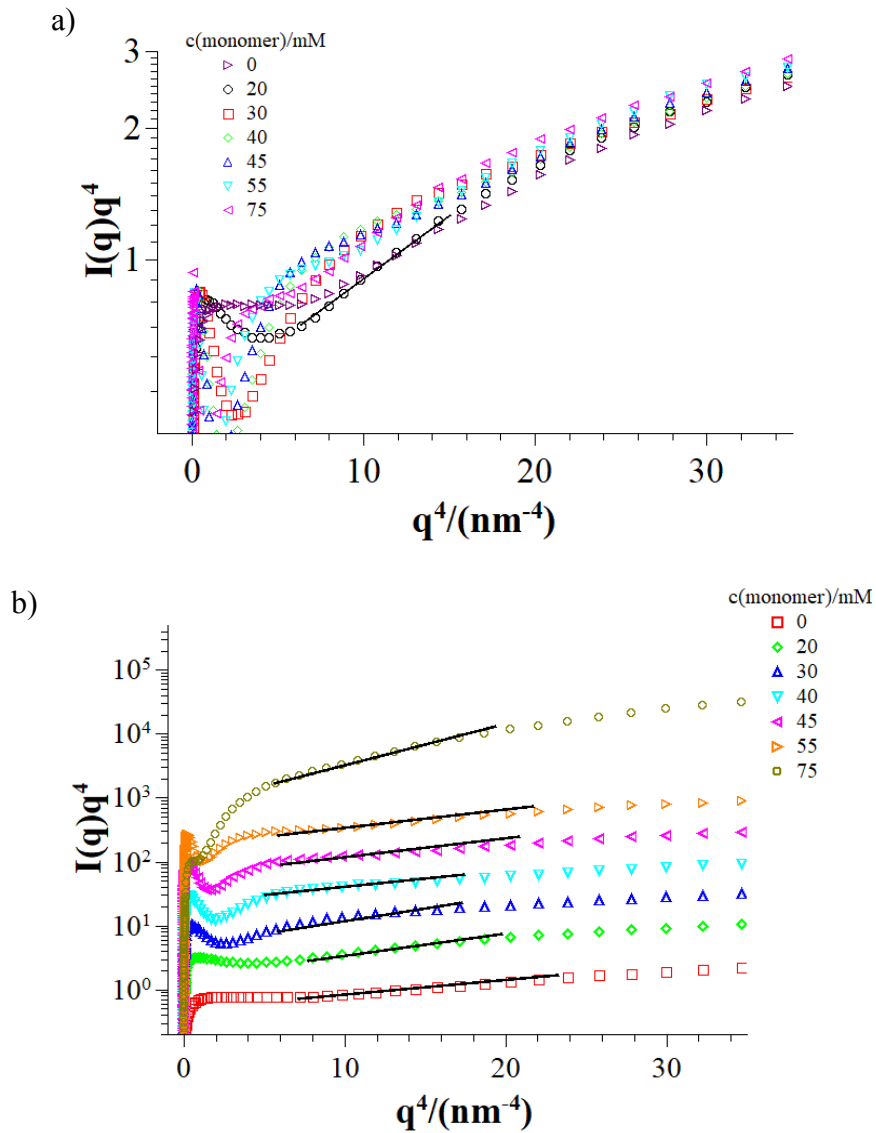


Figure A17. a) $I(q)q^4$ vs q^4 plots for the samples of 50 mM TDMAO / 0.5 mM L35 / different hexyl acrylate concentrations. **b)** For clarity the data sets were multiplied each with a scale factor of 3. The intercept of the straight line is the specific surface S/V .

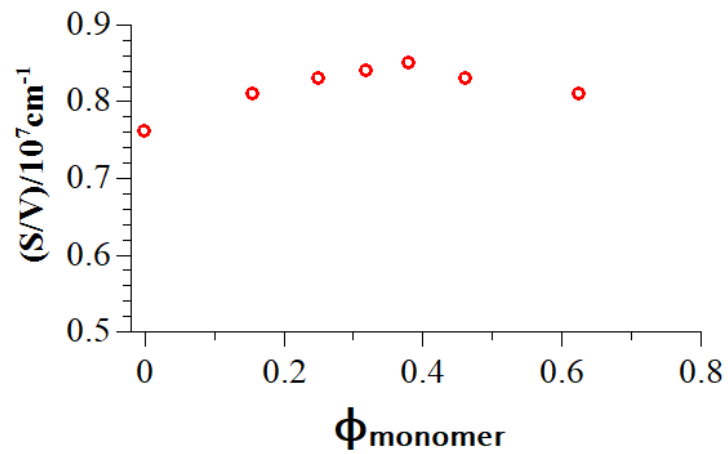


Figure A18. Specific surface of the system of 50 mM TDMAO / 0.5 mM L35 / different hexyl acrylate concentrations deduced by Porod analysis as function of monomer volume fraction.

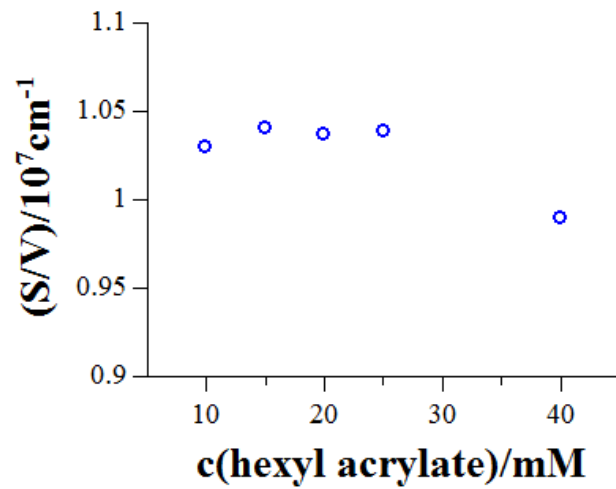


Figure A19. Specific surface of the polymerized sample of 27.5 mM TDMAO / 0.275 mM L35 / 22.5 mM LiPFOS / different hexyl acrylate concentrations deduced by Porod analysis as function of monomer concentration.

9.3.3.4 Small Angle Neutron Scattering (SANS) of samples before and after polymerization

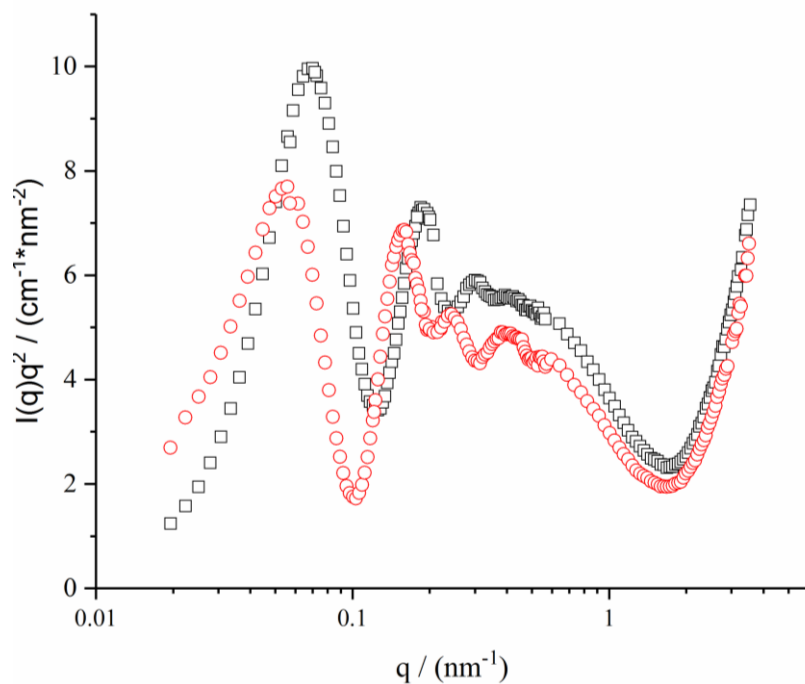


Figure A20. $I(q)q^2$ vs q plot of the SANS data for sample 27.5 mM TDMAO / 0.275 mM L35 / 22.5 mM LiPFOS / 10 mM hexyl acrylate *black square*: before polymerization, *red circle*: after polymerization.

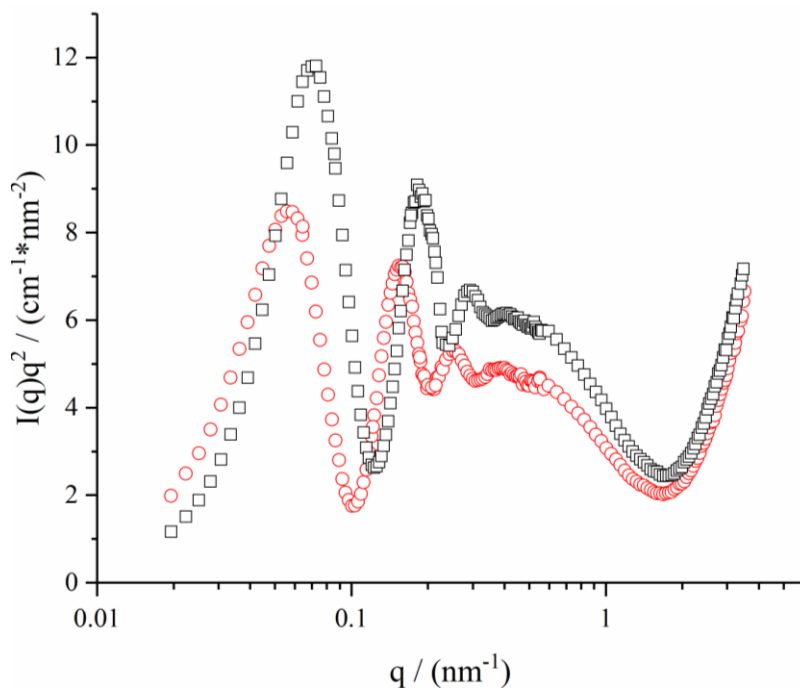


Figure A21. $I(q)q^2$ vs q plot of the SANS data for sample 27.5 mM TDMAO / 0.275 mM L35 / 22.5 mM LiPFOS / 15 mM hexyl acrylate *black square*: before polymerization, *red circle*: after polymerization.

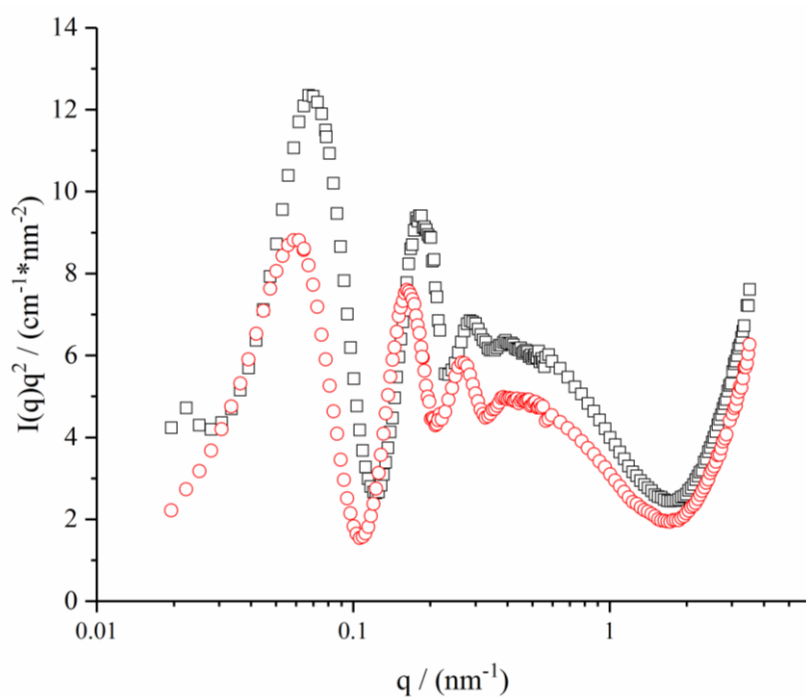


Figure A22. $I(q)q^2$ vs q plot of the SANS data for sample 27.5 mM TDMAO / 0.275 mM L35 / 22.5 mM LiPFOS / 20 mM hexyl acrylate *black square*: before polymerization, *red circle*: after polymerization.

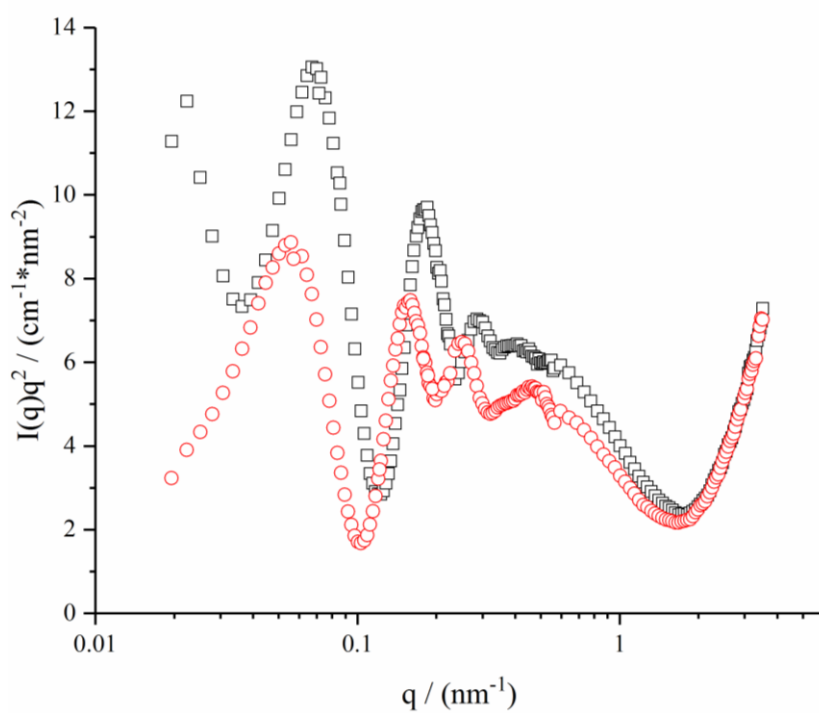


Figure A23. $I(q)q^2$ vs q plot of the SANS data for sample 27.5 mM TDMAO / 0.275 mM L35 / 22.5 mM LiPFOS / 25 mM hexyl acrylate *black square*: before polymerization, *red circle*: after polymerization.

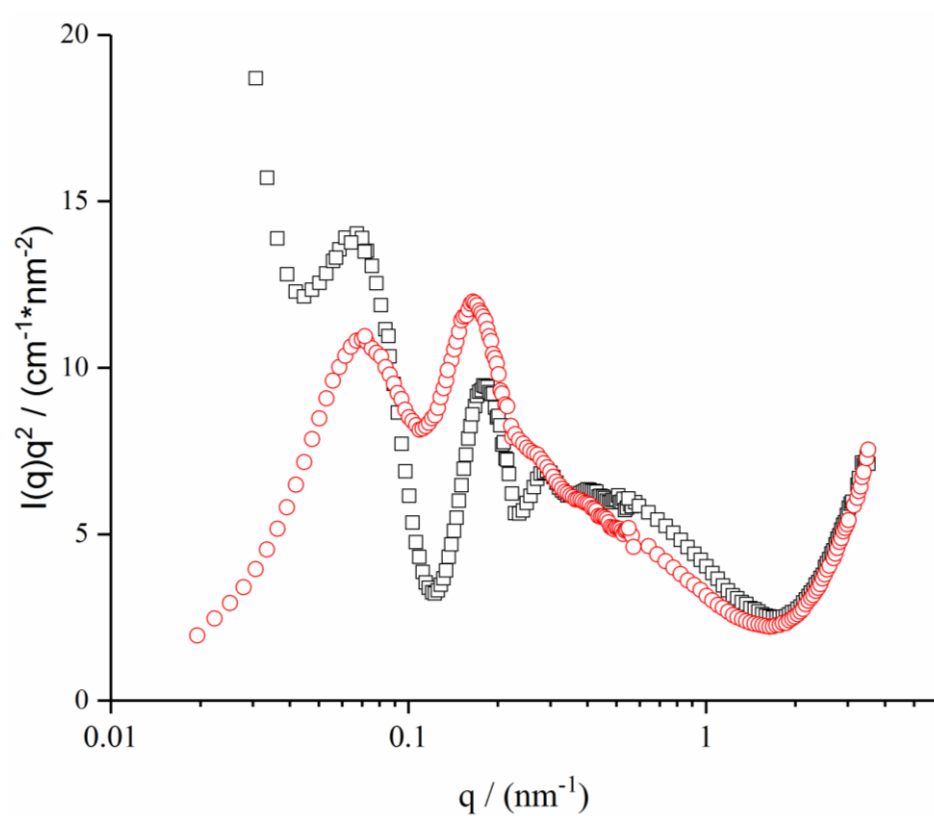


Figure A24. $I(q)q^2$ vs q plot of the SANS data for sample 27.5 mM TDMAO / 0.275 mM L35 / 22.5 mM LiPFOS / 40 mM hexyl acrylate *black square*: before polymerization, *red circle*: after polymerization.

9.3.3.5 Neutron spin echo measurements

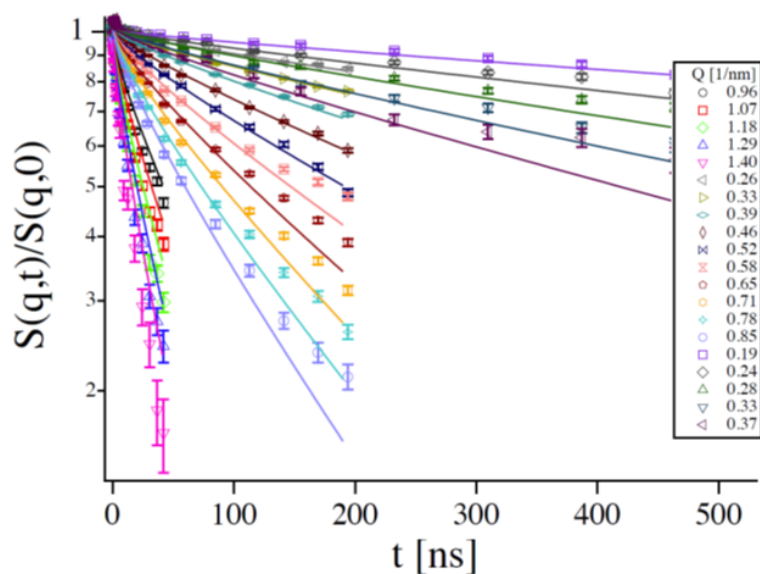


Figure A25. $S(q,t)$ of unpolymerized vesicles consisted from mixture of 27.5 mM TDMAO / 0.275 mM L35 / 22.5 mM LiPFOS / 20 mM hexyl acrylate ([Sample 2](#)). Solid lines are the fits of Zilman-Granek model.

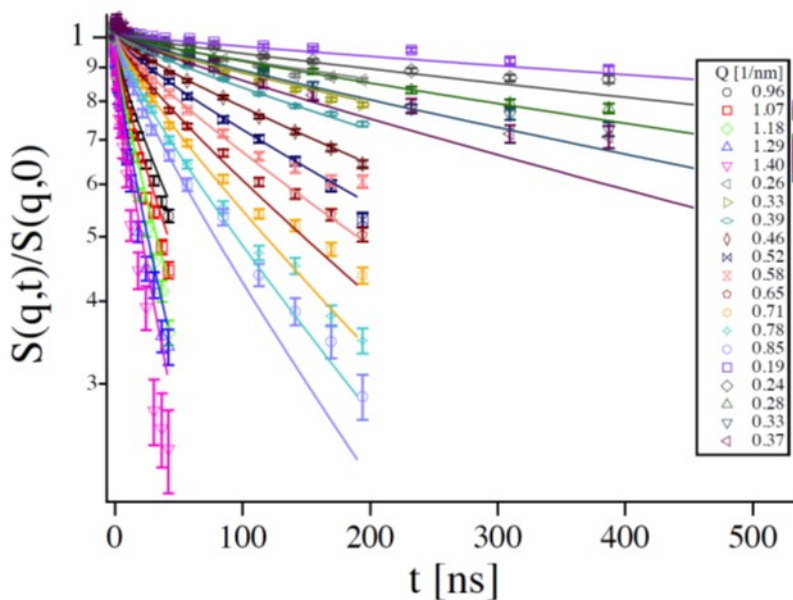


Figure A26. $S(q,t)$ of cross-linked polymerized vesicles consisted from mixture of 27.5 mM TDMAO / 0.275 mM L35 / 22.5 mM LiPFOS / 15 mM hexyl acrylate // 0.1 molar ratio of 1, 6-hexanediol diacrylate (with respect to the total monomer amount) ([Sample 3](#)). Solid lines are the fits of Zilman-Granek model.

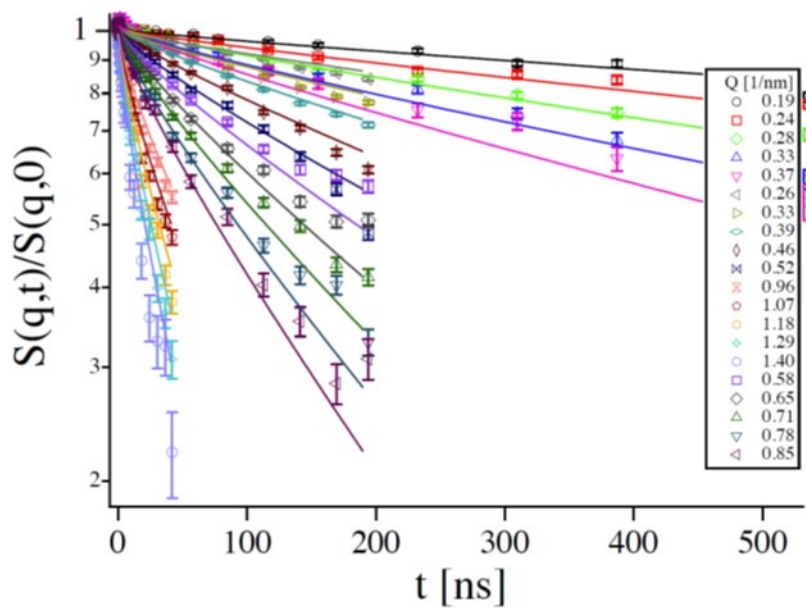


Figure A27. $S(q,t)$ of cross-linked polymerized vesicles consisted from mixture of 27.5 mM TDMAO / 0.275 mM L35 / 22.5 mM LiPFOS / 20 mM hexyl acrylate // 0.1 molar ratio of 1, 6-hexanediol diacrylate (with respect to the total monomer amount) ([Sample 4](#)). Solid lines are the fits of Zilman-Granek model.